FIBER BRAGG GRATING CHARACTERIZATION BY OPTICAL LOW COHERENCE REFLECTOMETRY AND SENSING APPLICATIONS

THÈSE N° 2726 (2003)

PRÉSENTÉE AU DÉPARTEMENT DE MICROTECHNIQUE

ECOLE POLYTECHNIQUE FÉDÉRALE DE LAUSANNE

POUR L'OBTENTION DU GRADE DE DOCTEUR ÈS SCIENCES

Par

Philippe Giaccari

Ingénieur Physicien diplômé de l'Ecole Polytechnique

Fédérale de Lausanne, Suisse

de nationalité suisse

Jury :

Prof. R. Salathé, directeur de thèse

Dr. H. Limberger, rapporteur

Prof. J. Botsis, rapporteur

Prof. E. Brinkmeyer, rapporteur

Prof. Ch. Boisrobert, rapporteur

Dr. H. Gilgen, rapporteur

Lausanne, EFPL

2003

Abstract

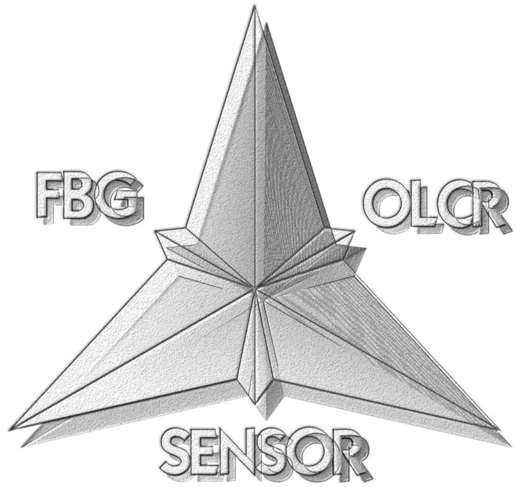

This work connects of three domains of fiber optics : the fiber Bragg gratings (FBG), the optical low coherence reflectometry (OLCR) and the fiber optical sensors (using FBGs, the OLCR or a combination of both).

Fiber Bragg gratings are fiber optic devices characterized by permanent and periodic changes of the fiber core refractive index, which translates into a narrowband spectral reflection. FBGs are widely used nowadays in the telecommunications field, for example as reflection filters or dispersion compensators. Moreover, their sensitivity to temperature and strain make them ideal for sensing applications, in particular due to their very small size, their immunity against electromagnetic fields and their multiplexing capabilities.

The major challenge with FBGs is to locally characterize the grating properties, in particular the core refractive index distribution along the grating. These data allow correcting imperfections during the writing process or to determine the distributions in sensing applications. In this work, we have reconstructed the complex coupling coefficient distribution of the grating by combining the OLCR technique and a reconstruction technique called "layer-peeling". A novel design for the OLCR has been proposed and realized. This instrument measures precisely the amplitude and phase of the complex fiber Bragg grating impulse response with micrometer resolution and a noise level below -120 dB. Using the layer-peeling method, the FBG complex coupling coefficient can be retrieved with a 20 μm resolution and an error of less than 5% (this value is obtained by comparing the reconstructions from both sides of the grating).

Many studies have been conducted on axial strains in various samples and various experimental conditions. The most promising result concerns the study of non-homogeneous strain fields with the reconstruction technique that combines the OLCR and the "layer-peeling". The study of transversal strain field has also been conducted with FBGs written in birefringent fibers. A non-linear behavior has been observed and explained with the rotation of the fiber eigen axis. An important sensitivity anisotropy for different angles has been observed, but not fully explained.

The influence of humidity and temperature on a polyimide coated FBG was also investigated. The sensitivities were measured as a function of the coating thickness. From this analysis a novel concept for an intrinsic relative humidity sensor using polyimide-recoated fiber Bragg gratings has been proposed. Tests in a controlled environment indicate that the sensor has a linear, reversible and accurate response behavior between 10 and 90 %RH and between 13 and 60 °C.

The last but not least, a new fiber optic sub-nanometric scale vibrometer based on the OLCR technique has been developed. This sensor allows for the control of a fiber SNOM (Scanning Near-field Optical Microscopy) tip oscillations in the air and in water. A very good accuracy is achieved with a noise level around 1 pm. The compactness and the easiness to use (auto-calibration and stability) of this sensor open up new measurement fields for the SNOM technique as, for example, with biological samples in liquids.

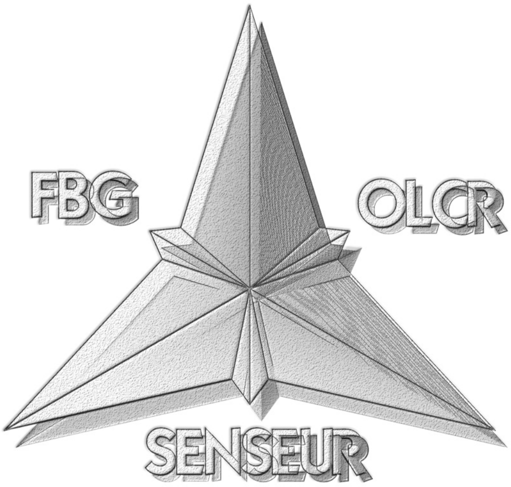

Résumé

Ce travail est la convergence de trois domaines des fibres optiques : les réseaux de Bragg dans les fibres optiques (FBG pour Fiber Bragg Gratings), la réflectométrie optique à basse cohérence (OLCR pour Optical Low Coherence Reflectometry) et enfin les senseurs à fibre optique (utilisant des FBGs, l'OLCR ou la combinaison des deux).

Les réseaux de Bragg dans les fibres optiques sont des changements permanents et périodiques de l'indice de réfraction du cœur de la fibre, qui réfléchissent une faible largeur spectrale. Les FBGs sont couramment utilisés dans le domaine des télécommunications, par exemple comme filtres en réflexion ou comme compensateurs de dispersion. Leur sensibilité aux variations de température et aux contraintes en font des éléments de premier choix pour diverses applications senseur, en particulier grâce à leur très petite taille, leur immunité aux champs électromagnétiques et enfin les multiples possibilités de multiplexage.

Le défi majeur dans l'utilisation des FBGs consiste à caractériser localement les propriétés du réseau, en particulier la distribution de l'indice de réfraction du cœur de la fibre le long du réseau. Une telle connaissance permet de corriger certaines imperfections lors de l'inscription du FBG ou de déterminer des distributions dans les applications senseur. Dans ce travail, nous sommes parvenus à reconstruire la distribution du coefficient de couplage complexe d'un réseau en combinant les mesures OLCR avec une méthode de reconstruction appelée "layer-peeling". Un design novateur d'OLCR a été proposé et réalisé. Cet instrument mesure précisément l'amplitude et la phase de la réponse impulsionnelle complexe du FBG avec une résolution micrométrique et un niveau de bruit inférieur à −120 dB. En appliquant la méthode de "layer-peeling", le coefficient de couplage complexe du réseau peut être retrouvé avec une résolution de 20 μm et une erreur inférieure à 5 % (cette valeur est obtenue par comparaison entre les reconstructions obtenues depuis les deux côtés du réseau).

De nombreuses études ont été menées sur les contraintes axiales dans différents échantillons et différentes conditions expérimentales. Le résultat le plus prometteur concerne l'étude de champs de contraintes non-homogènes grâce à la technique de reconstruction discutée précédemment qui combine l'OLCR et le "layer-peeling". L'étude de champs de contraintes transversales a également été conduite grâce à des FBGs gravés dans des fibres biréfringentes. Un comportement non linéaire est observé et expliqué par la rotation des axes propres de la fibre. Une importante anisotropie dans la sensibilité pour différents angles est également observée mais celle-ci n'a pu être totalement expliquée.

L'influence de l'humidité et de la température sur les réseaux de Bragg avec une gaine de protection en polyimide est étudiée. Les sensibilités ont également été mesurées en fonction de l'épaisseur de la gaine. A partir de cette analyse, un nouveau concept de capteur d'humidité relative est proposé basé sur des FBGs regainés avec du polyimide. Des tests en chambre climatique montrent que le senseur est linéaire, réversible et possède une réponse précise entre 10 et 90 %RH et entre 13 et 60 °C.

Pour terminer, un nouveau vibromètre sub-nanométrique à fibre optique a été développé, basé sur la technologie OLCR. Ce senseur permet le contrôle des oscillations d'une pointe SNOM dans l'air et dans l'eau (SNOM : Scanning Near-field Optical Microscopie ou Microscopie à balayage en champ proche). Une très bonne précision est obtenue avec un niveau de bruit autour de 1 pm. La compacité et la facilité d'utilisation (auto-calibration et stabilité) de ce capteur ouvrent de nouveaux domaines de mesures à la technique SNOM comme par exemple la mesure d'échantillons biologiques dans les liquides.

Table of Contents

Chapter 1

Introduction

1.1 State of the art

1.1.1 Fiber Bragg gratings

In 1978, Hill et al. reported the first formation of photoinduced gratings in germanosilicate optical fibers with an argon-ion laser light propagating inside the fiber core [1-1]. However, this discovery remained a lab curiosity since the inscription process only permitted the fabrication of gratings at the writing laser wavelength, and then these gratings fade away when used. A decade later, Meltz et al. introduced the side-writing interferometric technique, where the Bragg wavelength is independent from the writing laser wavelength [1-2]. This technique allows permanent Bragg gratings to be directly written into the fiber core using a holographic interferometer illuminated by a coherent ultraviolet light source. The grating profile can be completely tailored varying the refractive index modulation amplitude (apodization), the pitch period or the average refractive index (chirp) and the tilt (blaze).

Fiber Bragg gratings (FBG) have become a key component for optical fiber telecommunications as wavelength-division multiplexing devices, fiber laser reflectors, gain flattening devices and dispersion compensation element [1-3], and for sensing applications as temperature, strain, pressure, ultrasound, acceleration, high magnetic field and force, chemical elements [1-4, 1-5]. Temperature and strain effects are not independent and only one parameter can be determined from a single grating. In the general case, there are three strain components (one in the axial direction and two in the transverse plane) and the temperature. In a lot of situations the transverse strains are neglected and the temperature is constant so that a single grating can monitor the axial strain average in the grating region. A quasi-distributed mapping of strain (or temperature when the strain is constant) is achieved by multiplexing several grating in the wavelength, time or spatial domains or by a combination of these techniques [1-6]. The length of the gratings that can be produced ranges from 100 μm to several meters. Long gratings open new perspectives for distributed sensing and dispersion compensation, but in this case the local characterization of the grating parameters is required.

1.1.2 Local characterization of fiber Bragg gratings

An important topic of research about FBGs concerns the retrieval of the local grating parameters along the fiber axis, namely the refractive index distribution in the fiber core. Currently, two main directions are followed to spatially characterize a grating : side measurement techniques and mathematical reconstruction methods.

In the side measurement techniques, the refractive index modulation amplitude, average refractive index or grating period can directly be extracted from the diffraction measurement of a laser beam that crosses the grating in a direction orthogonal to the fiber axis [1-7 to 1-9]. Refractive index modulation amplitude as low as 10^{-5} can be detected with a spatial resolution of 10 μm [1-8].

In the mathematical reconstructions methods, the distributed grating parameters are reconstructed from the spectral or impulse responses. The methods that are limited to amplitude or phase information solely are not interesting in arbitrary FBG characterization as they have strong requirements, for example monotonic varying chirp functions [1-10 to 1-12]. For week gratings, the complex coupling coefficient of the grating is proportional to the complex impulse response that can be directly measured or obtained by the Fourier transform of the complex spectral response [1-10, 1-13]. For stronger gratings, a backscattering technique is necessary [1-14, 1-15]. Some methods use an iterative process where at each step a theoretical grating profile and his reflection or phase spectrum are generated and compared with a measured spectrum [1-16 to 1-18].

The side measurement techniques are not suitable for sensing applications where the FBG is embedded in other materials, for example composite devices. For this reason, we have focused on the mathematical reconstruction methods. The most performing mathematical methods, based on back-scattering techniques, require a complex spectral or impulse response of the grating.

1.1.3 Optical low coherence reflectometry

An efficient way to measure the complex impulse response of a fiber Bragg grating is based on its analysis with an optical low coherence reflectometer (OLCR). The OLCR technique was first used to characterize single mode fibers in the late 80s [1-19 to 1-22]. An OLCR uses a broadband source coupled to an all-fiber Michelson interferometer. The reference arm contains a broadband mirror, whereas the interrogation arm contains the device under test. The portion of the test arm that should be analyzed is selected by balancing its optical path length with that of the reference arm and can be defined with a micrometer precision [1-23]. The complex OLCR measurement of a FBG corresponds to the convolution between the complex impulse response of the grating and the degree of coherence of the light source. The degree of coherence of a Gaussian light source is also a Gaussian function, for which the time bandwidth corresponds to the light coherence time (inversely proportional to the spectral bandwidth of the light source).

The OLCR technique has been used to find the position, the length and the coupling coefficient of homogenous Bragg gratings [1-23, 1-24], to demultiplex several gratings in the space domain [1-25] and to measure the complex spectral response of FBGs [1-26 to 1-28]. The most promising aspect of OLCR is the possibility to retrieve the spatial information along the grating for distributed measurements [1-29].

1.2 Motivation and thesis outline

Recently, a very efficient backscattering technique called layer-peeling has been applied to the FBG domain for designing new kinds of gratings that exhibit special features, for example zero dispersion properties [1-30, 1-31]. The layer-peeling method is based on the causality principle and therefore strongly depends to the FBG impulse response. This indicates that the OLCR measurements and the layer-peeling reconstruction method form a promising pair to locally characterize FBGs.

In this work, a new OLCR interferometer has been conceived and realized to accurately measure the complex impulse response of a FBG (amplitude and phase). The reconstruction of different types of FBGs has been performed using the layer-peeling method. The local characterization of an axial strain field has also been determined by the combination of a FBG gauge, OLCR measurement and layer-peeling.

Other sensing applications have been studied, including transversal strain measurement (FBG gauges written in polarization maintaining fibers), humidity and temperature measurements (polyimide coated FBG gauges) as well as vibration amplitude measurements (OLCR interferometer technique).

Chapter 2 presents the fundamentals of fiber Bragg gratings : definition and properties, fabrication and characterization methods used in this work. A new writing set-up is presented that allows the writing of FBGs with different Bragg wavelengths using the same phase mask.

Chapter 3 describes the theoretical simulations of the spectral response using the T-matrix method, and the theoretical reconstructions of the grating distributions from the grating complex spectral response using the layer-peeling method. Several simulations have been made to study the important parameters concerned in the reconstruction process. An evolution of the T-matrix and the layer-peeling algorithm is proposed, which takes account propagation losses in the grating.

Chapter 4 focuses on the OLCR fundamentals, the development of the new OLCR set-up and the experimental reconstruction of several homogeneous and non-homogeneous FBGs.

Chapter 5 presents the combined use of FBGs and the reconstruction method (OLCR & layer-peeling) for distributed axial strain field characterization; the behavior of FBGs subjected to transversal strain fields is also studied for gratings written in low-birefringent or in polarization maintaining fibers.

Chapter 6 resumes the analysis conducted on the sensitivity of polyimide coated FBGs to temperature or relative humidity changes.

Chapter 7 describes the vibration amplitude sensor developed for the control of SNOM tips (Scanning Near-field Optical Microscopy).

1.3 References

1-1 K.O. Hill, F. Fujii, D. C. Johnson and B. S. Kawasaki, "*Photosensitivity on optical fiber waveguides; application to reflection filter fabrication*", Appl. Phys. Lett. 32, 647-9 (1978)

1-2 G. Meltz, W. W. Morey and W. H. Glenn, "*Formation of Bragg gratings in optical fiber by transverse holographic method*", Opt. Lett. 14, 823-5 (1989)

1-3 V. Mizrahi, "*Components and devices for optical communications based on UV-written-fiber phase gratings*", Tech. Digest Int. Conf. on Optical Fiber Commun. (CA, USA), 243-4 (1993)

1-4 Y.-J. Rao, "*In-fiber Bragg grating sensors*", Meas. Sci. Technol. 8, 355-75 (1997)

1-5 A. D. Kersey, M. A. Davis, H. J. Patrick, M. LeBlanc, K. P. Koo, C. G. Askins, M. A. Putnam and E. J. Friebele, "*Fiber Grating Sensors",* Journ. of Lightwave Tech. 15, 1442-63 (1997)

1-6 A.D. Kersey, M.A. Davis, H.J. Patrick, M. LeBlanc, K.P. Koo, C.G. Askins, M.A. Putnam and E.J. Friebele, "*Fiber Grating Sensors",* Journ. of Lightwave Tech. 15, 1442-63 (1997)

1-7 M. Janos, J. Canning, M.G. Sceats, "*Incoherent-scattering Losses in Optical-Fiber Bragg Gratings*", Optics Letters, 21, p.1827-1829 (1996)

1-8 P.A. Krug, R. Stolte, R. Ulrich, "*Measurement of index modulation along an optical fiber Bragg grating*", Optics Letters, 20, p. 1767 (1995)

1-9 F. El-Diasty, A. Heaney, T. Erdogan, "*Analysis of fiber Bragg gratings by a side-diffraction interference technique*", Applied Optics, 40, **6**, p. 890-896 (2001)

1-10 S. Huang, M. M. Ohn, M. LeBlanc and R. M. Measures, "*Continuous arbitrary strain profile measurements with fiber Bragg gratings*", Smart Mater. Struct. 7, 248-56 (1998)

1-11 M. A. Muriel and A. Carballar, "*Phase, time delay, and impulse response reconstruction from reflected power in uniform fiber Bragg gratings*", Proc. LEOS'96, 380-1 (1996)

1-12 J. Skaar and H. E. Engan, "*Distributed intragrating sensing using phase retrieval*", Proc. OFS'13, 588-591 (1999)

1-13 M. A. Muriel, J. Azaña and A. Carballar, "*Time-frequency representation applied to fiber grating synthesis*", Proc. ECOC'98, 383-4 (1998)

1-14 E. Brinkmeyer, "*Simple algorithm for reconstruction fiber gratings from reflectometric data*", Opt. Lett. 20, 810-12 (1995)

1-15 M. Froggatt, "*Distributed measurement of the complex modulation of a photoinduced Bragg grating in an optical fiber*", Appl. Opt. 35, 5162-4 (1996)

1-16 S. Huang, M. M. Ohn, M. LeBlanc and R. M. Measures, "*Bragg intragrating structural sensing*", Appl. Opt. 34, 5003-9 (1995)

1-17 M. A. Muriel and A. Carballar "*Internal Distributions in fiber Bragg gratings*", IEEE Phot. Tech. Lett. 9, 955-7 (1997)

1-18 J. Skarr and K. M. Risvik, "*A genetic algorithm for the inverse problem in synthesis of fiber gratings",* Journ. of Lightwave Tech. 16, 1928-32 (1998)

1-19 K. Takada, I. Yokohama, K. Chida and J. Noda, "*New measurement system for fault location in optical waveguide devices based on an interferometric technique*", Appl. Opt. 26, 1603-6 (1987)

1-20 B. L. Danielson and C. D. Whittenberg, "*Guided-wave reflectrometry with micrometer resolution*", Appl. Opt. 26, 2836-42 (1987)

1-21 H.H. Gilgen, R.P. Novak, R.P. Salathé, W. Hodel, P. Beaud, "*Submillimeter optical Reflectometry*", Journal of Lightwave Technology, 7 (8), p. 1225-1233 (1989)

1-22 P. Beaud, J. Schultz, W. Hodel, H.P. Weber, H.H. Gilgen, R.P. Salathé, "*Optical reflectometry with micrometer resolution for investigation of integrated optical devices*", IEEE Journal of Quantum Electronics, 25 (4), p. 755-759 (1989)

1-23 H. G. Limberger, P.Y. Fonjallaz, P. Lambelet and R. P. Salathé, "*OLCR characterization of efficient Bragg grating in optical fiber*", Proc. SPIE 2044, 272-83 (1993)

1-24 P. Lambelet, P.Y. Fonjallaz, H. G. Limberger, R. P. Salathé, Ch. Zimmer and H. H. Gilgen; "*Bragg grating characterization by optical low-coherence reflectometry*", IEEE Phot. Tech. Lett. 5, 567-7 (1993)

1-25 M. Volanthen, H. Geiger and J. P. Dakin, "*Distributed grating sensors : an alternative to multiplexed grating arrays ?*", Proc. SPIE 3042, 372-82 (1997)

1-26 M. Volanthen, H. Geiger, M. J. Cole, R. J. Laming and J. P. Dakin, "*Low coherence technique to characterize reflectivity and time delay as a function of wavelength within a long fiber grating*", Electr. Lett. 32, 757-8 (1996)

1-27 I. Petermann, B. Sahlgren, J. Skaar, P.Y. Fonjallaz and R. Stubbe, "*Phase distribution measurement of fiber Bragg gratings with white light interferometry",* Proc. ECOC'98, 399-400 (1998)

1-28 S.D. Dyer and K.B. Rochford, "*Low-coherence interferometric measurements of fibre Bragg grating dispersion*", Electron. Lett., 35, 1485-1486 (1999)

1-29 M. Volanthen, H. Geiger and J. P. Dakin, "*Distributed grating sensor using low-coherence reflectometry",* Journ. of Lightwave Tech. 15, 2076-82 (1997)

1-30 R. Faced, M.N. Zervas and M.A. Muriel, "*An efficient inverse scattering algorithm for the design of nonuniform fiber Bragg gratings*", J. Quantum Electron., 35, p. 1105-1115 (1999)

1-31 J. Skaar, L. Wang and T. Erdogan, "*On the systhesis of fiber Bragg gratings by layer peeling*", J. Quantum Electron., 37 (2), p. 165-173 (2001)

Chapter 2

Fiber Bragg Gratings

The main principles of optical fibers and fiber Bragg gratings (FBG) are described in this chapter. The FBG fabrication and optical fiber photosensitivity characterization are also discussed. Finally, the characterization methods for FBGs and the gratings sensitivity to temperature and strain are presented.

2.1 Optical fiber

2.1.1 Optical fiber principle

An optical fiber consists of an inner cylinder with a diameter of a few micrometers (core) surrounded by an outer cylindrical layer of smaller refractive index (cladding), as seen in Fig. 2-1. The refractive index difference ensures total reflections at the core-cladding interface, allowing for propagation of the light along the fiber. The maximum entrance angle θ (Fig. 2-1) corresponds to an internal reflection angle at the critical angle θ_c, and it is found from the law of refraction (Snell's Law)

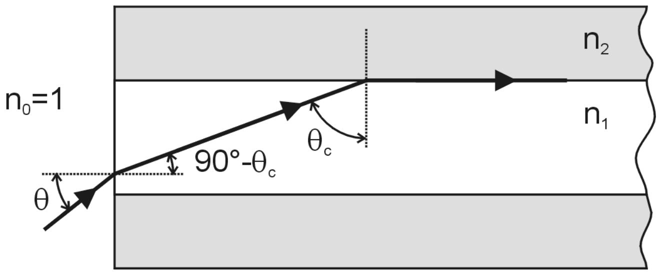

Fig. 2-1 Fiber geometry for total reflection at the critical angle

$$\begin{aligned} n_0 \sin(\theta) &= n_1 \sin(\pi/2-\theta_c) = n_1 \cos(\theta_c) \\ n_1 \sin(\theta_c) &= n_2 \sin(\pi/2) = n_2 \end{aligned} \tag{2-1}$$

The numerical aperture NA of the fiber is defined as $n_0 \cdot \sin(\theta)$, and it can be found from equations (2-1), and the following relation is obtained :

$$NA = \sin(\theta) = \sqrt{n_1^2 - n_2^2} \tag{2-2}$$

where n1 and n2 are the refractive index of the core and the cladding, respectively. The electromagnetic field propagation in waveguides was solved at the beginning of the 20th century from Maxwell's equations and it was shown that a finite number of modes can propagate along the fiber (Appendix A). Waveguides as optical fibers also support radiative modes, which form a continuum and correspond to unguided refracted rays. All the guided modes have their own propagation velocity and their specific field distribution. Moreover, the guided modes present a cutoff wavelength, apart from the lowest order mode.

The entire fiber can also guide modes with the propagation conditions at the cladding-air interface. Such modes are called cladding modes. Energy transfer is possible between the core modes and the cladding modes.

Pure silica glasses are mainly used to fabricate optical fibers. Adding dopants like germanium, nitrogen, and phosphorus in the fiber core creates the refractive index difference between the core and the claddings and modifies the core photosensitivity. Co-dopants like tin and boron are used to modify the fiber numerical aperture and the photosensitivity. Optically active fibers are obtained by integration of rare earth dopants. Sufficient index difference and fairly close thermal-expansion coefficients have to be guaranteed. Standard telecom fibers are made of pure silica claddings and about 3% wt. germanium doped silica core. Other glass materials are sometimes used as borosilicate (for example in polarization maintaining fibers, as shown in section 2.1.2) and fluoride glasses.

2.1.2 Types of optical fibers

The optical fibers can be classified as a function of the number of modes supported at a given wavelength :

- Single-mode fiber : only the fundamental mode is possible, with two orthogonal polarizations admitted
- Multi-mode fiber : several modes are supported by the waveguide, each one exhibiting a different field distribution and propagation constant

Standard single-mode fibers are of step-index type, that is, there is a discontinuity of refractive index between the core and the cladding. For single mode operation in the range 1300 – 1550 nm, the fiber core has a diameter between 4 and 9 μm (the fiber cladding diameter is 125 μm for fibers used in telecommunications). Multi-mode fibers are sometimes of step-index type but often they are of graded index type. In graded index fibers, the refractive index varies continuously between the core and the cladding in order to compensate the modal dispersion in multimode fibers (the shortest path has the highest index, and therefore the propagation velocity will be slower for the light following this path than for the zigzag rays propagating in lower-index regions).

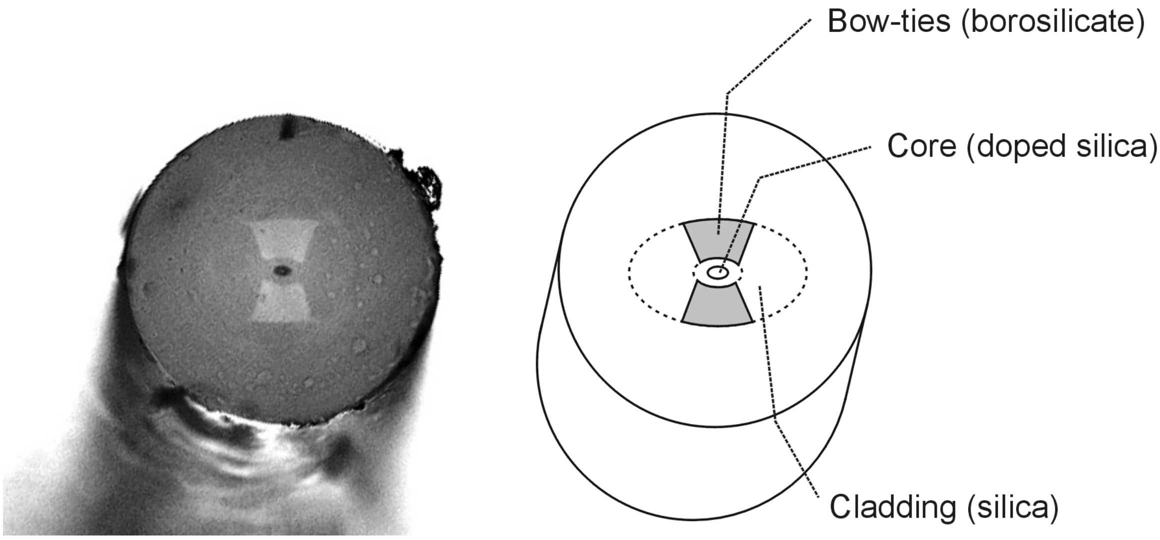

Fig. 2-2 Polarization maintaining fiber of bow-tie type (left) and main regions (right)

Single-mode fibers with a cylindrical symmetry can be considered as two modes structures, since two orthogonal polarizations are permitted. Both modes are degenerated. Small perturbations in the fiber geometry or material properties (structural or induced by external conditions) lead to birefringence that changes the velocity of both polarization modes and removes the degenerency. Due to nearly identical propagation constants, important cross-talk between the modes induces non negligible polarization mode dispersion (PMD). To avoid this dispersion, polarization-maintaining

(PM) fibers are used where both modes have well separated propagation constants. The separation is obtained by modifying the fiber geometry (elliptical core) or by inducing a refractive index anisotropy in the transverse plane of the fiber (birefringence induced by stress applying regions inside the cladding). For example in this work, we have used PM fibers of the bow-tie type. A micrograph of the cross-section of this fiber is presented in the left part of Fig. 2-2. The schematic drawing in the right picture fits precisely the left micrograph.

The bow-tie region is made of borosilicate. The silica and the borosicate glasses have different thermal expansion coefficient and then, residual stresses are created into the fiber perform during the cooling-down processus. Typical effective refractive index differences of $4 \cdot 10^{-4}$ are observed for our bow tie PM fiber. We observe in Fig. 2-2 that the core geometry is also modified, as it appears elliptical.

2.1.3 Fiber Parameters

a) Effective refractive index

We consider a single-mode, step index optical fiber and we define a relative index difference Δ :

$$\Delta = \frac{n_1 - n_2}{n_2} \tag{2-3}$$

In practice, for step index fibers, the relative index difference Δ is smaller than 1 % and weak guidance is admitted. We define a dimensionless parameter V called the normalized frequency

$$V = \frac{2\pi a}{\lambda}\sqrt{n_1^2 - n_2^2} \cong a k n_2 \sqrt{2\Delta} \tag{2-4}$$

where a is the core radius, λ the wavelength and $k = 2\pi/\lambda$. The V parameter indicates how far away from the cutoff (condition where the mode is no more guided) a given mode is. The closer to the cutoff the mode is, the deeper the evanescent field extends in the cladding. A single-mode-operating condition is possible when $V < 2.405$. The propagation constant β in the fiber corresponds to the solutions of the mode equations and then an effective refractive index of the guided mode n_{eff} can be defined as

$$n_{eff} = \beta / k \tag{2-5}$$

A good approximation of the effective refractive index n_{eff} is found in Appendix A and it can be expressed in terms of the V parameter, the wavelength and the fiber parameters (n_1, n_2 and a)

$$n_{eff}^2 \cong n_2^2 + \left(\frac{\lambda}{2\pi a}\right)^2 \left(1.1428 \cdot V - 0.9960\right)^2 \tag{2-6}$$

As the relative refractive index difference is small, the longitudinal components can be almost neglected and the mode is considered transversely linearly polarized (LP_{01} mode). We also define a cutoff wavelength under which another mode appear

$$\lambda_c = V\lambda / 2.405 \tag{2-7}$$

b) Group refractive index

The group delay τ that characterize the propagation time per unit length is well approximated by (Appendix A)

$$\tau = \frac{d\beta}{d\omega} = \frac{1}{c}\frac{d\beta}{dk} = \frac{N_2}{c}\left(1 + \Delta \cdot \left(1.3060 - \left(0.9960/V\right)^2\right)\right) \tag{2-8}$$

where $N_2 = d(kn_2)/dk$ is the group index of refraction of the cladding. For silica in the wavelength range 1300–1500 nm, the relative difference between N_2 and n_2 is less than 1.5 % [2-1]. The group delay is the inversely proportional to the group velocity and the group refractive index is defined as

$$n_g = \frac{c}{v_g} = c \cdot \tau \tag{2-9}$$

c) Dispersion

There are two differences between the light traveling in vacuum and along an optical fiber :

- Time delay : expresses the propagation delay per unit length
- Dispersion : expresses the time delay variation with the wavelength

Dispersion effects are a problem in telecommunication transmission since they broaden the pulse width. Four kind of dispersion can be identified :

- Material dispersion : the refractive index of the cladding and core are frequency dependent; for fused silica, the dispersion is negative at wavelength below 1300 nm and positive above 1300 nm
- Waveguide dispersion : equation (2-6) takes into account that the propagation constant for a given mode is wavelength dependent in a non linear manner, leading to another dispersion component
- Modal dispersion : each propagation mode has its own propagation parameters and then different modes travel at different velocities for the same wavelength
- Polarization mode dispersion : the birefringence in fibers modifies the propagation constant

For the single-mode fibers used in our experiments, the modal dispersion was negligible. Due to the sign change of the material dispersion around 1300 nm a zero-dispersion propagation is possible when the waveguide and material dispersion compensate each other. For step-index fibers, the zero-dispersion wavelength is close to 1300 nm. The tailoring of the waveguide structure (core profiling or segmenting) modifies the waveguide dispersion and then the zero-dispersion condition can be shifted (for example at 1550 nm) [2-2].

2.2 Fiber Bragg grating

2.2.1 Bragg reflections

In the study of crystals, it is known that X rays are reflected at well-defined directions due to the periodic arrangement of the atoms and these reflections are described by the Bragg equation. In the same way but at larger wavelengths, a periodic refractive index variation in the core of an optical fiber will exhibit specific reflections at the Bragg condition with an angle π (i.e. back-reflection)

$$\lambda_b = 2 \cdot n_{eff} \cdot \Lambda \cdot m \tag{2-10}$$

where λ_b is the peak reflection amplitude wavelength, n_{eff} the effective refractive index of the guided mode, Λ the grating period (Fig. 2-3) and m = 1, 2 , 3, … is the Bragg reflection order. For this reason these structures are called fiber Bragg gratings (FBG). FBGs in silica-based optical fiber (with approximate effective refractive index of 1.45) have a grating period between 450 and 500 nm for the lowest Bragg reflection order in the 1300–1500 nm range. Higher orders of reflection are possible but not considered here. Fig. 2-3 shows that a broadband light around the Bragg wavelength launched in the fiber (in(λ)) is partly back-reflected (r(λ)) with a resonance peak at the Bragg wavelength; the remaining light is instead transmitted (t(λ)). In the coupled-mode formalism [2-2], the FBG can be seen as a coupling perturbation between the forward and backward waves traveling in the fiber (Appendix C). It should be noted that a small part of the back-reflected light is also coupled in the cladding. For much larger grating periods, tens or hundreds of microns instead of half micron, the coupling of energy between the forward propagating core mode and the forward propagating cladding modes is possible. Such kind of grating is called long-period grating (LPG).

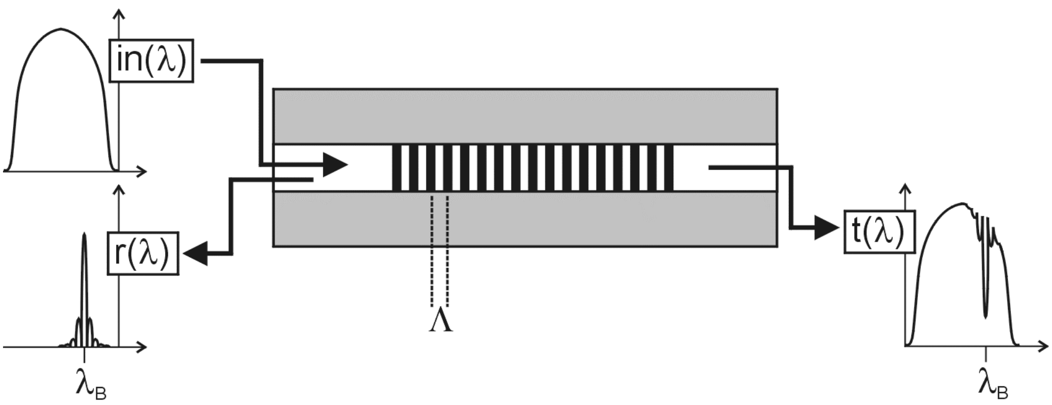

Fig. 2-3 Fiber Bragg grating and spectral effects

2.2.2 Photosensitivity in fibers

a) History

Hill and co-workers (1978, [2-3]) discovered photosensitivity of germanium-doped silica fibers. In their experiment, the 488nm laser light coupled into a fiber interfered with the Fresnel reflected beam and thus formed a weak standing-wave intensity pattern and a correspondent permanent index change. Lam and Garside (1981,[2-4]) showed that the magnitude of the photoinduced refractive index change depended on the square of the writing power, suggesting a two-photon process as the possible mechanism of refractive-index change. In 1989, Meltz et al. ([2-5]) demonstrated that a strong index of refraction change occurred when a germanium-doped fiber was exposed to UV light close to the absorption peak of a germania-related defect at a wavelength range of 240-250nm (single-photon process).

b) Origin of the photosentivity

The mechanisms that create the refractive index change are not fully understood. Several models have been proposed. The recurrent element in these theories is that the germanium-oxygen vacancy defects, Ge-Si or Ge-Ge (the so-called "wrong bonds") are responsible for the photoinduced index changes. The main models for the photosensivities of optical fibers are :

- The color center model [2-6, 2-7] : the breaking of the GeO defect by the UV light results in a GeE' center and the released electron is free to move within the glass matrix; when this electron is trapped, an additional absorption center appear in the glass and due to the Kramers-Kronig relation, a refractive index change is observed
- The dipole model [2-8, 2-9] : the photo-excitation of defects forms built-in periodic space-charge electric fields
- The stress-relief model [2-10, 2-11] : a refractive index change arises from the alleviation of built-in thermo-elastic stresses in the core of the fiber that was created during the fiber fabrication
- The compaction model [2-12, 2-13] : the laser irradiation induces density variations of the glass that also change the refractive index

c) Enhanced photosensitivity in silica optical fibers

i. Dopant concentration increase

The photosensitivity is highly increased by a high concentration of germanium. Nevertheless, this kind of fiber exhibits high NA, incompatible with telecommunication devices. Then, fibers containing boron have an enhanced photosensitivity. The maximal refractive index changes are higher and achieved faster than for any other kind of fiber. Boron codoping increases the photosensitivity of the fiber by allowing photoinduced stress relaxation. Another benefit of boron co-doping is the compatible NA with standard telecommunication fibers. Other co-doping as tin has been reported.

ii. Hydrogen loading of the fiber

Hydrogen loading is carried out by diffusing hydrogen molecules into the optical fiber at high pressures. The reaction of hydrogen molecules at the Ge sites produces germanium-oxygen deficiency centers when exposed to UV light [2-14]. This is not a permanent effect, and as the hydrogen diffuses out, the photosensibility decreases.

iii. Irradiation with a UV laser at 193 nm

Bragg gratings fabricated silica fibers using 193nm UV light have stronger reflectivity than gratings inscribed with 248nm under similar excitation conditions [2-15].

2.2.3 FBG fabrication by the phase mask technique

A phase mask is a quartz plate on which a periodic corrugation has been engraved. The period and depth of the mask grating are optimized to maximize the first order of the Bragg reflection for a given light wavelength. The superposition of the ± 1 order generates an interference pattern with a period that is half the mask period. The interference can only occur if the illumination light source exhibits a sufficient coherence length (temporal and spatial). If the fiber is placed in the interference region, a FBG with half the phase mask period can be written. Typical values of 40 % energy in each first order of diffraction are observed. The remaining zero order (less than 1 % to 5 % of the incident beam) reduces the fringe visibility of the interference pattern and induces a constant refractive index change. The realized writing set-up is presented in Fig. 2-4.

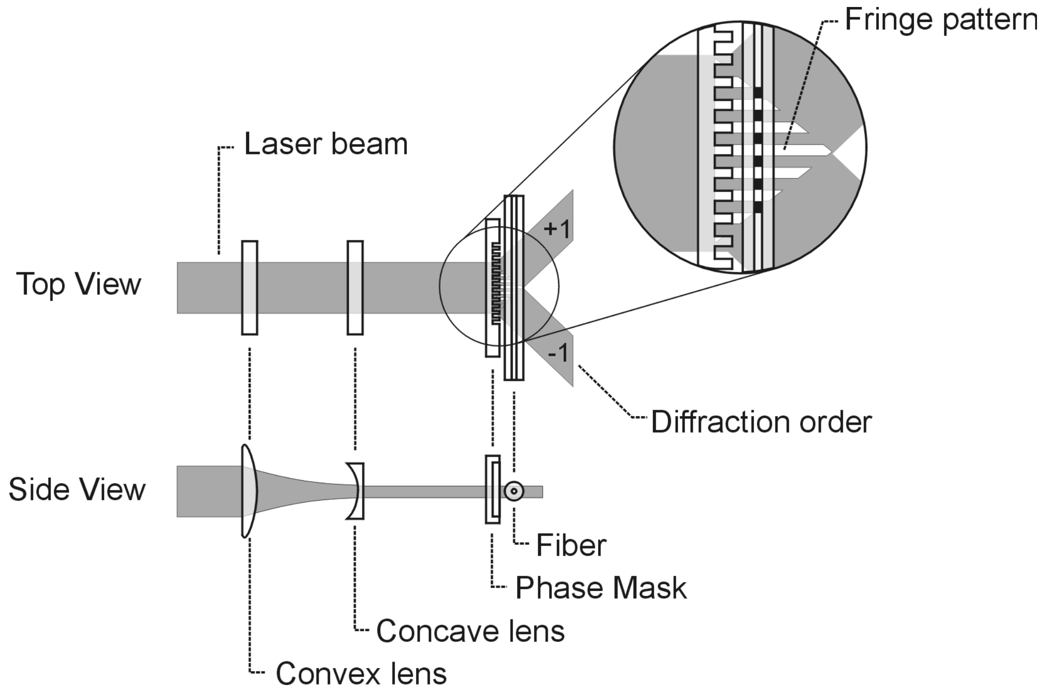

Fig. 2-4 FBG writing set-up with the phase mask technique

The maximal photosensitivity depends partly on the laser fluence and for this reason the laser beam height is reduced by a factor three. The beam reducer system is composed of the convex and concave cylindrical lens that can be seen in the side view of Fig. 2-4. The beam is preferably kept parallel to protect the phase mask from beam focusing that could damage the grating, but some experiments have required focalizing the beam to reach the maximal fluence on the fiber.

The illumination source is a pulsed excimer laser operating at 193 nm (ArF) with energy ranging from a few millijoules to 240 mJ per pulse. In addition, another cylinder lens can be introduced in the system to enlarge the beam width from 6mm to 3cm and thus increasing the possible grating length. The laser beam width is limited by a slit limits placed before the phase mask. The phase masks can be changed or removed very easily. A CCD video system is used to align the fiber in front of the phase mask with respect to the laser beam. The setup shows a good mechanical stability since grating erasure was observed only at high total dose. Without the phase mask, the setup allows homogeneous post-exposure of the fiber to increase the mean refractive index and permits hence a wavelength fine tuning.

2.3 FBG properties

2.3.1 Refractive index profile

A FBG is completely characterized by its refractive index distribution along the fiber n(z) [2-16]:

$$n(z) - n_0 = \Delta n_{ac}(z) \cdot \cos\left(2\pi z / \Lambda + \theta(z)\right) + \Delta n_{dc}(z) \qquad \text{(2-11)}$$

where z is the position, n_0 the refractive index prior to grating inscription, Δn_{ac} the refractive index modulation amplitude, Λ a design grating period, θ the period chirp (slowly varying with z), and Δn_{dc} the average change in refractive index (Fig. 2-5). The refractive index modulation amplitude remains sinusoidal until the exposed region reaches the maximal refractive index change. Then, if the UV exposure continues, the modulation change from sinusoidal to rectangular.

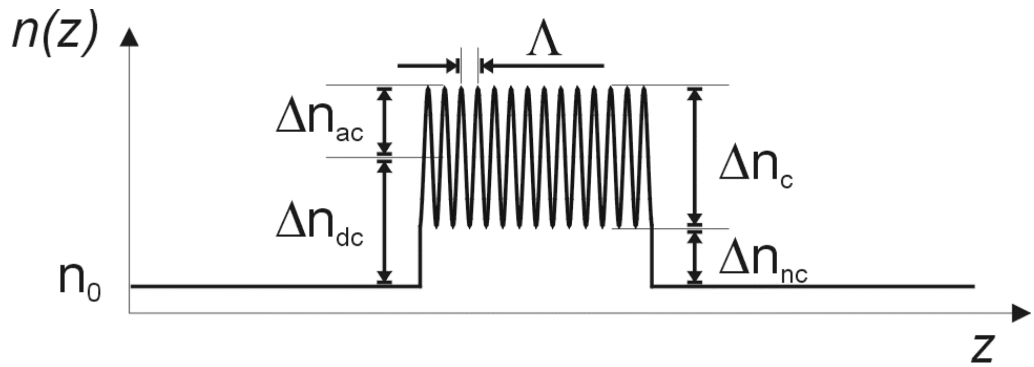

Fig. 2-5 Fiber Bragg grating refractive index

For gratings approaching the photosensitivity saturation, the modulation shape became rectangular.

2.3.2 FBG types

a) Homogeneous FBG

Homogeneous gratings are characterized by a rectangular function for the modulation amplitude envelope Δn_{ac} and the index offset Δn_{dc} with Λ kept constant (Fig. 2-6 left). The strong index step at the input and output of the grating induces important reflections bands, called side-lobes, outside the main Bragg peak. This effect can be understood by considering the grating edge as a Fabry-Perot structure.

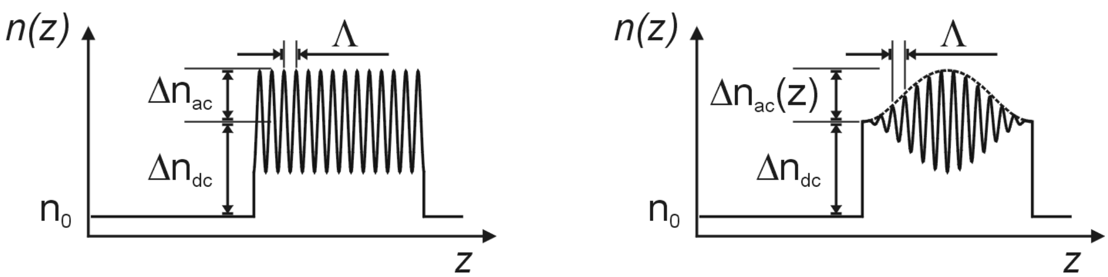

Fig. 2-6 FBG index profile : homogeneous (left), apodized (right)

The spectral reflectivity $r(\lambda) = |r(\lambda)| \cdot \exp(i \cdot \phi(\lambda))$ of such a grating has been calculated by the T-Matrix method that will be extensively explained in section 3.1.4. The results are presented in Fig. 2-7. The parameters used for the simulations are : an effective refractive index of 1.45, a maximal refractive index modulation of $2 \cdot 10^{-4}$, a grating period corresponding to a Bragg condition of λ_b = 1300 nm and a grating length of 5 mm (a fringe visibility of 1 is assumed). The homogeneous FBG is calculated in one layer. We observe in Fig. 2-7 that in the reflection amplitude $|r(\lambda)|$, the side-lobes are equally placed at both sides of the main Bragg peak resonance. The maximal reflectivity is 97 % and the first side-lobes show a reflectivity of 22 %. The delay time $d\phi(\lambda)/d\omega$ (where ω is the angular frequency) tends asymptotically to a value of 24 ps for $|\lambda-\lambda_b|>>0$. For strong gratings, part of the light is coupled in the cladding modes, inducing excess losses. This effect cannot be studied with reflection spectra but looking at the transmission light.

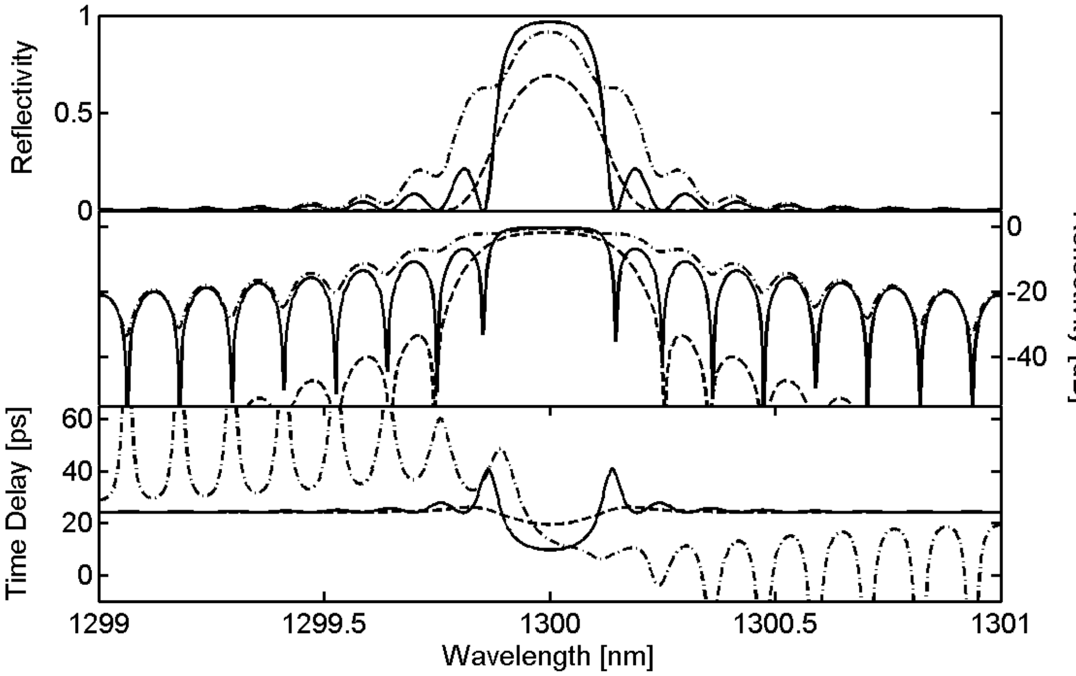

Fig. 2-7 FBG reflection intensity in linear scale (top), in dB (middle) and time delay (bottom) for an homogeneous FBG (solid line), an apodized FBG (dashed line) and a period chirped FBG (dashed-dotted line)

The amplitude and power reflection coefficients $r(\nu)$ and $R(\nu) = |r(\nu)|^2$, respectively, are given by [2-16, 2-17]

$$r(\delta) = \frac{-q^* \sinh(\gamma L)}{\gamma \cosh(\gamma L) - i\delta \sinh(\gamma L)}$$

$$R(\delta) = \frac{\sinh^2(\gamma L)}{\cosh^2(\gamma L) - (\delta/|q|)^2} \tag{2-12}$$

where $\gamma^2 = |q|^2 - \delta^2$, $\delta = \beta - \pi/\Lambda$, $|q| = \kappa = \eta \cdot \pi \cdot \Delta n_{ac}/\lambda$, $\mathrm{Arg}(q) = \pi/2$, $\beta = 2\pi n_{eff}/\lambda$ and $n_{eff} = n_0 + \Delta n_{dc}$.

The maximal reflectivity R_{max} is given by

$$R_{\max} = \tanh^2(\kappa L) \tag{2-13}$$

The grating bandwidth $\Delta\lambda_{BW}$, defined as the wavelength range between the first zeros apart from the Bragg peak is given by

$$\Delta\lambda_{BW} = \lambda_b \frac{\Delta n_{ac}}{n_{eff}} \sqrt{1 + \left(\frac{\lambda_b}{\Delta n_{ac} L}\right)^2} \tag{2-14}$$

Depending on the grating parameters, the Bragg reflector can operate as a narrow-band or a broadband filter or mirror.

b) Apodized FBG

A variation along the fiber in the envelope of the refractive index modulation amplitude, Δn_{ac}, is called apodization. The period Λ and the DC refractive index function Δn_{dc} are considered constant. Since the apodization can prevent any discontinuities in the Δn_{ac} profile (Fig. 2-6 right), the Fabry-Perot effect observed for rectangular gratings is greatly reduced. This can be observed in Fig. 2-7 where the side-lobes are suppressed by about 30 dB. The simulation has been performed by considering a 100-layered grating and a Hann apodization function. The other parameters are the same used for the homogeneous grating. The reflectivity at the resonance is reduced to 68 % due to the refractive index envelope. The delay time range is reduced by a factor 4.5.

c) Chirped FBG

If the period Λ or the DC refractive index Δn_{dc} changes within the grating, different Bragg conditions exist and a larger bandwidth of wavelengths is reflected (at the price of smaller reflectivity). Both cases of chirping are presented in Fig. 2-8. The two chirping effects are independent and then they can be combined to reduce or enhance the total grating chirp.

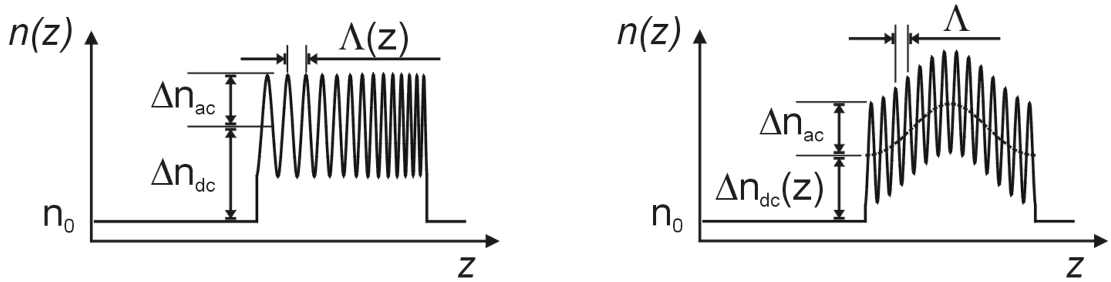

Fig. 2-8 Chirped FBG index profile : period chirp (left), index chirp (right)

The spectral reflection response of these gratings is also presented in Fig. 2-7. The grating parameters are the same as the homogeneous FBG, but the grating is divided in 100 layers for which the period function linearly varies from a Bragg condition of 1299.8 to 1300.2 nm. We observe a reduction of the maximal reflection to 92 % and an important relative increase of the side-lobes. The Fabry-Perot effect is also reduced due to the fact that the both sides of the grating reflects different wavelengths. For a larger chirp the reflectivity spectrum becomes much more complicated and not so easily predictable. We observe for the delay time a completely different behavior. Singularities appear and an anti-symmetric delay time is found. Chirped gratings can be used as dispersion compensators to compress temporally broadened pulses, it can also be used (broadband chirped grating) for pump rejection and recycling of unabsorbed pump light from an erbium-doped fiber amplifier.

d) Blazed (or tilted) grating

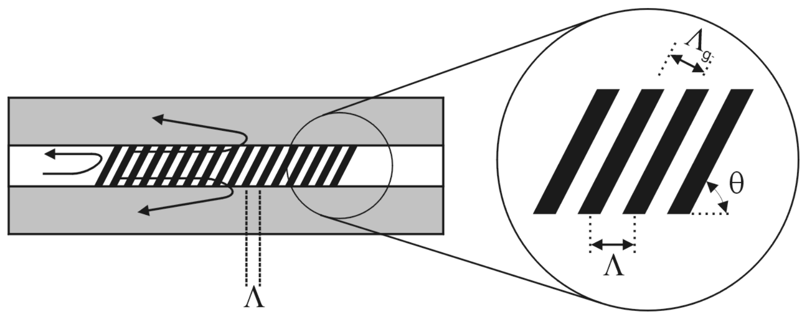

Fig. 2-9 Blazed fiber Bragg grating

When the grating planes are not orthogonal to the fiber axis (Fig. 2-9), the grating is called blazed or tilted. For a tilt angle θ and a phase mask period of $\Lambda_g/2$, the effective period Λ that determines the Bragg condition is given by $\Lambda = \Lambda_g/\cos(\theta)$. The overall effects are a reduced fringe visibility factor and transfer of a part of the energy to the cladding modes [2-17]. It is important to note that the energy coupled in the cladding modes is considered as excess loss.

The tilt of the grating planes and the strength of the index modulation determines the coupling efficiency and the bandwidth of the light that is tapped out. Multiple blazed gratings can be used to flatten the gain spectrum of erbium-doped fiber amplifiers. Another application of blazed gratings is in mode conversion.

e) FBG with phase shifts

Phase shifts in FBG consist of some discontinuities in the functions Δn_{dc} or $\theta(z)$. The fiber grating can be designed as a narrow-band transmission filter with the introduction of phase shift across the fiber grating whose location and magnitude can be adjusted to design a specific transmission spectrum.

f) Arbitrary FBG

An arbitrary FBG can be characterized by any kind of functions $\Delta n_{ac}(z)$, $\Delta n_{dc}(z)$ and $\Lambda(z)$, and thus have simultaneously apodization, period and refractive index chirp, phase shifts and tilt. The design of complicated FBG is required when specific spectral responses are expected, for example limited delay time over a large wavelength bandwidth. Sometimes the Δn_{ac}, Δn_{dc} and Λ functions are not completely under control, due to fabrication problems or specific grating environment (temperature or strain). Arbitrary FBGs are difficult to characterize since three different distributions need to be known to fully determine the grating (if we neglect the tilt effects).

2.3.3 Temperature and strain sensitivity

Temperature changes induce two effects on the FBG parameters. The thermal elongation of the fiber dilatation modifies the grating period Λ and the thermo-optic effects modify the refractive index functions (Δn_{ac}, Δn_{dc}). In the same manner, an applied stress on the fiber will lead to a geometric effect on the grating period and a refractive index change due to the photoelastic effect. Both effects can coexist and the Bragg wavelength shift $\Delta\lambda_b$ can be expressed as

$$\Delta\lambda_b = 2\left[\left(\Lambda\frac{\partial n_{eff}}{\partial L} + n_{eff}\frac{\partial\Lambda}{\partial L}\right)\Delta L + \left(\Lambda\frac{\partial n_{eff}}{\partial T} + n_{eff}\frac{\partial\Lambda}{\partial T}\right)\Delta T\right] \tag{2-15}$$

where L represent the grating length and T the temperature. We have assumed that the temperature and the strain fields are constant over the grating length. More details on the strains effects are presented in Chapter 5 and 6, while thermal effects are presented in Chapter 7.

The strain field is described with a tensor that derives from the stress tensor. The stress tensor can be approximated in many cases by a vector (σ_x, σ_y, σ_z) representing the stresses in the three orthogonal directions as indicated in Fig. 2-10

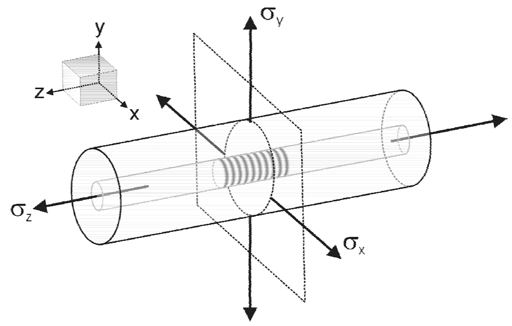

Fig. 2-10 Stress components

The high sensitivity of FBGs to temperature and axial stress has been widely used for sensing applications. Transversal stress measurements are more difficult as the sensitivity is much lower than the axial stress sensitivity and the directions x and y are not defined a priori except for gratings written in PM fibers. This aspect is presented in Chapter 5.

2.4 Experimental results

2.4.1 FBG fabrication

a) Standard phase mask technique

We present in Fig. 2-11 the spectral response of a FBG fabricated in our institute with the standard phase mask technique. This spectral response is compared to the simulated response for an homogeneous grating of 2.7 mm length and a refractive index modulation is $2.5{\cdot}10^{-4}$. The agreement between both spectral response is good indicating a nearly homogeneous UV light beam.

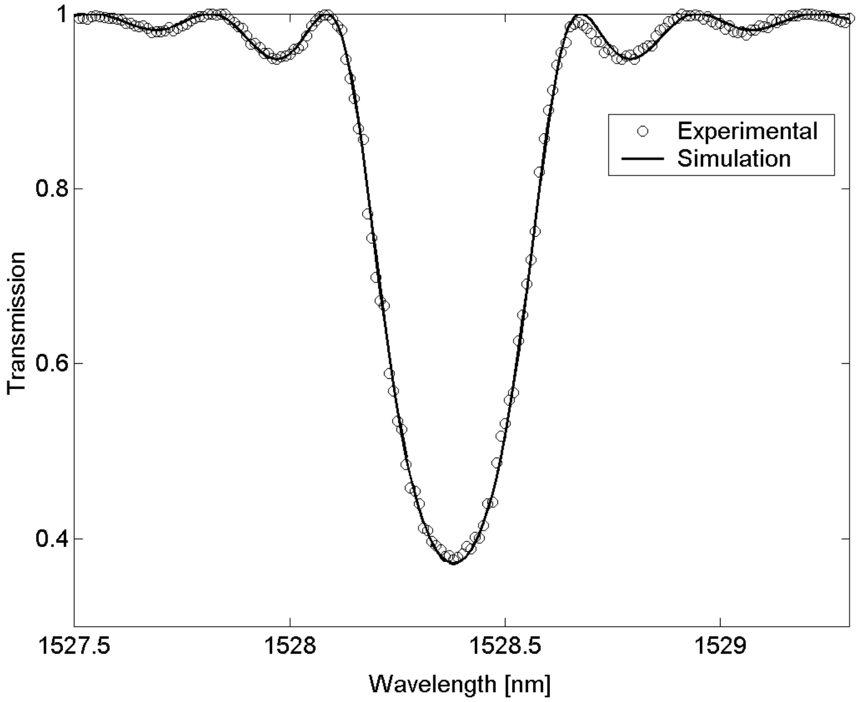

Fig. 2-11 FBG written in standard fiber and theoretical calculation

b) Modified phase technique for Bragg wavelength tuning

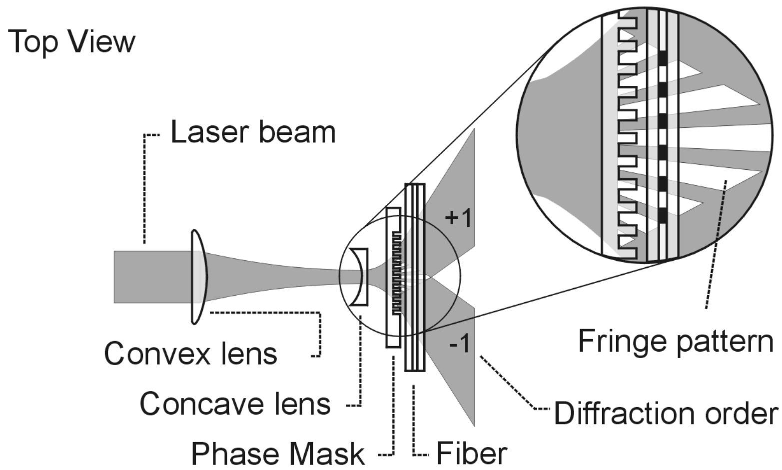

Fig. 2-12 FBG writing set-up with the modified phase mask technique

For given phase mask and fiber, the Bragg wavelength is determined by the effective index of the fiber, n_{eff}, and the phase mask period Λ_M: $\lambda_B=n_{eff}\Lambda_M$, where the grating period is $\Lambda=\Lambda_M/2$. It is possible to tune λ_B to higher wavelengths using post-exposure or to tune λ_B to lower wavelengths by stretching the fiber during the writing process. To have more flexibility with the same phase mask, an optical system including several lenses has been studied. The basic idea was to magnify the image of the grating onto the fiber as shown by Fig. 2-12. Compared to the standard writing set-up (top view of Fig. 2-4), two cylindrical lenses have been added, a convex one with focal length f_x and a concave one with focal length f_v.

Using ray optics, we find that the Bragg wavelength change $\Delta\lambda_b$, with respect to the Bragg wavelength with a parallel beam $\lambda_{b,0}$, is given by (Appendix B)

$$\Delta\lambda_b = \lambda_{b,0} \cdot \alpha \cdot d$$

$$\alpha = \left(d_2 - \frac{(d_1 - f_x)\cdot f_v}{d_1 - (f_x + f_v)} \right)^{-1} \qquad (2\text{-}16)$$

where d is the distance between the phase mask and the fiber core, d_1 the distance between the lenses and d_2 the distance between the concave lens and the phase mask. We observe that a Bragg wavelength change is obtained even with the fiber touching the phase mask due to the cladding thickness. The parallel alignment between the phase mask and the fiber is very important, since the Bragg condition strongly changes with d. Misalignment will lead to an important chirp.

We fabricated several FBGs with this set-up formed by two lenses and the same phase mask. The reflection spectrum of six different of such FBGs are presented in Fig. 2-13. We observe a tuning range of 10 nm and a small bandwidth change, indicating a good alignment of the fiber in front of the grating. The smaller reflectivity of FBG 6 is probably due to a misalignment of the fiber in the laser beam (then reducing the total dose).

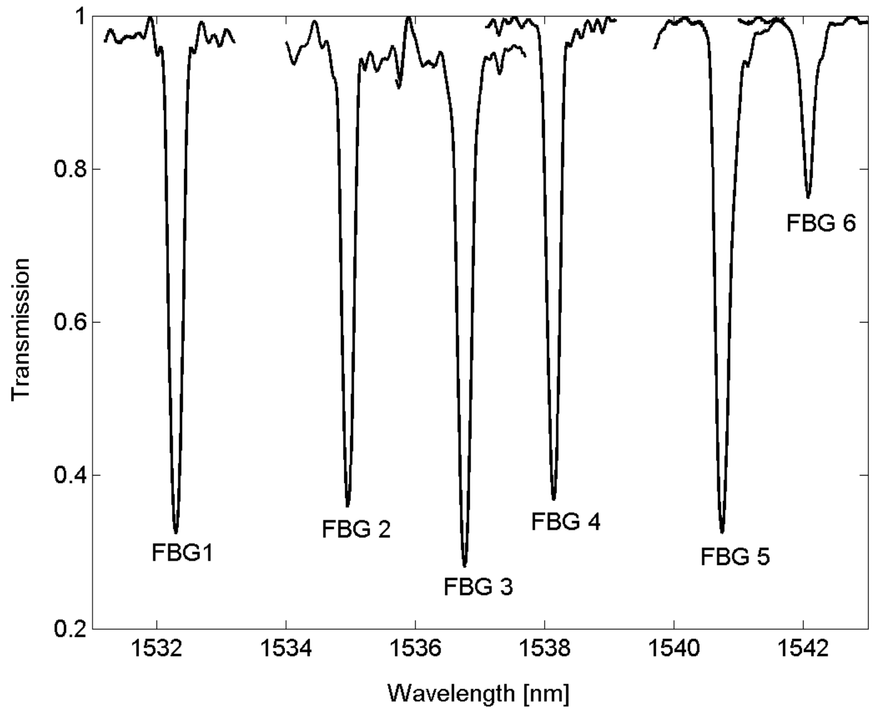

Fig. 2-13 Reflection spectrum of six FBG's written with the modified phase mask technique

2.4.2 Spectral characterization

Spectral amplitude or intensity measurements can be performed in reflection or in transmission. We have used a tunable laser or a broadband light source to measure the intensity responses. Fig. 2-14 shows the measurement set-up based on the tunable laser. The polarized light of the laser is launched in one arm of a coupler (eventually goes through a polarization controller to excite in a defined manner the polarization modes if a PM fiber is used). The reflected intensity from the grating is collected by the detector D_R and the transmitted intensity by the detector D_T. It should be noted that the remaining spontaneous light of the laser source limits the maximal dynamic range of the measurement (60 dB for the tunable laser available during this work). In the second method, the tunable laser is replaced by a broadband light source and the detectors by an optical spectrum analyzer or a monochromator.

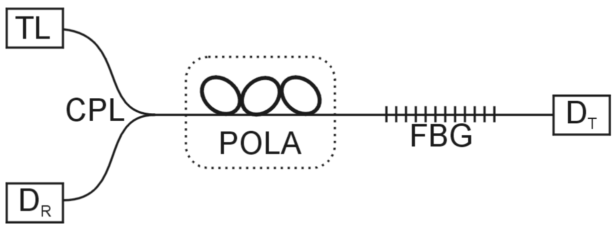

Fig. 2-14 Reflection and transmission intensity measurement set-up with a tunable laser; tunable laser (TL), coupler (CPL), polarization controller (POLA), fiber Bragg grating (FBG), detector for reflection intensity (D_R) and for transmission intensity (D_T)

The time multiplexed OLCR set-up developed for the measurement of the grating impulse response has also been used as a spectral measurement system (§4.3.7). In this case, the reflection amplitude (not the intensity) and the reflection phase are collected. We note that the Fourier transform of an OLCR measurement gives also the complex reflection amplitude.

2.4.3 Bragg wavelength determination

For sensing applications when a homogeneous FBG is placed in a homogeneous temperature or strain field, the important information is the Bragg wavelength shift. We have used two different methods to extract this wavelength shift depending on the spectral resolution.

For small resolution measurements, the Bragg wavelength is defined as the zero crossing point of the linear fit of the reflectivity slope between the maximal and minimal values (corresponding to inflexion points). This can be seen in Fig. 2-15 where the spectral response has been simulated for a homogeneous grating (10 mm long and $\Delta n_{ac} = 5 \cdot 10^{-5}$) with 2 % of noise and a resolution of 4 pm. Apart from the maximal reflectivity peak, we identify the inflexion points (slope maximum and minimum). The zero crossing point is indicated with an arrow.

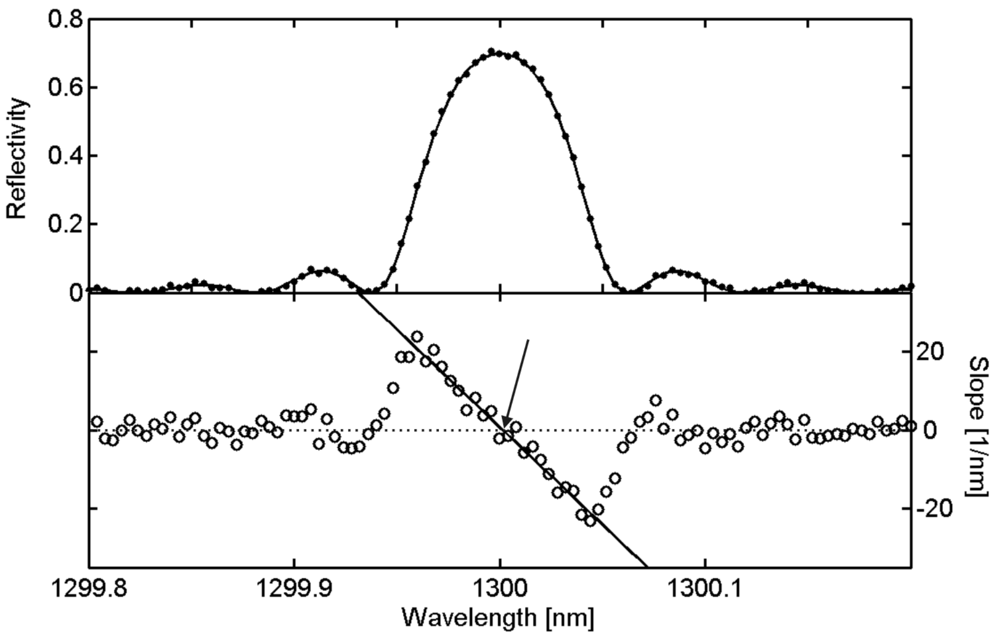

Fig. 2-15 Bragg wavelength measurement for low spectral resolution measurement; top : theoretical reflectivity intensity (solid line) and noisy data (dots); bottom : discrete slope (circles) and linear fit between the maximum and the minimum (solid line)

For a high spectral resolution measurement, this method is no more valid as the discrete slope is dominated by the noise and in this case the second method presented hereafter is recommended (or a re-sampling at smaller resolution needs to be performed).

The second technique used to measure the wavelength shift in an experiment is to use the mass center of the reflectivity curve

$$\lambda_b = \frac{\sum_m R(\lambda_m)\cdot\lambda_m}{\sum_m \lambda_m} \tag{2-17}$$

where λ_m and R are a measured wavelength and reflection intensity, respectively. This method requires a high spectral resolution (at least 200 measured points in the Bragg reflectivity peak). This method is also interesting for gratings subjected to non-homogeneous environmental conditions, for example a non-homogeneous strain field, as the Bragg wavelength at the mass center is related to the average Bragg condition. For FBGs with high spectral bandwidths, the mass center calculation should be performed in the frequency domain where the spectral density is proportional to the energy.

2.4.4 Characterization of the photosensitivity

a) Method based on the variation of the refractive index modulation amplitude

In this method, the measurement of a FBG reflectivity at different irradiation values gives the amplitude Δn of the refractive index modulation through the following equations

$$R = \tan^2(\kappa\cdot L)$$
$$\kappa = \frac{\pi\cdot\Delta n\cdot\eta}{\lambda_b} \tag{2-18}$$

where R is the reflectivity, κ the coupling coefficient, L the length of the grating, η the overlap integral between the LP_{01} mode and the fiber core, and λ_b the Bragg wavelength. The above equations are only useful for gratings that are not too strong. For this reason, very small grating are used for this measurement (around 0.2 mm). If the fringe visibility is 100 %, the mean index is equal to the amplitude. In case of a smaller fringe visibility, the mean index has to be measured independently.

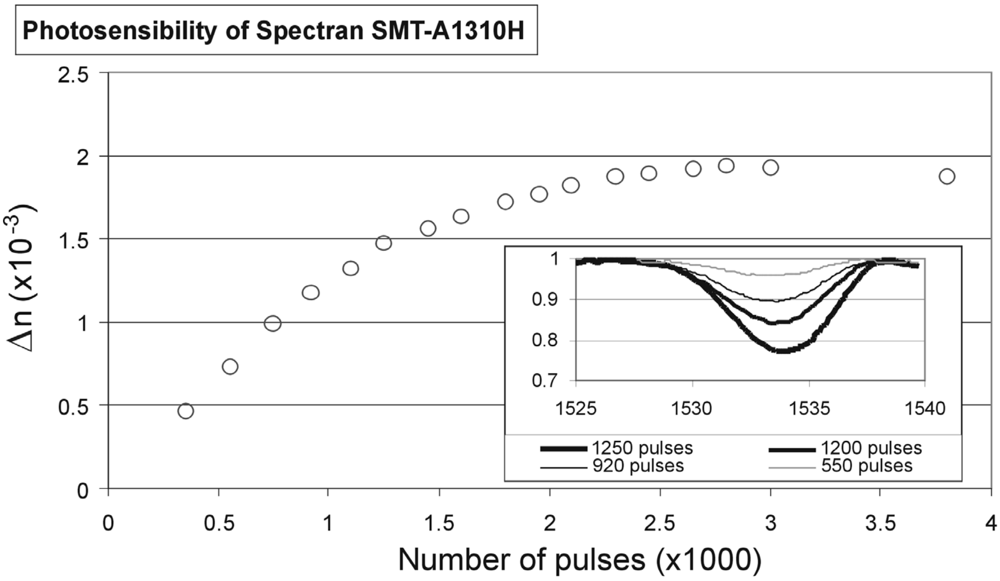

Fig. 2-16 Photosensitivity of a standard fiber (Inset: FBG transmission spectra for different number of total pulses).

The photosensitivity of a standard fiber (Spectran SMT-A1310H) has been determined with this method. The fiber was hydrogen loaded (7 days at 150 bars) and irradiations were performed at 193 nm. Different transmission spectra of the FBG (Fig. 2-16 inset) are used to retrieve the refractive index modulation amplitude Δn as a function of the total dose (proportional to the number of pulses). Figure Fig. 2-16 shows four of these transmission spectra and the photosensitivity curve. The maximal refractive index modulation amplitude is $2 \cdot 10^{-3}$.

b) Method based on the variation of the mean effective refractive index

To measure the mean index, a weak FBG (as small as possible) is used. The exposure of the grating region with a homogeneous laser beam increases the refractive index of the core and thus the mean effective refractive index $\overline{\Delta n_{eff}} = \overline{\Delta n}\,\eta$, which can be measured with the shift of the Bragg wavelength λ_b

$$\Delta\lambda_b = \lambda_b \cdot \overline{\Delta n_{eff}} / n_{eff} \tag{2-19}$$

The photosensitivity of the polarization maintaining fiber (Fibercore HB1250P) has been measured with this method. The fiber is also hydrogen loaded. Different transmission spectra of the FBG are used to retrieve the mean effective refractive index $\overline{\Delta n_{eff}}$ as a function of the total dose (proportional to the number of pulses). Fig. 2-17 shows the photosensitivity curve. The photosensitivity of the polarization maintaining fiber saturates at $7 \cdot 10^{-3}$.

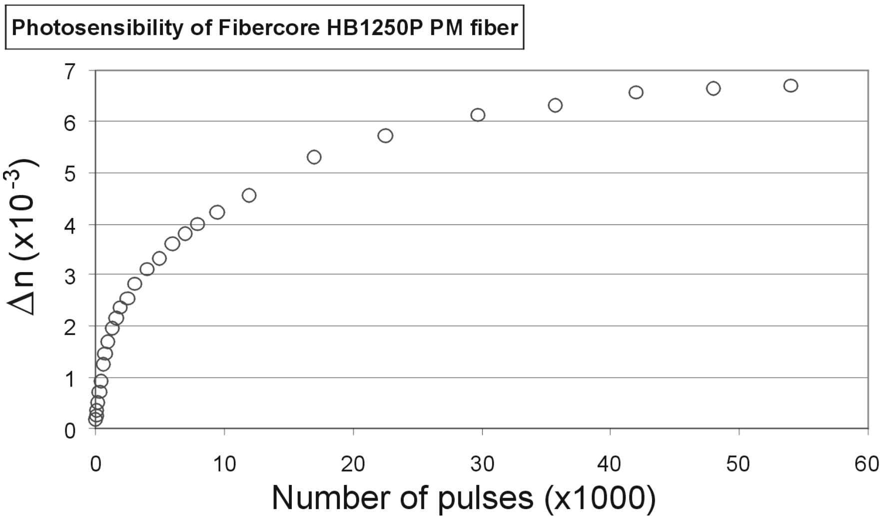

Fig. 2-17 Photosensitivity of the polarization maintaining fiber Fibercore HB1250P.

2.5 Summary

We have described the main parameters which describe a fiber Bragg grating, from the fiber itself to the different aspects of the FBGs. The important equation is the refractive index distribution (2-11) where we see that the grating is described with three independent functions, the refractive index modulation amplitude, the average effective refractive index change and the grating period. We have seen that variations of these distributions can lead to various spectral and impulse responses. The high sensitivity of FBGs to temperature and stress fields has also been presented. We will see in Chapter 5 and 6 different sensing applications from point axial or transverse stress sensors to distributed axial stress sensor and finally temperature and humidity sensors (that profit from the swelling properties of the coating that induce strain on the FBG).

2.6 References

2-1 I.H. Malitson, J. Opt. Soc. Am., 55 (10), p. 1205-1209 (1965)

2-2 H. Kogelnik, "*Filter response of nonuniform almost-periodic structures*", Bell-System-Technical-Journal., 55(1), p.109-26 (1976)

2-3 K.O. Hill, Y. Fujii, D.C. Johnson, B.S. Kawasaki, "*Photosensitivity in optical fiber waveguides: application to reflection filter fabrication*", Applied Physics Letters, 32 (10), p. 647-649 (1978)

2-4 D.K.W. Lam, B.K. Garside, "*Characterization of single-mode optical fiber filters*", Applied Optics, 20 (3), p. 440-445 (1981)

2-5 G. Meltz, W.W. Morey, W.H. Glenn, "*Formation of Bragg gratings in optical fibers by a transverse holographic method*", Optics Letters, 14 (15), p. 823-825 (1989)

2-6 D.P. Hand, P.St.J. Russel, "*Photoinduced refractive index changes in germanosilicate optical fibers*", Optics Letters, 15 (2), p. 102-104 (1990)

2-7 P.St.J. Russel, D.P. Hand, Y.T. Chow, L.T. Poyntz-Wright, "*Optically-induced creation, transformation and organization of defects and color-centers in optical fibers*", Proceedings of SPIE, Vol. 1516, p. 47-54 (1991)

2-8 D.L. Williams, B.J. Ainslie, R. Kashyap, G.D. Maxwell, J.R. Armitage, R.J. Campbell, R. Wyatt, "*Photosensitive index change in germania doped silica glass fibers and waveguides*", Proceedings of SPIE, Vol. 2044, p. 55-68 (1993)

2-9 J.P. Bernardin, N.M. Lawandy, "*Dynamics of the formation of Bragg gratings in germanosilicate optical fibers*", Optics Communications, 79 (3), p. 194-199 (1990)

2-10 D. Wong, S.B. Poole, M.G. Skeats, "*Stress birefringence reduction in elliptical-core fibers under ultraviolet irradiation*", Optics Letters, 17 (24), p. 1773-1775 (1992)

2-11 M.G. Sceates, G.R. Atkins, S.B. Poole, "*Photolytic index changes in optical fibers*", Annual Review of Material Science, 23, p. 381-410 (1993)

2-12 H.G. Limberger, P.-Y. Fonjallaz, R.P. Salathé, F. Cochet, "*Compaction- and photoelastic-induced index changes in fiber Bragg gratings*", Applied Physics Letters, 68 (22), p. 3069-3071 (1996)

2-13 C. Fiori, R.A.B. Devine, "*Ultraviolet irradiation induced compaction and photoetching in amorphous, thermal SiO_2*", Proceedings of Material Research Society Symposium, Vol. 61, p. 187-195 (1986)

2-14 J.P. Lemaire, R.M. Atkins, V. Mizrahi, W.A. Reed, "*High pressure H_2 loading as a technique for achieving ultrahigh UV photosensitivity and thermal sensitivity in GoO_2 optical fibers*", Electronics Letters, 29 (13), p. 1191-1193 (1993)

2-15 B. Malo, J. Albert, F. Bilodeau, T. Kitagawa, D.C. Johnson, K.O. Hill, K. Hattori, Y. Hibino, S. Gujarathi, "*Photosensitivity in phosphoruous-doped silica glass and optical waveguides*", Applied Physics Letters, 65, p. 394-396 (1994)

2-16 J. Skaar, PhD dissertation, The Norwegian University of Science and Technology, Ch. 2, 5-15 (2000)

2-17 T. Erdogan, "*Fiber Grating Spectra*", JLT, 15 (8), p. 1277-1294 (1997)

Chapter 3

FBG simulation and reconstruction

Fig. 3-1 presents a synthetic view of the subjects treated in this chapter. A FBG can be described in three domains : space (z), frequency (ν) and time (τ). The methods used to go from one representation to the other are also indicated. The T-matrix method allows to calculate the complex spectral response $r(\nu)$ when the complex coupling coefficient distribution $q(z)$ is known [3-1]. The complex coupling coefficient amplitude is proportional to the refractive index modulation amplitude $\Delta n_{ac}(z)$, while its phase represents the chirp function that mixes the average refractive index $\Delta n_{dc}(z)$ and the period $\Lambda(z)$. Inversely, $q(z)$ can be retrieved from $r(\nu)$ by the layer-peeling method [3-2]. This method is based on the coupled-mode formalism [3-3]. The impulse response $h(\tau)$ can be obtained from the spectral response by Fourier transform.

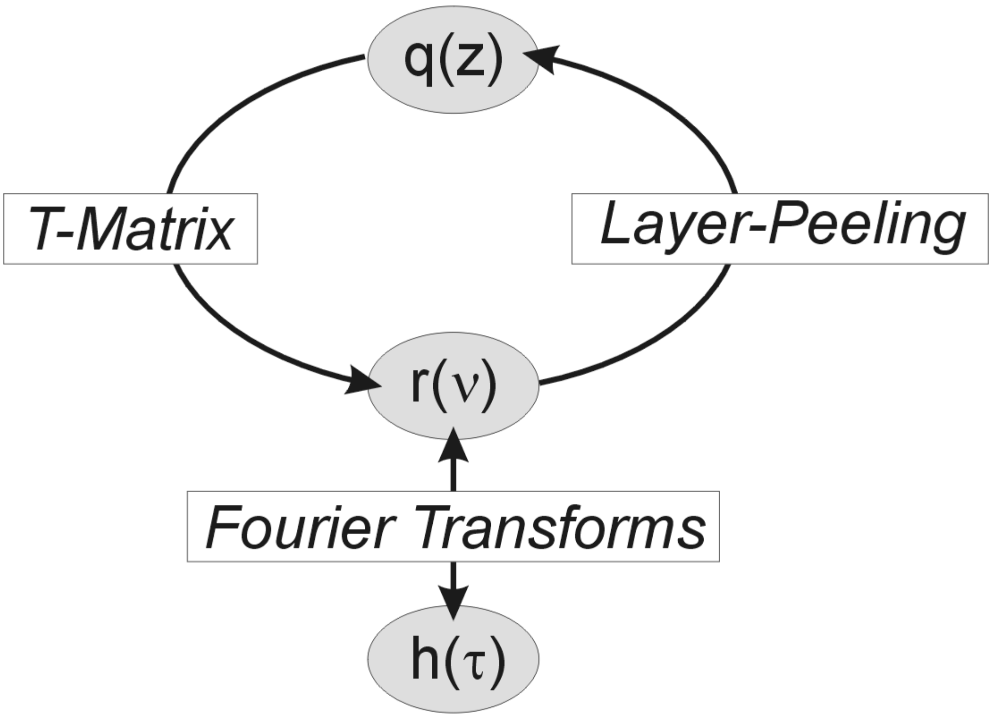

Fig. 3-1 Different paths between the FBG representations

This chapter presents the T-matrix and the layer-peeling methods. The T-matrix is used to calculate the spectral and impulse response of homogeneous and non-homogenous gratings. From these responses, the layer-peeling method is studied and the optimal reconstruction parameters are presented. We also analyze the reconstruction limits observed for gratings with nearly 100 % reflectivity.

The T-matrix and the layer-peeling methods are only defined for lossless FBGs and for this reason we have adapted the two methods to takes account of loss effects.

3.1 FBG spectral response simulation in the coupled-mode formalism

3.1.1 Coupled-mode equations

The fiber is assumed lossless, single mode and weakly guiding (small refractive index difference between the cladding and the fiber core). The electromagnetic field is supposed transverse to the fiber axis z, with the polarization state that is conserved along the propagation (e.g. x-polarized). Moreover, the refractive index modulation of the grating is assumed to be homogeneous and restricted to the fiber core.

The core refractive index perturbation n(z) is defined as (Chapter 2, §2.3.1)

$$n(z) = n_0 + \Delta n_{ac}(z)\cos\left(\frac{2\pi}{\Lambda_d}z + \theta(z)\right) + \Delta n_{dc}(z) \tag{3-1}$$

where n_0 is the refractive index of the non-perturbed fiber core, Δn_{ac} and Δn_{dc} are the "ac" and "dc" index change amplitudes, respectively, and Λ_d is the design period, which is chosen in order to have a slowly varying period phase function $\theta(z)$. The forward and backward propagating field envelopes (u and v, respectively) are mutually coupled by the coupled wave equation for weak coupling coefficients (see Appendix C for full description)

$$\begin{aligned} \frac{du(z,\delta)}{dz} &= +i\delta u + q(z)v \\ \frac{dv(z,\delta)}{dz} &= -i\delta v + q^*(z)u \end{aligned} \tag{3-2}$$

where $\delta = \beta - \pi/\Lambda_d$ is called the wavenumber detuning ($\beta = kn_{eff}$ is the propagation constant). The function q(z) is called the coupling coefficient and its amplitude and phase are defined as

$$\begin{aligned} |q(z)| &= \frac{\eta\pi\cdot\Delta n_{ac}(z)}{\lambda} \\ Arg(q(z)) &= \frac{\pi}{2} + \theta(z) - 2\eta k\int_0^z \Delta n_{dc}(z')dz' \end{aligned} \tag{3-3}$$

where η is the fraction of the modal power contained in the fiber core.

3.1.2 Analytic solution for homogeneous FBGs

A homogeneous FBG has constant values for Δn_{ac}, Δn_{dc} and Λ in the range $0 \le z \le L$. In this case, the coupled mode equations can be solved analytically by differentiating equations (3-2) and substituting the first derivatives by the equations (3-2); for example for $u(z,\delta)$, we have

$$\frac{d^2u(z,\delta)}{dz^2} = \left(|q|^2 - \delta^2\right)u \tag{3-4}$$

The same kind of equation is obtained for $v(z,\delta)$ [3-2]. Using the appropriate boundary conditions, the reflection amplitude $r(\delta)$ and the transmission amplitude $t(\delta)$ are found to be

$$\begin{aligned} r(\delta) &= \frac{-q^*\sinh(\gamma L)}{\gamma\cosh(\gamma L) - i\delta\sinh(\gamma L)} \\ t(\delta) &= \frac{\gamma}{\gamma\cosh(\gamma L) - i\delta\sinh(\gamma L)} \end{aligned} \tag{3-5}$$

where $\gamma^2 = |q|^2 - \delta^2$. A meaningful expression of q is obtained for a design period that corresponds exactly to the physical period Λ and for an effective refractive index set to $n_0+\Delta n_{dc}$ (and then the integral term in equation (3-3) vanishes). In this case, the coupling coefficient phase factor reduces to $\pi/2$ and then $q = i|q| = i\cdot\eta\cdot\pi\cdot\Delta n_{ac}/\lambda$.

3.1.3 Numerical solution of the Riccati equation for non-homogeneous FBGs

We define the function r(z,d) = v(z,d)/u(z,d) [3-2] and the Riccati equation can be found by differentiating r with respect to z and substituting equations (3-2)

$$\frac{dr(z,\delta)}{dz} = -q(z)r^2 - 2i\delta r + q^*(z) \tag{3-6}$$

Using the boundary condition $r(L,\delta) = 0$, the equation can be numerically solved from the end of the grating backward to z = 0 using a Runge-Kutta method. The reflection coefficient amplitude is found to be $r(\delta) = r(0,\delta)$. The calculation needs a larger number of steps in the Runge-Kutta routine to converge than for the T-matrix method presented hereafter.

3.1.4 T-matrix method

In the T-matrix method [3-2 to 3-4], the grating is divided in N sections of width Δ_j (j = 1, …, N), where the parameters Δn_{ac}, Δn_{dc} and Λ are constant. The grating is then defined by N sections with coupling coefficients q_j and physical thickness Δ_j (Fig. 3-2).

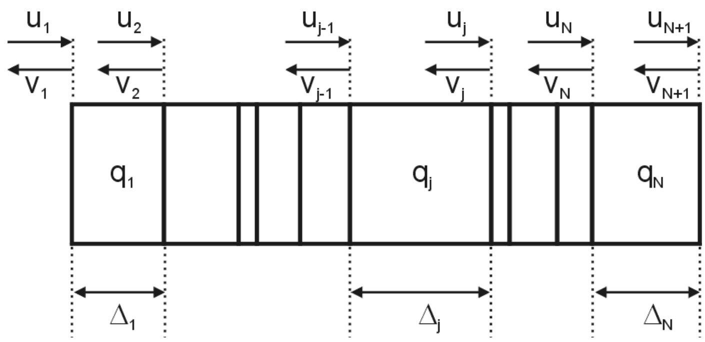

Fig. 3-2 FBG Slicing in sub-sections for the T-matrix method

The knowledge of the fields u_j and v_j at the entrance of section j allows to find the fields u_{j+1} and v_{j+1} at the layer output. This relation can be expressed in the form of a transfer matrix relation

$$\begin{bmatrix} u_j \\ v_j \end{bmatrix} = T_j \begin{bmatrix} u_{j-1} \\ v_{j-1} \end{bmatrix} \tag{3-7}$$

where

$$T_j = \begin{bmatrix} \cosh(\gamma_j\Delta_j) + i\dfrac{\delta}{\gamma_j}\sinh(\gamma_j\Delta_j) & \dfrac{q_j}{\gamma_j}\sinh(\gamma_j\Delta_j) \\ \dfrac{q_j^*}{\gamma_j}\sinh(\gamma_j\Delta_j) & \cosh(\gamma_j\Delta_j) - i\dfrac{\delta}{\gamma_j}\sinh(\gamma_j\Delta_j) \end{bmatrix} \tag{3-8}$$

where $\gamma_j^2 = |q_j|^2 - \delta^2$. The fields u_1, v_1 and u_{N+1}, v_{N+1} at the grating entrance and output respectively, are then related to each other by

$$\begin{bmatrix} u_{N+1} \\ v_{N+1} \end{bmatrix} = T_N \cdot \ldots \cdot T_j \cdot \ldots \cdot T_1 \begin{bmatrix} u_1 \\ v_1 \end{bmatrix} = T \begin{bmatrix} u_1 \\ v_1 \end{bmatrix} = \begin{bmatrix} T_{11} & T_{12} \\ T_{21} & T_{22} \end{bmatrix} \begin{bmatrix} u_1 \\ v_1 \end{bmatrix} \tag{3-9}$$

The reflection coefficient amplitude $r(\delta)$ is determined with the limit conditions $u_1 = 1$ and $v_{N+1} = 0$: $r(\delta) = v_1 = -T_{21}/T_{22}$. The transmission coefficient amplitude $t(\delta)$ is found from the limit conditions $u_1 = 0$ and $v_{N+1} = 1$: $t(\delta) = v_1 = 1/T_{22}$.

The proposed T-matrix formulation takes into account the overlap integral η that is often neglected [3-1, 3-4] and the fringe visibility effect can be integrated in the definition of the refractive index distributions Δn_{dc} and Δn_{ac}.

3.1.5 Causal T-matrix method

For the section j of thickness Δ_j, the grating effect can be approximated by a single complex reflector of reflectivity ρ_j (Fig. 3-3). The complex reflectivity factor ρ_j is defined from the complex coupling coefficient q_j as

$$\rho_j = -\tanh\left(\left|q_j\right| \cdot \Delta_j\right) \cdot \frac{q_j^*}{\left|q_j\right|} \tag{3-10}$$

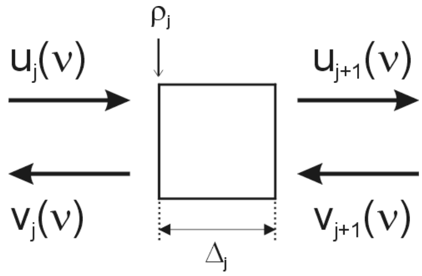

Fig. 3-3 Parameters for section j

In this case, the matrix T_j that represents the section j, can be formulated as the product of a pure propagation matrix $T_{\Delta,j}$ and of a transfer matrix $T_{\rho,j}$ [3-5]

$$T_{\Delta,j} = \begin{bmatrix} e^{i\delta\Delta_j} & 0 \\ 0 & e^{-i\delta\Delta_j} \end{bmatrix}$$

$$T_{\rho,j} = \frac{1}{\sqrt{1-\left|\rho_j\right|^2}} \begin{bmatrix} 1 & -\rho_j^* \\ -\rho_j & 1 \end{bmatrix} \tag{3-11}$$

that is

$$T_j = T_{\Delta,j} \cdot T_{\rho,j} \tag{3-12}$$

The factor $(1-|\rho_j|^2)^{-1/2}$ corresponds to the transmission amplitude. The matrix $T_{\rho,j}$ can also be obtained from equation(3-8) by letting $q_j \rightarrow \propto$ and the matrix $T_{\Delta,j}$ by letting $q_j \rightarrow 0$ holding the factor $q_j\Delta_j$ constant.

From equations (3-11), the fields propagation can be expressed in a recursion form (instead of a matrix product)

$$r_{j+1}(\delta) = \frac{r_j(\delta) - \rho_j}{1-\rho_j^* \cdot r_j(\delta)} e^{-i\delta \cdot 2\Delta_j} \tag{3-13}$$

This recursion formula allows calculating the reflectivity r_{j+1} of the FBG constituted of the sections j to N. This propagation process is one of the required steps of the layer-peeling reconstruction method presented later in this chapter.

We have denominated this method "causal" as all reflections in the section are located in a single point. This method is similar to Rouard's method used in the simulation response of thin films [3-6]. The difference is in the thickness of the sections. For Rouard's method, each grating period would be divided in several sections (for a FBG this would lead to Δ_j of a few tens of nanometers) while in the causal T-matrix, only the necessary number of sections is used to represent the slowly varying coupling coefficient (thickness of tens of micrometers are possible). This method is the direct counterpart of the layer-peeling reconstruction method, which allows to recover the complex coupling coefficient for a given complex reflectivity response.

3.2 FBG synthesis and reconstruction

This section presents an overview of the different methods used to retrieve the local parameters of a grating. A large emphasis has been given to the layer-peeling method, which has been employed in this work.

3.2.1 Overview of reconstruction methods

The retrieval of the grating parameters distribution from the grating spectral response has been widely studied. Several papers have been published where only the spectral amplitude or phase was exploited. In this case, the grating distributions needs to be monotonic [3-7, 3-8] or a priori assumption needs to be postulated (for example a gradient direction) [3-9]. As a consequence, only one parameter can be retrieved. For weak gratings, the knowledge of the intensity and the phase of the spectral response permits to reconstruct the grating profile via a Fourier Transform [3-2, 3-10]; for strong gratings, a backscattering technique is instead necessary [3-11, 3-12]. The layer-peeling technique discussed hereafter is a backscattering technique, which is highly efficient and not very sensitive to the measurement noise, when applied to the complex impulse response. Some methods use an iterative process where at each step a theoretical grating profile and its reflection or phase spectrum are generated and compared with a measured spectrum [3-13 to 3-16].

3.2.2 Discrete Layer-peeling

The layer-peeling method has an origin in the geologic field. It has been developed to retrieve the ground properties from the seismic impulse response measured when a explosive charge is activated. The method is based on the propagation description of the fields through a discrete structure with simultaneous retrieval of the material impedance based only on causal arguments. The rigorous mathematical description of the method has been achieved for one-dimensional systems [3-17, 3-18] and its application in various other fields has been found. Application for the synthesis of FBG has been proposed by Faced et al. [3-19] and a simpler formulation has been proposed by Skaar et al. [3-5], where a continuous version of the layer-peeling is also presented but with no advantage over the discrete method. The method is briefly explained hereafter. It is based on the formulation of Skaar et al. and a modified version is also proposed for FBGs where some losses are observed during the propagation (for example tilted gratings).

The layer-peeling method is a backscattering method based on the complex impulse response of an unknown structure (Fig. 3-4).

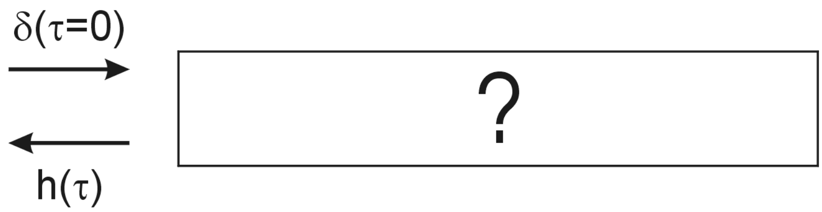

Fig. 3-4 Backscattering problem

The structure is divided in N layers of a physical thickness Δ. For a given impulse time τ, only the part of the grating that has been illuminated during the time interval of τ/2 can contribute to the impulse response (causality principle). This is represented by the white layers in Fig. 3-5.

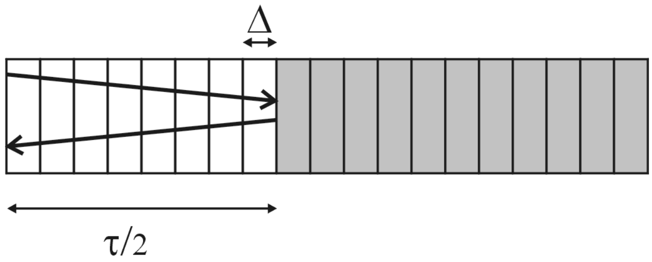

Fig. 3-5 Layers and causality principle

The causality principle imposes that all reflections in a layer occur at a single point (Fig. 3-6).

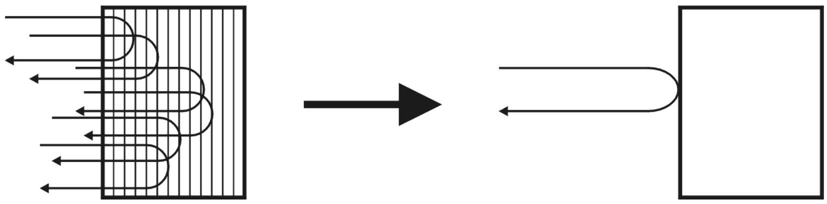

Fig. 3-6 Single point reflection approximation

It was assumed in the causal T-matrix that for a small enough layer, the FBG can be represented by a single, localized and complex reflector, as defined in equation (3-10).

The complex reflection amplitude of the grating $r_1(\nu)$ is given by the Fourier transform of the impulse response $h_1(\tau)$ (and vice-versa). For $\tau = 0$, only the first layer contribute to the impulse response and the complex reflector ρ_1 is described by the impulse response for $\tau = 0$, $h_1(0)$, as seen in Fig. 3-7.

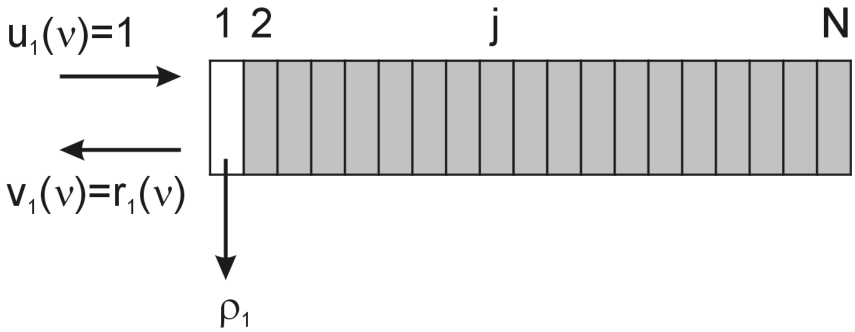

Fig. 3-7 First layer case

The calculation of ρ_1 from the discrete form of the spectral response is given by the discrete Fourier transform of $r_1(\delta_m)$ for $\tau = 0$ for which the exponential factor is canceled and then ρ_1 is given by

$$\rho_1 = \frac{1}{M}\sum_{m=1}^{M} r_1(\delta_m) \qquad (3\text{-}14)$$

where the number of spectral points M must be greater than the number of layers N and where the detuning range $|\delta|$ is determined from the layer thickness :

$$|\delta| \leq \frac{\pi}{2\Delta} \qquad (3\text{-}15)$$

From the complex reflectivity r_1 and the complex reflector ρ_1, it is possible to use the equation (3-13) to calculate the reflectivity $r_2 = v_2/u_2$ for the FBG without the first layer (peeled-off), which is represented in Fig. 3-8 by the gray layers (u and v are the forward and backward propagating modes).

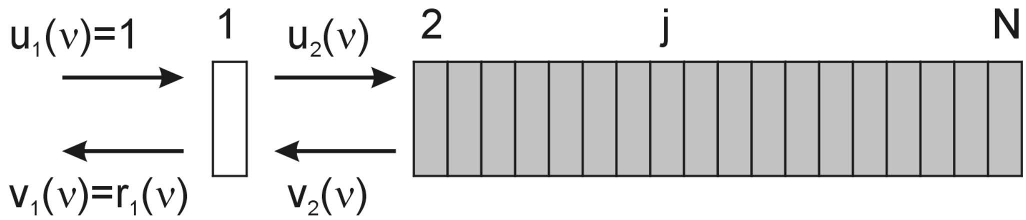

Fig. 3-8 Field propagation through the first layer

Only considering the remaining grating constituted of the layers 2 to N, we observe that its spectral response is known, namely r_2. Then the same calculation process can be performed to retrieve the complex reflector value ρ_2 of the second layer and the reflection response r_3 of the grating constituted of layers 3 to N (Fig. 3-9). The whole grating complex reflector ρ_j are thus recursively reconstructed.

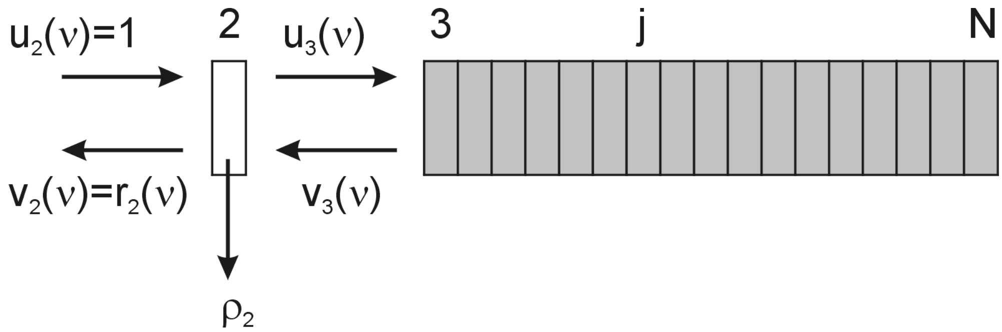

Fig. 3-9 Second layer reconstruction

The layer-peeling reconstruction algorithm is the counterpart of the causal T-matrix method (§3.1.5).

In summary, from the starting reflection amplitude $r_1(\delta)=r(\delta)$, the grating is reconstructed in an iterative way. At each step, ρ_j is calculated for the first layer of the remaining structure at the step j and a new reflection amplitude $r_{j+1}(\delta)$ is calculated for the structure without the layer j (peeled off) :

$$\rho_j = \frac{1}{M}\sum_{m=1}^{M} r_j(m) = -\tanh\left(\left|q_j\right|\Delta\right)\frac{q_j^*}{\left|q_j\right|} \tag{3-16a}$$

$$r_{j+1}(m) = \frac{r_j(m)-\rho_j}{1-\rho_j^* r_j(m)}\cdot e^{-i(\delta+i\alpha)2\Delta} \tag{3-16b}$$

where $r_j(m)$ is the discrete form of $r_j(\delta)$ for $|\delta| \le \pi/2\Delta$, $M \ge N$ and $\delta = \beta - \beta_B$ is the wavenumber detuning, $\beta = 2\pi n_{eff}/\lambda$ the light wavenumber and $\beta_B = \pi/\Lambda = 2\pi n_{eff}/\lambda_B$ the Bragg design wavenumber.

3.2.3 Reconstructed FBG interpretation

The complex coupling coefficients q_j are calculated from the complex reflectors ρ_j through the equation (3-16a). The complex coupling coefficient distribution q(z) can then be calculated by interpolation between the positions j·Δ. The complex coupling coefficient gives the local grating strength and its chirp and is related to the three distributions $\Delta n_{ac}(z)$, $\Delta n_{dc}(z)$ and $\theta(z)$ by the following equations :

$$\Delta n_{ac}(z) = \frac{\lambda}{\eta\pi}\cdot\left|q(z)\right| \tag{3-17a}$$

$$\phi_q(z) = \frac{\pi}{2} + \theta(z) - 2\eta k\int_0^z \Delta n_{dc}(z')\,dz' \tag{3-17b}$$

$$\frac{d\phi_q(z)}{dz} = \frac{d\theta(z)}{dz} - 2\eta k \Delta n_{dc}(z) \qquad (3\text{-}17c)$$

where $\phi_q = \mathrm{Arg}(q)$ and k has been evaluated at the design wavelength ($\lambda_d = 2\, n_{eff}\, \Lambda_d$). We can notice that a single reconstruction cannot distinguish a period chirp from a DC refractive index chirp. For this reason, an effective grating period Λ_{eff} for each layer is defined, which represents the chirp function :

$$\frac{2\pi}{\Lambda_{eff}(z)} = \frac{2\pi}{\Lambda_d} + \frac{d\phi_q(z)}{dz} \quad or \quad \Lambda_{eff}(z) = \Lambda_d \left(1 + \frac{\Lambda_d}{2\pi}\frac{d\phi_q(z)}{dz}\right)^{-1} \qquad (3\text{-}18)$$

where Λ_d is the design period. The local Bragg wavelength corresponds to $2\Lambda_{eff}\cdot n_{eff}$. The effective grating period can be expressed as a function of the Δn_{dc} and θ distributions

$$\Lambda_{eff}(z) = \Lambda_d \left(1 + \frac{\Lambda_d}{2\pi}\frac{d\theta(z)}{dz} - \eta \cdot \frac{\Delta n_{dc}(z)}{n_{eff}}\right)^{-1} \qquad (3\text{-}19)$$

3.3 Calculated FBG spectral and impulse responses

This section presents different results obtained by the simulations of the spectral response of lossless FBGs by T-matrix and the corresponding impulse responses calculated by Fourier transformation. A Bragg condition in the 1300 nm range has been chosen as for the experimental FBGs fabricated and characterized in chapter 4. The used algorithm is based on the T-matrix formalism of Erdogan [3-1], where the overlap integral η is not considered. The effective refractive index is adapted to keep the average refractive index constant to a value of 1.45.

The representation of the impulse responses has been chosen to be as close as possible from OLCR measurements. For this reason, we have used a distance scale OPLD instead of a time scale τ. The relation between OPLD and τ is simply OPLD = $c_0\cdot\tau$ (c_0 is the light speed in vacuum), that is, the OPLD corresponds to the traveled distance in vacuum during a time τ (in the context of OLCR, the OPLD corresponds to the optical path length difference in vacuum between the reference and test arms). Moreover, the representation of the impulse response amplitude in decibel scale is preferred, but in this case, a reference illumination light source needs to be defined. In order to remain consistent with the experiments presented in Chapter 4, a Gaussian light source with 40 nm spectral bandwidth and centered at the Bragg wavelength is used. The influence of the source bandwidth and the wavelength detuning between the FBG and the source central source wavelength is nevertheless described at the end of this section.

3.3.1 Homogeneous FBG examples

Homogeneous gratings are the simplest type of gratings that can be fabricated, and a good understanding of their spectral and impulse responses is very important. Two parameters can be adjusted for a given grating period : the grating length L and the refractive index modulation Δn_{ac}. The cases of constant L, constant Δn_{ac} and constant $L\cdot\Delta n_{ac}$ are presented hereafter.

a) Constant length

The grating length is set to 10 mm and the refractive index modulation amplitude to the following values : 10^{-6}, 10^{-5}, $5\cdot10^{-5}$ and $2\cdot10^{-4}$. The spectral response is presented in Fig. 3-10. The reflectivity amplitude shows saturation in the stop-band for refractive index modulation above $5\cdot10^{-5}$ and for $2\cdot10^{-4}$, even the side-lobes positions are slightly moved. We observe that the reflection amplitude slopes are very close in the ripples regions for refractive index modulation under 10^{-4}.

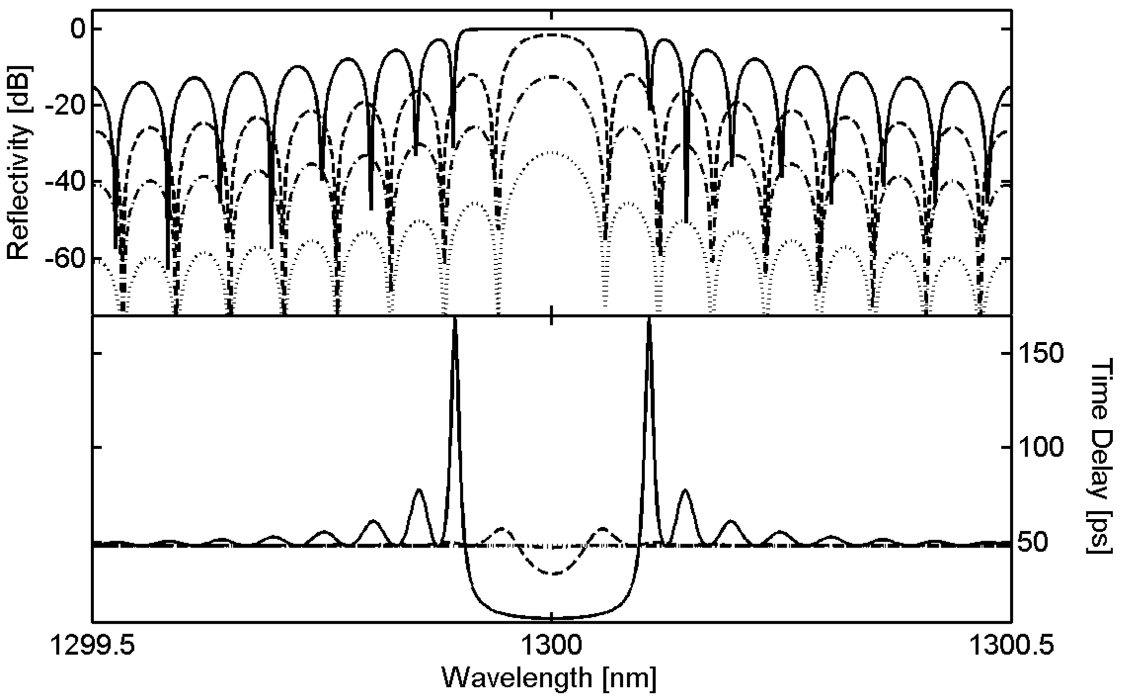

Fig. 3-10 Spectral reflectivity amplitude response in dB scale (top) and time delay (bottom) for homogeneous gratings of 10 mm length and refractive index modulation amplitude of 10^{-6} (dotted lines), 10^{-5} (dashed-dotted lines), $5\cdot10^{-5}$ (dashed lines) and $2\cdot10^{-4}$ (solid lines)

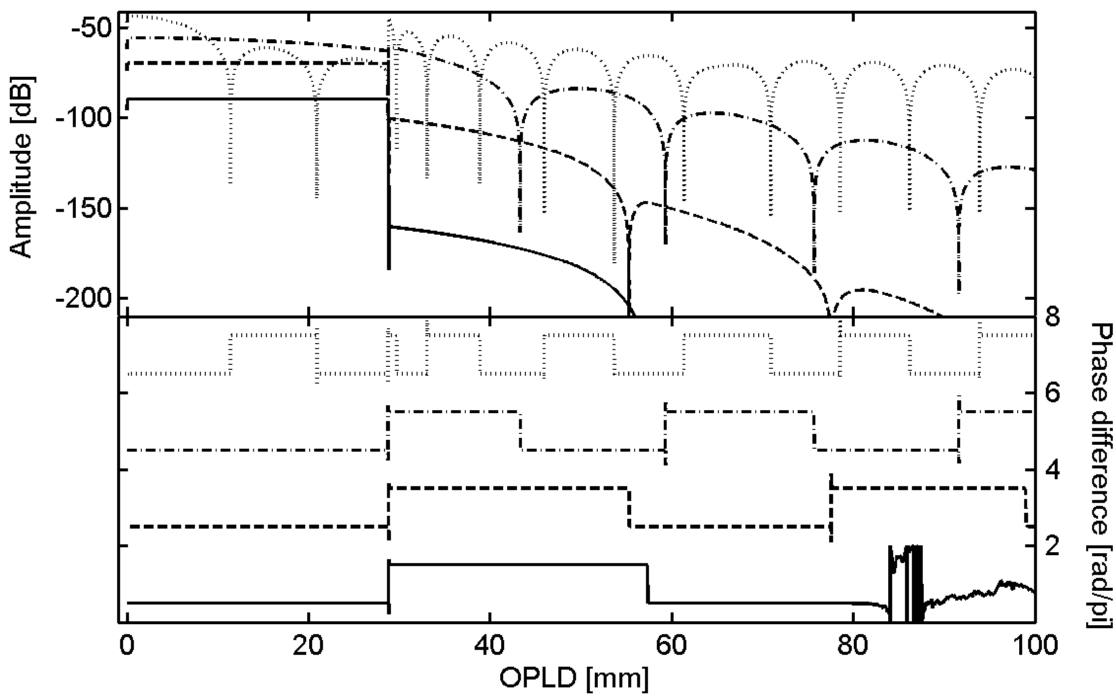

Fig. 3-11 Impulse response amplitude (top) and phase difference with the Bragg wavelength propagation phase (bottom) for homogeneous gratings of 10 mm length and refractive index modulation amplitude of 10^{-6} (solid lines), 10^{-5} (dashed lines), $5\cdot10^{-5}$ (dashed-dotted lines) and $2\cdot10^{-4}$ (dotted lines)

The time delay τ is defined as the derivative of the reflective amplitude phase with respect to the angular frequency ω

$$\tau = \frac{d\phi_r}{d\omega} = -\frac{\lambda^2}{2\pi c}\frac{d\phi_r}{d\lambda} = \frac{1}{2\pi}\frac{d\phi_r}{d\nu} \tag{3-20}$$

The reflection phase (of the amplitude signal) exhibits π shifts that induce discontinuities in the delay time simulation. For this reason, the time delay is calculated from the reflection phase of the intensity signal, which is twice the time delay obtained from the amplitude signal. The π shifts in the amplitude response become 2π shifts in the intensity and disappear in the unwrapping process (and then also the discontinuities). We observe that, away from the Bragg wavelength, the time delay asymptotically tends to the same value of 48.36 ps and independently from the grating strength Δn_{ac}. (Fig. 3-10 bottom), corresponding to the time needed to travel back and forth in the grating.

The corresponding impulse responses are presented in Fig. 3-11. Two regions are identified. The first one is the grating zone, with the OPLD inside the grating, that is OPLD < $2n_gL$, where n_g is the group refractive index. The second one is related to the region after the grating output. The impulse response in the grating region is dominated by the reflections occurring at the corresponding position in the grating. In the region after the grating output, the impulse response is given by light that has been reflected several times in the structure, as for a Fabry-Perot resonator.

At the grating entrance, all the light energy is available and the amplitude of the reflected signal is proportional to the refractive index modulation amplitude. While propagating in the grating, a part of the energy is gradually reflected for selected wavelengths and the amount of energy decreases.

For small Δn_{ac}, the pulse attenuation is also small and nearly constant impulse amplitude is observed ($\Delta n_{ac} < 10^{-5}$). The impulse amplitude after the grating is very small indicating negligible multiple reflections. In this case, the complex coupling coefficient is directly the complex impulse response within the grating. This approximation is known as the Fourier approximation where only the first reflection is considered [3-3].

When the refractive index modulation increases, this approximation breaks and the impulse amplitude shows a more or less important decrease in the grating region and even total amplitude annihilation for a more important Δn_{ac} (two times for $\Delta n_{ac} = 2 \cdot 10^{-4}$). In the region after the grating, the signal amplitude is important and multiple reflections are observed.

The phase difference between the impulse phase and the phase for propagation at the Bragg wavelength is constant except at amplitude poles and at the grating output where π-shifts are observed. This can be seen at the bottom of Fig. 3-11. This effect is similar to the phase shift observed for a reflection at a mirror interface.

b) Constant refractive index modulation amplitude

The spectral and impulse responses for a FBG at the constant refractive index modulation Δn_{ac} of 10^{-4} have been calculated for FBG lengths of 0.1, 1, 10 and 100 mm. The impulse response amplitudes are presented in Fig. 3-12, where the OPLD is given in a logarithmic scale. The phase difference is not presented as only the π-shifts are observed. The amplitude responses for positions inside the gratings are perfectly superposed due to the fact that all gratings have the same Δn_{ac}. This means that the impulse response for a given OPLD is only influenced by the grating part between the grating entrance and a position inside the grating at a distance OPLD/($2n_{eff}$) from this entrance. This is due to the causality principle that states that energy cannot be reflected at a grating position before the light has reached this region. It will be shown in the next section that this causality principle is the fundamental argument of the layer-peeling reconstruction method (§3.2). After the grating output position, the amplitude level increase with the grating length due to the fact that more photons are trapped inside the grating for several longer round-trips. For the smallest grating, the impulse response amplitude after the grating drops under −130 dB while for the 10 mm length grating, the output level is nearly as high as the grating entrance level.

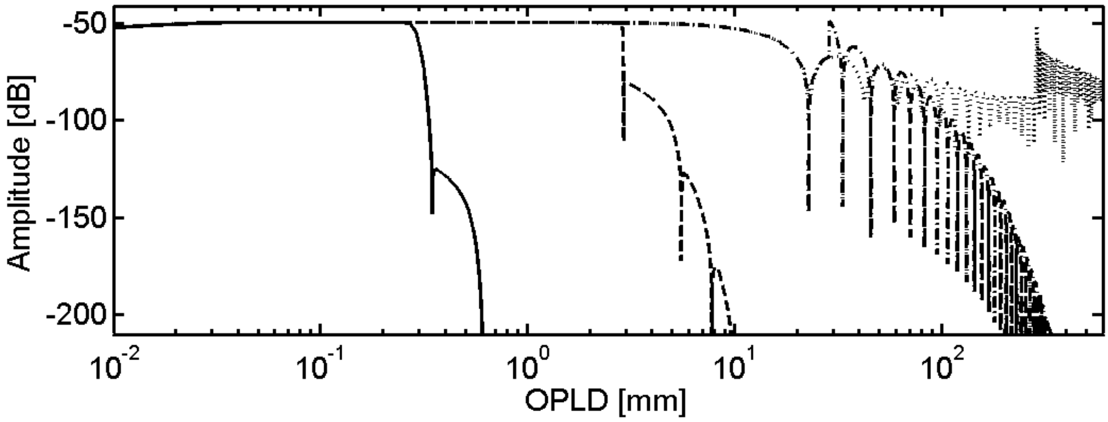

Fig. 3-12 Impulse response amplitude of homogeneous FBGs with constant refractive index modulation amplitude and a length of 0.1 (solid line), 1 (dashed line), 10 (dashed-dotted line) and 100 mm (dotted line)

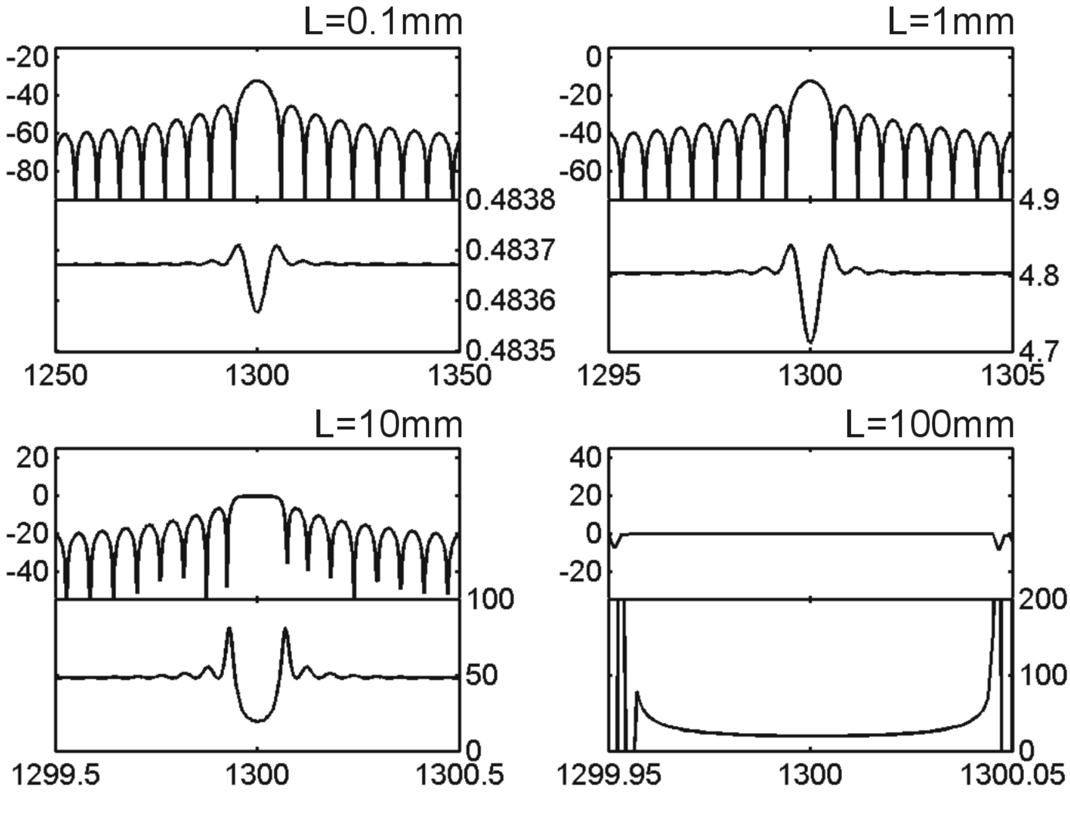

Fig. 3-13 Spectral response amplitude [dB] and time delay [ps] as a function of the wavelength [nm] for the four FBGs with constant $\Delta n_{ac} = 10^{-4}$ and length of 0.1, 1, 10 and 100 mm

The corresponding spectral responses are presented in Fig. 3-13. There is a wavelength range scaling factor that is inversely proportional to the grating length (100 nm at 0.1 mm, 10 at 1, 1 at 10 and 0.1 at 100). The reflection amplitude level increases with the grating length up to the saturation reflectivity of 0 dB. For the 100 mm grating, the saturation is observed even for some of the side-lobes, resulting in a much wider band-gap. The time delay behavior also shows a scaling factor, which in this case is proportional to the grating length.

c) Constant product of the length and the refractive index modulation amplitude

Interesting scaling properties can be deducted in the case of FBGs for which the product $\Delta n_{ac} \cdot L$ is kept constant. The spectral and impulse response of four gratings with $\Delta n_{ac} \cdot L = 10^{-6}$ have been calculated for grating lengths of 0.1, 1, 10 and 100 mm (the corresponding Δn_{ac} are 10^{-2}, 10^{-3}, 10^{-4} and 10^{-5} respectively). The impulse amplitudes are presented in Fig. 3-14 with respect to the OPLD on a logarithmic scale. As we can see, the shape of the responses is identical. The amplitude level is proportional to Δn_{ac} while the OPLD range is proportional to the grating length.

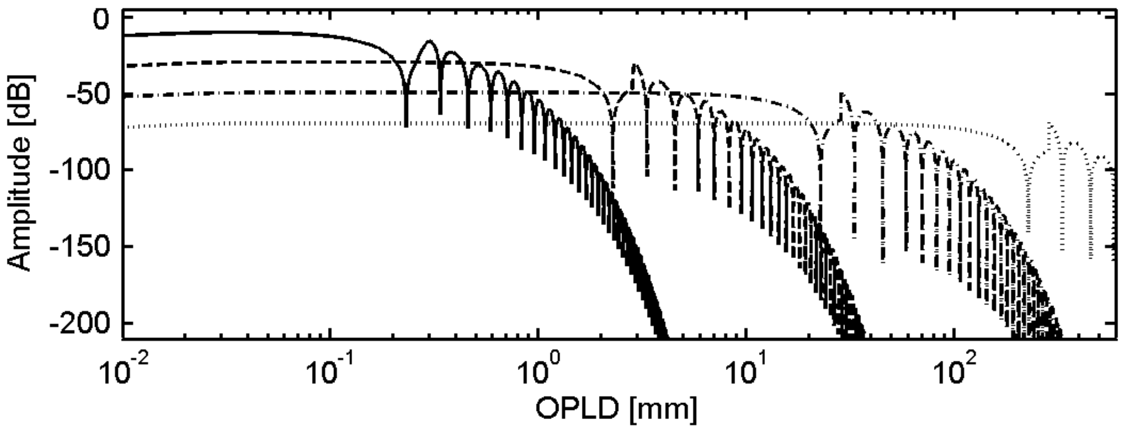

Fig. 3-14 Impulse response amplitude for constant $\Delta n_{ac}\cdot L = 10^{-6}$ with (L = 100 mm, $\Delta n_{ac} = 10^{-5}$) in dotted line, (10, 10^{-4}) in dashed-dotted line, (1, 10^{-3}) in dashed line, (0.1, 10^{-2}) in solid line

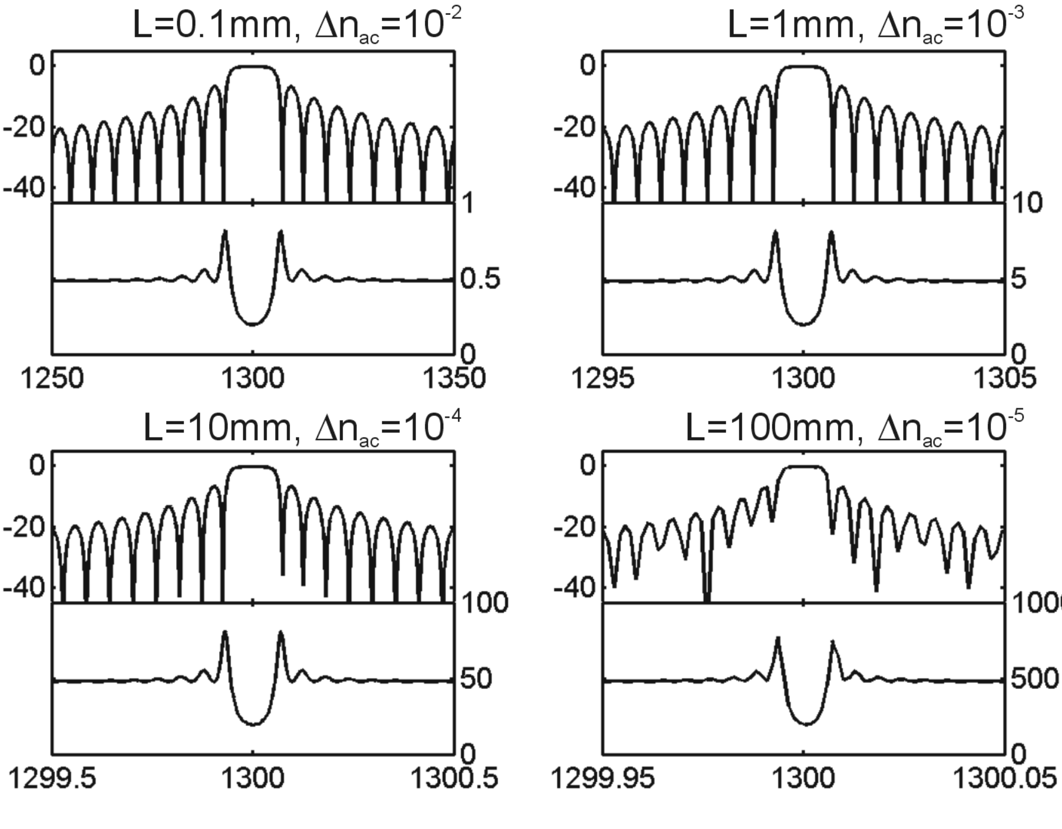

Fig. 3-15 Spectral response amplitude in [dB] and time delay in [ps] for the four FBG's with constant constant $\Delta n_{ac}\cdot L$ of 10^{-6}

The corresponding spectral responses are presented in Fig. 3-15. The amplitude shape is identical, with the same amplitude level but with different wavelength bandwidth, which is inversely proportional to the grating length. The time delays also exhibit the same shape, with the same bandwidth change but with an amplitude scaling factor proportional to the grating length. The relative poor definition of the spectral response of the 100 mm grating is due to the limited resolution of the simulation.

3.3.2 Non homogeneous FBG examples

We define in this section two non-homogeneous gratings that will be important to characterize the reconstruction process. The first grating exhibits discontinuities and linear variations of the refractive index modulation amplitude and of the grating period. The second grating is a period step-chirped grating.

a) Non homogeneous grating with discontinuities and ramps

In order to study the influence of the different parameters in the reconstruction process, a particular non-homogeneous FBG has been designed. Such grating exhibits discontinuities, constant and ramp parts in the Δn_{ac}, Δn_{dc} and Λ distributions. The refractive index modulation and local Bragg condition are presented in Fig. 3-16. The grating is divided in six sections of 2 mm length. The average refractive index distribution Δn_{dc} is opposite to the refractive index modulation amplitude Δn_{ac} to keep the effective refractive index to a constant value of 1.45. The sections where the refractive index modulation and the Bragg condition are constant are simulated in a single layer. In the cases where a ramp exists, the section is divided in 100 layers and the varying parameter is linearly distributed. This grating is labeled FBG1.

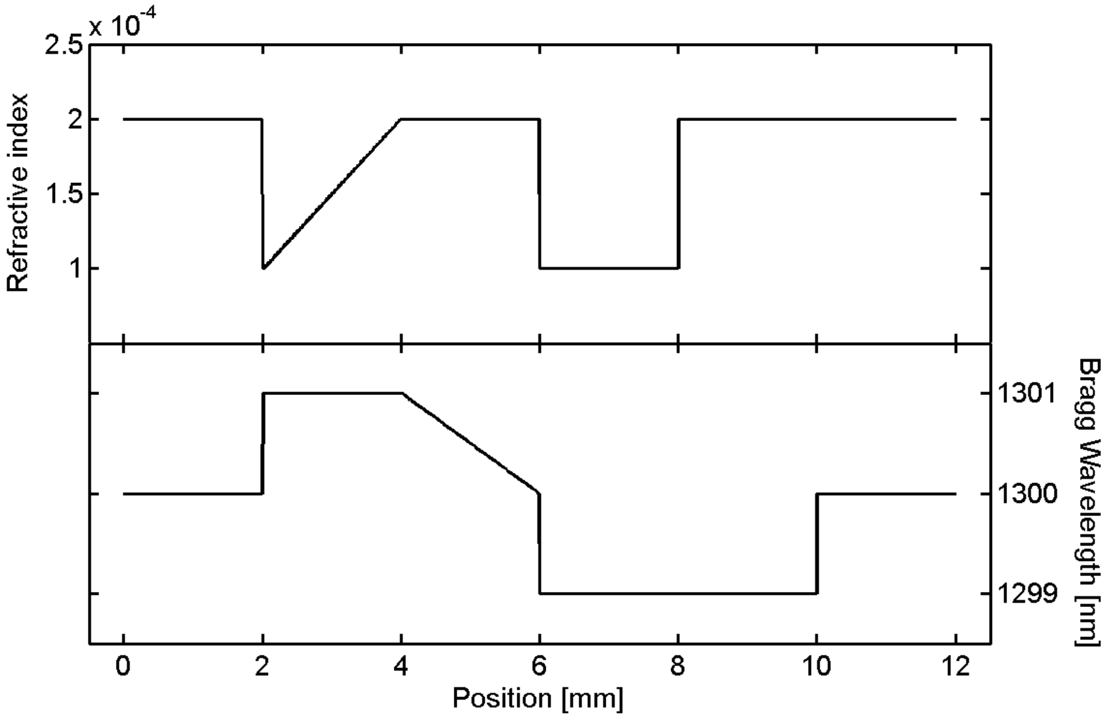

Fig. 3-16 Special FBG1 refractive index modulation amplitude Δn_{ac} (top) and local Bragg condition $2n_{eff}\Lambda$ (bottom)

The spectral response for this grating is presented in Fig. 3-17. The main spectral region extends from 1298 to 1302 nm and a very complicated spectral amplitude and time delay are observed.

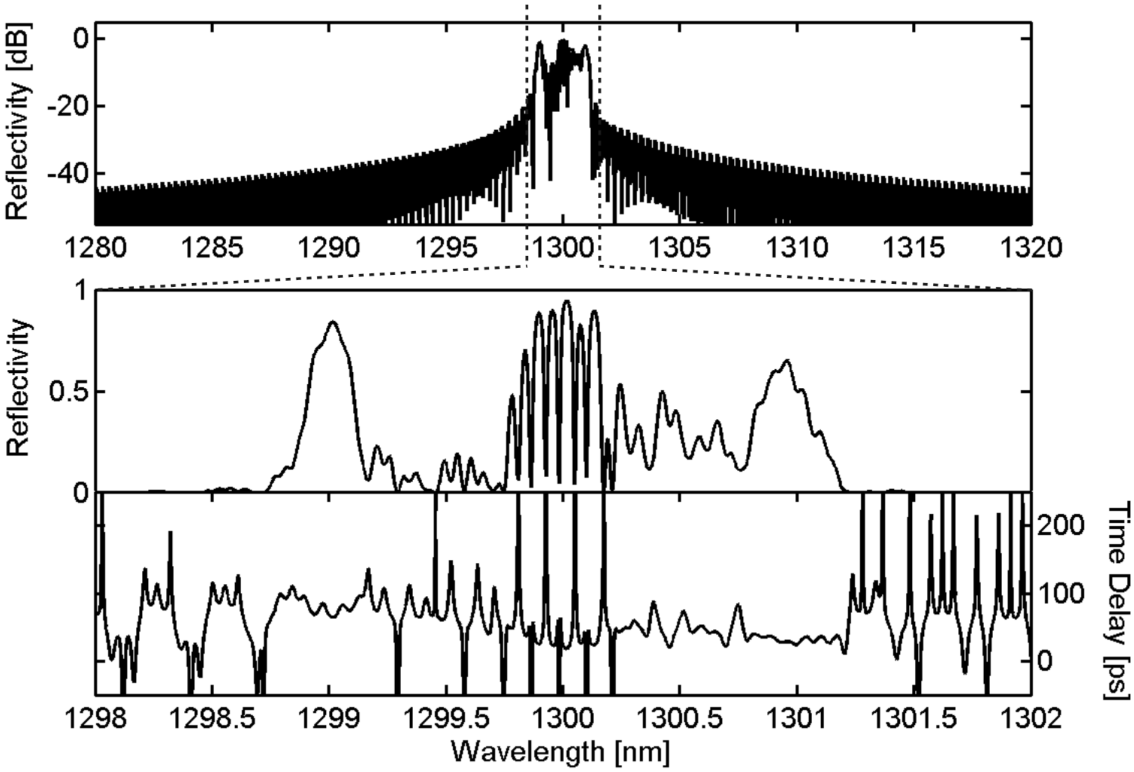

Fig. 3-17 Spectral response amplitude [dB] (top), linear scale (middle) and time delay (bottom) for FBG1

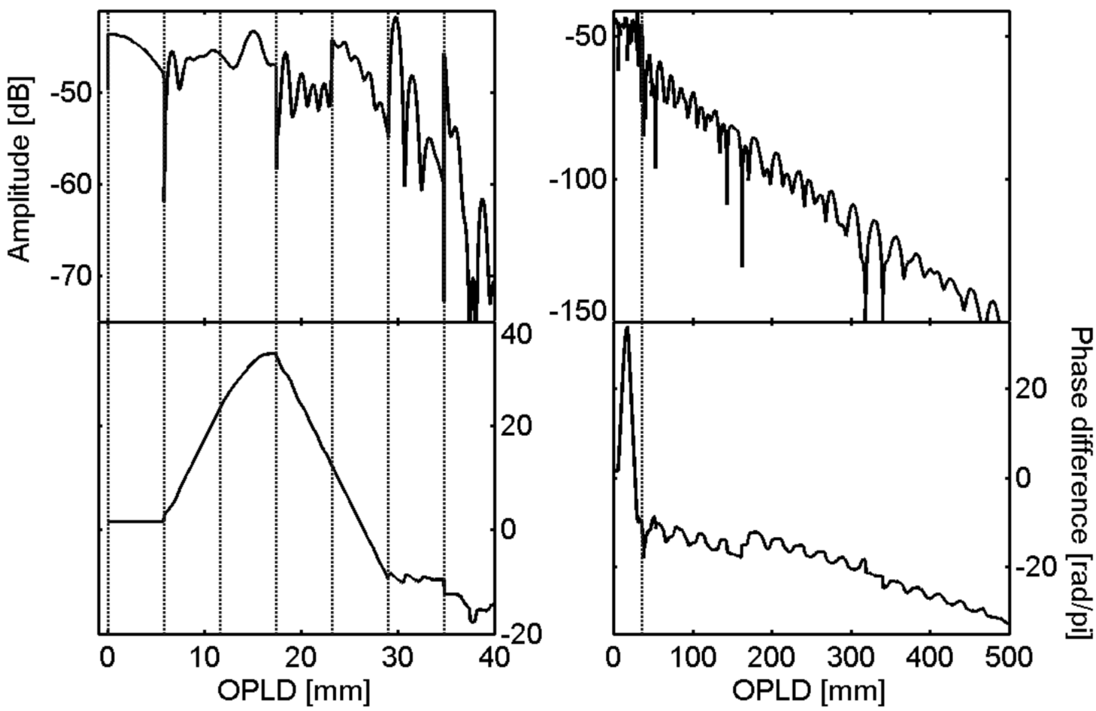

Fig. 3-18 Impulse response amplitude [dB] (top) and phase difference of the impulse phase with respect to the phase of a propagation at 1300 nm (bottom) for FBG1 with two OPLD scales; the vertical lines in the left part of the figure indicate the grating sections limits

The impulse response of FBG1 is then presented in Fig. 3-18. The left part of the figure presents the details of the grating region, where the vertical lines indicate the limits of each section of the grating. The first section exhibits a large amplitude decrease due to the high Δn_{ac}. The amplitude after the first section is difficult to directly interpret due to the high grating strength that greatly modifies the pulse spectral properties during the propagation. The reconstruction for this kind of grating is then very important.

b) Period step-chirped grating

A second non-homogeneous grating, FBG2, has been simulated to investigate the reconstruction limits. The length is 10 mm, the refractive index modulation is constant ($5 \cdot 10^{-4}$) and the grating period is divided in ten sections with different values linearly distributed to give Bragg conditions between 1298 to 1302 nm. The refractive index modulation amplitude (Δn_{ac}) and the Bragg wavelength ($2\Lambda n_{eff}$) distributions of such grating are seen in Fig. 3-19.

The corresponding spectral response is shown in Fig. 3-20. The amplitude exhibits a nearly rectangular response between 1298 and 1302 nm. The amplitude and the time delay responses show ripples.

The impulse response amplitude of FBG2 (Fig. 3-21) shows an important amplitude drop for the first section, but then the signal increases at the entrance of any other section and the overall level is constant in the grating region. This is explained by the fact that each section reflects a different part of the source spectrum. The amplitude drop greater than 20 dB at the grating output indicates that few photons are trapped inside the structure for several round-trips. We observe that the second derivative of the phase difference, $d^2\Delta\phi/dOPLD^2$ ($\Delta\phi$ is the phase difference), is negative in the grating region and then constant after the grating output. This effect is explained by the decrease of the Bragg condition distribution along the grating.

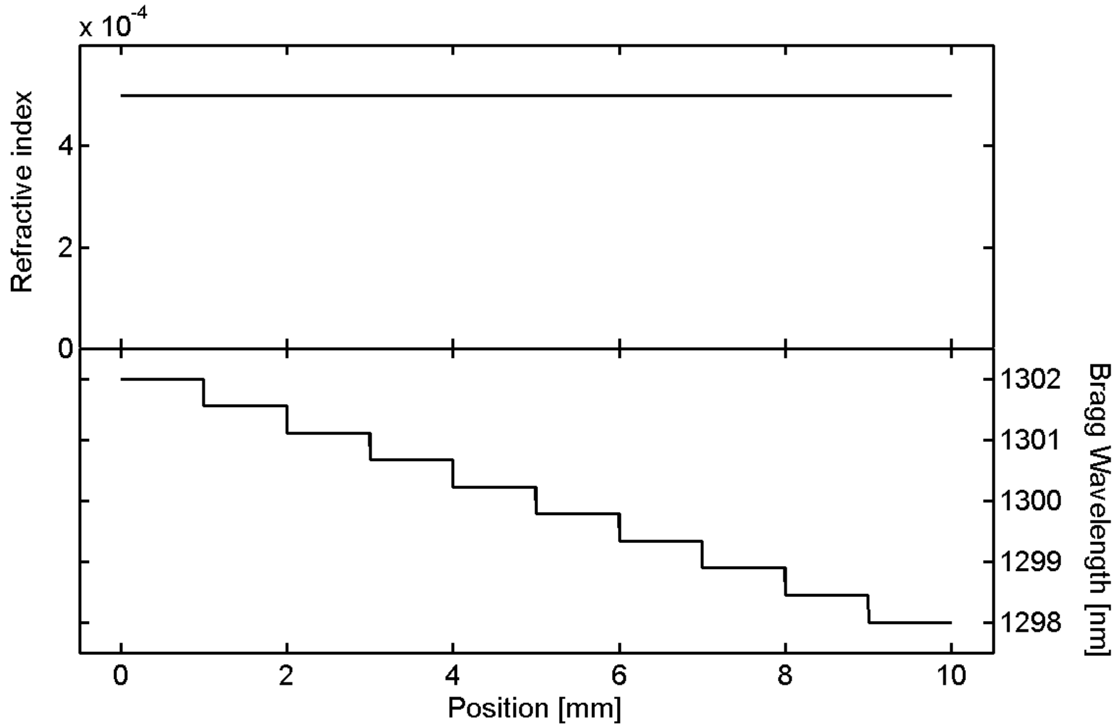

Fig. 3-19 Special FBG2 refractive index modulation amplitude (top) and local Bragg condition (bottom)

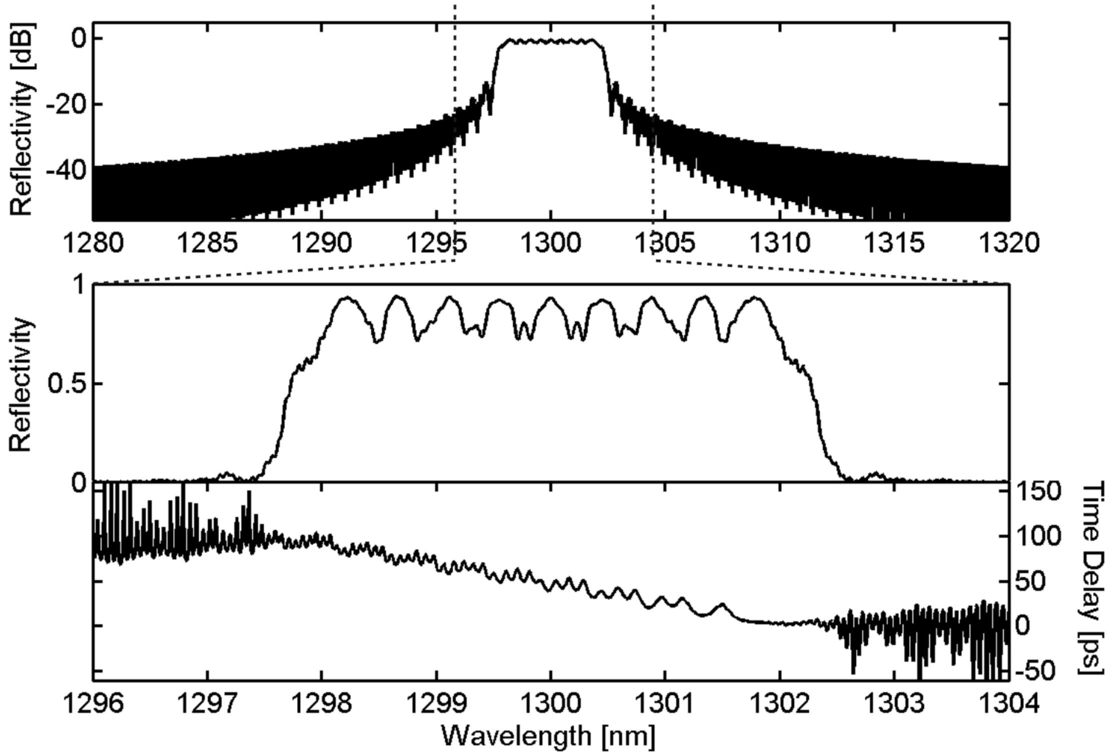

Fig. 3-20 Spectral response amplitude in dB (top) and in linear scale (middle), and time delay (bottom) for the FBG2

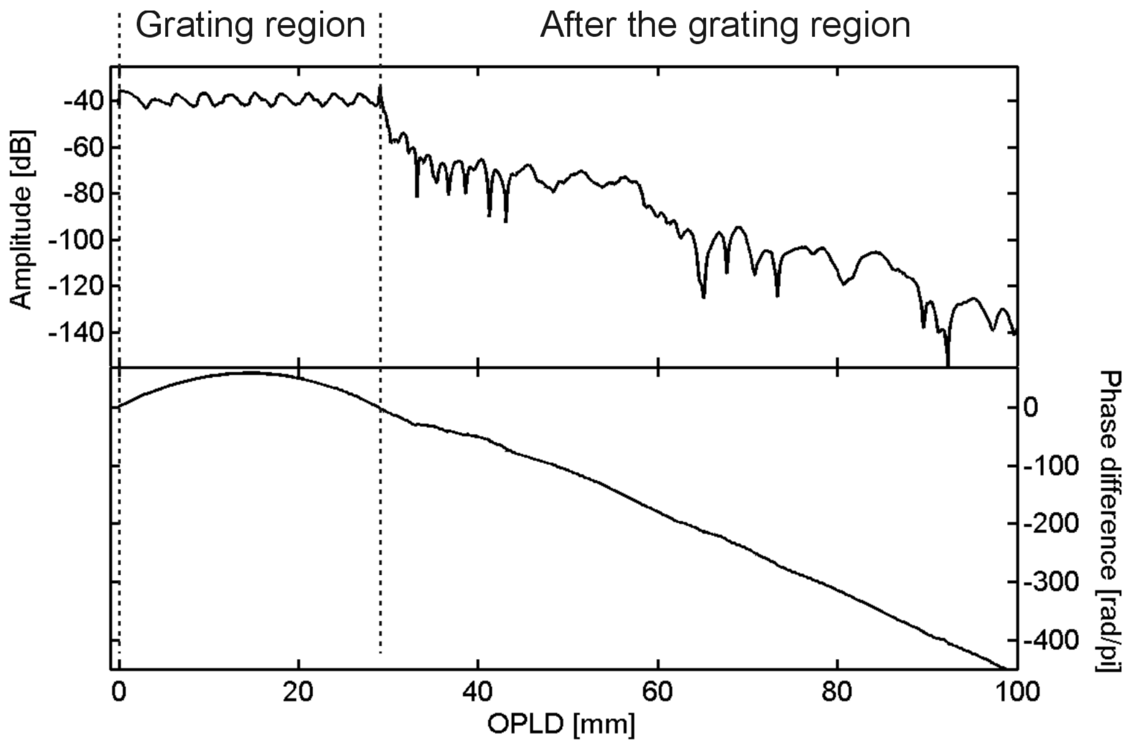

Fig. 3-21 Impulse response amplitude (top) and phase difference with the phase of propagation at 1300 nm (bottom) for FBG2

3.3.3 Source effect

The decibel scale representation of the impulse response amplitude depends on the spectrum of the light propagating in the grating. For simulation purpose, a theoretical light source with Gaussian spectral shape is defined, which is determined by its central wavelength and bandwidth. The influence of these parameters in the calculation of the impulse response can be seen as a windowing effect applied to the Fourier transform of the grating spectral response.

a) Source bandwidth effect

The influence of the source bandwidth is presented in Fig. 3-22. The FBG is homogeneous, 10 mm long with a refractive index modulation amplitude of $2{\cdot}10^{-4}$. The central wavelength of the light source is set to the Bragg wavelength of 1300 nm. The impulse response obtained for a theoretical source with bandwidth of 1, 5, 25 and 125 nm is shown. The impulse response amplitude is inversely proportional to the source bandwidth. This can be explained since for smaller bandwidth sources, the coherence length is larger and then the coherent reflection is higher. The counterpart to higher amplitude is a wider transition region that is observed at the grating input and output. The convolution process with a function of higher coherence length explains this. It is important to notice that this "smoothing" effect does not affect the impulse response amplitude near poles (impulse response position for which the amplitude sharply drops to zero and the phase difference has a π–shift). Moreover, we can observe that the phase difference is not affected by the source bandwidth.

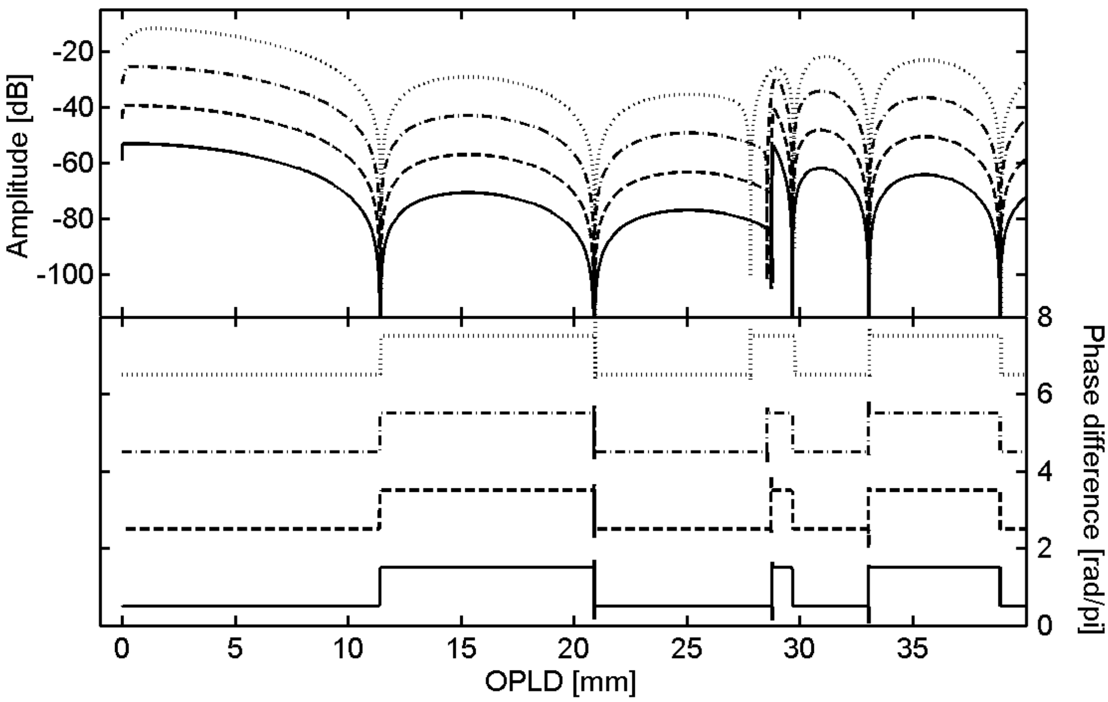

Fig. 3-22 Source bandwidth effect on the complex impulse response amplitude (top) and phase difference (bottom) for a 10 mm homogeneous grating with $2{\cdot}10^{-4}$ refractive index modulation; 125 nm (solid lines), 25 nm (dashed lines), 5 nm (dashed-dotted lines) and 1 nm (dotted lines) source bandwidth have been simulated

b) Source detuning effect

The influence of the detuning wavelength between the FBG and the broadband source central wavelength has been studied for a 40 nm bandwidth source. The results are shown in Fig. 3-23 for a detuning of 0, 10, 30 and 50 nm, respectively. The impulse responses for a detuning smaller than 10 nm are very close to the case without detuning. For a more important detuning, the impulse amplitude drops consistently due to the reduced overlap between the FBG and the source. Another effect also appears : for high detuning, the amplitude signal at the grating input and output presents an peak due to the refractive index step that acts like a broadband mirror. This is presented in the zoomed view of the grating output in Fig. 3-23 (the curves has been shifted in the OPLD axis for clarity). The phase difference shows a smoothing effect, that is the π-shifts are spread over an OPLD range proportional to the detuning.

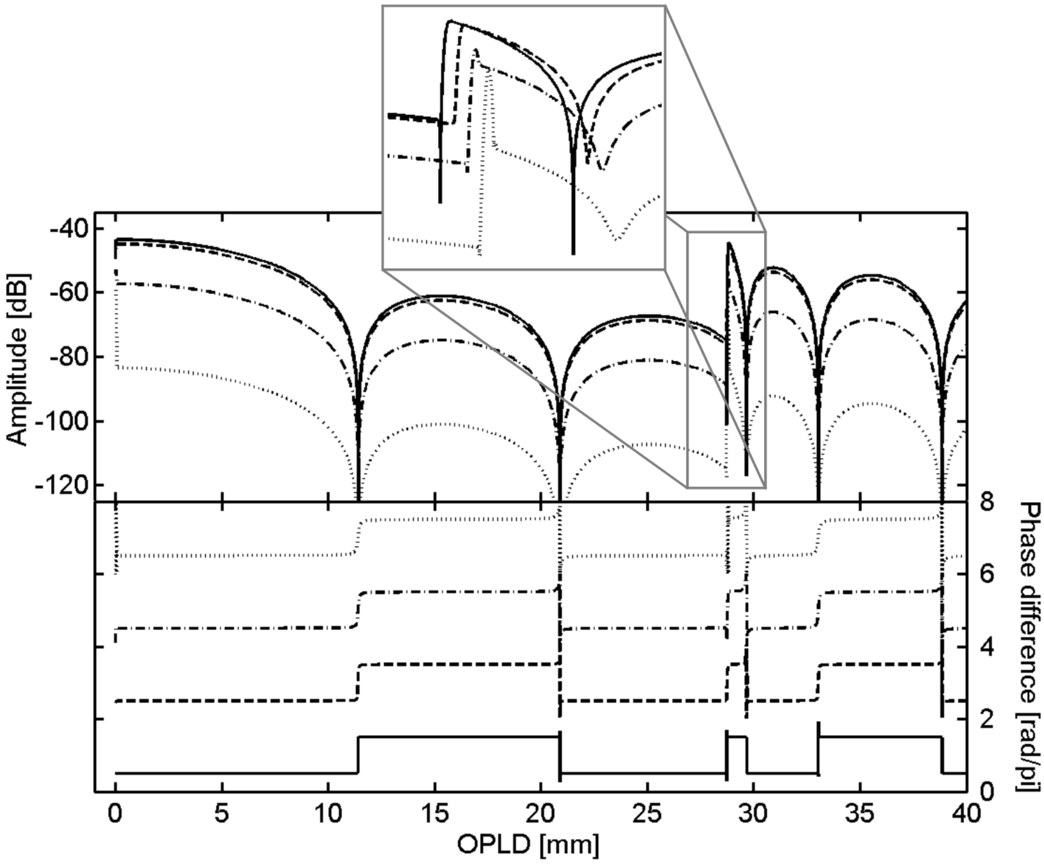

Fig. 3-23 Source detuning effect on the complex impulse response amplitude (top) and phase difference (bottom) for a 10 mm homogeneous grating with 2·10⁻⁴ refractive index modulation; 0 nm (solid lines), 10 nm (dashed lines), 30 nm (dashed-dotted lines) and 50 nm (dotted lines) detuning values are considered

3.4 Reconstruction examples

This section studies the principal parameters that intervene in the reconstruction of FBG by layer-peeling. The limits of the reconstruction methods are presented. The influence of the layer thickness and the number of used spectral points is evaluated. The reconstruction from a starting complex reflection response or impulse response is analyzed from the point of view of the available dynamic range and the influence of noise.

3.4.1 Reconstruction limits

We have shown in section 3.3.1 that the spectral reflectivity of homogeneous gratings can saturate when the grating length and refractive index modulation amplitude are sufficiently important. This effect is explained by the fact that the light components, for which the wavelength is in the saturation bandwidth, are completely reflected before the grating output. This effect is not limited to homogeneous FBGs.

For such gratings that have a saturation bandwidth in reflection, the reconstruction by layer-peeling reaches its limits as a part of the grating is not probed by all possible wavelengths. This can be observed in the reconstruction of homogeneous gratings with different lengths and identical refractive index modulation amplitude (Δn_{ac} of $2{\cdot}10^{-4}$), as presented in Fig. 3-24. The reconstruction of the 1 mm long grating is complete, but for the 10 mm grating, the last 2 mm show a small coupling amplitude decrease and also a small remaining coupling amplitude after the grating output position, indicating reconstruction errors. The layer-peeling algorithm clearly fails to reconstruct the 20 mm long FBG as we observe that the amplitude and phase information of the coupling coefficient are not reconstructed for more than half the grating length. We have performed the reconstruction of the 20 mm long FBG with two spectral resolution values and if a better reconstruction is observed for the higher spectral resolution, the complete reconstruction also failed in this case.

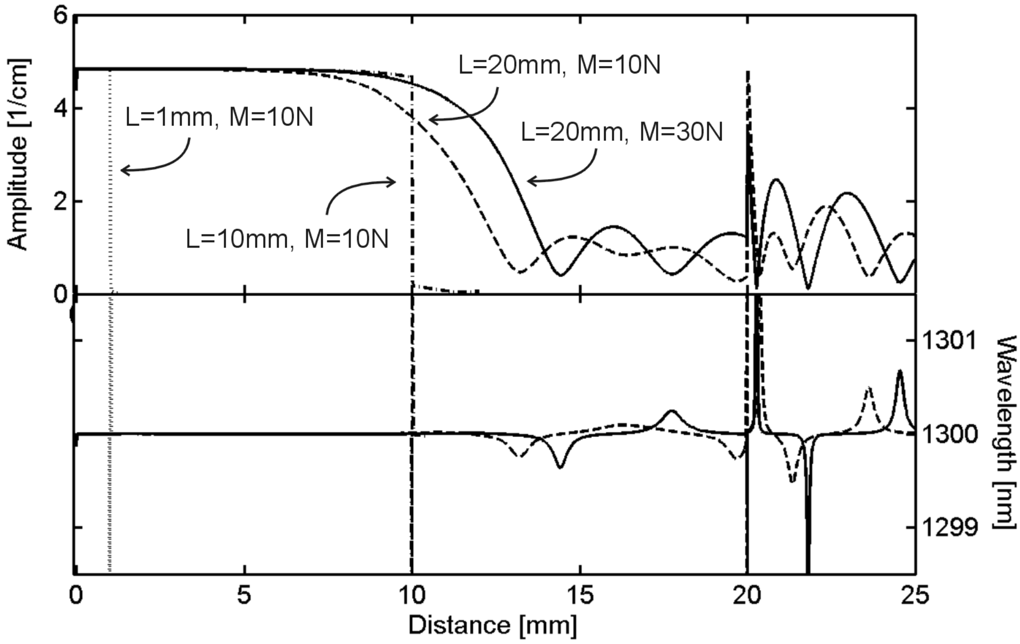

Fig. 3-24 Layer-peeling reconstruction with 5 μm layer thickness of the coupling coefficient amplitude (top) and local Bragg wavelength calculated from the coupling coefficient phase (bottom) for homogeneous gratings of refractive index modulation of $2{\cdot}10^{-4}$ for different lengths L and number of spectral points M (N represents the number of layers)

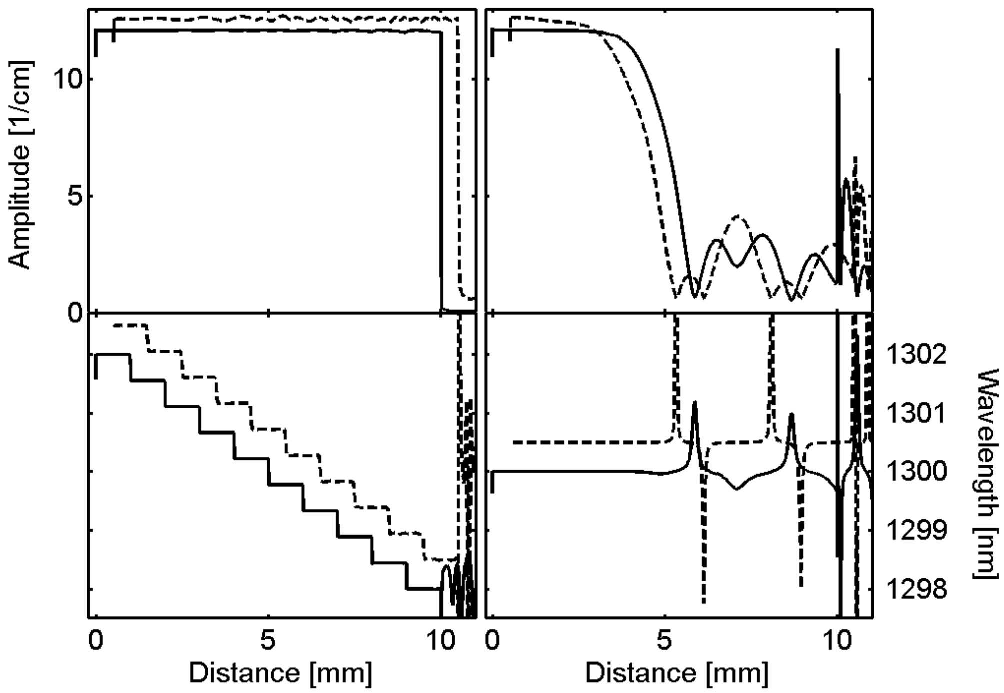

Fig. 3-25 Layer-peeling reconstruction of the coupling coefficient amplitude (top) and local Bragg wavelength calculated from the coupling coefficient phase (bottom) for the FBG2 (left) and a 10 mm long homogeneous FBG with a Δn_{ac} of $5{\cdot}10^{-4}$; the reconstruction parameters are : Δ = 3 μm, M = 30 N for solid lines and Δ = 20 μm, M = 10 N for dashed lines; the dashed lines are shifted for clarity

Another illustration of this spectral depletion effect that limits the reconstruction by layer-peeling is presented in Fig. 3-25 where the reconstruction of a 10 mm long and period chirped FBG with constant Δn_{ac} (FBG2) is compared to the reconstruction of a FBG with the same parameters but without the chirp. The homogenous grating reconstruction falls down after 3 to 4 mm, while the complete chirped grating can be reconstructed. The chirped grating has a smaller maximal reflection amplitude and a broader bandwidth that prevents the complete depletion of a particular spectral bandwidth.

Recently, it has been demonstrated that the worst-case error amplification factor in reconstructing a grating from its complex reflection spectrum by layer-peeling is of the order of $1/T_{min}$, where T_{min} is the minimum transmission amplitude through the grating [3-20].

The limitations of the reconstruction for not too strong FBGs can be partially overcome in two ways. The first possibility is to reconstruct the grating from both sides and to combine only the first half of the reconstruction distributions. The second alternative is an experimental method that is a consequence of the results presented in Fig. 3-25, where a predefined chirp function is applied to the grating by a temperature ramp or a strain ramp. The applied chirp needs to be sufficient to reduce the maximal reflectivity of the grating.

3.4.2 Layer thickness

The reconstructions of the FBG1 for different layer thickness (5, 20, 50 and 100 μm) are presented in Fig. 3-26. The number of spectral points M is set to ten times the number of layers (it will be seen in the next sub-section that a higher number of spectral points is not necessary). Apart from the reduced resolution observed at discontinuities, the reconstructions are not much affected from the layer thickness.

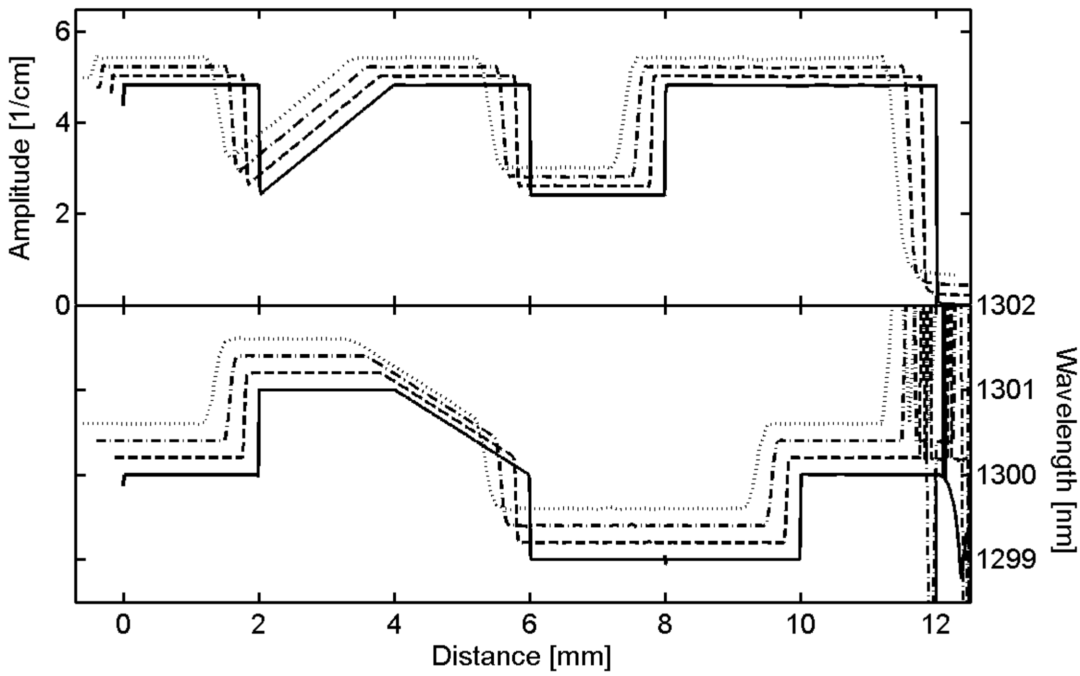

Fig. 3-26 Reconstructed coupling coefficient amplitude (top) and local Bragg wavelength (bottom) for the FBG1 performed with M = 10N and different layer thickness parameters : 5 μm for the solid lines, 20 μm for the dashed lines, 50 μm for the dashed-dotted lines and 100 μm for the dotted lines; the curves are translated for clarity

3.4.3 Number of points

The choice of the number of spectral points M required for the reconstruction process by layer-peeling is not absolute but depends on the number of layers N (and is then inversely related to the layer thickness). Fig. 3-27 presents the reconstructions of FBG1 performed with a 3 μm–layer thickness and a ratio M/N of 1, 2, 5 and 10, respectively. The reconstruction is poor for M = N and fairly good for M = 2N. For M/N higher than 5 or ten, the results are very close. For very strong gratings, a ratio increase to 30 or 50 improves the reconstruction, but not in a significantly way (Fig. 3-24).

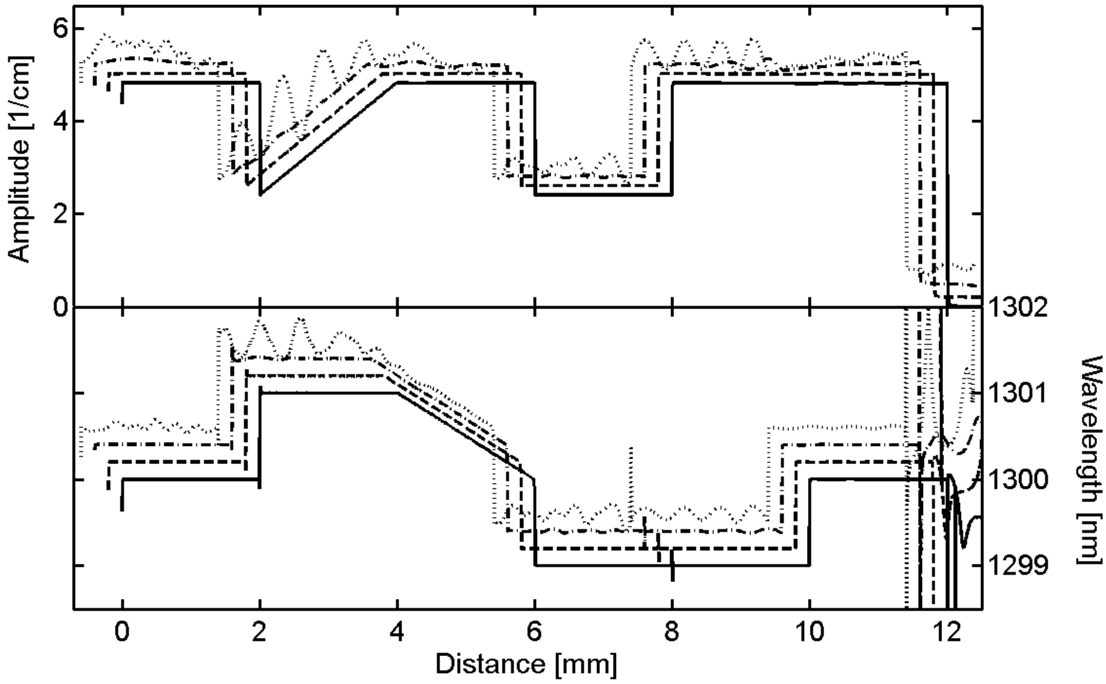

Fig. 3-27 Reconstructed coupling coefficient amplitude (top) and local Bragg wavelength (bottom) for the FBG1 performed with layers thickness of 3 μm and different ratio M/N : 10 for the solid lines, 5 for the dashed lines, 2 for the dashed-dotted lines and 1 for the dotted lines; the curves are translated for clarity

3.4.4 Reduction of the Gibb's effect

The calculation of the ρ_j values is performed through a Fourier transform and it is known that Fourier transforms of bandwidth limited spectral function give some oscillation at each discontinuity (Gibb's phenomenon). A standard way to limit these oscillations is to window the original spectral response with an apodization function. Another way is to reduce the resolution by averaging the Fourier transform over several points. This windowing effect has been simulated and the results are presented in Fig. 3-28. The solid lines for the case without windowing clearly show the Gibb's oscillations and exhibits very good reconstruction at the other locations. The dashed lines (which represent the reconstruction from the spectral response windowed with a Hann function) show that the oscillating effects at the edges are suppressed but the reconstruction is less efficient after 7 mm due to the energy loss induced by the windowing. We could notice this effect because the FBG1 has been design not to be easily reconstructed.

The most interesting results are found for the third (dashed-dotted lines) case where the spectral response is not windowed but the resulting reconstruction is averaged over 3 points

$$f\left(p_j\right)=\frac{f\left(p_{j-1}\right)+2f\left(p_j\right)+f\left(p_{j+1}\right)}{4} \qquad (3\text{-}21)$$

where f is the coupling amplitude or the local Bragg wavelength and p_j is the discrete position j. This method offers the best reconstruction results at the price of a slightly reduced resolution (that can be recovered by reducing the layer thickness).

3.4.5 Reconstruction from the complex spectral response

Here, we consider the simulation of the reconstruction from experimental complex spectral response. The influence of the available dynamic range and of the noise is analyzed.

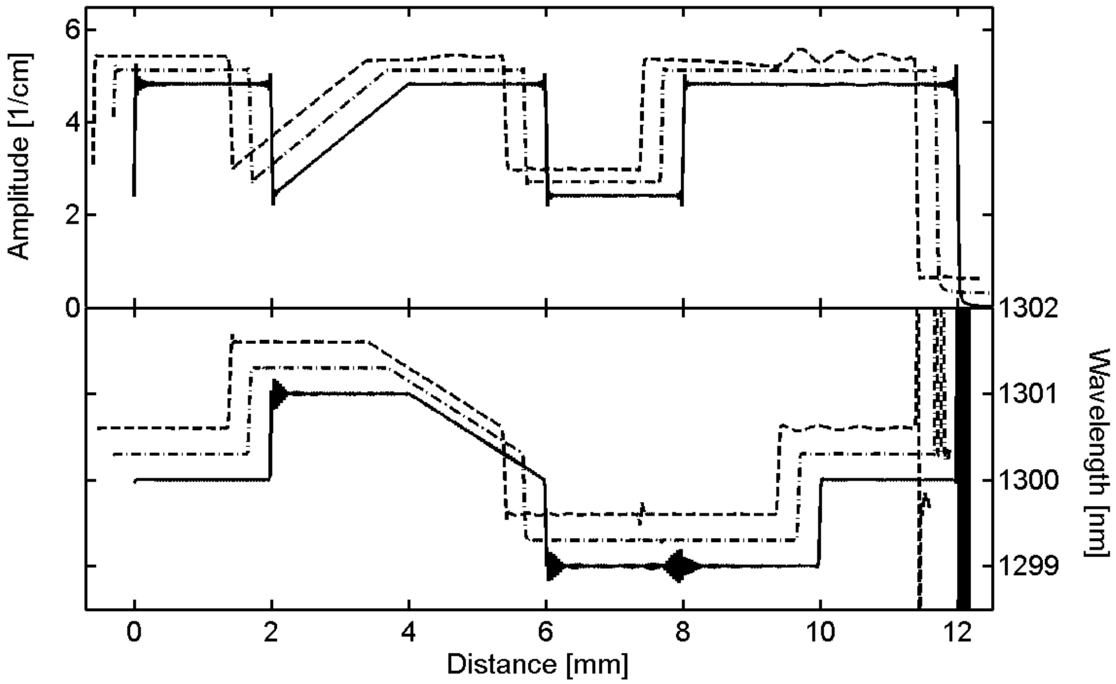

Fig. 3-28 Reconstructed coupling coefficient amplitude (top) and local Bragg wavelength (bottom) for the FBG1 performed with layers thickness of 20 μm, a ratio M/N = 10 without windowing (solid lines), without windowing but with averaging (dashed-dotted lines) and with hann windowing (dashed lines); the curves are translated for clarity

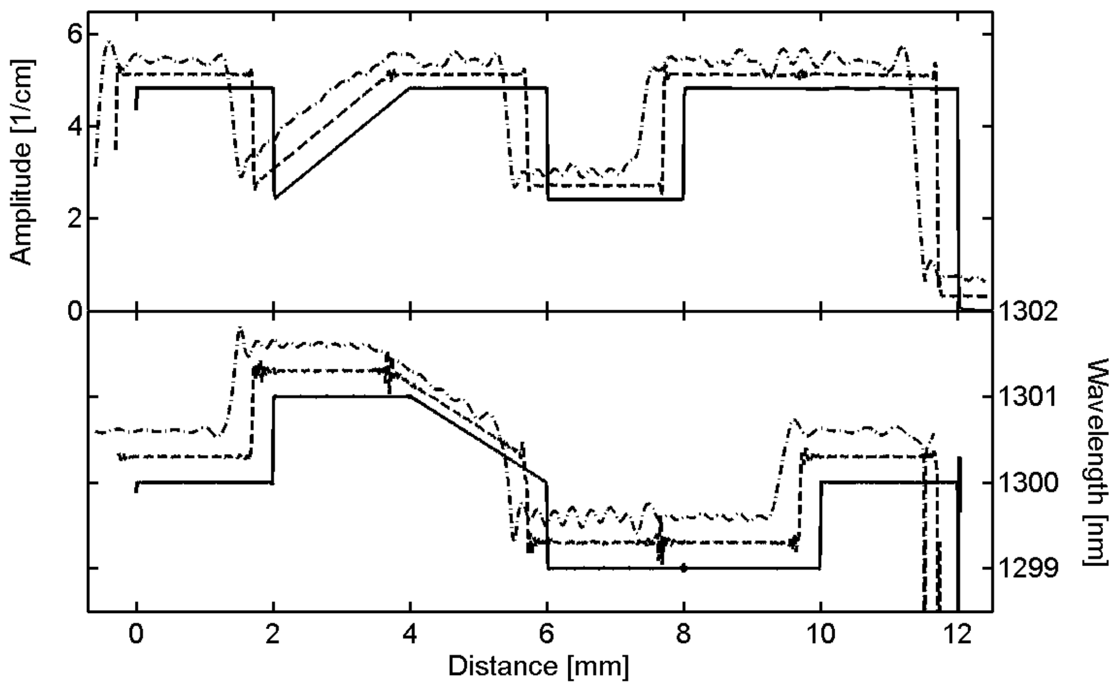

Fig. 3-29 Reconstructed coupling coefficient amplitude (top) and local Bragg wavelength (bottom) for the FBG1 performed with layers thickness of 5 μm, a ratio M/N = 10, and for a spectral intensity range of 60 dB (solid lines), 40 dB (dashed lines) and 20 dB (dashed-dotted lines); the curves are translated for clarity

a) Spectral response dynamic range

The dynamic range is defined in our context as the available signal range between the maximal value and the noise level. The spectral signal considered is the reflection intensity. The impact of the available dynamic range is presented in Fig. 3-29 for 20, 40 and 60 dB dynamic range. The reconstruction is relatively poor for the 20 dB limited dynamic range and quite good for the 40 dB case, except from some non compensated oscillations at the section edges. The reconstruction with a dynamic range of 60 dB or higher is very good.

b) Spectral response noise

Noise in experimental measurement is inevitable and its influence on the reconstruction from the spectral response is simulated hereafter. For a given spectral point $r = |r| \cdot e^{i\phi}$, a noisy spectral point $r_n = |r_n| \cdot e^{i\phi_n}$ is calculated :

$$\begin{aligned} |r_n| &= A_o \cdot rand + (1 + A_s \cdot rand) \cdot |r| \\ \phi_n &= P_o \cdot rand + (1 + P_s \cdot rand) \cdot \phi \end{aligned} \qquad (3\text{-}22)$$

where A_o and A_s are the noise amplitude offset and scale factor, respectively; P_o and P_s the noise phase offset and scale factor, respectively; and finally "rand" a random number between ± 0.5. The most important parameters are the noise amplitude scale factor A_s and the noise phase offset factor P_o. The results for 5, 10, 20 and 30 % scale noise and phase offset of π/100, π/50, π/20 and π/10, respectively, are presented in Fig. 3-30. It is seen that even for the smallest noise case the reconstruction encounters problems and oscillations are observed. For more noisy data, the oscillations increases and reconstruction errors becomes very important.

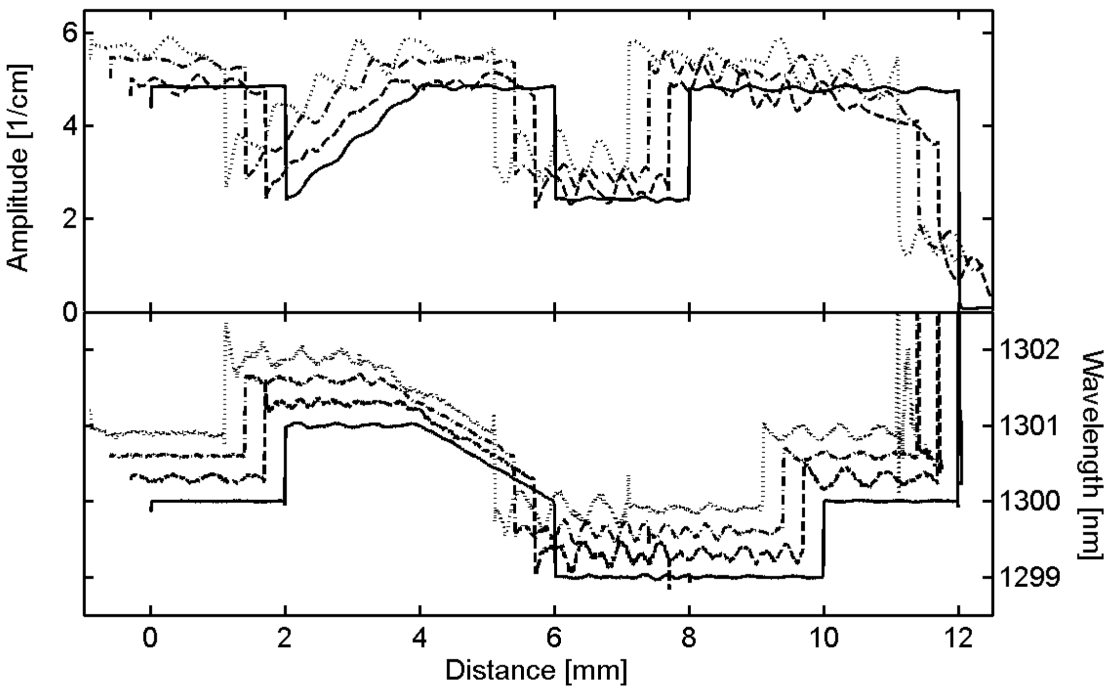

Fig. 3-30 Reconstructed coupling coefficient amplitude (top) and local Bragg wavelength (bottom) for the FBG1 performed with layers thickness of 5 μm, a ratio M/N = 10 for a different noisy spectral responses; solid lines : $A_o = 10^{-6}$, $A_s = P_s = 5\%$, $P_o = \pi/100$; dashed lines : $A_o = 10^{-5}$, $A_s = P_s = 10\%$, $P_o = \pi/50$; dashed dotted lines : $A_o = 10^{-4}$, $A_s = P_s = 20\%$, $P_o = \pi/20$; dotted lines : $A_o = 10^{-3}$, $A_s = P_s = 30\%$, $P_o = \pi/10$; the curves are shifted for clarity

3.4.6 Reconstruction from the complex impulse response

Here, the simulation of the reconstruction from the complex impulse response is discussed. The dynamic range and noise effect are also considered.

a) Impulse response dynamic range

The impact of the available dynamic range is presented in Fig. 3-31 for 20, 40, 60 and 80 dB of dynamic range, respectively. In this case, the dynamic range is defined from the dB representation of the impulse response amplitude with an illumination light source centered at 1300 nm with 40 nm bandwidth. Some oscillations are observed for the smaller dynamic range examples, especially at the last third of the grating reconstruction. Nevertheless, the impact is less important as what has been observed in Fig. 3-29 for the reconstruction case from the spectral response.

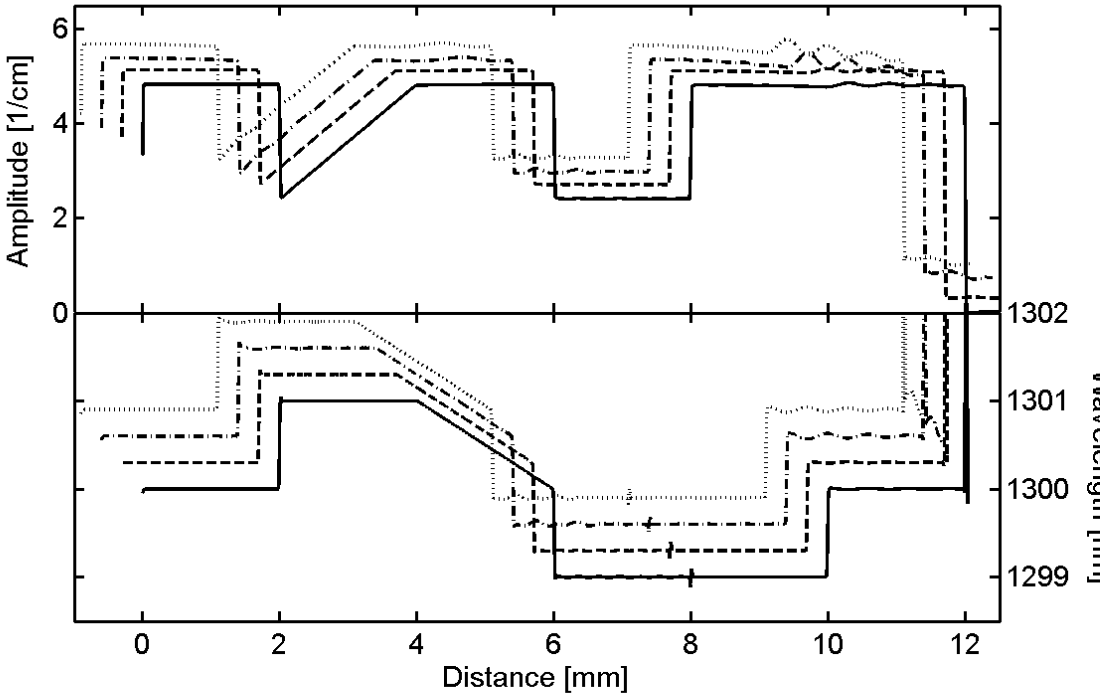

Fig. 3-31 Reconstructed coupling coefficient amplitude (top) and local Bragg wavelength (bottom) for the FBG1 performed with layers thickness of 5 μm, a ratio M/N = 10 for a impulse amplitude range of 80 dB (solid lines), 60 dB (dashed lines), 40 dB (dashed-dotted lines) and 20 dB (dotted lines); the curves are translated for clarity

b) Impulse response noise

The starting functions are the impulse response amplitude h_a and the phase difference h_p. The noisy impulse response is calculated in a similar manner as it has been performed for spectral data in equation (3-22)

$$\begin{aligned} h_{a,n} &= A_o \cdot rand + \left(1 + A_s \cdot rand\right) \cdot h_a \\ h_{p,n} &= P_o \cdot rand + \left(1 + P_s \cdot rand\right) \cdot h_p \end{aligned} \qquad (3\text{-}23)$$

where A_o and A_s are the noise amplitude offset and scale factor, respectively; P_o and P_s the noise phase offset and scale factor, respectively; and finally "rand" a random number between ± 0.5. The results for 5, 10, 20 and 30 % scale noise and phase offset of $\pi/100$, $\pi/50$, $\pi/20$ and $\pi/10$, respectively, are presented in Fig. 3-32. The local Bragg wavelength, calculated from the derivative of the coupling coefficient phase, has been necessarily performed on several reconstruction points to limit the high variations of the noise. This procedure was not necessary for the reconstruction from the noisy spectral response as the noise effect is spread over the whole grating reconstruction. The coupling coefficient amplitude shows only localized noise, but not an overall shape change, except from some oscillations for very noisy cases. This indicates that the impulse noise impact in the reconstruction is mainly restricted to the corresponding grating position. Other experiments with single defect measurement impulse response points have shown that the reconstruction presents also a single defect point at the corresponding grating location. This explains that even for small phase noise, the derivative noise is very important but the underlying local Bragg wavelength is conserved if averaged on several points. Compared to the reconstruction from a noisy spectral response, the reconstruction from a noisy impulse response exhibits better results.

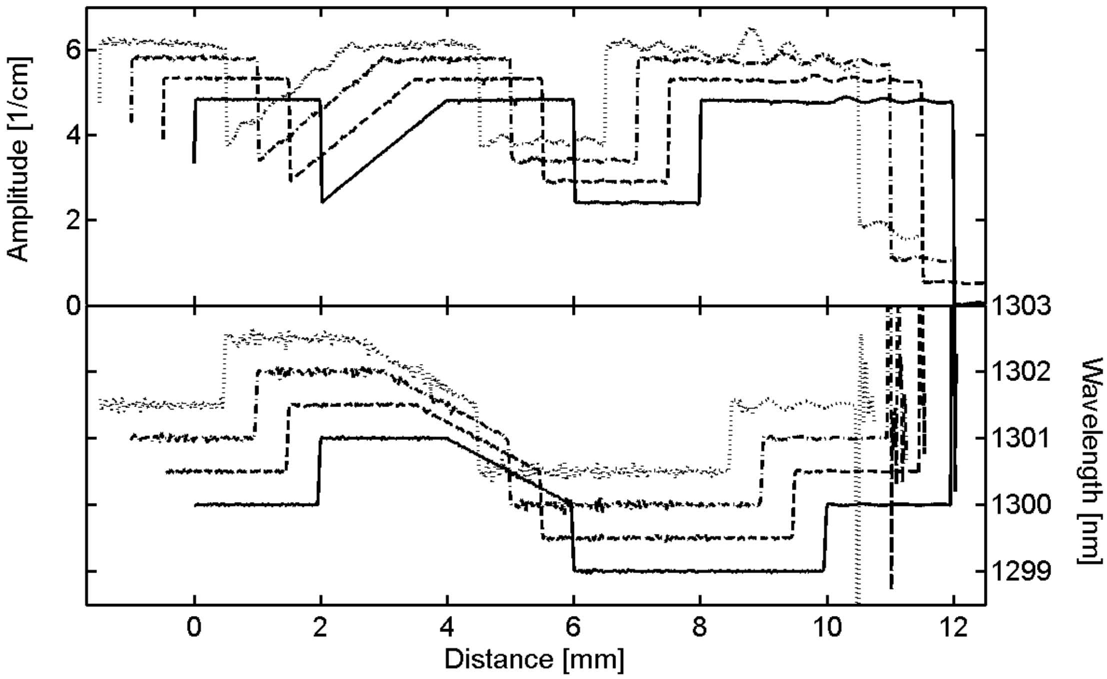

Fig. 3-32 Reconstructed coupling coefficient amplitude (top) and local Bragg wavelength (bottom) for the FBG1 performed with layers thickness of 5 μm, a ratio $M/N = 10$ for a different noisy impulse responses; solid lines : $A_o = 10^{-7}$, $A_s = P_s = 5\%$, $P_o = \pi/100$; dashed lines : $A_o = 10^{-6}$, $A_s = P_s = 10\%$, $P_o = \pi/50$; dashed dotted lines : $A_o = 10^{-5}$, $A_s = P_s = 20\%$, $P_o = \pi/20$; dotted lines : $A_o = 10^{-4}$, $A_s = P_s = 30\%$, $P_o = \pi/10$; the curves are translated for clarity

3.5 Methods for characterizing FBGs with loss or with refractive index and period chirp components

3.5.1 Characterization of FBGs with loss

In Chapter 2, we have seen that a tilt in the grating is associated with an excess loss. In a first approximation these losses are assumed to be frequency independent and they are included in a loss matrix $T_{\alpha j}$ defined as

$$T_{\alpha,j} = \begin{bmatrix} e^{-\alpha\Delta_j} & 0 \\ 0 & e^{\alpha\Delta_j} \end{bmatrix} \qquad (3\text{-}24)$$

The similarity with the pure propagation matrix allows to define a new propagation matrix that takes account of the loss :

$$T_{\Delta\alpha,j} = T_{\Delta,j} \cdot T_{\alpha,j} = \begin{bmatrix} e^{i(\delta+i\alpha)\Delta_j} & 0 \\ 0 & e^{-i(\delta+i\alpha)\Delta_j} \end{bmatrix} \tag{3-25}$$

The loss matrix can be adapted to other types of loss, frequency dependent or not via the parameter α. The recursion equation becomes in this case

$$r_j(\delta) = \frac{r_{j-1}(\delta) - \rho_j}{1 - \rho_j^* \cdot r_{j-1}(\delta)} e^{-i(\delta+i\alpha)\cdot 2\Delta_j} \tag{3-26}$$

The reconstruction for FBGs experiencing losses, which can be described with the loss matrix $T_{\alpha,j}$, is possible with the layer-peeling method by using the recursive equation (3-26) instead of (3-13).

3.5.2 Method to distinguish period chirp and DC refractive index chirp

The Δn_{dc} and Λ distributions can be found if the FBG parameters are reconstructed for different temperature or strain states. We consider here the case of two reconstructions q_1 and q_2 of the same grating at two different temperatures T_1 and T_2, respectively. The temperature effect on the grating modify the physical grating period Λ and the effective refractive index n_{eff}

$$\begin{aligned} n_{eff}(T_2) &= n_{eff}(T_1)\left(1 + \frac{1}{n_{eff}}\frac{dn}{dT}\Delta T\right) = n_{eff}(T_1)(1 + \alpha_n \Delta T) \\ \Lambda(T_2) &= \Lambda(T_1)\left(1 + \frac{1}{\Lambda}\frac{d\Lambda}{dT}\Delta T\right) = \Lambda(T_1)(1 + \alpha_\Lambda \Delta T) \end{aligned} \tag{3-27}$$

where $\Delta T = T_2 - T_1$, α_Λ is the thermal expansion coefficient for the fiber material (approximately $0.55\cdot 10^{-6}$ for silica) and α_n represents the thermo-optic coefficient ($8.6\cdot 10^{-6}$ for germania-doped, silica-core fiber). The changes in the Δn_{ac} and Δn_{dc} are neglected as the refractive index changes due to the temperature mainly modify the effective refractive index ($\Delta n << n_{eff}$). The reconstructed coupling coefficients are performed using $n_{eff}(T_1)$ and $n_{eff}(T_2)$. The coupling coefficient phases ϕ_1 and ϕ_2 are given by equation (3-17) and their difference $\Delta\phi$ is reduced to

$$\Delta\phi(z) = \phi_2(z) - \phi_1(z) = \theta_2(z) - \theta_1(z) = \Delta\theta(z) \tag{3-28}$$

The grating period Λ is given by

$$\frac{2\pi z}{\Lambda(z)} = \frac{2\pi z}{\Lambda_d} + \theta(z) \tag{3-29}$$

where Λ_d is the design period used in the layer-peeling reconstruction process. Combining equations (3-27) to (3-29), the grating period for temperature T_1 is then found to be

$$\Lambda(T_1, z) = \frac{-2\pi z \alpha_\Lambda \Delta T}{\Delta\theta(z)\cdot(1 + \alpha_\Lambda \Delta T)} = -\frac{2\pi z \alpha_\Lambda \Delta T}{\Delta\phi(z)\cdot(1 + \alpha_\Lambda \Delta T)} \tag{3-30}$$

From the grating period, the distribution Δn_{dc} can be obtained from equation (3-17b)

$$\begin{aligned} \Delta n_{dc}(T_1, z) &= \frac{1}{2\eta k} \cdot \frac{d\left(\theta(T_1, z) - \phi_q(T_1, z)\right)}{dz} \\ \theta(T_1, z) &= 2\pi z\left(\frac{1}{\Lambda_d} \cdot \frac{1}{\Lambda(T_1, z)}\right) \end{aligned} \tag{3-31}$$

3.6 Summary

An evolution of the causal T-matrix method has been proposed to take account of the losses that can occur in gratings, for example in the cases of blazed FBGs. This evolution has leaded to a modified layer-peeling reconstruction method that can be applied on grating with distributed losses.

We have seen that the reconstruction by layer-peeling allows to find the grating strength, function of Δn_{ac}, and the chirp function. In order to differentiate the period chirp from the DC refractive index chirp, at least two reconstructions at different temperatures (or axial strains) are required.

The simulation of the reconstruction with different parameters has shown that the required dynamic range of the starting spectral or impulse response is not fundamental and that the number of spectral point has to exceed 10 times the number of layers. Observation of the reconstruction of noisy data has shown that the influence of noise is less important for the reconstruction starting from the impulse response. Finally, the reconstruction process by layer-peeling is limited for very strong gratings for which a spectral bandwidth is depleted before the grating end. Measurements from both sides and application of a temperature or axial strain ramp can improve partially the reconstruction of these strong gratings.

3.7 References

3-1 T. Erdogan, “*Fiber Grating Spectra*”, JLT, 15 (8), p. 1277-1294 (1997)

3-2 J. Skaar, PhD dissertation, The Norwegian University of Science and Technology, Ch. 2, 5-15 (2000)

3-3 H. Kogelnik, “*Filter response of nonuniform almost-periodic structure*”, Bell Syst. Tech. J., 55, p. 109-126 (1976)

3-4 M. McCall, “*On the Application of Coupled Mode Theory for Modeling Fiber Bragg Gratings*”, JLT, 18 (2), p. 236-242 (2000)

3-5 J. Skaar, L. Wang and T. Erdogan, “*On the systhesis of fiber Bragg gratings by layer peeling*”, J. Quantum Electron., 37 (2), p. 165-173 (2001)

3-6 L.A. Weller-Brophy and D.G. Hall, “*Analysis of waveguide gratings: application of Rouard’s method*”, J. Opt. Soc. Am. A, 11, p. 2027-2037 (1985)

3-7 S. Huang, M. M. Ohn, M. LeBlanc and R. M. Measures, “*Continuous arbitrary strain profile measurements with fiber Bragg gratings*”, Smart Mater. Struct. 7, p. 248-256 (1998)

3-8 M. A. Muriel and A. Carballar, “*Phase, time delay, and impulse response reconstruction from reflected power in uniform fiber Bragg gratings*”, Proc. LEOS'96, p. 380-3811 (1996)

3-9 J. Skaar and H. E. Engan, “*Distributed intragrating sensing using phase retrieval*”, Proc. OFS'13, 588-591 (1999)

3-10 M. A. Muriel, J. Azaña and A. Carballar, “*Time-frequency representation applied to fiber grating synthesis*”, Proc. ECOC’98, p. 383-384 (1998)

3-11 E. Brinkmeyer, “*Simple algorithm for reconstruction fiber gratings from reflectometric data*”, Opt. Lett., 20, p. 810-812 (1995)

3-12 M. Froggatt, “*Distributed measurement of the complex modulation of a photoinduced Bragg grating in an optical fiber*”, Appl. Opt., 35, p. 5162-5164 (1996)

3-13 S. Huang, M. M. Ohn, M. LeBlanc and R. M. Measures, “*Bragg intragrating structural sensing*”, Appl. Opt., 34, p. 5003-5009 (1995)

3-14 M. A. Muriel and A. Carballar, “*Internal Distributions in fiber Bragg gratings*”, IEEE Phot. Tech. Lett., 9, p. 955-957 (1997)

3-15 J. Skaar and K. M. Risvik, “*A genetic algorithm for the inverse problem in synthesis of fiber gratings*”, Journ. of Lightwave Tech., 16, p. 1928-1932 (1998)

3-16 K. Peters, Ph. Pattis, J. Botsis, Ph. Giaccari, "*Experimental verification of response of embedded optical fiber Bragg grating sensors in non-homogeneous strain fields*", Journal of Optics and Lasers in Engineering, Vol 33, pp. 107 (2000)

3-17 A.M. Bruckstein, B.C. Levy and T. Kailath, “*Differential methods in inverse scattering*”, SIAM J. Appl. Math., 45 (2), p. 312-335 (1985)

3-18 A.M. Bruckstein and T. Kailath, "*Inverse scattering for discrete transmission-line models*", SIAM Rev., 29 (3), p. 359-389 (1987)

3-19 R. Feced, M.N. Zervas and M.A. Muriel, "*An efficient inverse scattering algorithm for the design of nonuniform fiber Bragg gratings*", J. Quantum Electron., 35, p. 1105-1115 (1999)

3-20 J. Skaar and R. Feced, "*Reconstruction of gratings from noisy reflection data*", J. Opt. Soc. Am. A, 19 (11) (2002)

Chapter 4

FBG characterization by optical low coherence reflectometry

Precise characterization of the grating parameters is essential and the knowledge of the local distributions (Δn_{ac}, Δn_{dc} and Λ) is often desired during the writing process or in distributed sensing. It has been shown that optical low coherence reflectometry (OLCR) is a powerful method to characterize the position, length, and index modulation of homogeneous FBGs [4-1].

Measurements using interferometers can be affected by small perturbations, like temperature variations or vibrations, in both interferometer arms that modify the optical path length difference (OPLD). Corresponding drifts of the interference signal phase have to be compensated or the measurement has to be performed in a few milliseconds for assuring high accuracy. A high speed OLCR set-up has been developed to retrieve the complex spectral properties of chirped gratings [4-2]. The drawback is a limited S/N (shot noise) of typically −80 dB [4-3]. In this work, we built a new OLCR set-up, where the S/N is only limited by the Rayleigh scattering in the fiber and the phase drifts are compensated. The OLCR phase information of a FBG is precisely measured by comparing it with the phase of a tunable laser at the same wavelength.

In this chapter, we will show that the OLCR response is mainly the impulse response of the measured FBG. Moreover, the interference of partially coherent light is presented and its application to the OLCR case is developed. Two interfereometers have been conceived and realized, where the reference laser was either wavelength multiplexed or time multiplexed. The reconstruction process of the complex coupling coefficient from the measured OLCR response is exposed. Several FBGs with different properties were measured and their local properties reconstructed.

4.1 Methods for measuring the complex impulse response of a grating

It has been shown in chapter 3 that the complex coupling coefficient q(z) of a grating can be reconstructed from the grating complex impulse response in reflection $h(\tau)$ (z is the position along the grating and τ the time). The representation of a FBG in the time domain is not as usual as in the frequency domain. For such reason, we present here in Fig. 4-1 the spectral and the impulse responses of a homogeneous grating. The grating is 5 mm long with a refractive index modulation amplitude of $2 \cdot 10^{-4}$, an effective refractive index of 1.45 and a period corresponding to a Bragg wavelength of 1.3 μm (Fig. 4-1a). The reflection intensity $|r|^2$, where r is the reflection amplitude, and the time delay of the grating are shown in Fig. 4-1b. The impulse response amplitude $|h(\tau)|$ (Fig. 4-1c) shows that the interesting time range is about 200 ps. Fig. 4-1d reports the real part $Re(h(\tau))$ of the FBG impulse respones. The period of Re(h) is 4.34 fs, which corresponds to a phase change of 2π for $h(\tau)$. The impulse response can also be viewed in a distance scale x, corresponding to the travel distance in free-space for the given impulse time ($x = c_0\tau$ where c_0 is the vacuum light speed). The distance for 200 ps is 6 cm and the phase period is the 1.3 μm of the Bragg wavelength.

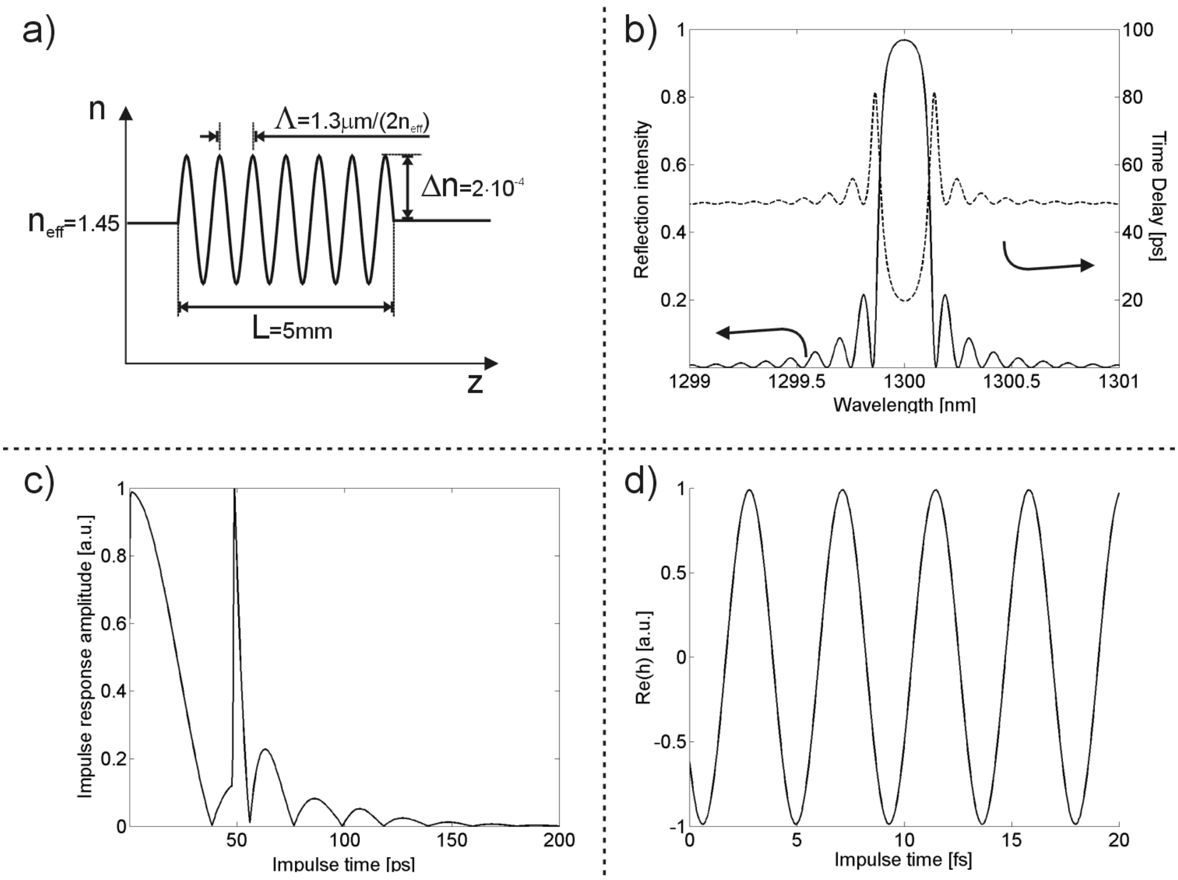

Fig. 4-1 Parameters of a homogeneous FBG (a); Spectral reflection intensity and time delay (b); Impulse response amplitude (c) and real part (d)

There are three main ways to experimentally obtain h(τ) :

- Direct method : launch a light pulse at the entrance of the grating and collect the time response h(τ) of the reflected light
- OLCR (optical low coherence reflectometry) method : measure the interference signal between a low coherence light reflected by the FBG with a delayed part of the same source light
- Spectral method : measure the complex reflection spectral response and then perform a Fourier transform

The *direct method* is very difficult to realize due to the very small time scales (200 ps duration with periodic modulation of 4 fs for the grating presented in Fig. 4-1). The light pulse, ideally a Dirac function of time, would need to be as short as a few femtoseconds. The detection system also would need to be extremely fast to measure the electric field variations. These constraining technical requirements explain why such FBG characterization method has not been used yet.

The *OLCR method* uses the property inherent to a broadband light source to interfere only with a very small delayed version of itself, corresponding to a travel distance of a few micrometers, which is defined as the coherence length [4-4]. The resulting interference signal corresponds to the impulse response h(τ) smoothed over a few micrometers due to a convolution with the source coherence function. A detailed description of the OLCR method is presented in the following section 4.2.

The *spectral method*, consisting in the measurement of the FBG reflection amplitude and phase, has been published recently, but several drawbacks can be identified. Actually, the precise measurement of the spectral response phase is difficult and slow [4-2]. The measurements errors have important effects on the calculated Fourier transform that limits the h(τ) dynamic range and introduce a large amount of noise in the reconstructed coupling coefficient (§3.4.5).

4.2 OLCR measurement of the complex impulse response

4.2.1 Overview

This section presents the main aspects of an OLCR and its application to the characterization of the FBG impulse response h(τ). The OLCR technique is based on a scanning Michelson or Mach-Zender interferometer coupled with a broadband light source. Fig. 4-2a presents a simplified all-fiber Michelson type OLCR set-up for FBG characterization. The 3 dB-coupler (X) splits the low coherent source light (L) in two components that propagate in the so-called reference and test arms. Partial or total reflections occur on the moveable mirror (M) and inside the FBG (FBG). Half the reflected light from the reference and test arms is sent back to the detector (D) through the coupler. The position P_t in the test arm is located at the FBG entrance. The optical path length in the reference arm between the coupler and the position P_r corresponds to the optical path length in the test arm between the coupler and the position P_t. The physical distances from coupler to P_r and P_t are different due to the free-space part of the reference arm (i.e. a distance d in vacuum corresponds to a distance d/n_g in the fiber where n_g is the group index of the fiber). The optical path length matching implies that the input electrical fields E_0 at P_r and P_t have the same phase. As a consequence, the reflected fields at the detector are a delayed version of E_r and E_t at P_r and P_t, respectively, with the same delay time and with half the intensity due to the coupler ($\sqrt{1/2}$ in amplitude).

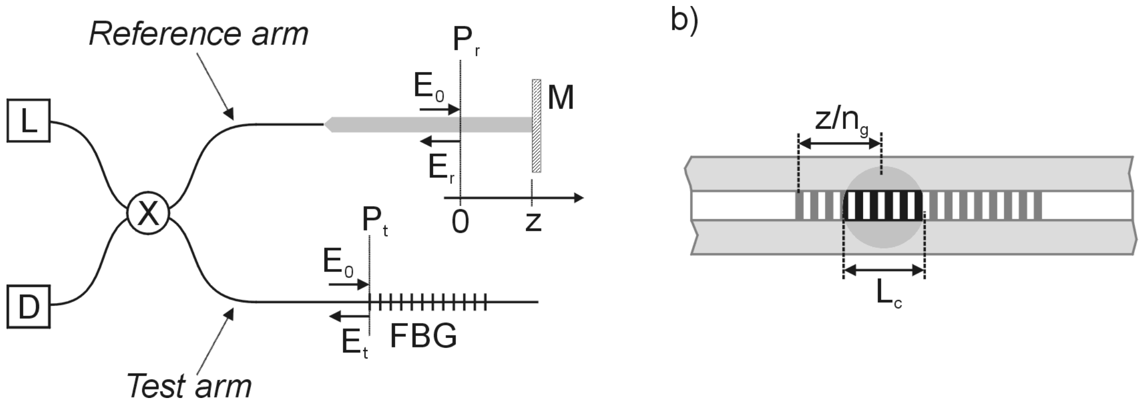

Fig. 4-2 Basic OLCR set-up for FBG characterization (a) and main interfering region in the FBG for a mirror position z

The measured optical intensity by the detector, I(z), can then be expressed as

$$I(z)=\frac{1}{2}\left|E_r(z)+E_t\right|^2=\frac{1}{2}\left(\left|E_r(z)\right|^2+\left|E_t\right|^2\right)+\mathrm{Re}\left(E_r(z)E_t^*\right) \qquad (4\text{-}1)$$

where z is the mirror position (z = 0 coincides with P_r). The first term corresponds to the sum of the intensities of each signal and the second one is the interfering contribution. For a mirror position z, the interference signal can be seen as the superposition of the mirror reflected light and the reflection of the small FBG part located at z/n_g of width L_c (Fig. 4-2b) where L_c is the light coherence length (a few micrometers). This intuitive description does not take into account the input light attenuation along the grating and multiple reflections. We will show in the following sections that the measured OLCR signal corresponds to the interference intensity

$$I_{OLCR}(z)=\mathrm{Re}\left(E_r(z)E_t^*\right)=\frac{1}{2}I_s\,\mathrm{Re}\left(\gamma(\tau)*h(\tau)\right) \qquad (4\text{-}2)$$

where I_s is the light source intensity, γ(τ) the complex degree of coherence of the light source, h(τ) the impulse response of the FBG, c_0 the light speed in vacuum and $\tau = 2z/c_0$. The impulse response h(τ), in reflection, is defined at the FBG entrance, P_t, and corresponds to the Fourier transform of the complex reflection amplitude r(ν). We will show that γ(τ) is the normalized Fourier transform of the light source spectral power density (equation (4-9)).

In the following subsections, the formal frame to describe the temporal coherence effects is introduced. The complete description of the OLCR signals of FBGs will be derived in the case of fibers with or without dispersion.

4.2.2 Temporal coherence in vacuum

The light electric field (E) oscillation frequencies are extremely high, that is hundreds of terahertz for frequencies corresponding to a period of a few femtoseconds, and conventional detectors cannot measure directly E. For stationary fields, the time average of E is null and this explains why detectors are set to measure a time average of the square field amplitude called the intensity I as defined in equation (4-3)

$$I = \lim_{T\to\infty} \frac{1}{2T}\int_{-T}^{T} dt\left|E\right|^2 = \left\langle \left|E\right|^2 \right\rangle \tag{4-3}$$

Standard detection systems have averaging range of a few picoseconds to several nanoseconds. This averaging process of the signal intensity leads to three types of coherence functions [4-5] :

- the temporal coherence function that represents the ability of a light source to interfere with a delayed version of itself
- the spatial coherence function that represents the ability of a light source to interfere with a spatially shifted version of itself
- the polarization coherence function that represents the ability of a light source to interfere with another state of polarization version of itself

Here, the spatial coherence is neglected by assuming localized light source and one-dimensional propagation. The polarization coherence function is also not considered by assuming non-polarized light and propagation preserving the polarization.

In order to theoretically describe the temporal coherence, the electric field E is represented in the orthogonal basis of frequency with a single parameter of time t

$$E(t) = \begin{bmatrix} E(\nu_1,t) \\ \vdots \\ E(\nu_n,t) \\ \vdots \end{bmatrix} = \left[E_\nu(t)\right] \tag{4-4}$$

This is a continuous and infinite decomposition, and frequency components of E cannot interfere with each other since they are orthogonal. The intensity I(t) is then found to be

$$I(t) = \left\langle \left|E(t)\right|^2 \right\rangle = \left\langle \int d\nu \left|E_\nu(t)\right|^2 \right\rangle = \left\langle \int d\nu E_\nu(t) E_\nu^*(t) \right\rangle = \int d\nu S(\nu) \tag{4-5}$$

where $S(\nu)$ is defined as the spectral power density. $S(\nu)$ constant with time due to the stationary properties of the light considered in this case.

The temporal coherence effects occur when two delayed version of the same light are superposed. For this reason, we now consider two light waves with electrical field E_1 and E_2 defined as

$$\begin{aligned} E_1(t) &= E_s(t) = \left[\sqrt{S(\nu)} e^{i2\pi\nu t} e^{i\phi(\nu)}\right] \\ E_2(t) &= E_s(t+\tau) = \left[\sqrt{S(\nu)} e^{i2\pi\nu(t+\tau)} e^{i\phi(\nu)}\right] \end{aligned} \tag{4-6}$$

where E_1 and E_2 represent two delayed versions of the same light, with source electric field signal E_s and intensity I_s emitted at time t and t + τ. The frequency dependent phase factor $\phi(\nu)$ is related to the emission process. The intensity $I(\tau)$, given by the superposition of E_1 and E_2, is independent of the time due to the stationary properties of the light and is expressed as

$$I(\tau) = \left\langle \left|E_1(t) + E_2(t)\right|^2 \right\rangle = \left\langle \left|E_1(t)\right|^2 \right\rangle + \left\langle \left|E_2(t)\right|^2 \right\rangle + 2\,\mathrm{Re}\left(\left\langle E_1(t) E_2^*(t) \right\rangle\right) \tag{4-7}$$

$$I(\tau) \quad = 2I_s + 2\,\mathrm{Re}\left(\left\langle E_s(t) E_s^*(t+\tau)\right\rangle\right) = 2I_s + 2\,\mathrm{Re}\left(\Gamma(\tau)\right)$$

where $\Gamma(\tau)=\langle E_s(t)E_s^*(t+\tau)\rangle$ is the autocorrelation function of the light source also called the temporal coherence function. From equation (4-6) we can see that

$$\Gamma(\tau) = \left\langle \int d\nu \left(\sqrt{S(\nu)} e^{i2\pi\nu t} e^{i\phi(\nu)}\right)\left(\sqrt{S(\nu)} e^{-i2\pi\nu(t+\tau)} e^{-i\phi(\nu)}\right)\right\rangle = \int d\nu S(\nu) e^{-i2\pi\nu\tau} \qquad (4\text{-}8)$$

which is the well known Wiener-Khintchine theorem, with $\Gamma(\tau)$ and $S(\nu)$ forming a Fourier pair. It is often more convenient to use a normalized coherence function $\gamma(\tau)$ called the *degree of coherence* and defined as

$$\boxed{\gamma(\tau) = \frac{\Gamma(\tau)}{\Gamma(0)} = \frac{1}{I_s}\int d\nu S(\nu) e^{-i2\pi\nu\tau}} \qquad (4\text{-}9)$$

The intensity I(t) becomes

$$\boxed{I(\tau) = 2I_s\left(1 + \mathrm{Re}\left(\gamma(\tau)\right)\right)} \qquad (4\text{-}10)$$

4.2.3 Propagation in vacuum

a) Michelson interferometer example

A free-space Michelson interferometer can be used as a simple experimental method for measuring $\gamma(\tau)$ (Fig. 4-3a). The light source (L) with its spectrum centered at $\bar{\lambda}$ emits the stationary electric field $E_s(t)$. The test (M_{test}) and reference mirrors (M_{ref}) are placed at a distance h_1 and h_2 respectively from the beam splitter (BS). The signals back-reflected from reference and test arms E_{ref} and E_{test} interfere at the detector (D).

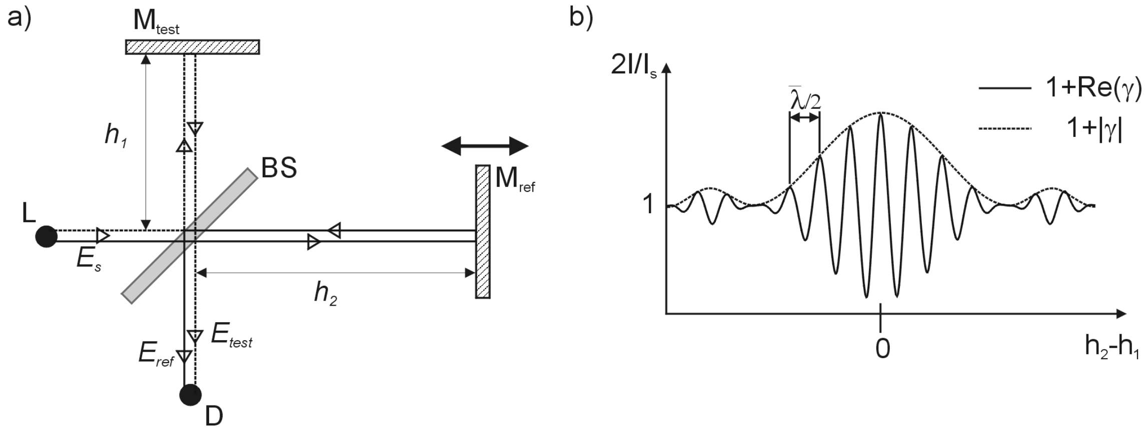

Fig. 4-3 Free-space Michelson interferometer set-up (a) and simulated interferogram (b)

We consider perfects mirrors with 100 % reflectivity coefficients and a 3 dB beam splitter (these assumptions influence only the constant coefficients). In this case, the reference and test intensities are identical and equal to a forth of the light source intensity I_s. The light propagation constant in vacuum is $k = 2\pi\nu/c_0$, $c_0 = 3\cdot10^8$ m/s is the light speed in vacuum and then

$$\begin{aligned} E_{ref}(t) &= \frac{1}{2}\left[E_{s,\nu} e^{i\omega t} e^{ik(2h_2)}\right] = \frac{1}{2}\left[E_{s,\nu} e^{i\omega t} e^{i2\pi\nu\frac{2h_2}{c_0}}\right] \\ &= \frac{1}{2}\left[E_{s,\nu} e^{i\omega t} e^{i\omega\tau_2}\right] = \frac{1}{2}\left[E_{s,\nu} e^{i\omega(t+\tau_2)}\right] = \frac{1}{2}E_s(t+\tau_2) \end{aligned} \qquad (4\text{-}11)$$

where the electric field is decomposed in its frequency components E_ν, $\tau_2 = (2h_2)/c_0$ is the time needed for all frequencies to travel a distance $2h_2$ and $\omega = 2\pi\nu$ is the light angular frequency. It is important to note that the time τ_2 becomes frequency dependent if the light does not propagate in vacuum as the propagation constant becomes $\beta(\nu) = n(\nu)\cdot k$, where $n(\nu)$ is the refractive index. In this case, equation (4-11) is not valid anymore. This point will be discussed in section 4.2.4 with the introduction of the group velocity in dielectric materials. For the test signal, a similar expression is obtained with $E_{test}(t) = E_s(t+\tau_1)/2$ where $\tau_1 = (2h_1)/c_0$. Small algebraic manipulations show that the interference signal $I(h_1,h_2)$ is

$$I(h_1,h_2) = I(\tau) = \frac{I_s}{2}\left(1+\mathrm{Re}\left(\gamma(\tau)\right)\right) \qquad (4\text{-}12)$$

and only depends of the factor $\tau = \tau_2 - \tau_1$. The factor difference of 4 between equations (4-10) and (4-12) is due to the beam splitter.

The typical normalized interferogram $2I/I_s = 1+\mathrm{Re}(\gamma)$ is shown in Fig. 4-3b. We observe a maximal signal for $\tau = 0$ with constructive interference. Then the signal drops symmetrically and the first destructive interferences occur at a distance mismatch of $\bar{\lambda}/2$ (the factor 2 is due to the back and forth travel distance). Then other constructive and destructive interferences are observed but with a decreasing amplitude $|\gamma|$. Side-lobes are also observed and fully explained by the Fourier transform of the source power spectral density. For a Gaussian light source described by a Gaussian function, $S(\nu)$, the degree of coherence envelope $|\gamma|$ is also a Gaussian function and side-lobes are totally suppressed.

b) Phase decorrelation view

The temporal coherence can be seen as a phase decorrelation of each frequency light component. As an example, a light source with only five monochromatic components of the same intensity and different wavelength λ_i is considered.

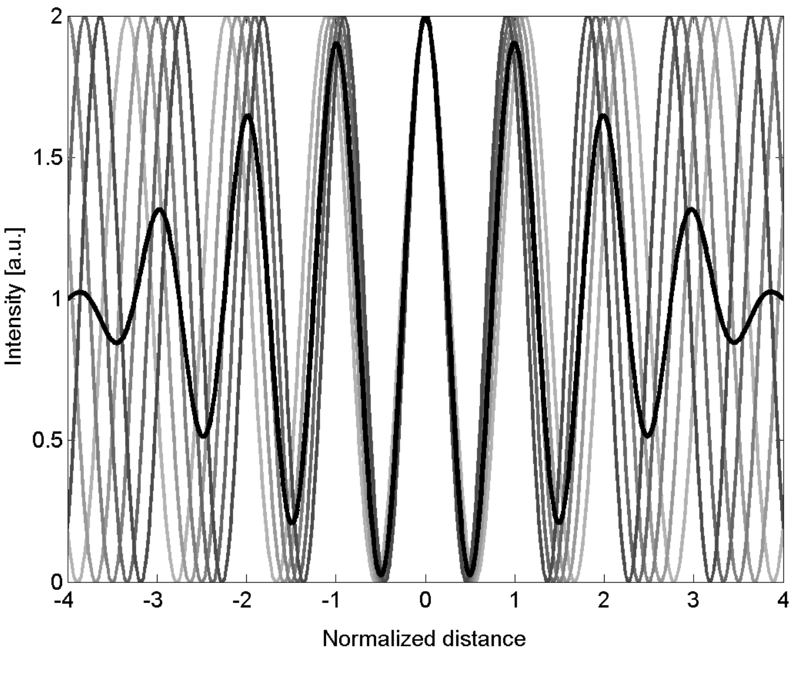

Fig. 4-4 Interference amplitude for five different frequencies (thin gray lines) and amplitude sum (thick black line); the normalized distance corresponds to twice the distance divided by the average wavelength

Fig. 4-4 shows the interference signals for each monochromatic component (thin grey lines) and the normalized total intensity (thick black line). The normalized distance is defined as $z_n = 2z/\bar{\lambda}$ where $\bar{\lambda}$ is the central wavelength. The interference signal for the monochromatic components is a cosinus with a period proportional to the wavelength. A perfect phase matching between the components is observed at $z_n = 0$ but for an increasing distance $|z_n|$, the phase matching degrades and the partially destructive addition explains the modulation amplitude drop of the total intensity.

c) Coherence time and coherence length

The time distance τ_c where significant interference signal is observed is the coherence time of the light source. Several definitions of τ_c are found in the literature and the two principal ones are given hereafter. One possibility is to take the power equivalent width

$$\tau_c = \int_{-\infty}^{\infty} d\tau \left|\gamma(\tau)\right|^2 \qquad (4\text{-}13)$$

The other way is to take from the $\gamma(\tau)$ function the full width at half maximum (FWHM) τ_{3dB} or at $1/e$ of the maximum $\tau_{1/e}$. For a Gaussian light source with FWHM spectral range of $\Delta\nu$, the relation between τ_c, τ_{3dB} and $\Delta\nu$ is

$$\begin{aligned} \tau_c &= \sqrt{\frac{2\ln(2)}{\pi}} \cdot \frac{1}{\Delta\nu} \cong \frac{0.664}{\Delta\nu} \cong \frac{0.664}{c_0} \cdot \frac{\lambda^2}{\Delta\lambda} \\ &\boxed{\tau_{c,3dB} = \frac{4\ln(2)}{\pi} \cdot \frac{1}{\Delta\nu} \cong \frac{0.882}{\Delta\nu} = \frac{0.882}{c_0} \cdot \frac{\lambda^2}{\Delta\lambda}} \end{aligned} \qquad (4\text{-}14)$$

where λ and $\Delta\lambda$ are the central wavelength and the FWHM wavelength range of the source respectively. The detailed algebraic manipulations are found in [4-6] for τ_c and in appendix D for $\tau_{c,3dB}$.

The light source coherence length L_c is defined as the travel distance for a time corresponding to the coherence time, that is $L_c = \tau_{c,3dB} \cdot c_0$ in vacuum. For a Gaussian light source centered at 1300nm with a spectral width of 40 nm, the corresponding coherence length is 37 μm.

The spectral power density $S(\nu)$ can be obtained from the experimental determination $\gamma(\tau)$ by a Fourier transform. This spectroscopic method is widely used in the infrared and it is known as the Fourier spectroscopy.

4.2.4 Propagation in dielectric materials

A dielectric material is characterized by its refractive index $n(\nu) = c_0/c(\nu)$ where $c(\nu)$ is the phase velocity of the monochromatic light component of frequency ν. The propagation constant $\beta(\nu) = n(\nu) \cdot k$ is then frequency dependent and can be expressed as

$$\beta(\nu) = n(\nu)k = n(\nu)\frac{2\pi\nu}{c_0} = n(\nu)\frac{\omega}{c_0} = \frac{\omega}{c(\nu)} \qquad (4\text{-}15)$$

For a stationary light wave for which the electrical field function E(t) is known at a position z = 0, the same field at position z is given by

$$\begin{aligned} E(t,0) &= \left[E_\nu(t,0)\right] = \left[E_\nu e^{i\omega t}\right] = \left[\sqrt{S(\nu)} e^{i\omega t}\right] \\ E(t,z) &= \left[E_\nu e^{i\omega t} e^{-i\beta(\nu)z}\right] = \left[E_\nu(t,0) e^{-i\beta(\nu)z}\right] \end{aligned} \qquad (4\text{-}16)$$

where the phase term $\phi(\nu)$ from equation (4-6) has been omitted.

In most cases, the spectral width $\Delta\nu$ is small enough to allow a limited development at the first or at the second order of β around the central frequency ν_0

$$\beta(\nu) \cong \beta(\nu_0) + (\nu - \nu_0)\left.\frac{d\beta}{d\nu}\right|_{\nu=\nu_0} + \frac{1}{2}(\nu - \nu_0)^2 \left.\frac{d^2\beta}{d\nu^2}\right|_{\nu=\nu_0} \qquad (4\text{-}17)$$

The group velocity v_g that corresponds to the propagation velocity in a dielectric material of a light pulse centered at a frequency ν is defined as

$$\boxed{\frac{1}{\mathrm{v}_g} = \frac{1}{2\pi}\frac{d\beta}{d\nu} = \frac{d\beta}{d\omega}} \tag{4-18}$$

and the dispersion coefficient D_ν

$$\boxed{D_\nu = \frac{1}{2\pi}\frac{d^2\beta}{d\nu^2} = 2\pi\frac{d^2\beta}{d\omega^2} = \frac{d}{d\nu}\left(\frac{1}{\mathrm{v}_g}\right)} \tag{4-19}$$

The equation (4-17) can then be written as

$$\boxed{\beta(\nu) \cong \beta(\nu_0) + \frac{2\pi}{v_{g_0}}(\nu-\nu_0) + \pi D_{\nu_0}(\nu-\nu_0)^2} \tag{4-20)$$

where the group velocity and dispersion coefficients are defined at ν_0. Since $\beta(\nu_0) = k(\nu_0)\cdot n(\nu_0)$, the equation (4-20) can be expressed as

$$\beta(\nu) = k_0\Delta n_0 + \frac{2\pi}{\mathrm{v}_{g_0}}\nu + \pi D_{\nu_0}(\nu-\nu_0)^2 \tag{4-21a}$$

$$\Delta n_0 = n(\nu_0) - n_g(\nu_0) \tag{4-21b}$$

where $k_0 = k(\nu_0)$ and n_g is the group refractive index defined from the group velocity as

$$\boxed{n_g = \frac{c_0}{\mathrm{v}_g}} \tag{4-22}$$

a) Dielectric material without dispersion

We consider now the interference of two delayed versions of a lightwave that propagated in two different dielectric materials. The first lightwave traveled a distance z_1 in a dielectric material characterized by the refractive index function $n_1(\nu)$, while the second wave propagated a distance z_2 in a dielectric material with $n_2(\nu)$. We assume that both materials are not dispersive ($D_{\nu 0} = 0$). The two electric field amplitudes E_i ($i = 1,2$) at the interference location are given by

$$E_i(t,z_i) = \left[E_\nu(t,0)e^{-i\beta_i z_i}\right] = \left[E_\nu(t,0)e^{-i2\pi\nu\tau_i}e^{-ik_0 z_i\Delta n_i}\right]$$

$$\boxed{\tau_i = \frac{z_i}{v_{g_i}}} \tag{4-23}$$

where τ_i represent the time needed for the wave to travel the distance z_i (the travel distance in vacuum is $n_g z_i$) and $i = 1, 2$. The intensity signal obtained when the electrical fields E_1 and E_2 are superposed is found by noting that the factors $\exp(-ik_0 z_{1,2}\Delta n_{1,2})$ are frequency independent

$$\boxed{I(z_1,z_2) = 2I_s\left(1+\mathrm{Re}\left(e^{-ik_0(z_1\Delta n_1 - z_2\Delta n_2)}\gamma(\tau_1-\tau_2)\right)\right)} \tag{4-24}$$

The first difference observed by comparison with propagation in vacuum (4-10) is that delay times are related to the group velocity and not to the vacuum light speed (for a physical distance d in a dielectric material, the vacuum delay time corresponds to a travel distance of d/n_g). The second difference is the inner exponential factor $e^{-i\varphi} = \exp\left(-ik_0(z_1\Delta n_1 - z_2\Delta n_2)\right)$. This phase factor changes the position of the constructive and destructive interference but not the interference amplitude. It is interesting to calculate the typical behavior of φ for propagation in fibers around $\lambda = 1300$ nm where the dispersion is null (typical value of $\Delta n = -0.014$)

$$\varphi_{fibre,1.3\mu m} = k_{1.3\mu m}\left|\Delta n_{1.3\mu m}\right| z = \frac{2\pi}{\lambda}\left|\Delta n_{1.3\mu m}\right| z = 2\pi\cdot 10^{-2} z[\mu m] \tag{4-25}$$

For every step of distance z = 100 μm a complete scan of 2π is performed (an interference period has been added).

This effect is not fundamental for all-fiber interferometers operating at 1300 nm as the delay time is performed by a moving mirror in air ($\Delta n_{air} = 0$). Nevertheless, a fixed phase factor exists due to a material difference between the reference and test arms as can be seen in Fig. 4-5 (simplified view of Fig. 4-2a). The relevant part is the optical fiber section between the positions P_{te} and P_t in the test arm, where P_{te} and P_{fe} (fiber end position in the reference arm) have the same distance from the coupler. The typical length of this section is several centimeters and then the constant phase factor is not easily obtained.

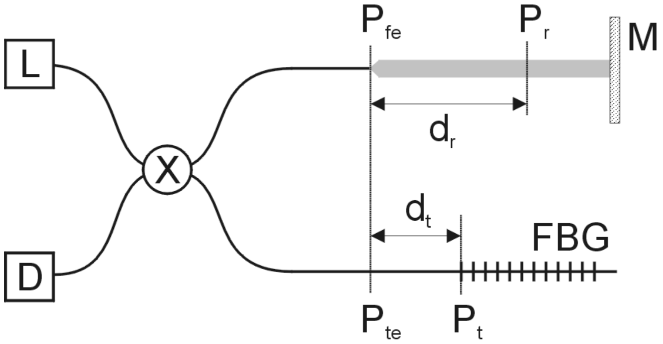

Fig. 4-5 Simplified OLCR set-up

b) Dielectric material with dispersion

We treat now the case of propagating waves in a dispersive dielectric material, where the second order of development of β is required (D_ν of equation (4-20) is not null). We again superpose two versions of the original wave that have traveled in different materials over different distances. For clarity, the first wave is assumed to have traveled through vacuum over a distance z_1. The correspondent electrical field E_1 is then simply

$$E_1(t,z_1) = E_s(t-\tau_1) = \left[E_s(t,\nu)e^{-ikz_1}\right] \tag{4-26}$$

where $\tau_1 = z_1/c_0$. Then, the second wave is assumed to have traveled in a dielectric media of refractive index n(ν) over a physical distance z_2 (assumed positive). The expression of the electric field E_2 includes the dispersion coefficient D_ν of the material through the propagation constant β(ν) developed at the second order

$$E_2(t,z_2) = \left[E_s(t,\nu)e^{-i\beta(\nu)z_2}\right] \tag{4-27}$$

The propagation time τ_2 is defined as $\tau_2 = z_2/v_{g_0}$. Thus, the interference intensity signal $I(z_1,z_2)$ is given by

$$\begin{aligned} I(z_1,z_2) &= 2I_s + 2\,\mathrm{Re}\left(\left\langle E_1^*(t,z_1)E_2(t,z_2)\right\rangle\right) = 2I_s\left(1+\mathrm{Re}\left(\tilde{\gamma}(\tau)\right)\right) \\ \tau &= \tau(z_1,z_2) = \tau_2(z_2) - \tau_1(z_1) = \frac{z_2}{v_{g_0}} - \frac{z_1}{c_0} \end{aligned} \tag{4-28}$$

where the modified coherence function $\tilde{\gamma}$ is found to be

$$\begin{aligned} \tilde{\gamma}(\tau) &= \left\langle E_1^*(t,z_1)E_2(t,z_2)\right\rangle / I_s \\ &= \frac{1}{I_s}\left\langle \int d\nu \left(E_s^*(t,\nu)e^{i2\pi\nu\tau_1}\right)\left(E_s(t,\nu)e^{-iz_2\left(\beta(\nu_0)+\frac{2\pi}{v_{g0}}(\nu-\nu_0)+\pi D_{\nu 0}(\nu-\nu_0)^2\right)}\right)\right\rangle \end{aligned} \tag{4-29}$$

$$\begin{aligned}\tilde{\gamma}(\tau) &= \frac{1}{I_s}\int d\nu S(\nu) e^{-i2\pi\left((\nu-\nu_0)\tau_2-(\nu-\nu_0)\tau_1-\nu_0\tau_1\right)} e^{-i\beta(\nu_0)z_2-i\pi D_{\nu_0}(\nu-\nu_0)^2} \\ &= \frac{e^{i2\pi\nu_0\tau_1-i\beta(\nu_0)z_2}}{I_s}\int d\nu S(\nu)\, e^{-i\pi z_2 D_{\nu_0}(\nu-\nu_0)^2} e^{-i2\pi(\nu-\nu_0)(\tau_2-\tau_1)}\end{aligned}$$

We introduce a variables change f = ν-ν0 and then the $\tilde{\gamma}$ takes the form

$$\begin{aligned}\tilde{\gamma}(\tau) &= \frac{e^{i2\pi\nu_0\tau_1-i\beta(\nu_0)z_2}}{I_s}\int df\, S(f+\nu_0)\, e^{-i\pi z_2 D_{\nu_0} f^2} e^{-i2\pi f(\tau_2-\tau_1)} \\ &= \frac{e^{i\varphi}}{I_s}\int df\, S(f+\nu_0)\, U_D(f) e^{-i2\pi f\tau} = e^{i\varphi}\left(e^{i2\pi\nu_0\tau}\gamma(\tau)\right) * u_D(\tau)\end{aligned} \qquad (4\text{-}30)$$

where u_D is the Fourier transform of $U_D = \exp(-i\pi z_2 D_{\nu,0} f^2)$ and

$$\boxed{u_D(\tau) = \frac{e^{i\pi\tau^2/\left(D_{\nu_0} z_2\right)}}{\sqrt{i\cdot\left|D_{\nu_0}\right| z_2}}} \qquad (4\text{-}31)$$

The following relations has been used to obtain the Fourier transform of U_D

$$\begin{aligned} TF\left(e^{-i\pi f^2}\right)(t) &= \frac{1}{\sqrt{i}} e^{i\pi t^2} \\ TF\left(g\left(b(f-a)\right)\right)(t) &= \frac{1}{|b|} G\left(\frac{t}{b}\right) e^{-i2\pi a t}\end{aligned} \qquad (4\text{-}32)$$

where TF means "the Fourier transform of". Finally

$$\begin{gathered}\boxed{I(z_1,z_2) = 2I_s\left(1+\mathrm{Re}\left(\tilde{\gamma}(\tau)\right)\right)} \\ \boxed{\tilde{\gamma}(\tau) = e^{ik_0 z_2\left(n_g(\nu_0)-n(\nu_0)\right)}\cdot\gamma(\tau) * u_D(\tau)} \\ \boxed{\tau = z_2 / v_{g_0} - z_1 / c_0}\end{gathered} \qquad (4\text{-}33)$$

The function u_D in equation (4-31) also describes the pulse broadening in dispersive dielectric materials [4-7]. As it can be seen from equation (4-33), the dispersion greatly modifies the interference response. For OLCR set-ups that operate at 1500 nm, the fiber dispersion coefficient is not negligible. It is necessary to compensate the dispersion produced by the fiber section between P_{te} and P_t (Fig. 4-5). The function $u_D(\tau)$ can be obtained from D_ν and then, a deconvolution is possible by dividing S(ν) by $U_D(\nu)$ in the frequency domain. Experimental measurement of D_ν can be obtained with two OLCR interferogram responses for a cleaved fiber of different length. A complete dispersion compensation algorithm based on a similar formalism can be found in the work of A. Kohlhaas [4-8] for multiple localized reflectors in the test arm.

The case of two wave components traveling in two different dispersive dielectric materials gives similar results. The modified coherence function $\tilde{\gamma}$ can also be expressed in the following form : $\exp(-i\varphi)\cdot\gamma(\tau) * u_2(\tau)$. The factor φ is identical to the case of non-dispersive materials (a)). The function $u_2(\tau)$ is similar to $u_D(\tau)$ defined in equation (4-31) but with $\left(D_{\nu 2}z_2 - D_{\nu 1}z_1\right)$ instead of $\left(D_{\nu 2}z_2\right)$ and $\tau = \tau_2 - \tau_1 = z_2 / v_{g2} - z_1 / v_{g1}$. This indicates another way to compensate the dispersion effect in all-fiber OLCR, that is by using in the reference arm a piece of fiber with bigger dispersion coefficient or by using in the test arm a piece of fiber with opposite sign dispersion coefficient. The total effect has to cancel the term $\left(D_{\nu 2}z_2 - D_{\nu 1}z_1\right)$.

4.2.5 OLCR measurement of FBG

We have now all the information required to derive the OLCR response of a FBG. The positions and physical distances are those indicated in Fig. 4-5. The spectral response to a stationary lightwave of a FBG at its entrance is given by the complex spectral function $r_{fbg}(\nu)$ that can be calculated by T-Matrix method (chapter 3, §3.1.4). The electric field E_r from the reference arm on the detector is given by

$$E_r(t,z) = \sqrt{a}\sqrt{R}\cdot\left[E_s(t,\nu)e^{-ik2(d_r+z)}\right] \tag{4-34}$$

where E_s is the source field, $a=\xi(1-\xi)$, ξ and $(1-\xi)$ are the intensity transmission coefficients of the coupler and R is the intensity reflection coefficient of the reference mirror. The test electric field E_t is given by

$$E_t(t) = \sqrt{a}\left[E_s(t,\nu)e^{-i\beta(\nu)2d_t}r_{fbg}(\nu)\right] \tag{4-35}$$

where the propagation constant is only developed to the first order (that is : $D_\nu = 0$) and using equations (4-20) and (4-21a), the following equation is obtained :

$$\beta(\nu) = k_0\Delta n_0 + \frac{2\pi}{v_g}\nu \tag{4-36}$$

As seen in §4.2.4, $\Delta n = (n(\nu)-n_g(\nu))$. The intensity I(z) measured by the detector is then

$$\boxed{I(z) = \left\langle\left|E_r(z)\right|^2\right\rangle + \left\langle\left|E_t\right|^2\right\rangle + 2\,\mathrm{Re}\left(\left\langle E_r(z)E_t^*\right\rangle\right) = I_{dc} + I_{ac}\,\mathrm{Re}\left(\tilde{\gamma}(\tau)\right)}$$
$$\boxed{\tau = 2z/c_0} \tag{4-37}$$

The constant intensity factor I_{dc} is

$$I_{dc} = a\cdot\left(RI_s + \int d\nu S(\nu)r_{fbg}(\nu)\right) \tag{4-38}$$

The modified coherence function $\tilde{\gamma}$ and the AC amplitude I_{ac} are found to be

$$I_{ac}\cdot\tilde{\gamma}(\tau) = 2\left\langle\int d\nu E_r E_t^*\right\rangle = 2a\sqrt{R}e^{i2d_t k_0\Delta n}\int d\nu S(\nu)r_{fbg}(\nu)e^{-i2\pi\nu\tau}$$
$$\boxed{I_{ac} = 2a\sqrt{R}I_s} \tag{4-39}$$
$$\boxed{\tilde{\gamma}(\tau) = e^{i2d_t k_0\Delta n}\cdot\gamma(\tau)*h_{fbg}(\tau)}$$

where $h_{fbg}(\tau)$ is the FBG impulse response in reflection (Fourier transform of the complex reflection amplitude $r_{fbg}(\nu)$).

The OLCR signal is defined as the interfering part of I(z), that is $I_{ac}\,\mathrm{Re}\left(\tilde{\gamma}(\tau)\right)$. Considering a 3 dB coupler (a = 0.5), a perfect reflecting reference mirror (R = 1) and neglecting the phase factor $\exp(i2d_t k_0\Delta n)$, the equation (4-2) is obtained. The OLCR signal is related through the grating impulse response amplitude $h_{fbg}(\tau)$ to the reflection amplitude $r_{fbg}(\nu)$ and for this reason the logarithmic scale representation is defined as

$$\boxed{\left|I_{OLCR}(\tau)\right|\left[dB\right] = 20\cdot Log_{10}\left(\left|I_{OLCR}\right|\right)} \tag{4-40}$$

where the factor 20 takes account for the *amplitude* signal.

The resolution in the fiber is defined as half the coherence length in the fiber

$$L_r = \frac{L_c}{2n(\nu_0)} \tag{4-41}$$

For a Gaussian light source centered at 1300nm with a spectral width of 40 nm propagating in a single mode fiber with n = 1.45, we find a resolution of L_r = 12.8 μm.

4.3 New OLCR set-ups

In this work, two OLCR set-ups have been realized that measure simultaneously the amplitude and the phase OLCR signals of FBG in the 1300 nm range. Both exhibits very high S/N only limited by the fiber Raleigh scattering. The essential difference between the two set-ups concerns the phase reference measurement method. In the first design, a reference laser at a wavelength different from the FBG wavelength propagate at the same time in the interferometer. The laser interference phase signal defines a distance reference where the OLCR phase is free of drifts (wavelength multiplexing scheme). In the second design, the reference laser is at the Bragg wavelength of the grating. In this case, the difference between the laser phase and the OLCR phase varies slowly with the OPLD and is free of drifts (time multiplexing). The time multiplexing method allows OPLD samplings as large as several tens of microns.

We first present the time multiplexing design. The following sections present the details on how to measure complex OLCR response, with an emphasis on the static method used in our set-ups, the balanced detection scheme, the polarization problem in all-fiber interferometers. The wavelength multiplexing design is then described. Finally, a comparison of the two set-ups is presented.

4.3.1 Time multiplexing OLCR design

Fig. 4-6 presents the OLCR scheme with the time multiplexing of the broad-band source and the reference laser. The signals under investigation are the OLCR amplitude and the phase difference between the OLCR signal and the reference laser phase.

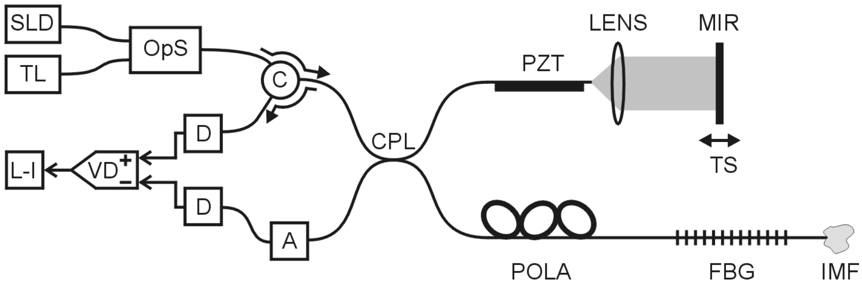

Fig. 4-6 Time multiplexing OLCR set-up : low coherence light source (SLD), tunable laser (TL), optical switch (OpS), circulator (C), coupler (CPL), piezoelectric plate (PZT), mirror (MIR), translation stage (TS), polarization controller (POLA), test FBG (FBG), fiber end in index matching fluid (IMF), attenuator (A), detectors (D), voltage difference module (VD) and lock-in amplifier (L-I)

The major feature is a time multiplexing by the optical switch of the low coherent light source and of the laser source operating at the same wavelength. The SLD is centered at 1318 nm and has a bandwidth of 40 nm FWHM corresponding to a coherence length L_C = 12.8 μm in the fiber (single mode telecom fiber). The laser source is tunable and its wavelength is set to the Bragg wavelength $\lambda_B = 2n_{eff}\Lambda$, where n_{eff} is the effective reflective index and Λ the FBG period. The 3 dB coupler splits the light to equally illuminate the reference and test arms. The reference arm includes a mirror (MIR) placed on a 25 cm translation stage used to scan the OPLD. The phase of the reference signal is ramp modulated by a piezoelectric plate over the OPLD of two fringes at a frequency of f = 178 Hz. The lens couples the light beam from fiber to free space and back to the fiber. The test arm contains the FBG under test and a polarization controller that optimizes the interference pattern. The fiber end of the test arm is placed in an index matching fluid to avoid unwanted light reflections. A balanced detection scheme is used, including a coupler, a circulator, an attenuator, two detectors and a voltage difference module. For a given mirror position, the interfering part of the total intensity (OLCR signal) is a 2f–sinus and the constant part of the total intensity signal is cancelled by the balanced detection.

The dual-phase lock-in amplifier extracts the amplitude and the phase information directly for the OLCR and the laser signals. The time interval between the laser and the OLCR phase measurements is 54 ms thus limiting phase drifts to below $\pi/100$. The measurement chronology for each OPLD is presented in Fig. 4-7. OPLD discretization from 1 to 200 μm have been used depending on the required resolution.

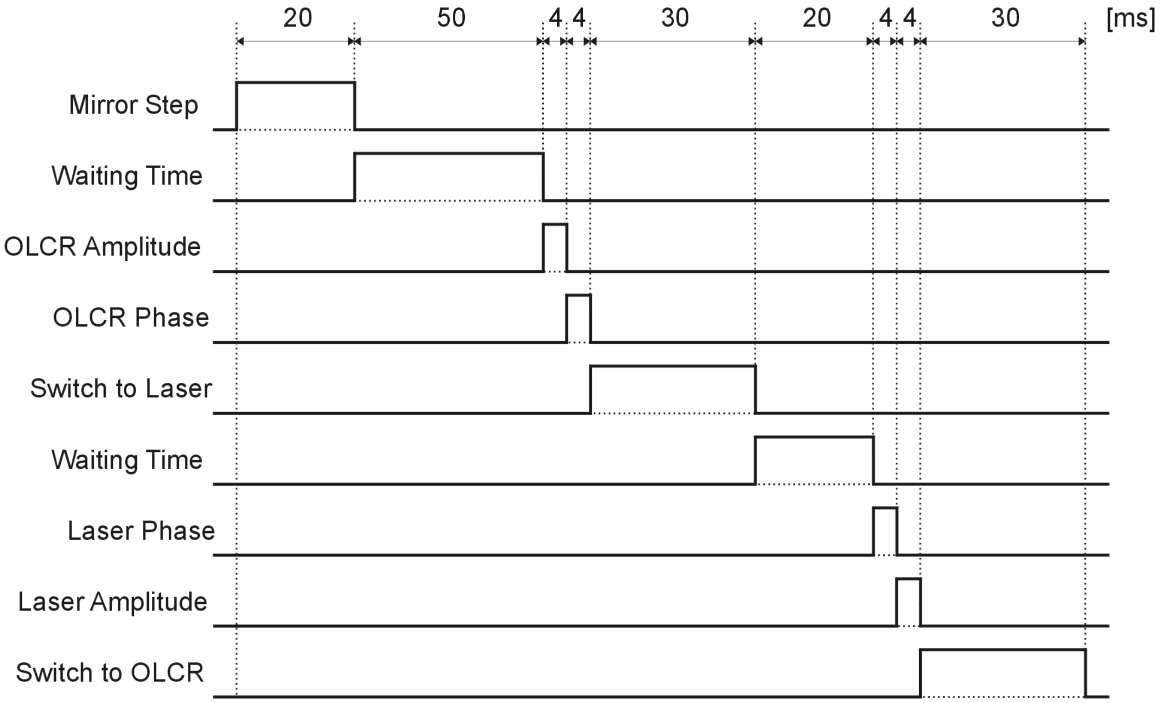

Fig. 4-7 Measurement chronology for the time multiplexing OLCR set-up

4.3.2 Measurement principle

Small perturbations (e.g. temperature variations) in both interferometer arms modify the optical path length difference (OPLD) and determine the phase drifts. Typical variations of 2π in the OLCR or laser phase signal are possible in a few seconds. For complex OLCR measurements, these phase drifts have to be either limited by very fast measurements or compensated by another reference laser signal when the measurements are slow. Two main complex OLCR measuring methods have been studied :

- Dynamic method : moving the mirror at constant speed produces a Doppler frequency used to measure the real part amplitude; the imaginary part is calculated by an Hilbert transformation and subsequently the complex response is obtained [4-2]
- Static method : for a given mirror position, the OPLD is ramp modulated over a multiple of the interference period producing a quasi sinusoidal signal (Fig. 4-8); a dual-phase lock-in amplifier then directly derives the amplitude and phase signals

Both methods have their own advantages and drawbacks :

- Dynamic method : the main advantages are the high speed (e.g. 42-m/s with rotating mirror cubes [4-9]) and the small phase drifts; on the other hand, the signal to noise ratio (S/N) is limited by the shot noise of the detectors, the phase reconstruction using the Hilbert transform is not optimal for small signals and a constant mirror speed is needed; moreover, a high precision reference distance and an OPLD resolution that fulfills the Nyquist criteria (under $\lambda/2$) are required
- Static method : the main advantages are the high dynamic range (only limited by the fiber Raleigh scattering around –120 dB) and an OPLD resolution that is not limited by the Nyquist criteria as only the phase difference between the laser and the OLCR phases is measured, which is slowly varying with the OPLD; on the other hand the measurement is slow (3 min/mm in our set-up) due to the ramp modulation process at

each position (150 Hz maximal frequency for piezoelectric plates) that limits the measurement speed and then requires to compensate the important phase drifts

The static method has been chosen for its high dynamic range that enables the measurement of weak FBGs. Fig. 4-8a shows the interference amplitude for the OPLD, ζ. The period is given by half the low coherence light source wavelength $\lambda/2$. For a given mirror position ζ (stationary condition), the OPLD is ramp modulated at frequency f as seen in Fig. 4-8b. The time dependent signal measured by the detector (Fig. 4-8c) is a piecewise reconstructed sinus function obtained by concatenation of the interference signal over a period. The amplitude $\alpha(\zeta)$ corresponds to the OLCR envelope amplitude and the phase difference $\beta(\zeta)$ between the ramp excitation and the signal minima gives the OLCR phase. The transition time between two ramps (between dotted and dashed lines) explains induced signal distortions that limit the modulation frequency. The reference laser signal is similar but the amplitude is nearly constant over the measurement range due to the much longer coherence length.

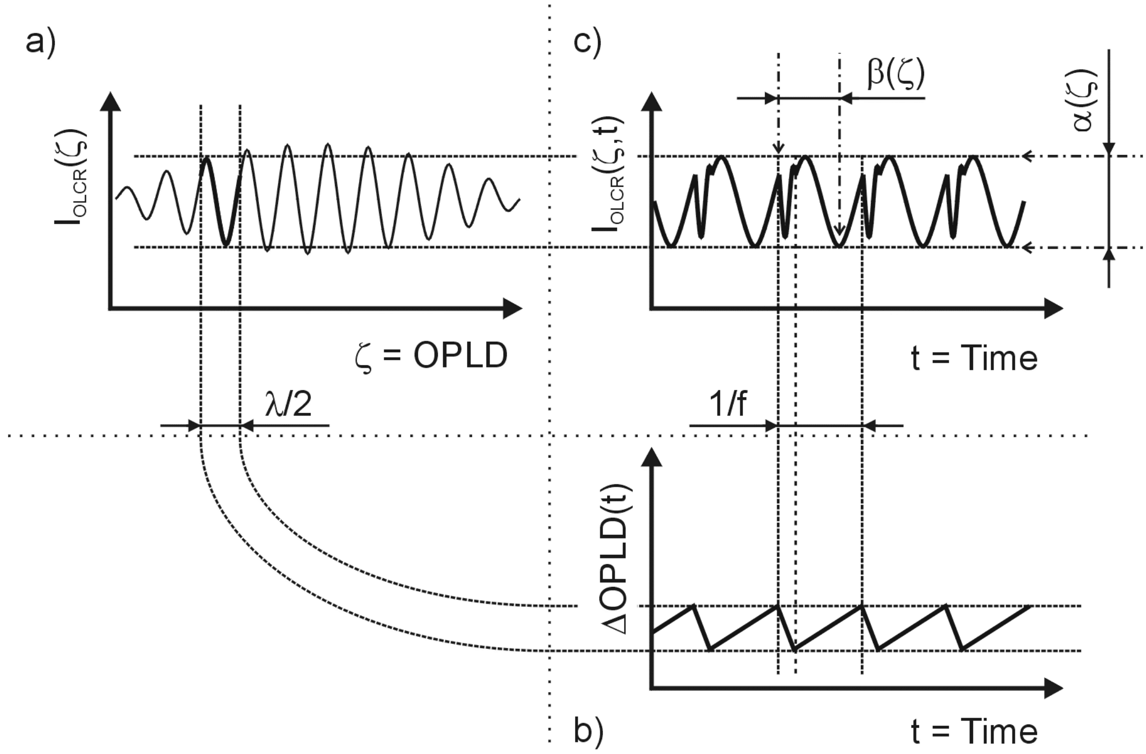

Fig. 4-8 Signal generation for OLCR set-ups with static method

4.3.3 Balanced detection scheme

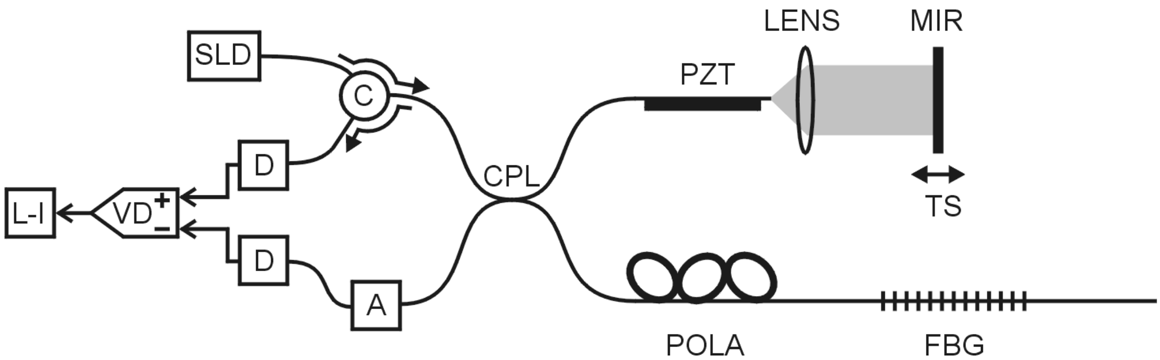

Fig. 4-9 OLCR set-up with balanced detection

The interference signals (AC) are very small compared to the constant part (DC) and amplitudes between −50 to −120 dB are expected for FBGs. Electronic filtering of the DC signal is not optimal as it adds a lot of noise that reduces the S/N. A balanced detection scheme is then preferred where the DC signal is differentially cancelled. Moreover, the balanced detection scheme within our set-ups (Fig.

4-9) not only suppresses the DC part but doubles the AC part at the same time. In order to discuss such point, Fig. 4-9 presents the principal parts of an OLCR set-up where the reference system has been omitted. A circulator is placed in the source arm and the returning signal in this arm is then redirected to the detector. An attenuator is used on the other arm to compensate the insertion loss of the circulator.

This balanced detection scheme is based on the properties of the coupler. For an input signal of amplitude E, the outgoing symmetric E_s and anti-symmetric E_a signals (Fig. 4-10a) exhibit a phase difference of $\pi/2$ for the same OPLD [4-10].

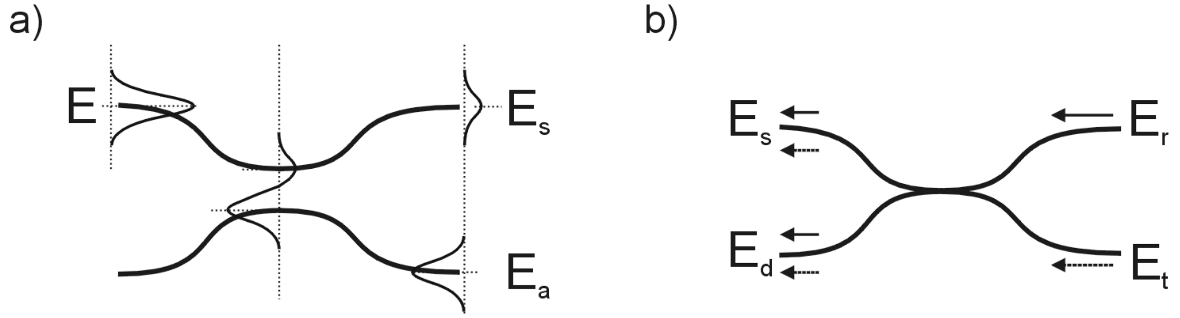

Fig. 4-10 Fiber coupler principle (a) and electric fields pertinent for balanced detection (b)

Considering the reference signal E_r and test signals E_t (Fig. 4-10b), the total signals in the source arm E_s and in the detection arm E_d are given by

$$\begin{aligned} E_s &= \frac{1}{\sqrt{2}}\left(E_r + E_t \cdot e^{-i\pi/2}\right)\cdot e^{i\varphi_s} \\ E_d &= \frac{1}{\sqrt{2}}\left(E_r \cdot e^{-i\pi/2} + E_t\right)\cdot e^{i\varphi_d} \end{aligned} \tag{4-42}$$

where $\varphi_{1,2}$ is a phase dependent factor that contains the propagation in the source and detection arm respectively. The corresponding intensities are

$$\begin{aligned} I_s &= \frac{1}{2}\left(I_r + I_t\right) + \mathrm{Re}\left(\int d\nu E_r \cdot E_t^* \cdot e^{i\pi/2}\right) \\ I_d &= \frac{1}{2}\left(I_r + I_t\right) + \mathrm{Re}\left(\int d\nu E_r \cdot E_t^* \cdot e^{-i\pi/2}\right) \end{aligned} \tag{4-43}$$

We observe that the DC intensity is identical but that the AC intensity part has a π phase factor difference. This means that when I_s shows a constructive interference, I_d shows a destructive interference. The intensity difference is obtained by using the relation $e^{i\pi} = -1$

$$I_{diff} = I_s - I_d = \mathrm{Re}\left(e^{-i\pi/2}\int d\nu E_r \cdot E_t^*\right) - \mathrm{Re}\left(e^{i\pi/2}\int d\nu E_r \cdot E_t^*\right) = 2\,\mathrm{Re}\left(e^{-i\pi/2}\int d\nu E_r \cdot E_t^*\right) \tag{4-44}$$

For a given mirror position, the difference intensity I_{diff} is the real part of the AC interference signal that would be obtained directly with E_r and E_t for a mirror $\lambda/4$ away from its current position. Experimentally, this means that the effective mirror position has a constant $\lambda/4$ offset.

As it concerns this detection, another point must be discuss. The S/N is strongly related to the detector noise that depends on the total optical power of the incoming light [4-11]. In our set-ups, the total light power is reduced in the reference arm by the in- and out-coupling (-50 dB at least) and in the test arm by the FBG itself, allowing by this lower detector noise. Moreover, the chosen balanced detection scheme improves the S/N [4-12]. The observed noise limit in our measurements is about −120 dB for FBGs. This level corresponds to the Rayleigh backscattering in telecom fibers [4-13]. Experiments conducted on cleaved fibers as sample have shown lower S/N several centimeters after the fiber end position around −140 dB.

4.3.4 Polarization effects

The polarization state of the light traveling in optical fibers is modified by fiber bending, geometrical perturbations and material inhomogeneities. The main effect is a changement of the polarization state. If the rotation angle is different for the reference and test signals, a reduction of the fringe visibility is observed due to the partial superposition of orthogonal polarization states. The polarization controller (POLA) placed in the test arm modifies the polarization state angle of the test signal in order to optimize the polarization matching with the reference signal. If θ is the polarization angle difference between the reference and the test lights at the detector input, the measured AC intensity signal is reduced by a factor $\cos(\theta)$ (see Appendix E for more details). The polarization controller is manually set to obtain $\theta = 0$.

The polarization effect is very important when an absolute measurement of the OLCR signal is required; in fact, temperature changes or vibrations can modify θ and then reduced the effective interference amplitude. Finally, we remark that other polarization coherence effects can be neglected for non-polarized light due to the initial lack of polarization cross-correlation.

4.3.5 Wavelength multiplexing OLCR design

The wavelength multiplexing OLCR design is presented in Fig. 4-11.

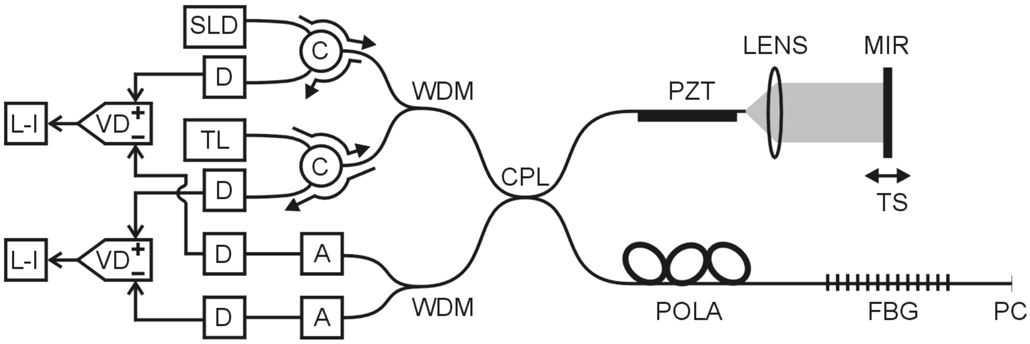

Fig. 4-11 Wavelength multiplexing OLCR set-up : wavelength division multiplexer (WDM), cleaved fiber end (PC)

The low coherence light source around 1318 nm and the reference laser around 1550 nm are launched together in the reference and test arms. The FBG (in the 1300 nm range) has very low reflectivity at the laser wavelength, and then another laser reference point in the test arm is required and a cleaved fiber end behind the grating is used for this purpose. The distance between the FBG and the PC has to be as small as possible to limit the laser phase noise (i.e. the interference of lights emitted at different time). The laser wavelength is calibrated with a wavemeter to improve the distance accuracy (relative distance uncertainty less than 10^{-6}).

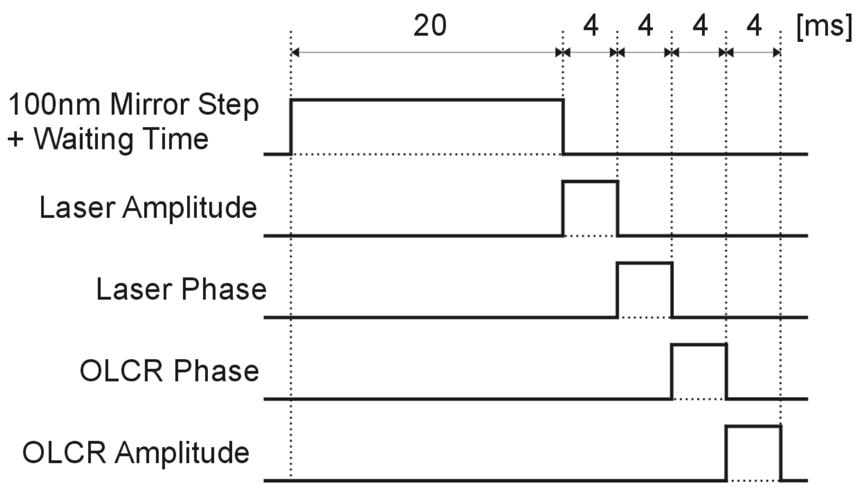

Fig. 4-12 Measurement chronology for the wavelength multiplexing OLCR set-up

The cross talk between the low coherence and reference laser signals is reduced by using 1310/1550 nm wavelength division multiplexers with isolation greater than 45 dB. The remaining cross talk disappears with the different levels used in the balanced detection of both signals. Spectral variation of the laser and broadband sources are kept below 2 pm with temperature control. Two dual-phase lock-in amplifiers extract amplitude (I_{oclr}, I_{laser}) and phase (φ_{olcr}, φ_{laser}) of the OLCR and laser signals. I_x and φ_x are measured at each mirror (MIR) position. The perfect symmetry of the set-up allows measuring FBG's at 1550 nm with a matching broadband source and a laser source at 1310 nm. The OPLD is sampled in order to fulfill the Nyquist criteria for the reference laser phase. The absolute distance without phase drifts for the OLCR phase is then calculated (i.e. OPLD = $\lambda_{laser}\cdot\varphi_{laser}/2\pi$). From the absolute distance, a linear resampling is applied to the OLCR amplitude and phase.

The measurement chronology is presented in Fig. 4-12. A small time delay of 4 ms is observed between both phase measurements.

4.3.6 Discussion of different OLCR designs

The first aspects concern both designs. The laser wavelength is used as phase reference and thus an acurate knowledge of the wavelength and its stability is essential. The tunable laser used in the time multiplexing set-up guaranties a wavelength stability better than 1 pm and the DFB laser used in the wavelength multiplexing set-up is temperature stabilized to ensure the same stability. A wavemeter has been used in parallel to track the exact wavelength position and eventual drifts (laser wavelength drifts smaller than 0.1 pm were observed). The thermal stability of the test FBG is fundamental as the measurement time goes from several minutes to several hours. Temperature changes in the test FBG modify its spectral properties (in first approximation a frequency shift) that are seen in the OLCR measurement by a phase difference slope modifications due to a different local Bragg condition.

The time multiplexing design shows several advantages over the wavelength multiplexing scheme :

- The laser reflective reference is the FBG itself and thus cancels completely the laser phase noise problem encountered with the cleaved fiber end as the reference
- The phase difference is ranged in tens of radians compared to the millions of radians range of the phase itself for the same scan distance (e.g. a few centimeters)
- The sampling is not limited by the Nyquist condition and this reduces considerably the measurement time (several minutes instead of several hours) and the amount of data (factor 10 to 100)
- The single wavelength operation divides by two the number of optical and electronic components (adding on the other hand an optical switch) and guaranties the perfect 2π modulation for both OLCR and laser phase signals

The wavelength multiplexing exhibits nevertheless interesting features :

- The wavelength symmetry enables measurements of FBG in the 1310 and 1550 nm range by simple source exchange
- For a dynamic measurement configuration (§4.3.2), the laser signal can be used directly as reference signal for the lock-in amplifier and then the phase difference is directly extracted without any other operation (accurate constant mirror velocity is required)
- The time delay between the laser and OLCR phase measurement is very small and can either be totally suppressed if the voltage difference of both lock-in is measured, reducing the marginal phase drifts well bellow the $\pi/100$ encountered for the time multiplexing design

We want now to discuss the minimal sampling distance required for FBGs OLCR measurements when the OLCR phase is obtained from the difference with the laser reference phase. The phase difference change $\Delta\phi$ for two different wavelength λ_1 and λ_2 over the same distance d is given by

$$\Delta\phi = \frac{2\pi d}{\lambda_1} - \frac{2\pi d}{\lambda_2} = \frac{2\pi d \Delta\lambda}{\lambda_1 \lambda_2} \qquad (4\text{-}45)$$

where $\Delta\lambda = \lambda_2 - \lambda_1$. The following table gives the minimal distance $d_{2\pi}$ for which a complete 2π phase change is obtained for λ_1 = 1310 nm.

λ_2 [nm]	$\Delta\lambda$ [nm]	$d_{2\pi}$ [μm]
1310.1	0.1	17'161
1311	1	1'716
1320	10	172
1410	100	17
1550	240	8.5

When measuring the phase difference between the laser and OLCR signals, the sampling has to be half the minimal distance $d_{2\pi}$ to fulfill the Nyquist criteria. We observe that the wavelength multiplexing design could also be used in the difference phase mode but with smaller sampling intervals and an independent distance measurement. In this discussion, we have neglected the phase changes introduced by the test FBG itself. For homogeneous FBGs, additional π shifts in the impulse response phase are observed due to global reflections at the grating interfaces and they are spread in the OLCR measurement over the broadband light source coherence length by convolution. For chirped grating, the Bragg condition change is usually smaller than 10 to 20 nm and then the corresponding $d_{2\pi}$ remains under 100 μm. The typical OPLD sampling distance (that is twice the incremental change of the mirror position) used in time multiplexing design was 20 μm, corresponding to 10 μm mirror step. Several experiments have also been conducted with 1 μm mirror steps for precise OLCR measurements and 100 μm for fast measurements.

4.3.7 Time multiplexing design in OFDR use

The time multiplexing design OLCR has also been used to measure directly the complex spectral response of FBGs. To achieve this, the mirror is placed at a position corresponding to an inner point of the grating in order to have a strong low coherence signal. Instead of moving the mirror to scan the OPLD, the light frequency is scanned by the tunable laser. The low coherent signal phase is used to compensate the phase drifts. This measurement method is known as optical frequency division reflectometry (OFDR). The obtained complex signal corresponds to the complex reflection amplitude $r(\nu)$ and not to the reflection intensity. For this reason, the dynamic range in dB is twice the one obtained with a direct intensity measurement. The dynamic range is nevertheless limited by the spontaneous light emission of the laser source. For the tunable laser we have used, the spontaneous light emission is under -60 dB. This dynamic limitation can be overcome for an amplitude measurement by placing the mirror at a position where the low coherence signal is canceled as the same will occur with the spontaneous part of the laser light, but the phase signal is lost in this case

4.3.8 Transmission impulse response OLCR set-up

The transmission impulse response (Fourier transform of the amplitude transmission spectrum) can be measured with an OLCR based on a Mach-Zender interferometer. Fig. 4-13 present a time multiplexing OLCR design set-up that use the same components as the set-up used for reflection measurements (at the exception of the second 3 dB coupler). The attenuator in the balanced detection has been omitted but it can be added if the second coupler shows a splitting ratio that is not exactly 50/50 in intensity.

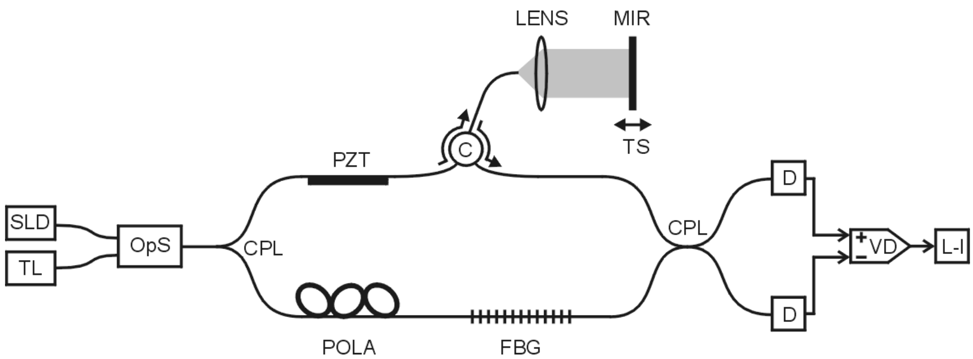

Fig. 4-13 OLCR set-up for transmission measurement

4.4 Reconstruction process

This section presents the treatment applied to the measured OLCR data to reconstruct the grating complex coupling coefficient. We limit the study to the time multiplexing case. The first operation produces the slowly varying complex OLCR response (amplitude and phase). The second step is the Fourier transform and the deconvolution from the interferometer signature to obtain the complex spectral response of the grating. The complex coupling coefficient is then calculated by layer-peeling (chapter 3, §3.3.2).

4.4.1 Complex OLCR signal reconstruction

The OLCR measurement consists of four signals : the low coherence light interference amplitude and phase (A_{lc} and ϕ_{lc}) and the laser interference amplitude and phase (A_L and ϕ_L). Only the phase difference $\Delta\phi = \phi_{lc} - \phi_L$ is important since all interferometer phase drifts are canceled in this signal. The OPLD, ξ, is determined directly by the translation stage control system with an accuracy of 100 nm and an absolute error after several centimeters bellow 1 μm (stepping-motor encoder error).

The laser signal amplitude is supposed to be constant over the scan range due to the large coherence length of the laser source. Nevertheless, the interference signal shows a parabolic behavior due to the coupling variation with the mirror position in the reference arm. The same variation is also observed for the low coherence signal. To correct this effect, a modified low coherence amplitude A_{OLCR} is calculated by dividing the low coherence amplitude by a parabolic fit of the laser amplitude $A_{L,2nd\ order}$

$$A_{OLCR} = A_{lc} / A_{L,2^{nd}order} \tag{4-46}$$

The slowly varying complex OLCR signal f(ξ) is then defined as

$$f(\xi) = A_{OLCR}(\xi) \cdot \exp\left(-i \cdot \Delta\phi(\xi)\right) \tag{4-47}$$

4.4.2 Complex FBG spectral response calculation

The complex reflection amplitude $r_{fbg}(\nu)$ is calculated from the slowly varying complex OLCR response through a FFT algorithm after a deconvolution from the broad-band spectral power density $S(\nu)$. As the OLCR measurement is not calibrated, a subsidiary calibration of $r_{fbg}(\nu)$ is required, using an independent transmission measurement of the grating.

a) Fourier transform performed with the FFT algorithm

The inverse Fourier transform is performed with the FFT algorithm. Nevertheless, the spectral resolution possible with such kind of algorithm strongly depends on the OPLD range. For this reason we artificially increase the ξ range by padding zeros after the last measured point (a resolution of 3.6 pm is found at 1309 nm with an OPLD range of 52 cm). This zero padding is equivalent to consider the OLCR signal equal to zero for values under −120 dB. The total number of points is set to a power of two for optimal FFT algorithm use. The Fourier transform of the slowly varying OLCR function produces a frequency shifted spectral response. The frequency shift corresponds to the laser frequency.

b) Deconvolution process

The complex slowly varying OLCR function f(ξ) is related to the grating complex spectral response $r(\nu)$ and the effective broadband power spectral density $S(\nu)$ that includes some spectral filtering of the interferometer

$$f(\xi) \cdot e^{i \cdot 2\pi\nu_0\xi/c} = A_{OLCR}(\xi) \cdot e^{i \cdot \phi_{lc}(\xi)} \sim \int d\nu S(\nu) \cdot r(\nu) e^{-i2\pi\nu\xi/c_0} \tag{4-48}$$

where the symbol "~" is used in the meaning of "proportional to" and ν_0 is the laser frequency. The frequency shifted inverse Fourier transform $F(\nu)$ of $f(\xi)$ is proportional to $S(\nu)\cdot r(\nu)$. The deconvolution of the interferometer signature is in the frequency domain a simple division, i.e. $F(\nu)/S(\nu)$. The function $S(\nu)$ is obtained when the FBG is replaced by cleaved fiber end, for which the reflectivity is constant over the light source frequency range. We can then write the following relation

$$r(\nu) \sim \frac{FT^{-1}\left(f_{fbg}(\xi)\right)}{FT^{-1}\left(f_{cleaved\ fiber}(\xi)\right)} = r_{nc}(\nu) \qquad (4\text{-}49)$$

where r_{nc} represents the FBG reflection spectral response that is not calibrated and FT means "Fourier transform of" and FT^{-1} "inverse Fourier transform".

We have to notice that $S(\nu)$ is supposed to be a real function and that the remaining dispersion, which can appear in the interferometer is assumed to be very small and thus neglected. For this reason we use the absolute value of $FT^{-1}(f_{cleaved\ fiber}(\xi))$. In the case where the dispersion cannot be neglected, a more complicated deconvolution is required, based on equations (4-33).

c) Normalization process

Finally, it remains to normalize the complex reflection amplitude. We have chosen not to calibrate the OLCR measurement as the polarization rotation drifts makes such calibration hard to maintain. We prefer an independent measurement of the FBG transmission intensity with the tunable laser to determine the maximal reflection intensity $R_{fbg,max}$

$$r(\nu) = \frac{r_{nc}(\nu)}{Max\left(\left|r_{nc}(\nu)\right|\right)}\cdot\sqrt{R_{fbg,max}} \qquad (4\text{-}50)$$

As long as the induced refractive index modulation of the grating is not modified (e.g. high temperature), the impulse response amplitude at the entrance $|h(\tau=0)|$ remains constant for different environmental conditions of temperature and strains. This property allows to perform a single calibration of $|h(0)|$ in a given state of strain and temperature to calibrate the grating in other environmental states.

4.4.3 Complex coupling coefficient reconstruction

We have seen in chapter 3 that the complex coupling coefficient of the grating can be reconstructed from the complex spectral response with a layer-peeling method. The FBG is divided in several layers of physical thickness Δ where the grating is assumed uniform and represented by a single complex reflector with reflectivity ρ. The required spectral range for the layer-peeling is directly related to the thickness Δ

$$|\delta| \le \frac{\pi}{2\Delta} \qquad (4\text{-}51)$$

where $\delta = \beta - \beta_d$ is the detuning wavelength and β_d is an arbitrary design wavelength (usually set to the Bragg wavelength). The smaller the layer is, the larger the required spectral range is and the smaller the reconstruction errors will be. For β_d = 1309 nm and Δ = 5 µm the spectral range goes from 1252.8 to 1371.2 nm. The relation between the reflectivity ρ and the local complex coupling coefficient q_j is given by

$$\rho_j = -\tan\left(\left|q_j\right|\Delta\right)\frac{q_j^*}{\left|q_j\right|} \qquad (4\text{-}52)$$

From the starting reflection amplitude $r_1(\delta)=r(\delta)$, the grating is reconstructed in an iterative way. At each step, ρ_j for the first layer of the remaining structure at the step j is calculated and a new reflection amplitude $r_{j+1}(\delta)$ is calculated for the structure without the layer j (peeled off)

$$\rho_j = \frac{1}{M}\sum_{m=1}^{M} r_j(m)$$
$$r_{j+1}(\delta) = \frac{r_j(\delta) - \rho_j}{1 - \rho_j^* r_j(\delta)} e^{-i\delta 2\Delta} \tag{4-53}$$

where $r_j(m)$ is the discrete form of $r_j(\delta)$. The number of points N for $r(\nu)$ in the range of δ has to be greater than the number M of reconstructed layers ($M \geq N$).

The reconstruction of the grating complex coupling coefficient is then conducted with the following procedure :

- The layer thickness Δ and the design wavelength λ_d are chosen, thus defining the detuning range
- The complex FBG spectral response is restricted to the detuning range
- The M complex reflection coefficients ρ_j are calculated
- The M complex coupling coefficient amplitude and phase are deduced from the ρ_j

We have seen in chapter 3 (§3.5.2) that the complex coupling coefficient is not enough to deduce all the FBG parameters as there are three distributions : the refractive index modulation Δn_{ac}, the physical period Λ (or the period chirp θ) and the refractive index chirp Δn_{dc}.

4.5 Reconstructed FBG

This section presents the reconstruction results obtained on a nearly homogeneous grating, a FBG with local pre-exposure that induce index chirp and finally the case of a blazed grating that exhibits insertion loss and then requires to use the modified layer-peeling method proposed in chapter 3, in section §3.3.2.

4.5.1 Homogeneous FBG

The FBG has been inscribed in an H_2-loaded SMF28 compatible fiber with a 193 nm ArF excimer laser through a 902.9 nm–pitch phase mask over a length of 5 mm. For an ideal homogeneous grating, Δn_{ac}, Δn_{dc} and $d\theta/dz$ are constant. In the reality, Δn_{ac} and Δn_{dc} could show some small variations due to laser beam inhomogeneities. Fig. 4-14 presents the spectral response of the grating (intensity) measured with a tunable laser and simulated curve with the best approaching homogeneous grating parameters. We can see an important difference between the curves, probably indicating the presence of non-homogeneities in the grating.

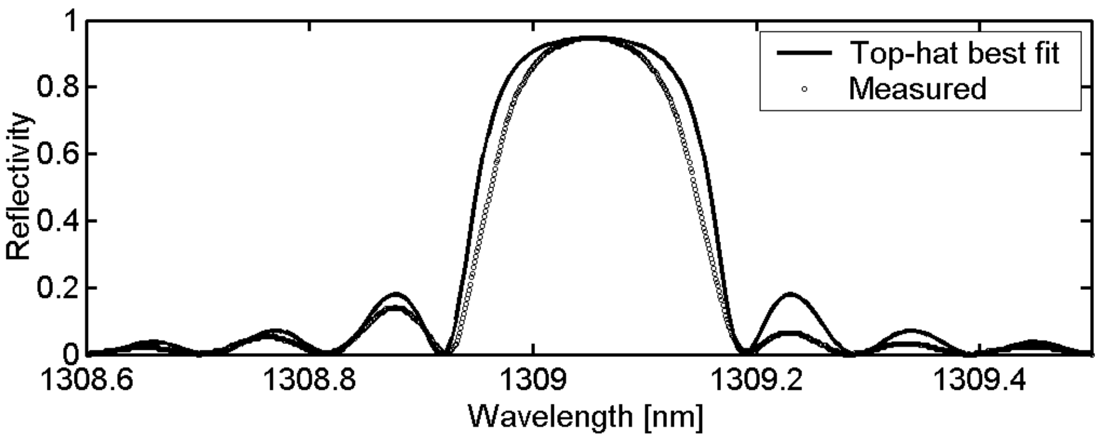

Fig. 4-14 Measured reflection intensity (circles) and spectral fit with the most approaching homogeneous grating

The OLCR measurement of the grating has been performed from both sides. Fig. 4-15 shows the results from one side measurement where A is the OLCR amplitude and $\Delta\phi$ the difference between the OLCR phase and the laser phase. The OPLD sampling interval is 20 μm, the scan speed is 3 mm/min and the laser wavelength is λ_B = 1309.33 nm.

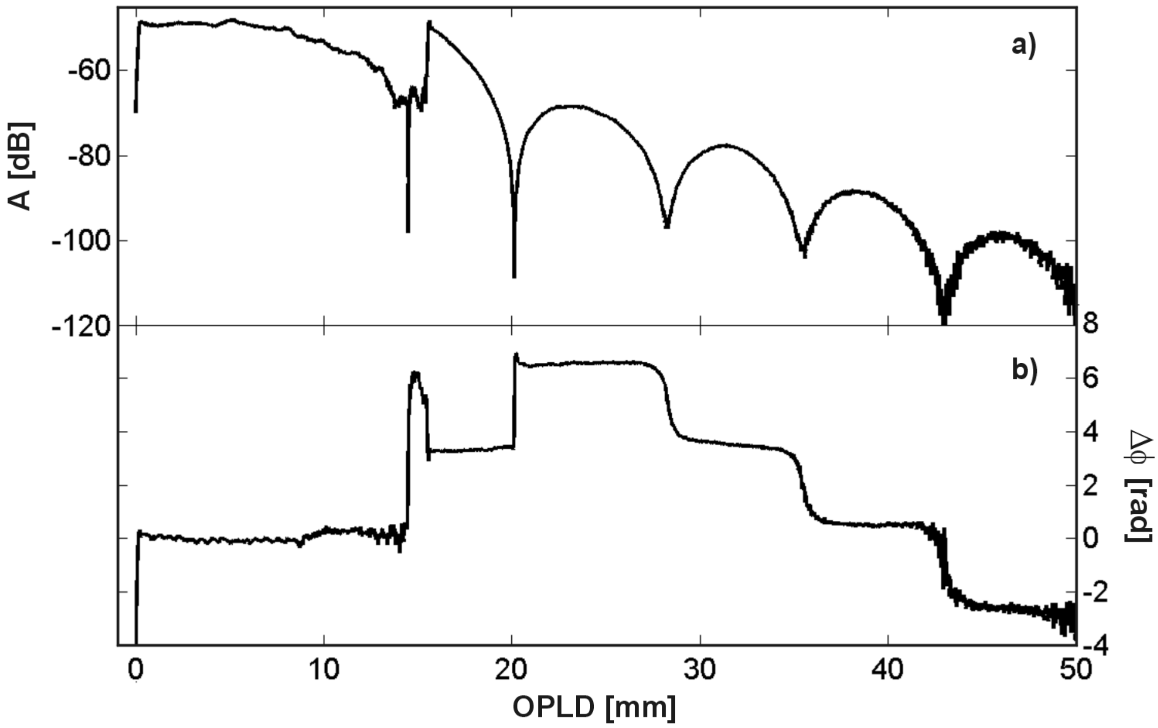

Fig. 4-15 OLCR amplitude (a) and phase difference between OLCR phase and reference laser phase at λ_B (b)

The S/N for the amplitude signal is −120 dB. The phase difference $\Delta\phi$ is nearly linear by parts as expected for a homogeneous grating and the slope is close to zero due to the perfect matching of the laser wavelength to the Bragg condition. It has to be noticed that the range of $\Delta\phi$ is less than ten radians, as compared to the range of the OLCR phase, which exceeds millions of radians for the same OPLD. The FBG entrance and output positions are located at $OPLD_1$ = 0.13 and $OPLD_2$ = 15.6 mm, respectively. Hence a grating length of $\Delta OPLD/(2n_g)$=5.33 mm is obtained using a group refractive index of n_g =1.45. Inside the grating, the OLCR signal is mainly due to a single reflection. The small variations observed are due to some UV-laser beam inhomogeneities. Behind the output, the FBG acts as a Fabry-Perot and the signal is due to multiple reflections. Each zero in the reflection amplitude (Fig. 2a) corresponds to a π shift in the phase difference (Fig. 2b). A zero is observed in the OLCR amplitude inside the grating region at 14.48 mm. This effect is expected by theory for strong FBGs [4-14]. At this position, the OCLR phase difference has a 2π shift due to noisy data that limits the unwrapping process.

The complex spectral reflectivity r(ν) is obtained from the OLCR measurement with the following parameters for the data processing : zero padding to an OPLD of 52 cm and a spectral resolution of 3.6 pm at 1309 nm. The transmission intensity measurement of the grating with the tunable laser gives a maximal reflection intensity of 87.9 ± 1 %. The layer-peeling algorithm has been applied on the r(ν) function using the following parameters : 2000 layers of 5μm with λ_B as design wavelength, an effective refractive index of 1.45. This corresponds to a spectral range between 1252.8 and 1371.2 nm with 36161 points out of the 2^{20} from the FFT. The reconstruction length is 10 mm. The maximal reflectivity has been adjusted to minimize the amplitude difference Δq from both sides. A value of 87.5 % was found, consistent with the transmission measurement.

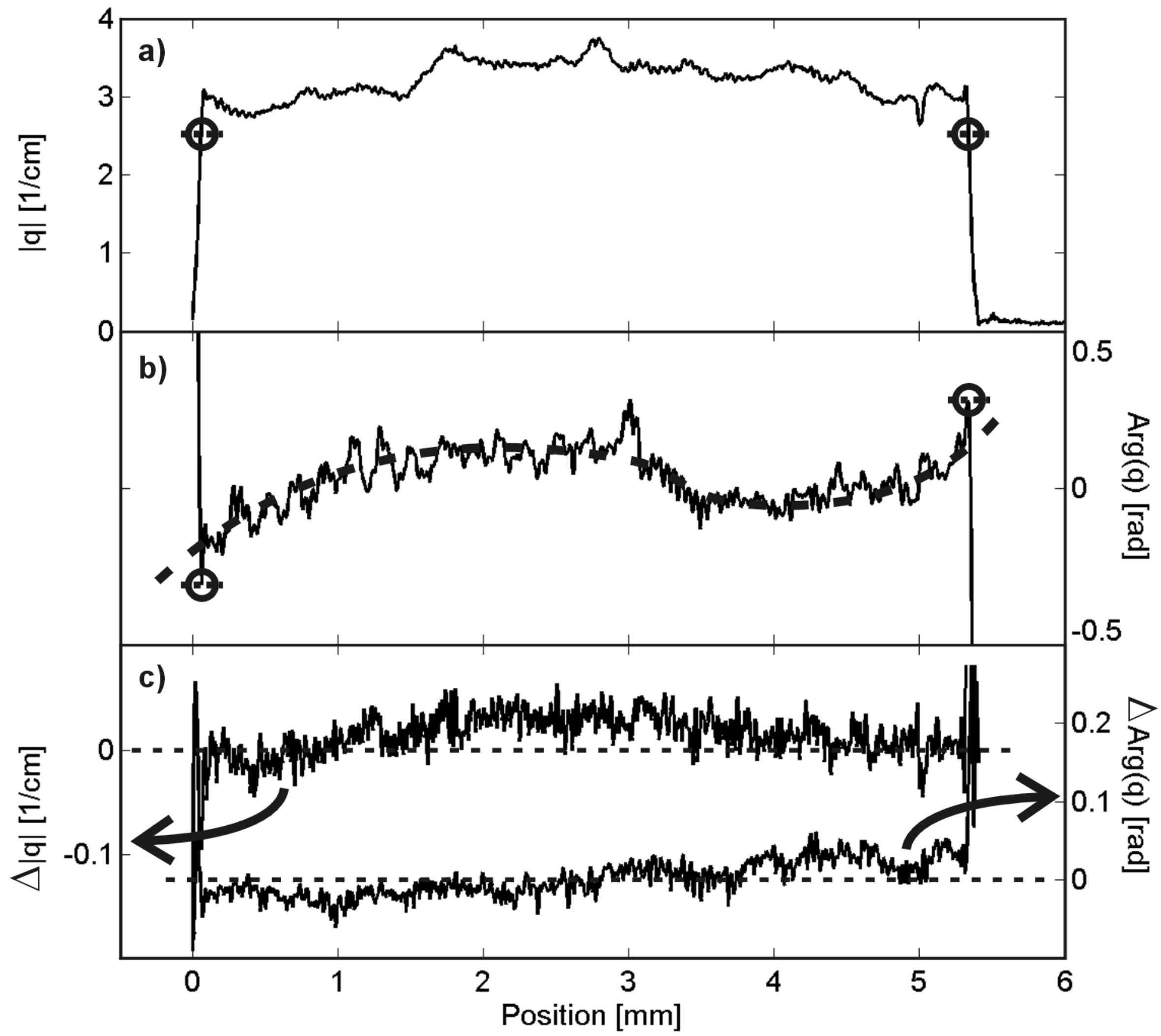

Fig. 4-16 Coupling coefficient amplitude (a); phase (solid line) and fit (dashed line) (b); differences between reconstructions from both sides (c)

Fig. 4-16 presents the reconstructed coupling coefficient amplitude (a) and phase (b) from one side. Fig. 4-16c shows the amplitude and phase differences between reconstructions from both sides. The longitudinal resolution is estimated at 20 μm from the smallest variations observed in both reconstructions. The grating limits (circles in Fig. 4-16) are found in the phase response where the phase variation is nearly asymptotic. The reconstructed grating is 5.33 mm long as expected and has an average coupling amplitude of 3.3 cm^{-1} ($\Delta n_{AC} = 1.25 \cdot 10^{-4}$) with 25 % variations. The coupling coefficient amplitude behind the grating remains at 0.1 cm^{-1} due to small propagating losses in the cladding that are not considered in the reconstruction algorithm. The coupling coefficient phase is limited to ± 0.3 radians, indicating small deviations from design wavelength. The dashed line in Fig. 3b corresponds to average change in Δn_{dc}. Other variations of Arg(q) are seen in the phase reconstruction but they are not completely understood. It has to be noted that these variations are not artifacts as they disappear in the phase difference ΔArg(q) from both sides (Fig. 3c). The amplitude difference $\Delta|q|$ from independent reconstruction of both sides is under 3 % of the average coupling coefficient amplitude. This indicates small OLCR measurement and reconstruction errors.

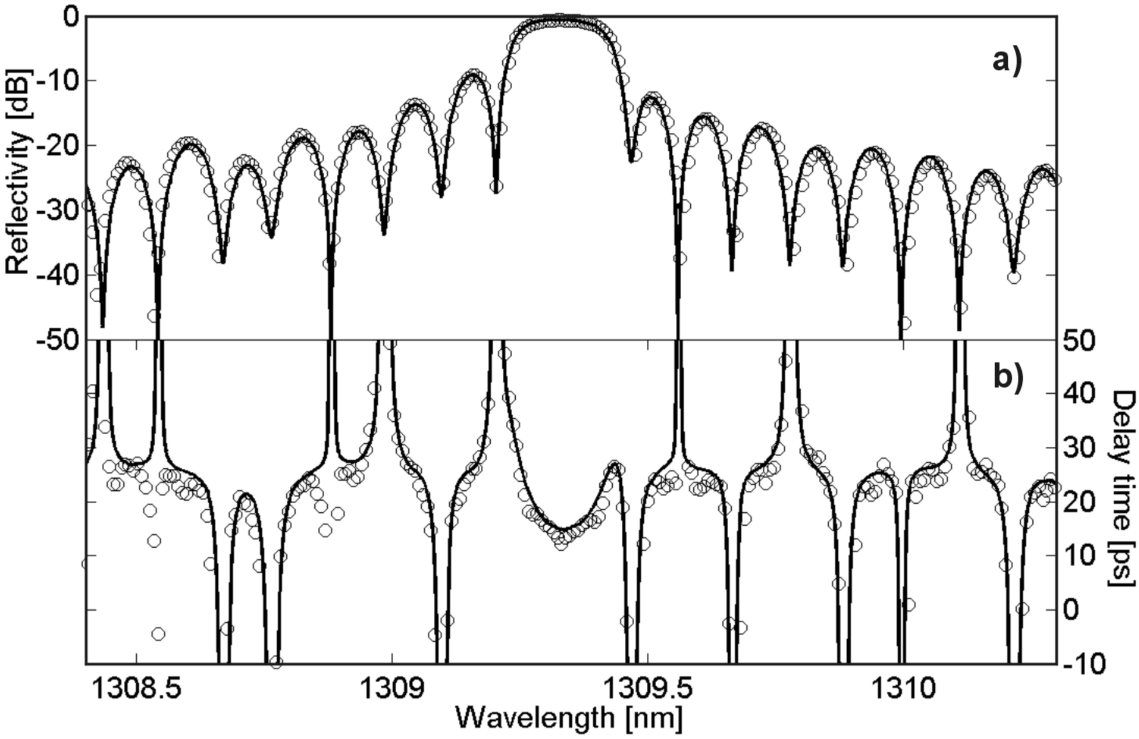

Fig. 4-17 Reflection intensity (a), delay time (b) calculated from the reconstructed coupling coefficient (solid line) and directly measured with a tunable laser (circles)

The T-matrix method is used to compute the reconstructed complex spectral response from the obtained coupling coefficient. A direct measurement of the complex spectral reflectivity of FBG is performed with the same set-up used in an OFDR configuration (optical frequency domain reflectometry, §4.3.7). In this case the laser frequency is scanned while the mirror has a defined position. The phase difference between the laser and the low coherent light source compensates the phase drifts in the same way as in the OLCR configuration. Fig. 4-17 shows both calculated and measured spectral responses. A good agreement is observed, confirming the validity of the entire reconstruction process.

4.5.2 Non-homogenous grating

The grating has been inscribed in a photosentive fiber (Spectran Photosil) with a 193 nm ArF excimer laser. The writing process consists of two irradiation steps :

- five localalized homogeneous irradiations through a 780 mm-pitch amplitude mask (2000 pulses)
- an homogeneous FBG exposure through a 902.9 nm–pitch phase mask over a length of 5 mm (500 pulses)

The FBG reflection intensity and time delay are presented in Fig. 4-18.

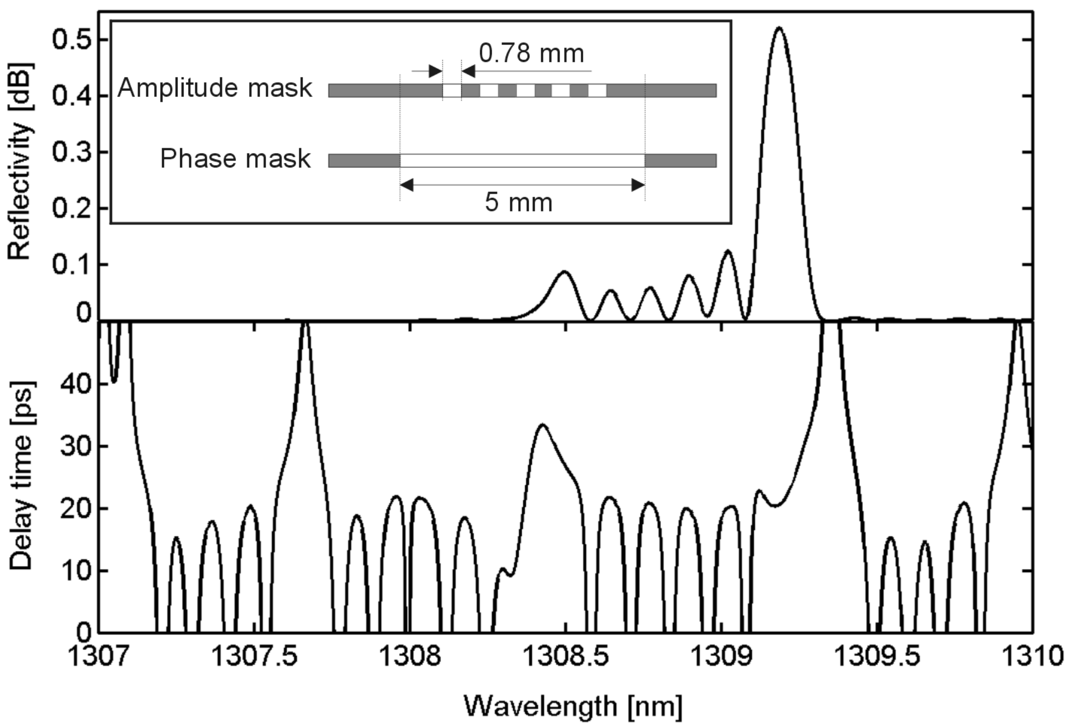

Fig. 4-18 Reflection intensity and time delay of the non-homogeneous FBG and amplitude / phase masks parameters

The first illumination added a constant index change Δn_{dc} to the exposed regions. The second exposure through a phase mask produces two different index modulation amplitudes $\Delta n_{ac1,2}$ due to the modified sensitivity in pre-exposed regions (Fig. 4-19a). Fig. 4-19b presents schematically n(z) where the pre-exposed region exhibits higher $\Delta n_{dc}(z)$ and lower $\Delta n_{ac,2}$.

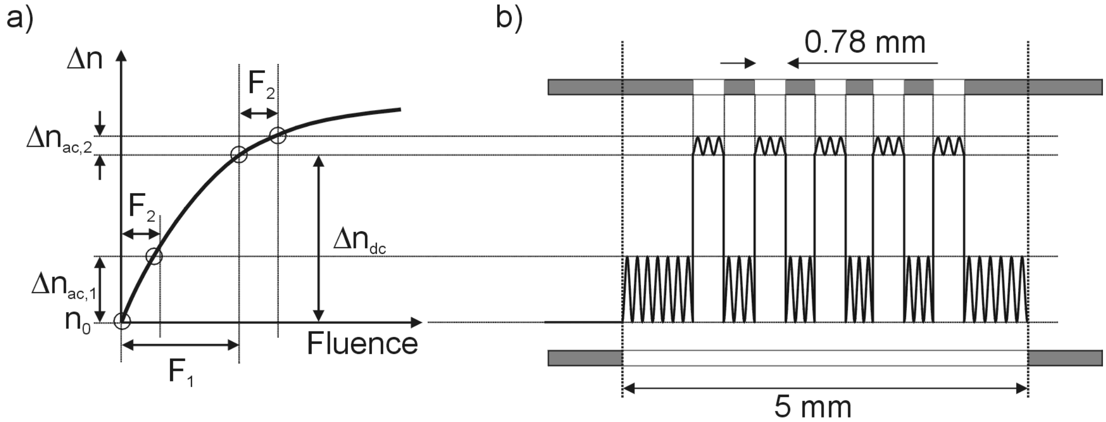

Fig. 4-19 Fiber photosentivity curve (a) and FBG refractive index function (b)

The OLCR measurement of our test FBG has been performed from both sides. Fig. 4-20 shows the results for one side where A is the OLCR amplitude and $\Delta\phi$ the difference between the OLCR phase and the laser phase. A sampling interval of 20 μm in air and a scan speed 3 mm/min have been used. The amplitude S/N is −120 dB. The matching of the laser wavelength with the Bragg wavelength limits $\Delta\phi$ to a 10 radians range. The grating entrance and output are marked with vertical dotted lines. The grating length is 5.13 mm (half the measured OPLD divided by the fiber group refractive index $n_g = 1.45$). The FBG regions that have been pre-exposed exhibit lower A and a lower $\Delta\phi$ slope. This is fully explained by the fabrication process. In the pre-exposed region the modulation amplitude $\Delta n_{ac,2}$ is lower than $\Delta n_{ac,1}$, (lower photosensitivity) and this results in lower local reflectivity. On the other hand, the added index offset Δn_{dc} leads to a locally higher n_g, resulting in a lower slope for $\Delta\phi$. The positive and negative slopes are given by the particular choice of the laser wavelength, that resides between the two local Bragg wavelengths. The amplitude drop at 7.3 mm in A and $\Delta\phi$ is probably due the fabrication process (small remaining coating part or local laser beam inhomogeneity). Small variations of A and $\Delta\phi$ in the grating can also be explained by UV-laser beam inhomogeneity. At the end of the grating the amplitude drops by 10 dB and then slowly decreases. The pre-exposure process suppresses the typical oscillations due to the global FBG Fabry-Perot effect observed in homogeneous FBG.

The reconstruction process uses the same parameters we have seen for the homogeneous grating reconstruction, except for the design wavelength (λ_d = 1309.25) and the maximal reflection intensity (52 ± 1 %) obtained from an independent measurement. Fig. 4-21 presents the reconstructed coupling coefficient amplitude (a) and phase (b) from one side. The grating limits (circles) have been defined by the phase response where the slope strongly increases. The reconstructed grating is 5.13 mm long as expected. The amplitude in the pre-exposed region is between 140 and 160 m^{-1}. Based on equation (2), we evaluate for $\Delta n_{ac,2}$ values ranging from 0.70 to $0.8 \cdot 10^{-4}$. The local amplitude variations are probably due to inhomogeneities in illumination during FBG fabrication. The amplitude level in the other regions is between 210 and 240 m^{-1} ($\Delta n_{ac,1}$ between 1.05 and $1.21 \cdot 10^{-4}$). The phase slope gives information about Δn_{dc} and the grating period deviation from the design period. Considering a 100 % fringe visibility, a 451.37 nm grating period is obtained from regions only exposed to the phase mask. This value is 0.08 nm smaller than half the phase mask period. This effect is expected as the fiber is stretched during inscription. The grating period is constant along the grating and then, the Δn_{dc} is found from pre-exposed region. A value of 5.5 to $6.0 \cdot 10^{-4}$ is calculated and Δn_{dc} is around five-time Δn_{ac}, compatible with the number of pulses used in both exposures, 2000 and 400 respectively.

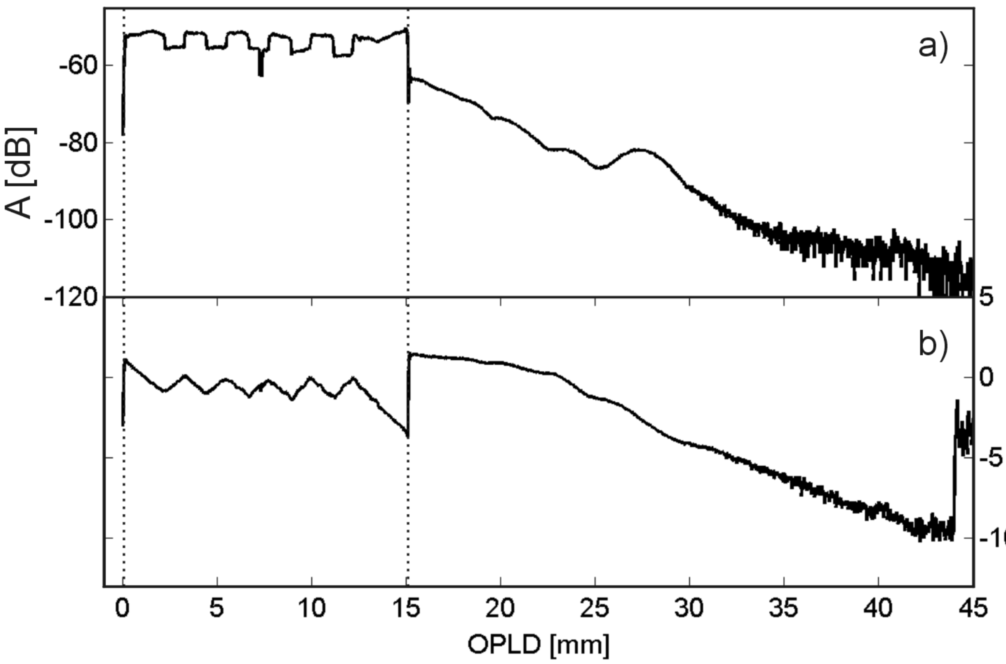

Fig. 4-20 OLCR amplitude (a) and phase difference between OLCR phase and reference laser phase at λ_B (b)

Fig. 4-21c is a close-up of the amplitude between the dotted vertical lines. The strong defect observed in the grating enables us to estimate the axial resolution to a value below 20 μm. Fig. 4-21d shows the amplitude and phase differences between reconstructions from both sides. The amplitude difference $\Delta|q|$ and phase difference $\Delta Arg(q)$ from independent reconstruction of both sides are below 5 % of the average coupling coefficient amplitude and phase signal respectively. This indicates small OLCR measurement and reconstruction errors. A small slope in the angle difference can be explained by a temperature difference between the measurements.

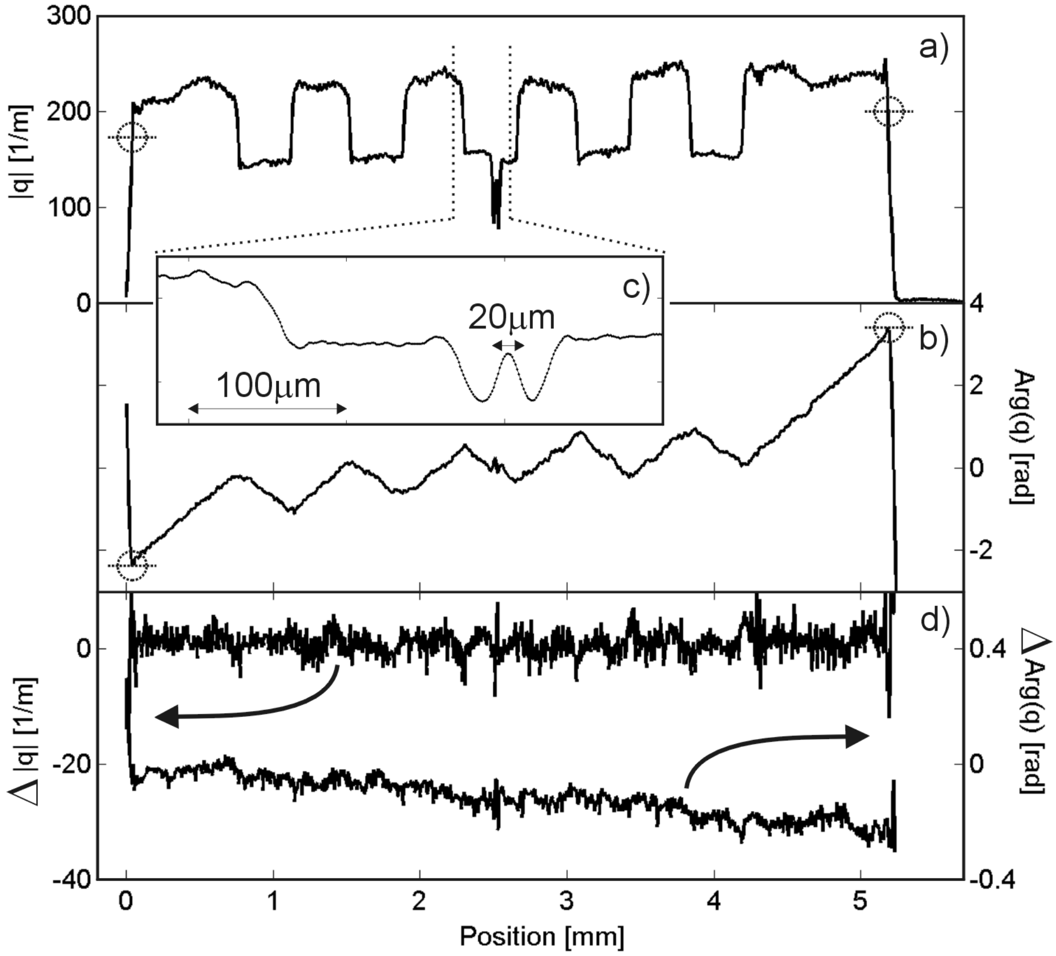

Fig. 4-21 Coupling coefficient amplitude (a); phase (b); expanded view of coupling coefficient amplitude (c); differences between reconstructions from both sides (d)

4.5.3 Fiber Bragg grating with excess loss

A preliminary experiment has been performed on a nearly homogeneous FBG that presents non-coincident reconstruction from both sides. The reconstruction problem is assumed to come from losses that occur inside the grating.

The FBG presented in this section has been fabricated with a CW–UV laser at 244 nm in a Spectran Photosil single mode fiber. The peak resonance Bragg wavelength λ_b is 1308.75 nm, the grating length is about 12 mm. The grating is assumed to have a small tilt as important transmission cladding losses are observed for wavelength under the Bragg wavelength.

In first approximation, the losses are assumed as a frequency independent excess loss E. Then, the equation that relates the reflection and the transmission amplitudes R and T, respectively, becomes

$$R(\lambda) + T(\lambda) = 1 - E \qquad (4\text{-}54)$$

where λ is the wavelength.

A transmission intensity measurement has been conducted and the ratio between the minimal and maximal transmission intensity is calculated. A value of 0.25 is obtained for T_{min}/T_{max}. A schematic view of the spectral intensity parameters is presented in Fig. 4-22.

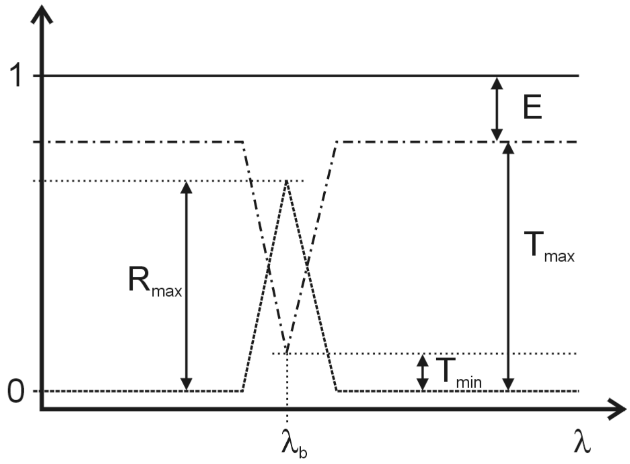

Fig. 4-22 Schematic view of the spectral intensity parameters

An OLCR measurement has been performed from both sides of the grating with an OPLD resolution of 20 µm. The reconstruction of the complex coupling coefficient has been performed for both OLCR measurements, considering two different cases, that is, considering or not the excess loss. The constant parameters between these reconstructions are the design wavelength of λ_b and the layer thickness of 5 µm.

If the excess loss is not considered, the maximal grating reflectivity is 75 % ($T_{max} = 1$ and $R + T = 1$). The coupling coefficient amplitudes are presented in Fig. 4-23 (top) and it is observed that the two curves are not identical, even if the local variations seem to be strongly related. The grating length L is 11.9 mm.

If the excess loss is considered, we have to determine the maximal intensity reflection R_{max} and the loss parameter α. The optimal parameters search has been conducted under two requirements : 1) minimize the difference between the reconstructed amplitudes of the coupling coefficient and 2) minimize the remaining amplitudes after the grating output position.

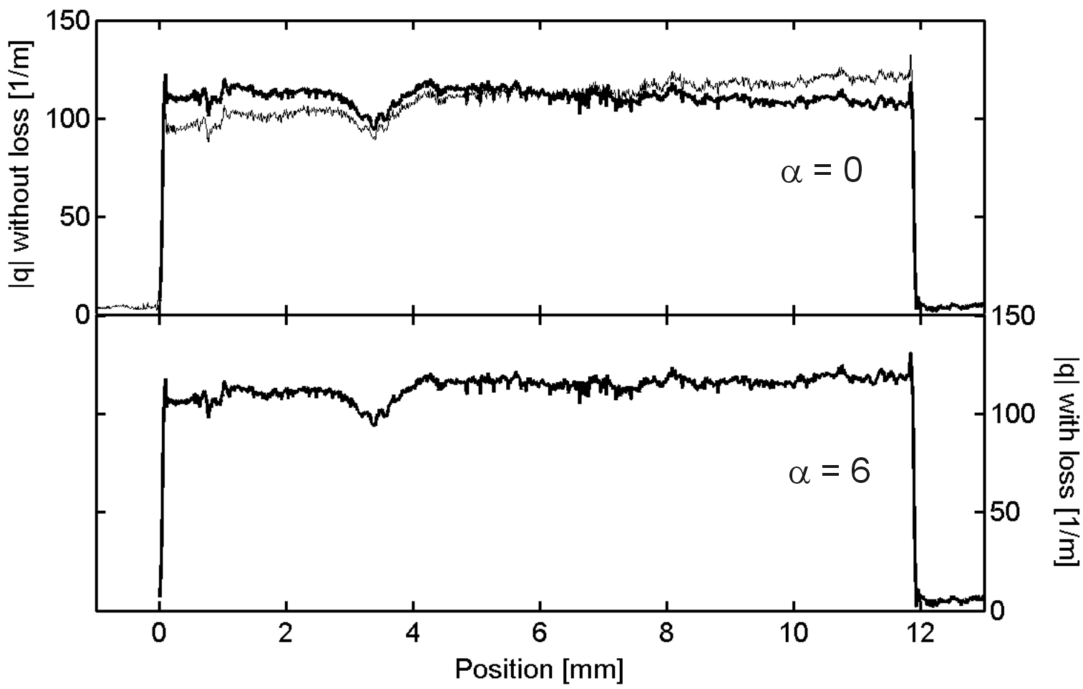

Fig. 4-23 Coupling coefficient amplitudes from the layer-peeling reconstructions performed from both sides of the grating (thin and thick lines), taking into account (top) or not (bottom) the loss effects

The values of 69 % and 6 m^{-1} have been found for R_{max} and α, respectively. The coupling coefficient amplitudes are presented in Fig. 4-23 and in this case, the two reconstructions are nearly identical for the grating positions and the remaining amplitude after the grating output position is under 3 % of the maximal coupling coefficient amplitude.

The difference between the coupling coefficient amplitudes reconstructed from both sides of the grating is presented in Fig. 4-24 (top) for the two reconstruction cases. It is observed that the differences are well approximated by straight lines and that for the reconstruction with loss, the line is horizontal and close to zero.

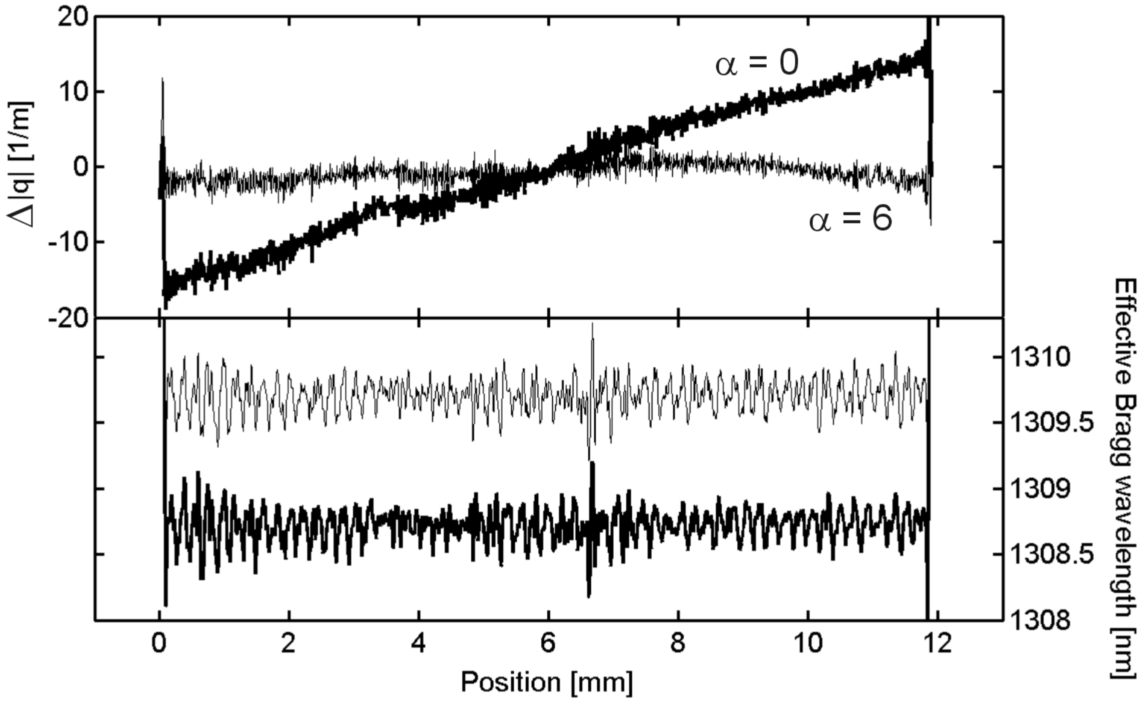

Fig. 4-24 Top : coupling coefficient amplitude difference for the case where the losses are not considered (thick line) and in the case with the loss in the reconstruction (thin line); Bottom : effective Bragg wavelength calculated for the reconstruction from both sides (the thin line has been shifted by 1 nm for clarity)

We have not yet presented the coupling coefficient phase information. We have observed that this phase information is not affected by the loss parameter α. For this reason, we limit the representation for the case with $\alpha = 6$. Instead of representing the coupling coefficient phase, we present in Fig. 4-24 (bottom) the effective Bragg wavelength distributions for the reconstruction from both sides (where one response has been shifted by 1 nm), which is a function of the first derivative of the phase information. The two curves are quite similar but some local differences are observed.

We have two possibilities to calculate the excess loss E from the optimal reconstruction parameters R_{max} and α used in the reconstruction that takes account of the loss. In the first case, $R_{max} = 0.69$ and using the ratio T_{min}/T_{max} and equation (4-54) an excess loss of 8 % is obtained. In the second case, the loss factor α of 6 m^{-1} gives an excess loss of 6.9 % calculated from the light beam attenuation over the grating distance L = 11.9 mm, where $I_{out}/I_{in} = \exp(-\alpha L)$. Both value are slightly different and can be due to wavelength dependent excess loss.

The spectral reflection and transmission intensities have been plotted in Fig. 4-25 for the case of constant excess loss of 8 %. We observe that for negative wavelength detuning values, R + T is not constant, indicating wavelength dependent excess loss.

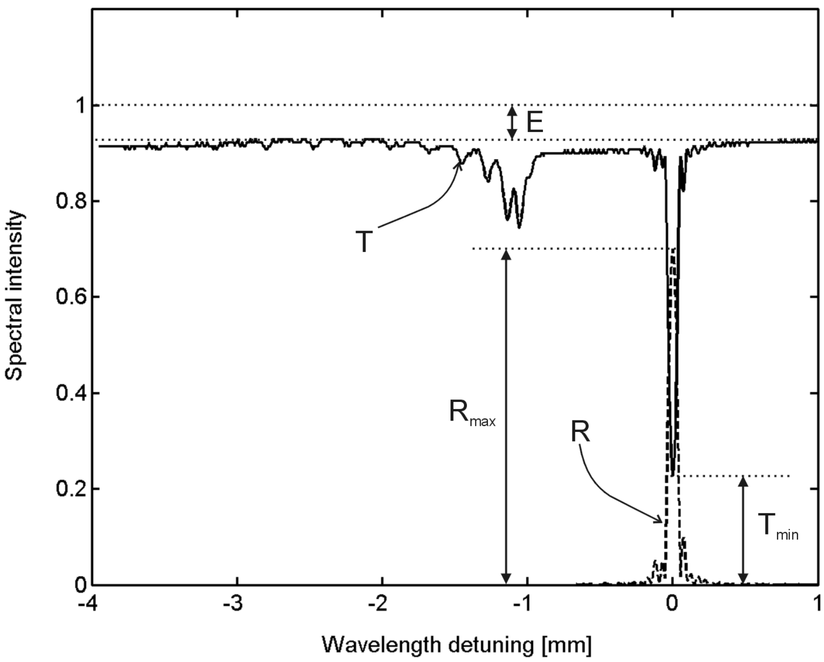

Fig. 4-25 Measured spectral reflection and transmission intensities, considering an wavelength independent excess loss of 8 %; the reference wavelength is the Bragg wavelength

The next step in the reconstruction of such grating would be to consider a wavelength dependent loss coefficient $\alpha(\lambda)$.

4.6 Summary

We have shown that for a wavelength bandwidth where the fiber dispersion is negligible, the complex OLCR response of a FBG corresponds to the convolution of the complex impulse response of the grating with the degree of coherence of the light source. We have also shown that the grating impulse response is less directly connected to the OLCR response in the case where the dispersion effects are not negligible. Nevertheless, it is experimentally or mathematically possible to retrieve the complex impulse response in this case.

We have detailed the new developed OLCR set-ups, explained the measurement method, the apparatus performances and the limitations. This instrument measures the amplitude and the phase information of the FBG. The main results concerns the time-multiplexing OLCR set-up that exhibits a noise level of −120 dB for optical fiber devices (limited by the Rayleigh back-scattering) and a large range of allowed OPLD resolution due to the phase difference measurement method.

The reconstruction process from the OLCR measurement to the complex coupling coefficient has been presented and the reconstruction of different FBGs has been shown. The main results are an axial resolution of 20 μm and a maximal absolute error of the amplitude and the phase of 5 % calculated by comparison between the reconstructions conducted from both side of the FBG. The reconstruction of a FBG that exhibits loss has also been reconstructed using the modified layer-peeling method and a good matching between the reconstructions from both sides is observed.

4.7 References

4-1 P. Lambelet, P.Y. Fonjallaz, H.G. Limberger, R.P. Salathé, C. Zimmer, and H.H. Gilgen, IEEE Phot. Techn. Lett. 5, 565-567 (1993)

4-2 S.D. Dyer and K.B. Rochford, "*Low-coherence interferometric measurements of fibre Bragg grating dispersion*", Electron. Lett., 35, 1485-1486 (1999)

4-3 F. Lindgren, R. Gianotti, R. Wälti, R.P. Salathé, A. Haas, N. Nussberger, M.L. Schmatz, IEEE Phot. Techn. Lett. 9, 1613-1615 (1997)

4-4 Born & Wolf, "Principles of Optics", Ch. 10, §7.3, edition, p. 540-544

4-5 P. Chavel, "*Coherence en optique*", Ecole Supérieure d'Optique, Institut d'Optique Théorique et Appliquée, cours de 1ère année (1995)

4-6 B.E.A. Saleh, M.C. Teich, "*Fundamentals of photonics*", John Wiley&Sons (1991), p. 348-352

4-7 B.E.A. Saleh, M.C. Teich, "*Fundamentals of photonics*", John Wiley&Sons (1991), p. 182-191

4-8 A. Kohlhaas, C. Frömchen and E. Brinkmeyer, "*High-resolution OCDR for testing integrated-optical waveguides : dispersion-corrupted experimental data corrected by a numerical algorithm*", JLT, 9, 10, p.1493-1502 (1991)

4-9 F. Lindgren, R. Gianotti, R. Wälti, R.P. Salathé, A. Haas, N. Nussberger, M.L. Schmatz, "*$-78-dB$ shot-noise limited optical low-coherence reflectometry at $42-m/s$ scan speed*", IEEE Phot. Techn. Lett. 9, 1613-1615 (1997)

4-10 M.J.F. Diagonnet, B.Y. Kim, "*Optical Fiber Sensors : principles and components*", Vol. One, Artech House Boston and London, Ch. 7, p. 210-219 (1988)

4-11 W.V. Sorin, D.M. Baney, "*A simple intensity noise reduction technique for optical low-coherence reflectometry*", IEEE Phot. Techn. Lett. 4, 1404-1406 (1992)

4-12 A.M. Rollins, J.A. Izatt, "*Optimal interferometer designs for optimal coherence tomography*", Opt. Lett., 24, 1484-1486 (1999)

4-13 W.V. Sorin, D.M. Baney, "*Measurement of Rayleigh backscattering at 1.55 μm with 32 μm spatial resolution*", IEEE Phot. Techn. Lett. 4, 374-376 (1992)

4-14 P-Y. Fonjallaz, "*Bragg gratings in single-mode optical fibers: characterization, stress modifications and out-couplers*", §3.2.4, Thesis work n° 1348, Ecole Polytechnique Fédérale de Lausanne (1995)

Chapter 5

FBG strain sensors

FBGs in low-birefringent optical fibers are very efficient axial stress sensors. Within the collaboration with the Laboratoire de mécanique appliquée et d'analyse de fiabilité (LMAF), FBGs fabricated in our institute have been used with success as strain gauges. A promising preliminary experiment on the reconstruction by OLCR and layer-peeling of non-homogeneous axial strain fields is developed in section 5.1. Other applications of FBGs for axial strain measurements, not detailed hereafter, include : 1) studies on bridging cracks in composites in collaboration with Michel Studer [5-1 to 5-3], 2) studies on the deformation behavior of composite laminates in collaboration with Federico Bosia [5-4 to 5-6] and 3) studies on the characterization of FBGs in non-homogeneous axial stress fields by simulation of the spectral intensity response in collaboration with Prof. Kara Peters and Philip Pattis [5-9, 5-10].

The behavior of FBGs subjected to transversal stress fields has been analyzed for gratings written in low-birefringent and polarization maintaining fibers. A diametric load experiment is presented in section 5.2 and applications in the measurement of transversal strain fields in composites have also been studied [5-7, 5-8].

5.1 Axial strain field distribution measurements

In this section, we describe the experiments conducted on a FBG located at the center of an epoxy sample subjected to non-homogeneous axial stress. First, the FBG behavior under axial stress is presented in section 5.1.1. The experiment is described in section 5.1.2. The OLCR measurements for different loading conditions, the derived spectral response and reconstructed complex coupling coefficients are presented in sections 5.1.3 to 5.1.5. From the complex coupling coefficient, an effective Bragg wavelength distribution λ_{eff} is defined ($\lambda_{eff}(z) = 2n_0\Lambda_{eff}(z)$ where $\Lambda_{eff}(z)$ is the effective period defined in equation (3-19) and n_0 is the effective refractive index of the fiber), which is used to calculate the axial strain distribution. A comparison with a finite element calculation is finally presented (5.1.6).

5.1.1 Axial stress effect on fiber Bragg gratings

We consider here the case of a fiber Bragg grating subjected to a homogeneous axial stress σ_z (Fig. 5-1). In this case, the other components are null ($\sigma_x = \sigma_y = \tau_{xy} = \tau_{yz} = \tau_{xz} = 0$). In this section, the relation between the relative change of the Bragg grating and the axial stress amplitude is determined.

From the Bragg equation $\lambda_b = 2\cdot n_{eff}\cdot\Lambda$, where λ_b is the Bragg wavelength, n_{eff} the effective refractive index and Λ the grating period, the relative Bragg wavelength variation is given by

$$\frac{\Delta\lambda_b}{\lambda_b} = \frac{\Delta\Lambda}{\Lambda} + \frac{\Delta n_{eff}}{n_{eff}} = e_z + \frac{\Delta n_{x,y}}{n_0} \tag{5-1}$$

where $n_0 = n_{eff}(\sigma_z = 0)$. The first term, e_z, is the geometric deformation (axial strain) of the FBG and the second term, $\Delta n_{x,y}/n_0$, is the variation of the refractive index in the plane orthogonal to the direction of the light propagation.

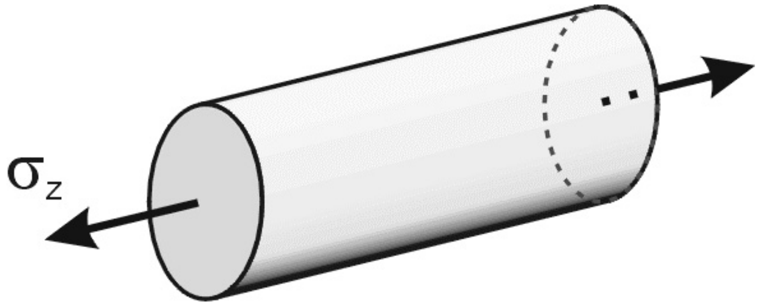

Fig. 5-1 : Axial Stress

The strain components e_i are related to the stress field through the elastic tensor, and, in the simple case of axial stress, we have the following equation

$$\begin{pmatrix} e_x \\ e_y \\ e_z \end{pmatrix} = \frac{1}{E}\begin{pmatrix} 1 & -\nu & -\nu \\ -\nu & 1 & -\nu \\ -\nu & -\nu & 1 \end{pmatrix}\begin{pmatrix} 0 \\ 0 \\ \sigma_z \end{pmatrix} = \frac{\sigma_z}{E}\begin{pmatrix} -\nu \\ -\nu \\ 1 \end{pmatrix} \tag{5-2}$$

where E is the Young modulus (E = 72 GPa for standard telecom fibers) and ν is the Poisson ratio ($\nu = 0.16$ for standard telecom fibers).

The dielectric tensor change, $\Delta\varepsilon_i^{-1}$, is related to the strain field through the elasto-optic tensor

$$\begin{pmatrix} \Delta\varepsilon_x^{-1} \\ \Delta\varepsilon_y^{-1} \\ \Delta\varepsilon_z^{-1} \end{pmatrix} = \begin{pmatrix} P_{11} & P_{12} & P_{12} \\ P_{12} & P_{11} & P_{12} \\ P_{12} & P_{12} & P_{11} \end{pmatrix}\begin{pmatrix} e_x \\ e_y \\ e_z \end{pmatrix} = \begin{pmatrix} P_{11}e_x + P_{12}\left(e_y + e_z\right) \\ P_{11}e_y + P_{12}\left(e_x + e_z\right) \\ P_{11}e_z + P_{12}\left(e_x + e_y\right) \end{pmatrix} \tag{5-3}$$

where P_{ij} are the photoelastic coefficients ($P_{11} = 0.113$ and $P_{12} = 0.252$ for standard telecom fibers).

The refractive index change Δn_i can be approximated, using the relation with the dielectric tensor ($n_i^2 = \varepsilon_i$), by

$$\Delta\varepsilon_i^{-1} = \Delta\left(\frac{1}{n_i^2}\right) \cong -2\frac{\Delta n_i}{n_i^3} \quad\Rightarrow\quad \frac{\Delta n_i}{n_i} \cong -\frac{n_i^2}{2}\cdot\Delta\varepsilon_i^{-1} \tag{5-4}$$

For the axial stress case, we have from equation (5-2) : $e_x = e_y = -\nu e_z = -\nu\cdot\sigma_z/E$, and then

$$\Delta\varepsilon_{x,y}^{-1} = e_z\left(\left(1-\nu\right)P_{12} - \nu P_{11}\right) \quad\Rightarrow\quad \frac{\Delta n_{x,y}}{n_0} \cong -\frac{n_0^2}{2}e_z\left(\left(1-\nu\right)P_{12} - \nu P_{11}\right) \tag{5-5}$$

From equations (5-1), (5-2) and (5-5), the relative Bragg wavelength change is found as

$$\frac{\Delta\lambda}{\lambda} = e_z\left(1 - \frac{n_0^2}{2}\left(\left(1-\nu\right)P_{12} - \nu P_{11}\right)\right) = e_z\left(1-p_e\right) = \sigma_z\frac{1-p_e}{E} \tag{5-6}$$

where p_e is the effective photoelastic constant for axial stress that can be deduced from $\Delta\lambda(\sigma_z)/\lambda$ for homogeneous axial loading. The effective refractive index remains uniform and constant in the transverse plane of the fiber core. The relative variation of the Bragg wavelength is linear with a stress σ_z. The geometric effect corresponds to the first term σ_z/E and the refractive index effect corresponds to the second term $-\,p_e\cdot(\sigma_z/E)$, which is opposite and about five times smaller than the geometrical effect.

The experimental determination of the effective photoelastic constant of the grating used in the experiment is presented in Fig. 5-2 ($p_e = 0.2148$). The calibration is performed applying an homogeneous axial stress field to the FBG.

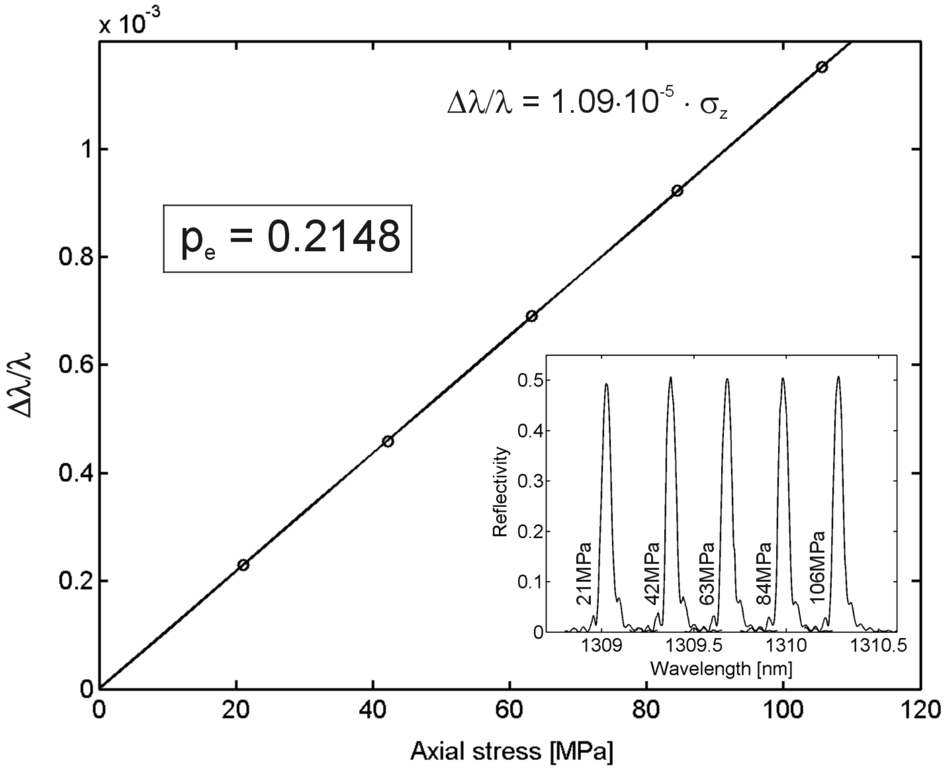

Fig. 5-2 Experimental calibration of p_e : reflectivity spectrum for different axial stress (insert) and relative Bragg wavelength change

5.1.2 Experiment description

A preliminary experiment has been conducted to study non-homogeneous axial stress fields and to apply the reconstruction method presented in Chapter 4. A 12 mm FBG has been placed in the middle of an epoxy sample (Fig. 5-3 left).

An axial stress has been applied on the sample using the device presented in Fig. 5-3 (right). Due to the two notches in the epoxy bloc, the resulting stress field in the grating region will be non-homogeneous. The sample was connected to a strain gauge and an extensometer was placed on half the sample height to measure the average displacement. A measurement of the spectral intensity and the complex OLCR response with 20 μm OPLD resolution were performed before and after embedding, and for four loading conditions (384, 299, 207 and 116 N).

The measurement procedure is presented in Fig. 5-4. First, the FBG is completely characterized before the embedding in the epoxy sample. The epoxy sample is then subjected to an axial loading of about 425 N (obtained by turning the force controlling wheel shown in Fig. 5-3 right). As the stress-applying device is not force-controlled, the relaxations in the sample lead to a force decrease. A relaxation time of about 8 hours was observed and then for a force value of 384 N a complete characterization of the FBG is conducted. Three other measurements have been performed for three loading conditions (299, 207 and 116 N). The relaxation time τ between these measurements is 1 hour. A complete unloading was necessary after the measurement at 299 N due to a loss of the force and deformation calibration. Nevertheless, the duration of this unloading and re-loading was only one minute and then, parasitic relaxation can be neglected. After this measurement, the sample is removed from the stress-applying device and a relaxation time of 8 hours is observed. The last measurement is then performed for the 0 N force condition.

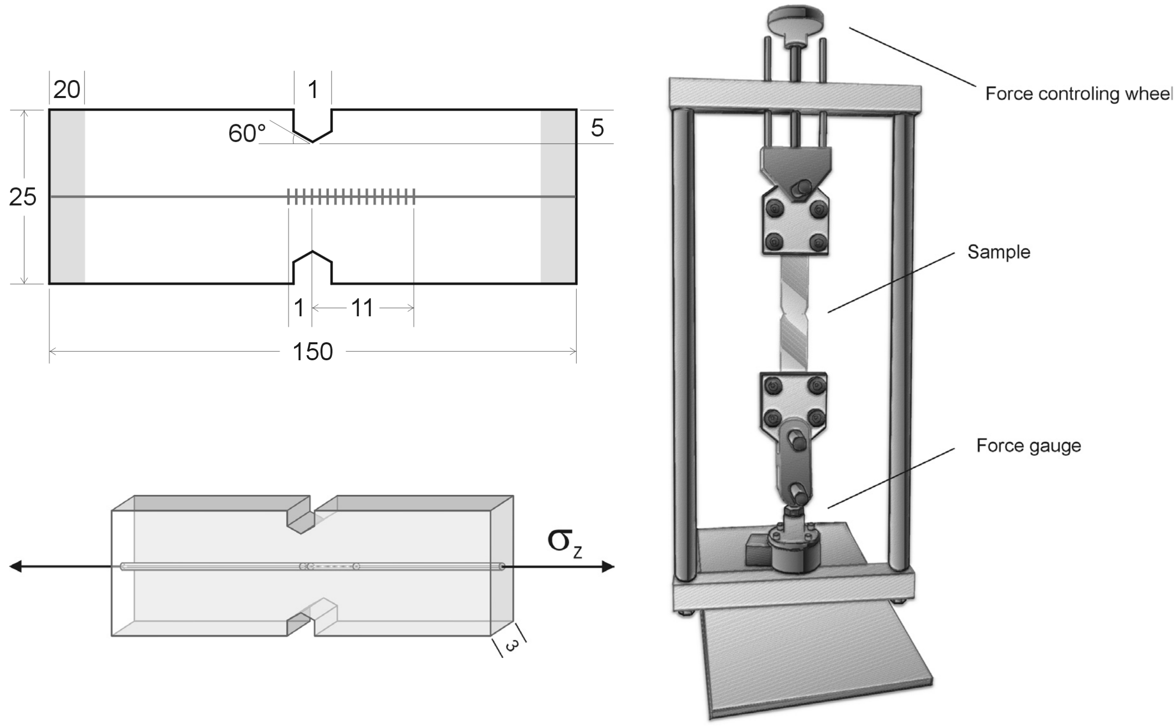

Fig. 5-3 Left : Sample used in experiment using a FBG and subjected to an axial stress; Right : Stress-applying device

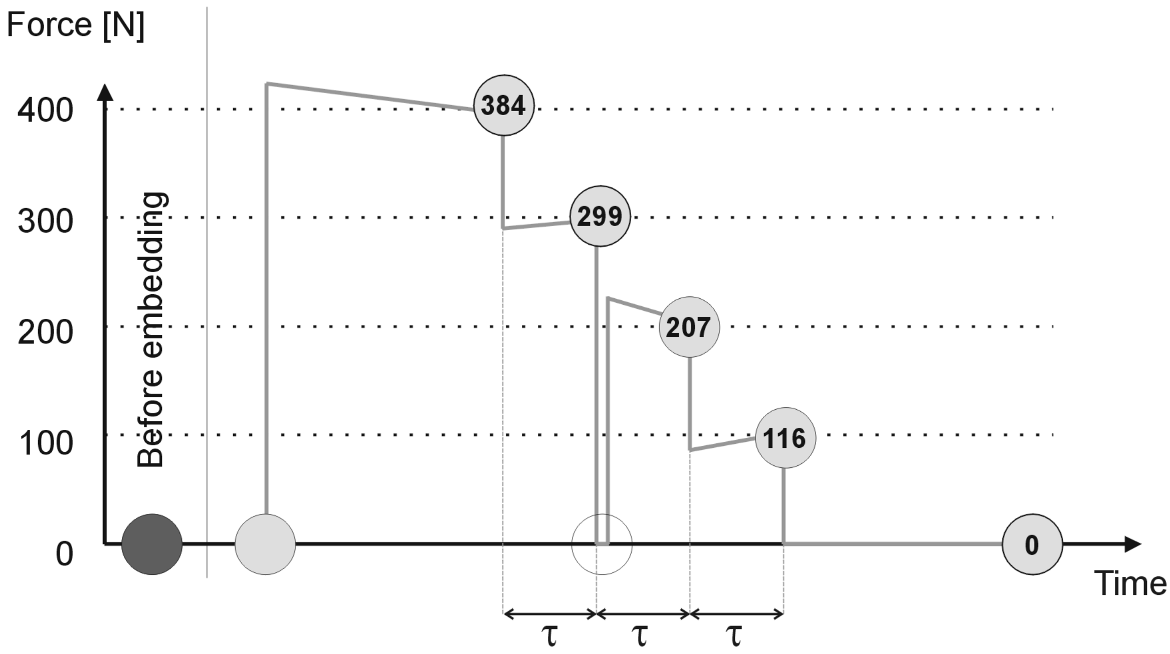

Fig. 5-4 Loading procedure

5.1.3 OLCR measurements

When the FBG is subjected to a non-homogeneous axial strain field, the Bragg condition depends on the position, and an effective Bragg wavelength $\lambda_{eff}(z)$ can be defined that takes into account the local chirp. An average Bragg wavelength λ_{mc} can be calculated from the reflectivity intensity as the mass center of the spectrum (equation 2-17), which depends on the applied force value F.

The complex OLCR measurement is performed with an arbitrary laser wavelength reference λ_L chosen in the stop-band wavelength range of the grating. Nevertheless, the OLCR phase difference $\Delta\phi$ in this case depends on the laser choice. For this reason, a new phase difference $\Delta\phi_{mc}$ is calculated for a reference wavelength corresponding to the average Bragg wavelength $\lambda_{mc}(F)$

$$\Delta\phi_{mc} = \Delta\phi + 2\pi \cdot OPLD\left(\frac{1}{\lambda_L} - \frac{1}{\lambda_{mc}}\right) \tag{5-7}$$

In this experiment, the spectral response has been calculated by Fourier transform from the complex OLCR measurements. We present in Fig. 5-5 the calculated average Bragg wavelengths $\lambda_{mc}(F)$.

The time interval between the three measurements at 384, 299, 207 and 116 N was the same. This explains the good linearity observed between these four points. The measurement at 0 N after the experiment has been performed after 8 hours of relaxation. The Bragg wavelength for this case is much lower than the expected value from the linear fit performed from the four previous points. It is also observed that the grating embedding process increase the Bragg wavelength. This wavelength increase is explained by the sample fabrication process, where an important charging force is applied to the fiber to guaranty the grating alignment and positioning. The fact that the Bragg wavelengths before and after the experiment are not coincident indicates that the applied loads are high enough to induce plastic deformations.

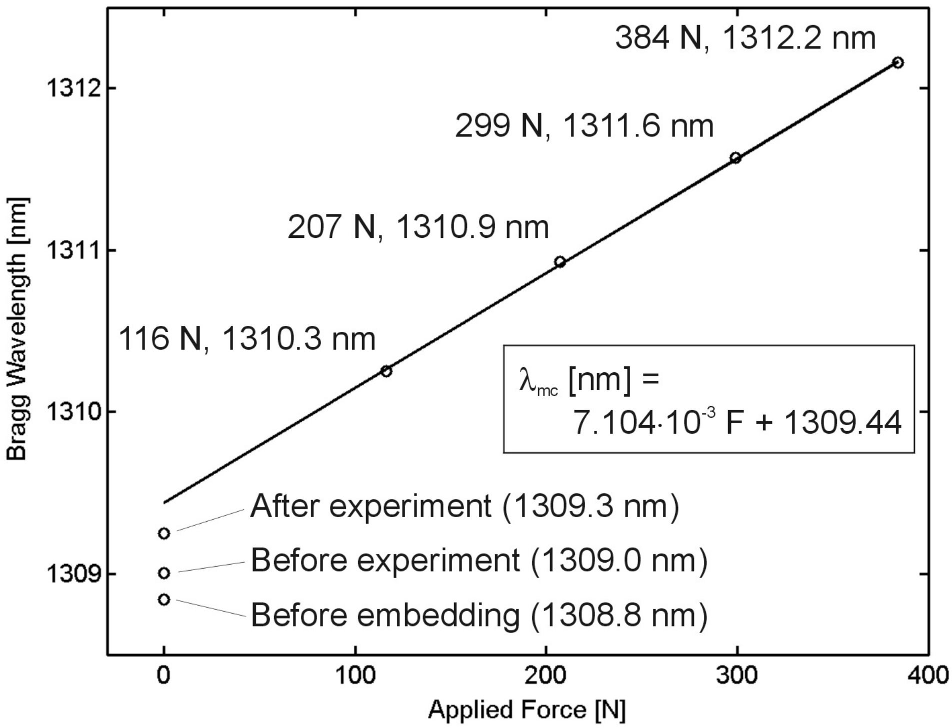

Fig. 5-5 Bragg wavelength obtained from the mass center of the frequency response calculated from the OLCR measurements; the solid line represents the linear fit for the loading cases between 116 and 384 N

The complex OLCR responses using the average Bragg wavelength at the mass center $\lambda_{cm}(F)$, where F is the force (Fig. 5-6).

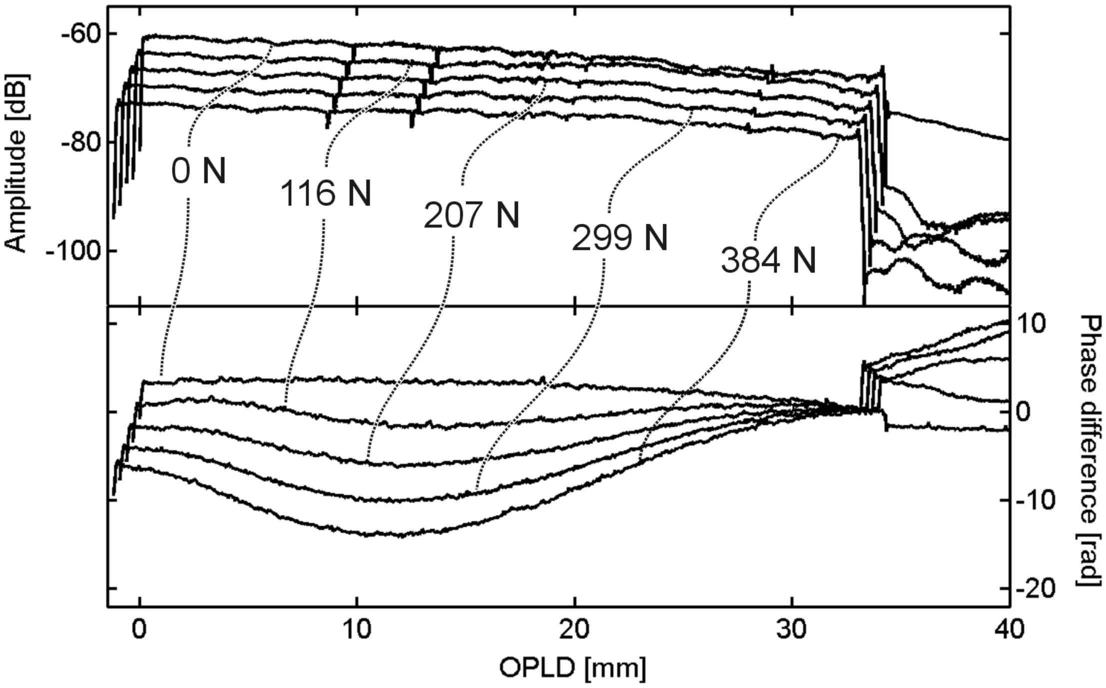

Fig. 5-6 OLCR measurements at different axial loads; amplitude (top) and phase difference (bottom), calculated from the Bragg wavelength at the mass center; the curves are shifted in order to improve the visibility

The OLCR amplitude is closely related to the refractive index modulation amplitude Δn_{ac}, but also takes into account the attenuation of the light beam propagating in the grating. The OLCR amplitude similarity is then explained by the fact that Δn_{ac} is not significantly modified by the applied stress, and except from the 0 N loading case, the induced chirp is important and then limits the light attenuation. Several inhomogeneities in the FBG are well observed, at the same place and with the same strength in all amplitude curves. The phase difference between the OLCR phase and the Bragg wavelength at the spectral mass center is obtained from equation (5-7). We observe that the phase difference variations increase with the loading amplitude. Locally, the phase difference shows important ripples, much bigger than those observed for the phase difference of the grating before the embedding in the sample (Fig. 5-7). This can be due to local inhomogeneous strain fields produced by the epoxy relaxation.

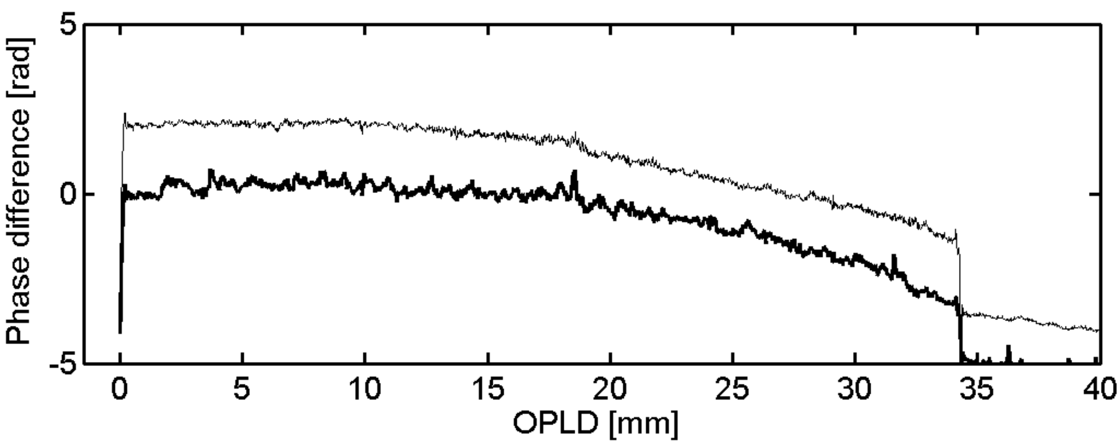

Fig. 5-7 Phase difference calculated from the Bragg wavelength at frequency mass center for the grating before embedding in the sample (thin line) and after the experiment at 0 N (thick line)

When the sample is charged, the grating length is increased (insert part of the figure Fig. 5-8 for the 384 N loading case) and the induced chirp reduces significantly the Fabry-Perot effect. This can be observed in Fig. 5-8 for the 384 N loading case, where the amplitude drop at the grating output is 20 dB deeper than for the 0 N case.

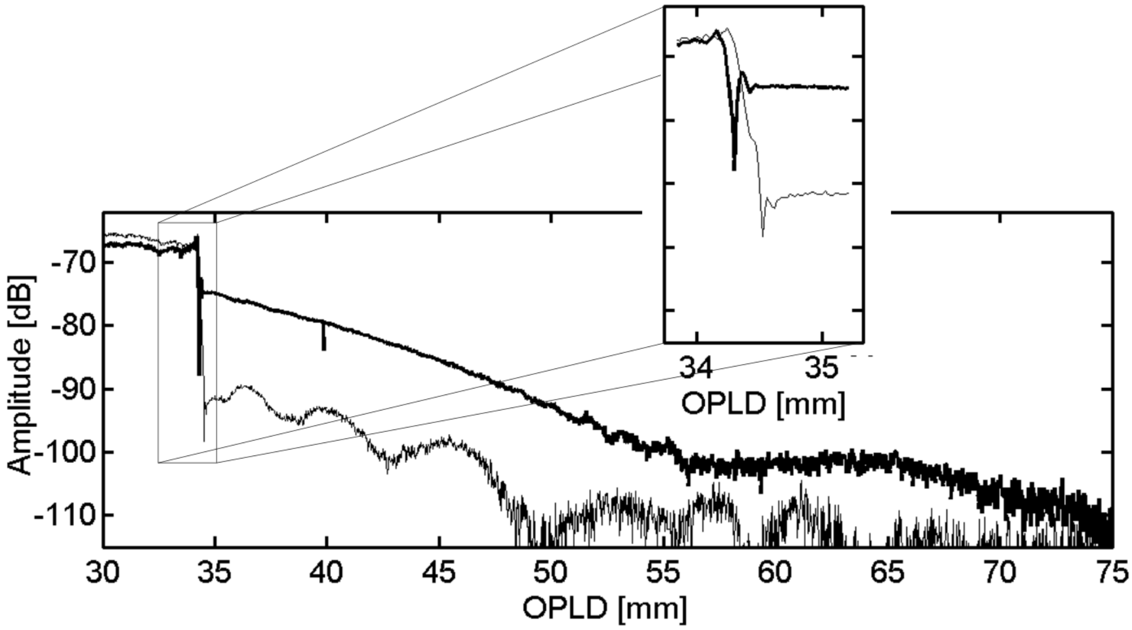

Fig. 5-8 OLCR amplitude response at 384 N (thin line) and 0 N (thick line)

5.1.4 Spectral responses

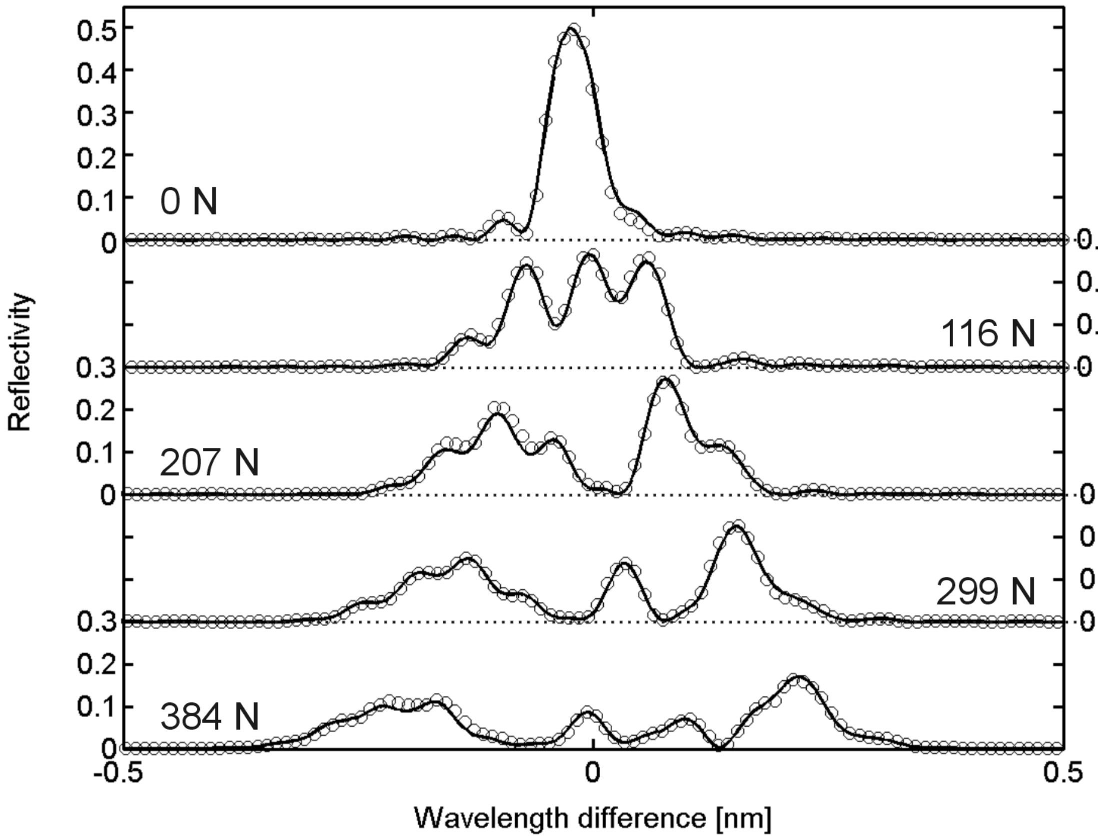

Fig. 5-9 Spectral intensity response calculated from the OLCR response (solid lines) and directly measured with a tunable laser (circles); the wavelength difference origin corresponds to the average Bragg wavelength $\lambda_{mc}(F)$

The Fig. 5-9 presents the spectral intensity response obtained for various loading forces (0 N corresponds to the measurement after the loading process and the relaxation rest). The wavelength difference is calculated from the average Bragg wavelength $\lambda_{mc}(F)$. A very good agreement is observed between the spectral responses calculated from the OLCR data and measured with a tunable laser. The maximal reflectivity is two third smaller at 384 N than without load, while at the same time, the spectral range is broadened by factor of 3.5.

5.1.5 Reconstruction of the complex coupling coefficient

The reconstruction of the complex coupling coefficient has been performed with the layer-peeling algorithm using 5 μm layer thickness and a design period corresponding to $\lambda_{cm}(F)$.

It is observed in Fig. 5-10 (top) that the applied strain field does not perturb the coupling coefficient amplitude. This is expected as the coupling coefficient amplitude is only related to the refractive index modulation amplitude and effective refractive index and these parameters are not significantly modified (0.22 % of relative variations). The local variations of the refractive index modulation amplitude are well determined and the reproducibility between the different measurements is very good.

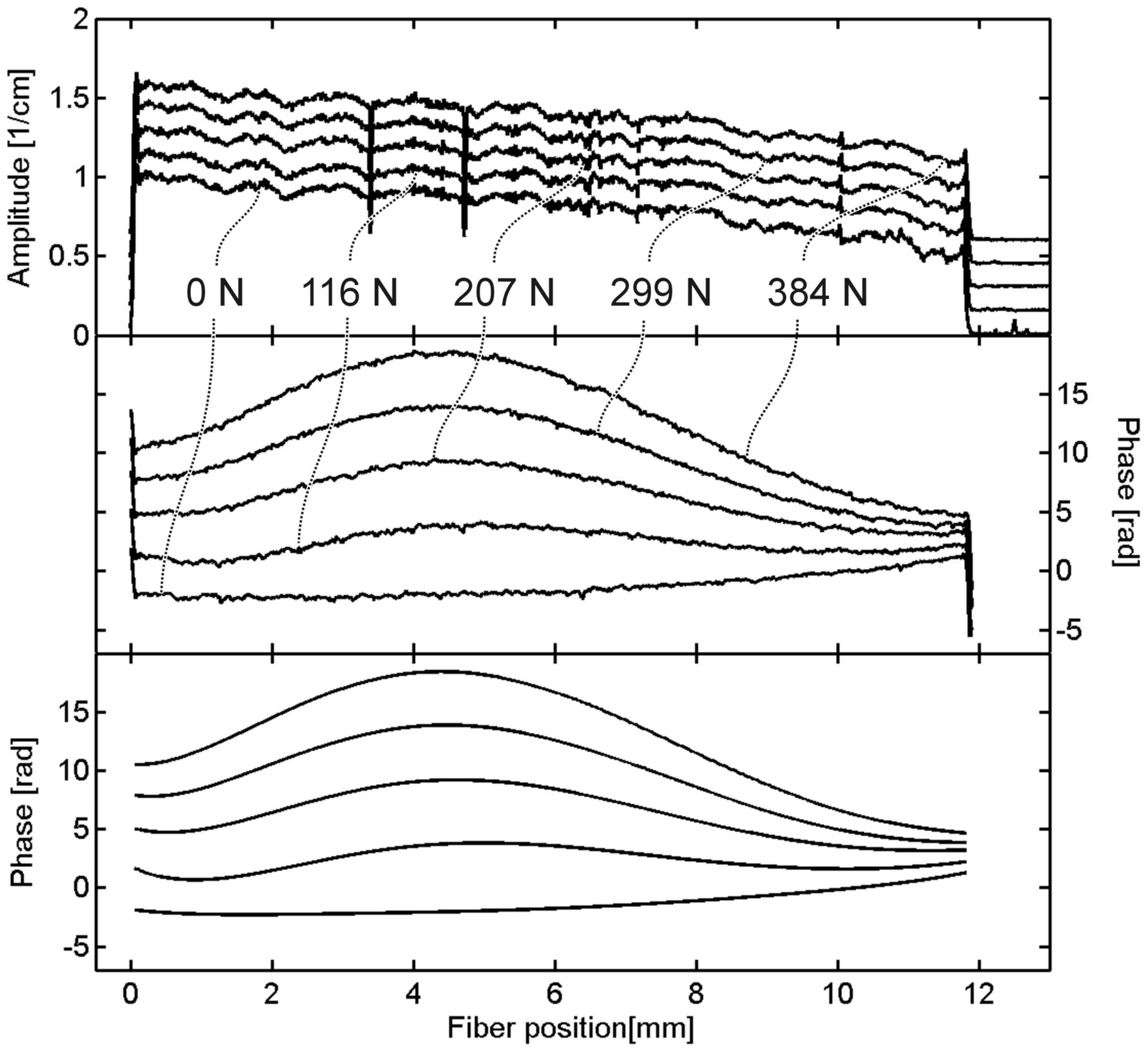

Fig. 5-10 Coupling coefficient amplitude (top), phase (middle) and phase polynomial fit at the 6th order (bottom) retrieved using the layer-peeling method; the design wavelength corresponds to the Bragg wavelength obtained from the frequency mass center; the curves are shifted to enhance the visibility

In the case of axial stress fields, we have seen in equation (5-6) that the stress is proportional to the relative Bragg wavelength change. In non-homogeneous axial strain fields, the effective Bragg wavelength distribution $\lambda_{eff}(z)$ is used and can be related to the coupling phase distribution ϕ_q (Fig. 5-10 middle) from equation (3-19) (where $\Lambda_d = \lambda_{mc}/2n_{eff}$)

$$\lambda_{eff}(z) = \left(\frac{1}{\lambda_{mc}} + \frac{1}{2\pi \cdot 2n_{eff}} \cdot \frac{d\phi_q(z)}{dz} \right)^{-1} \tag{5-8}$$

where n_{eff} is the effective refractive index (n_{eff} = 1.45 in this experiment).

A polynomial fit to the 6th order is performed on ϕ_q to reduce the local variations effects in the derivative operation needed to obtain λ_{eff} (Fig. 5-10 bottom).

The local Bragg wavelength is presented in Fig. 5-11 (left) and the difference with $\lambda_{mc}(F)$ in the right part. The polynomial fitting of the coupling coefficient phase shows larger errors at the extremities that are amplified by the derivative process. This explains that the first and last millimeter of the grating has been plotted in gray in the Bragg wavelength difference to indicate not well-defined values. We observe that the position in the fiber of the minimal Bragg wavelength difference (corresponding to the sample center) is displaced by 600 μm from 384 to 116 N. This could indicate a non-symmetric loading.

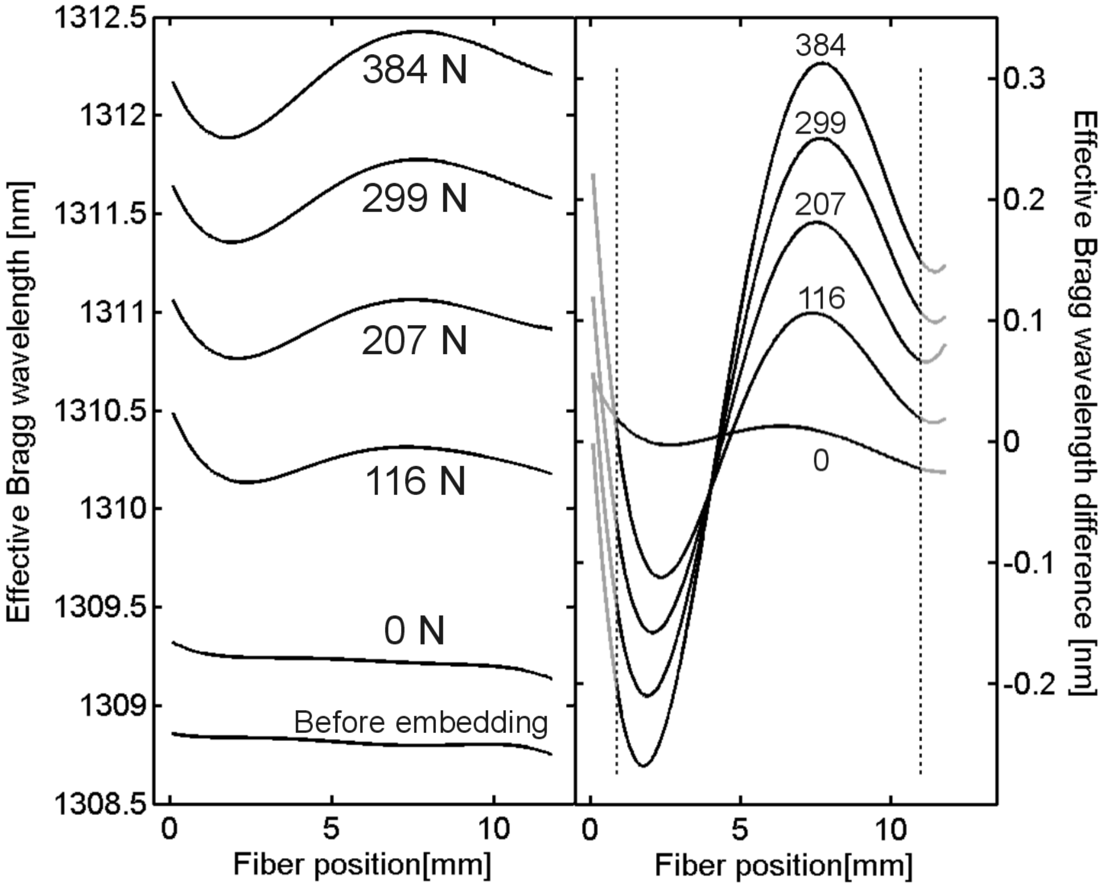

Fig. 5-11 Effective Bragg wavelength distribution (left) and effective Bragg wavelength difference with the average Bragg wavelength obtained from the frequency mass center (right)

From equation (5-6), the axial strain distribution $e_z(z)$ can be deducted from the effective Bragg wavelength

$$e_z(z,F) = \frac{1}{1-p_e} \cdot \left(\frac{\lambda_{eff}(z,F) - \lambda_{cm}(F)}{\lambda_{cm}(F)} \right) \tag{5-9}$$

5.1.6 Finite element simulations

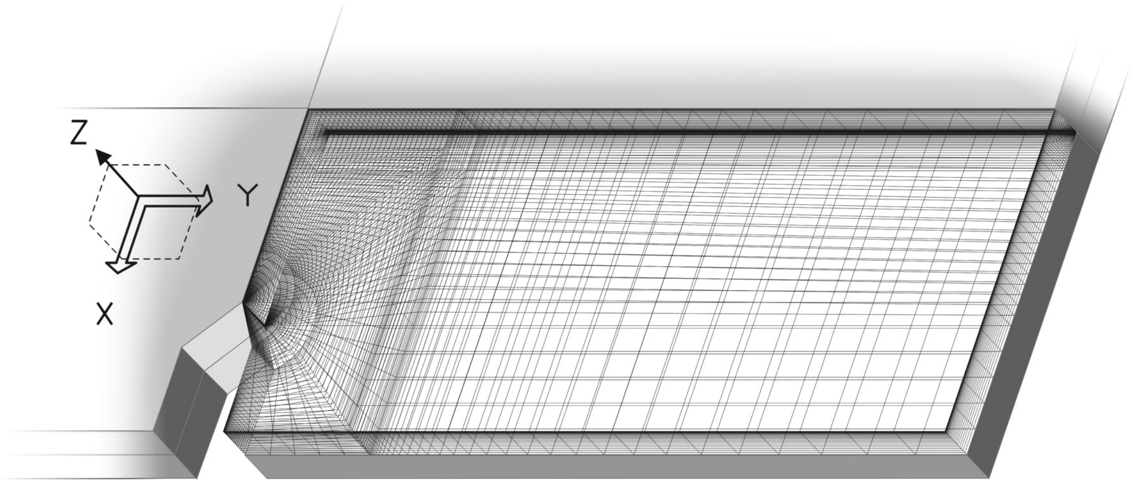

Fig. 5-12 Finite Element mesh used for the simulations

This experiment has also been simulated with the finite elements technique. The mesh definition and the calculations have been performed by Dr. Laurent Humbert (LMAF, EPFL). We present in Fig. 5-12 the defined mesh, where only one eighth of the sample has been considered due to the symmetry properties of the sample (adding limits conditions). The mesh density is increased near and inside the fiber region and near the notch region.

The linear behavior of the sample to axial stress loading allows defining a normalized strain distribution f(z) at the fiber core location

$$f\left(z\right)=\frac{e_z\left(z,F\right)}{e_z\left(L,F\right)} \tag{5-10}$$

This normalized strain function is presented in Fig. 5-13 (top). From equation (5-9), we have the experimental axial strain distribution $e_{z,b}(z)$ for $z \in [-1.4\ ,\ 9.1]$. In this range, the minimal strain $e_{z,b}(z = 0)$ can be used with the normalized value at the origin $f(z = 0) = 1.0476$ to calculate the finite element simulation axial strain distributions for the different loading cases. These simulations are presented in Fig. 5-13 (bottom).

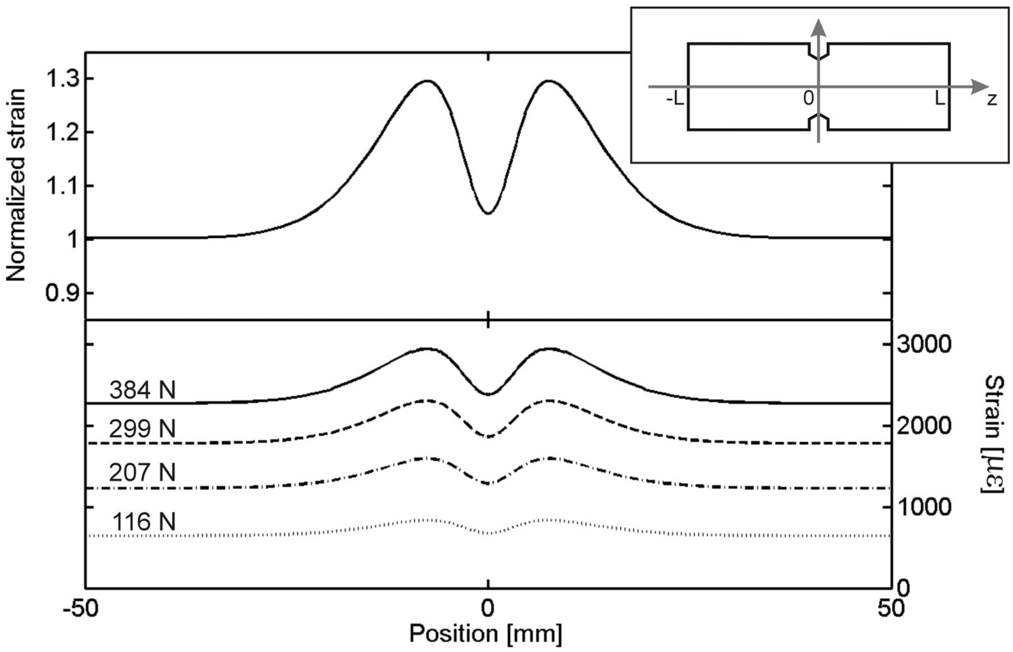

Fig. 5-13 Normalized strain distribution along the fiber (top) and axial strain distributions for the four loading cases (bottom)

The comparison with the experimental axial strain distributions is shown in Fig. 5-14. An overall agreement is observed but the position scale between experimental and calculated strains does not match well. This effect is not explained yet and further investigations on the finite element simulations are currently conducted.

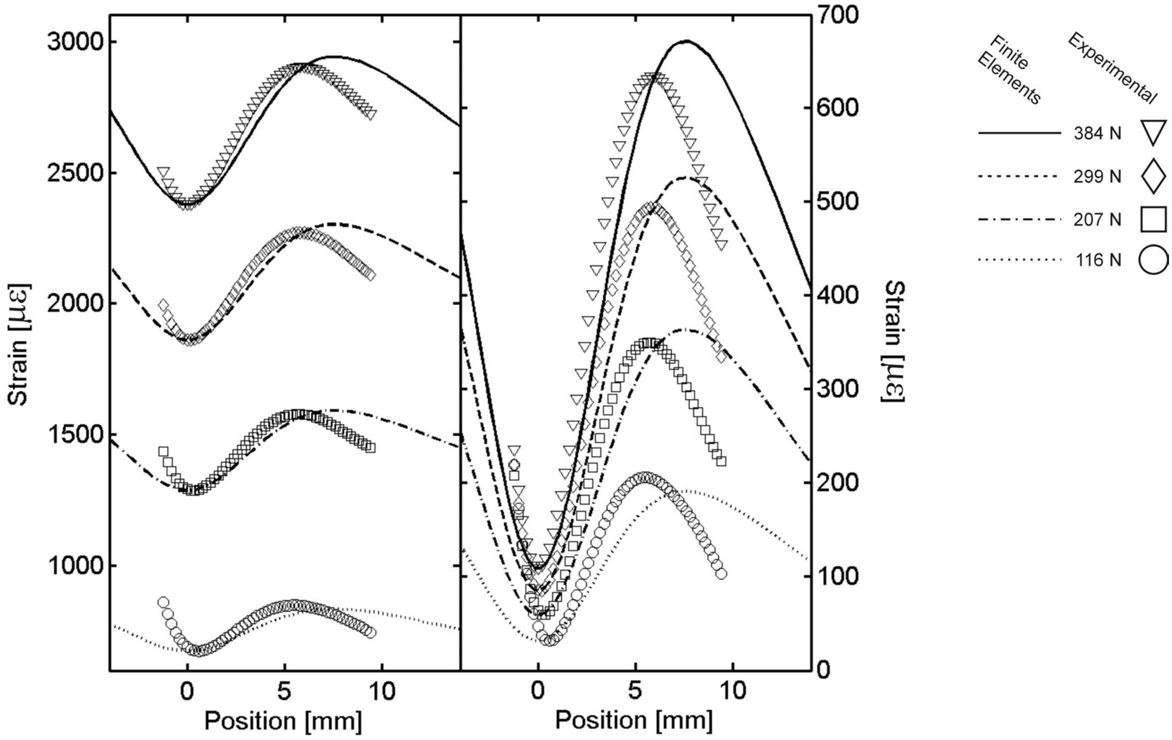

Fig. 5-14 Left : axial strain distributions for different axial stress loading forces and right : difference with the axial strain value at $z = L$; the discrete points represent the experimental results from the OLCR measurements and the lines represent the calculated values obtained with the finite element method

5.1.7 Conclusion

The results of this preliminary experiment are fairly good as the strain distribution is obtained along the grating (except for a little part less than 1 mm at each grating sides). Nevertheless, the applied loads were very high, inducing plastic deformations of the epoxy sample. This explains some unwanted side effects as the offset in the average strain. Further work will include improved finite elements simulations and other measurements performed in quasi-static states for lower load force values.

5.2 Characterization of a Fiber Bragg Grating under Diametric Loading

5.2.1 Introduction

When uniform transverse stresses are applied to a FBG gauge (Fig. 5-15), the refractive index becomes non-uniform in the transverse plane of the fiber. This leads to birefringence. The Bragg wavelength condition splits in two solutions, one for each refractive index along the fast and slow axis of the fiber

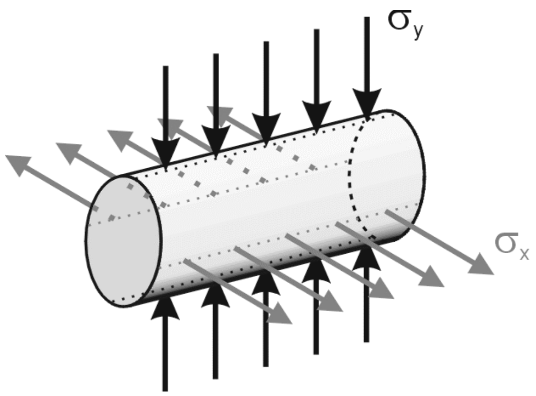

Fig. 5-15 :
Transverse Stresses

$$\begin{cases} \lambda_{B,fast} = 2 \cdot n_{fast} \cdot \Lambda \\ \lambda_{B,slow} = 2 \cdot n_{slow} \cdot \Lambda \end{cases} \tag{5-11}$$

where $\lambda_{B,i}$: Bragg wavelength for the fast and slow axis
Λ : FBG period
n_i : Refractive index of the fast and slow axis

If the fiber has a natural birefringence due to internal stresses included during the fiber preform fabrication, the birefringence due to loading can enhance or remove the natural birefringence of the fiber. If the transverse strains induce an axial deformation of the fiber, the Bragg wavelengths equations above need to be adapted.

Several articles report on experiments of transverse stresses applied to optical fiber. For example Wagreich et al [5-11] have conducted diametric load experiments on low-birefringent fiber. Good agreement between the proposed theory and experimental results were obtained. Lawrence, Nelson, and Udd [5-12, 5-13] performed similar work but in a polarization maintaining (PM) fiber. In this case, the proposed theory was unable to explain the experimental results.

Since we are interested in utilizing FBG's written in PM fibers in composite structures for monitoring transverse stresses, we need to characterize the FBG gauge when placed in a transverse stress field. A diametric loading technique has also been chosen to investigate FBG response in low and high-birefringent fibers. A simple theoretical model is proposed that explains also the results of FBG in high-birefringent fibers.

5.2.2 Experimental Setup

The mechanical setup allows for the application of uniform diametric load on an optical fiber and permits the reproducible rotation of the fiber around its axis. Fig. 5-16 shows the setup without the rotation system. The ball situated between the lever and the upper glass/steel part, ensures the transmission of a uniform force on both fibers from the suspended mass. Two fibers are used to ensure a perfect uniform loading.

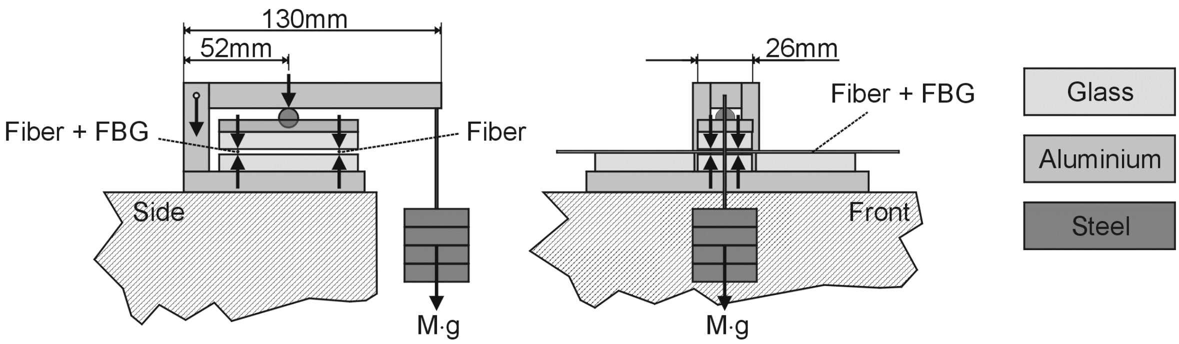

Fig. 5-16 : Side and Front view of the setup

The rotation system is based on a fiber magnetic clamp holder (insert of Fig. 5-17). The angle between the diametric load and the fiber is set with the metal handle that follows the angle graduation written on the white half-disk (Fig. 5-17).

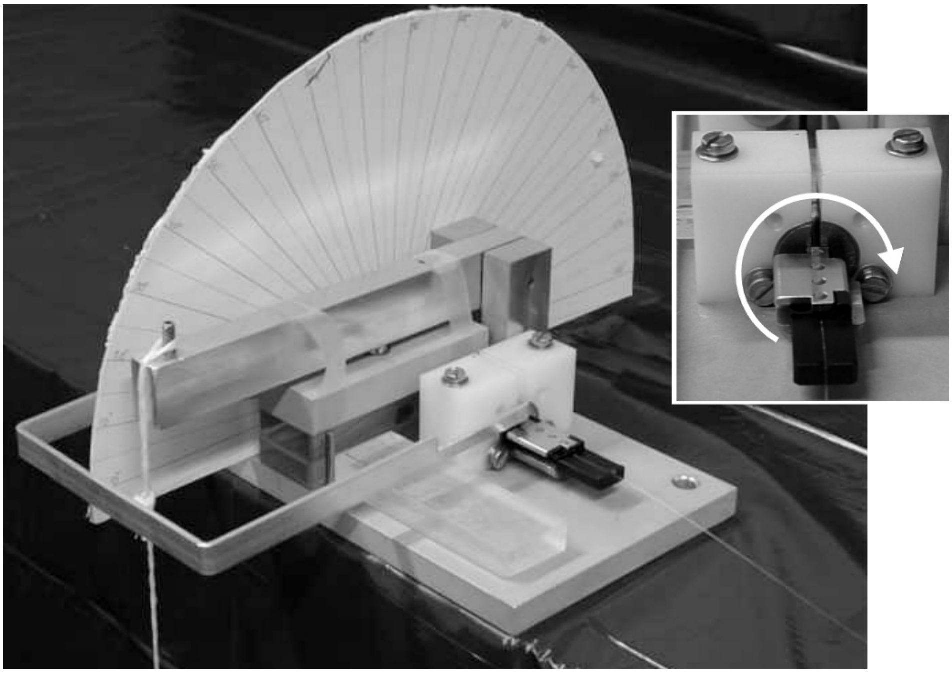

Fig. 5-17 : Pictures of the experimental setup for diametric load (insert : rotation system)

The optical setup for Bragg wavelength measurement in transmission is presented in Fig. 5-18. Another configuration in reflection using a 3 dB coupler has also been realized. Using a linearly polarized tunable laser and a polarization controller, each polarization mode can be measured separately.

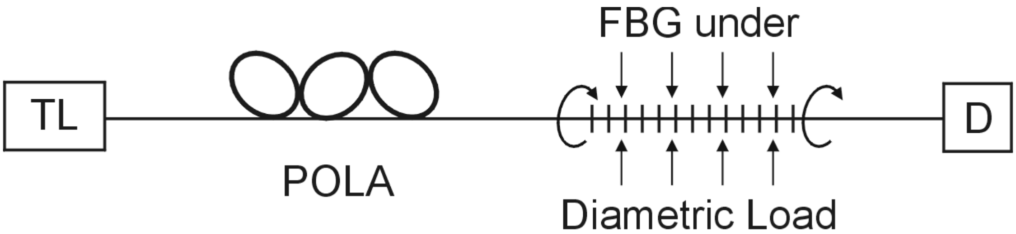

Fig. 5-18 : Transmission setup for Bragg wavelength measurement; TL : tunable laser, POLA : polarization controller, D : detector

5.2.3 Diametric Load of low-birefringent fiber

The model used to simulate the response of a FBG written in a low-birefringence fiber is based on the following hypotheses:

- The applying region of diametric load is longer than the FBG length, then the state of strain can be said Plane-strain (no deformation in the direction of the fiber axis)
- No shear stress
- The fiber is mechanically homogeneous, isotropic and the deformations are elastic (linearity between stresses and strains)
- The core fiber is dielectric, isotropic, homogeneous and non dispersive

From the Bragg wavelength equation, the variation of Bragg wavelength is

$$\lambda_{B,i} = 2 \cdot n_{i,eff} \cdot \Lambda \quad \Rightarrow \quad \frac{\Delta\lambda_{B,i}}{\lambda_{B,i}} = \frac{\Delta n_{i,eff}}{n_{i,eff}} + \frac{\Delta\Lambda}{\Lambda} = \frac{\Delta n_i}{n_i} + \frac{\Delta\Lambda}{\Lambda} \tag{5-12}$$

where

$\lambda_{B,i}$: Bragg wavelength for the fast and slow axis
$n_{i,eff}$: Effective refractive index of the fast and slow axis directions

n_i : Refractive index of the core fiber in the fast and slow axis directions
Λ : FBG period

The geometrical variation $\Delta\Lambda/\Lambda$, which correspond to the deformation along the Z axis, is zero due to the Plane-strain hypothesis. Then

$$\lambda_{B,i} = \lambda_{B,i,0} + \Delta\lambda_{B,i} = \lambda_{B,i,0} \cdot \left(1 + \frac{\Delta n_i}{n_i}\right) \tag{5-13}$$

In the reference where the inverse dielectric permeability tensor ε^{-1} is diagonal :

$$\varepsilon_{ij}^{-1} = \begin{pmatrix} \varepsilon_x^{-1} & 0 & 0 \\ 0 & \varepsilon_y^{-1} & 0 \\ 0 & 0 & \varepsilon_z^{-1} \end{pmatrix} = \begin{pmatrix} 1/n_x^2 & 0 & 0 \\ 0 & 1/n_y^2 & 0 \\ 0 & 0 & 1/n_z^2 \end{pmatrix} \quad \Rightarrow \quad \Delta\varepsilon_i^{-1} = \Delta\left(\frac{1}{n_i^2}\right) \cong -2\frac{\Delta n_i}{n_i^3} \tag{5-14}$$

and then

$$\begin{pmatrix} \Delta\varepsilon_x^{-1} \\ \Delta\varepsilon_y^{-1} \\ \Delta\varepsilon_z^{-1} \end{pmatrix} = \begin{pmatrix} P_{11} & P_{12} & P_{12} \\ P_{12} & P_{11} & P_{12} \\ P_{12} & P_{12} & P_{11} \end{pmatrix} \cdot \begin{pmatrix} e_x \\ e_y \\ e_z \end{pmatrix} \quad \text{and} \quad \begin{cases} e_x = \dfrac{1+\nu}{E} \cdot \left[(1-\nu)\cdot\sigma_x - \nu\cdot\sigma_y\right] \\ e_y = \dfrac{1+\nu}{E} \cdot \left[(1-\nu)\cdot\sigma_y - \nu\cdot\sigma_x\right] \end{cases} \tag{5-15}$$

where

ε^{-1}_{ij} : Dielectric permeability tensor
n_i : Refractive index of the fast and slow axis directions
P_{ij} : Strain-optic tensor
ε_i : Strain
S_{ij} : Elasticity tensor ($S_{11}=1/E$ and $S_{12}=-\nu/E$)
σ_i : Stress
E : Young Modulus
ν : Poisson Ratio

The relative Bragg wavelength sensitivity depends on light polarization and might be different in the x and y direction. Combining the equations above the variation of Bragg wavelength is given by

$$\begin{pmatrix} \Delta\lambda_{B,x}/\lambda_{B,x} \\ \Delta\lambda_{B,y}/\lambda_{B,y} \end{pmatrix} = \begin{pmatrix} \Delta n_x/n_x \\ \Delta n_y/n_y \end{pmatrix} = -\frac{n_0^2}{2}\begin{pmatrix} P_{11} & P_{12} \\ P_{12} & P_{11} \end{pmatrix} \cdot \frac{1+\nu}{E}\begin{pmatrix} 1-\nu & -\nu \\ -\nu & 1-\nu \end{pmatrix} \cdot \begin{pmatrix} \sigma_x \\ \sigma_y \end{pmatrix} \tag{5-16}$$

The relation between σ_i and e_i are derived from the general case and the hypothesis of Plain Strain ($e_z = 0$). In the last equation, n_x and n_y are approximated by n_0.

For the diametric load of an optical fiber, the core is small regarding the fiber diameter, therefore the stress should be uniform in the core and equal to the stress at (x,y)=(0,0) (Fig. 5-19) [5-14]:

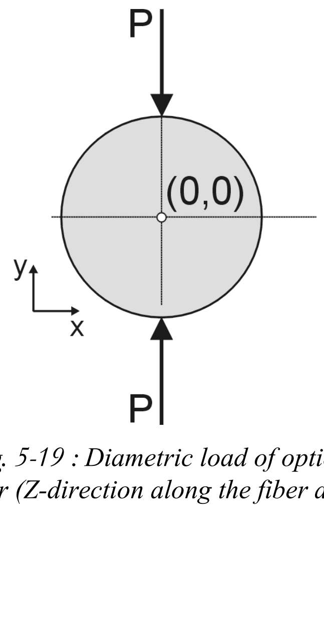

Fig. 5-19 : Diametric load of optical fiber (Z-direction along the fiber axis)

$$\begin{cases} \sigma_x = \dfrac{2P}{\pi t d} \\ \sigma_y = \dfrac{-6P}{\pi t d} \\ \tau_{xy} = 0 \end{cases} \tag{5-17}$$

where

d : Fiber diameter
R : Fiber radius
t : Length of diametric applying region
P : Diametric load in N (P/t is the line load density)

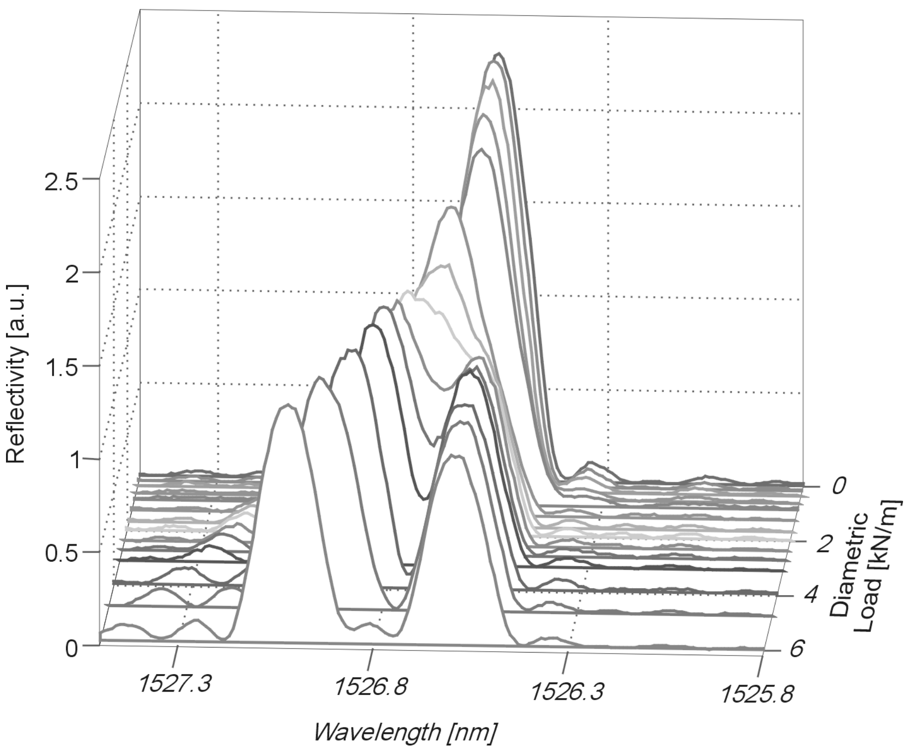

Fig. 5-20 FBG reflectivity under diametric load from 0 N to 155 N.

Fig. 5-20 shows the experimental results for a low-birefringence fiber under diametric load. Each curve represents two measurements for a given load applied on a length of 26 mm. Each spectrum is the superposition of the two independent polarization measurements. There is no initial birefringence. For small diametric load both modes are degenerated. For higher values the two modes are clearly separated. For 155 N the separation is about 0.45nm.

Fig. 5-21 shows the measured and calculated peak reflectivity as a function of applied load for the two polarization modes. The wavelength changes are strongly different for the two modes. Slow and fast axis have sensitivities of 31.0 10^{-4} and –1.36 10^{-4} nm/N. A very good agreement between experimental and calculated values is observed.

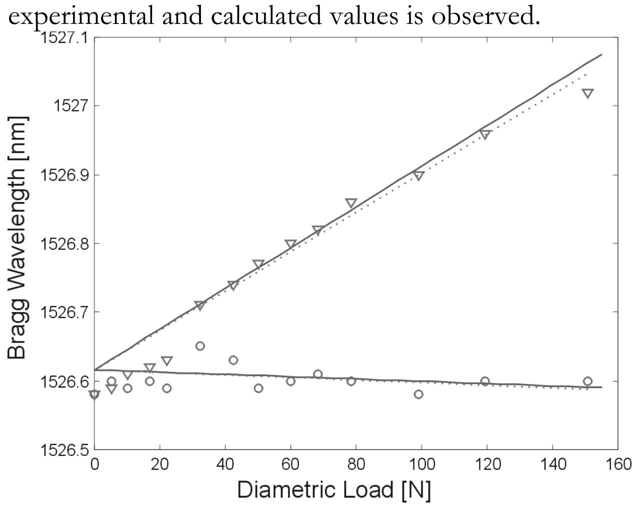

Fig. 5-21 *FBG Bragg wavelength under diametric load; circles or triangles: experimental data; solid line: calculated values*

In Fig. 5-21 the following values have been taken [5-15, 5-16] for the theoretical model:

$P_{11} = 0.113$
$P_{12} = 0.252$
E = 64.1 Gpa
$\nu = 0.16$
d = 125 μm
t = 26 mm
$\lambda_{B,0} = 1526.616$ nm
$n_0 = \lambda_{B,0} / 1058.5 = 1.442245$

5.2.4 Diametric Load of Polarization Maintaining Fiber

Diametric load has also been applied on FBG written in a PM fiber where a natural birefringence exists. The stress state in the fiber core, σ, is assumed to be the superposition of stress due to the natural birefringence, $\hat{\sigma}$, and diametric load $\tilde{\sigma}$. The natural PM fiber birefringence is described with a

Plane Stress, Plain Strain model. Two distinct materials compose the fiber: Silica and borosilicate in the stress-inducing region (like the "Bow-Ties" for the used fiber). These two materials have different mechanical properties (E and ν), therefore the fiber exhibits anisotropic mechanical behavior when stress is applied on the fiber surface. Even if the fiber core is isotropic, the resulting stresses at the fiber core for an external diametric load vary with the angle of applying load direction. The stress σ' is a function of the load P and the angle θ. To model the diametric load effect, we assume small external load leading to effective stresses.

The natural fiber birefringence, described with $\hat{\sigma}$, is in the principal axis system given by

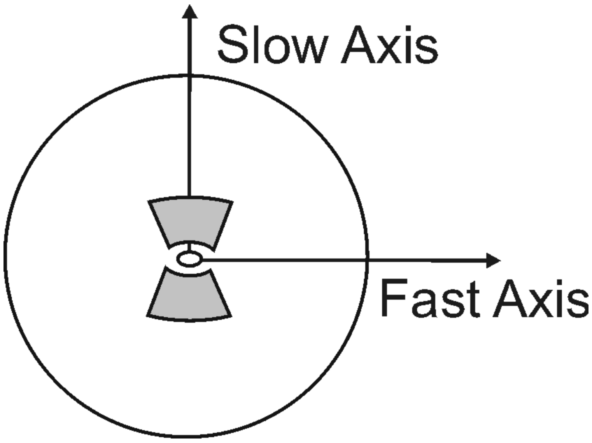

$$\hat{\boldsymbol{\sigma}} = \begin{pmatrix} -\dfrac{D_p}{\pi d} & 0 \\ 0 & \dfrac{D_p}{\pi d} \end{pmatrix} \qquad (5\text{-}18)$$

Fig. 5-22 : Polarization maintaining fiber geometry

In the PM fiber used, the natural birefringence is due to stress applying region in "Bow-Tie" shape (Fig. 5-22). In this case only one parameter D_p is needed to describe the natural birefringence. Using the low-birefringent fiber model, an equation for D_p is found for the case where the diametric load P=0

$$D_p = \frac{E\pi d\left[\left(\lambda_{B,x}\right)_{P=0} - \left(\lambda_{B,y}\right)_{P=0}\right]}{n_0^2\left(1+\nu\right)\lambda_{B,0}\left(P_{12} - P_{11}\right)} \qquad (5\text{-}19)$$

For a birefringence of 0.42nm at 1533.3nm, D_p = 21.5 kN/m.

The diametric load P is applied in a direction y' forming an angle θ with the y-axis (Fig. 5-23). The stresses are described by a matrix $\tilde{\boldsymbol{\sigma}}'$:

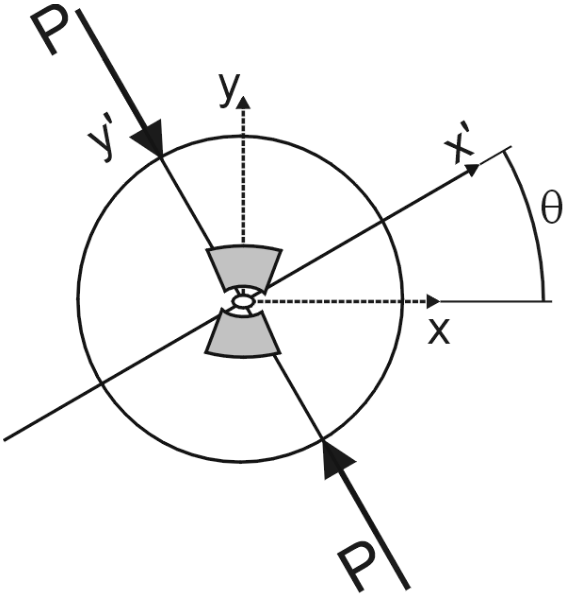

$$\tilde{\boldsymbol{\sigma}}' = \begin{pmatrix} \dfrac{2P}{\pi t d} & 0 \\ 0 & \dfrac{-6P}{\pi t d} \end{pmatrix} \qquad (5\text{-}20)$$

Fig. 5-23 : Diametric load on PM Fiber

$\tilde{\boldsymbol{\sigma}}'$ has to be transposed in $\tilde{\boldsymbol{\sigma}}_0$ in the (X,Y) reference using the rotation matrix $\mathbf{R}(\theta)$:

$$\tilde{\boldsymbol{\sigma}}_0 = \mathbf{R}^{-1}(\theta)\times\tilde{\boldsymbol{\sigma}}'\times\mathbf{R}(\theta) \tag{5-21}$$

We define effective stress tensor as $\tilde{\boldsymbol{\sigma}} = \boldsymbol{\alpha}\times\tilde{\boldsymbol{\sigma}}_0$, where the matrix $\boldsymbol{\alpha}$ considers the fiber specific anisotropy and is assumed to be independent on external load. In addition we assume that the stresses in the X and Y direction are much bigger than the shear stress. Therefore effective stresses in the X, Y directions are independent of the shear stress (α_{ij} =0). In addition we assume that the diagonal elements are independent of angle θ. $\tilde{\boldsymbol{\sigma}}$ becomes:

$$\tilde{\boldsymbol{\sigma}} = \boldsymbol{\alpha}\times\tilde{\boldsymbol{\sigma}}_0 = \begin{pmatrix}\alpha_1 & 0\\ 0 & \alpha_2\end{pmatrix}\times\tilde{\boldsymbol{\sigma}}_0 \tag{5-22}$$

The global stress state $\boldsymbol{\sigma}$ in the core of the fiber and in the (X, Y) reference is the superposition of the natural birefringence stress state $\hat{\boldsymbol{\sigma}}$ and the stress state due to diametric load $\tilde{\boldsymbol{\sigma}}$:

$$\boldsymbol{\sigma} = \hat{\boldsymbol{\sigma}} + \tilde{\boldsymbol{\sigma}} \tag{5-23}$$

If the angle θ is different from k·π/2, the shear stress τ_{xy} is not zero. In this case the secondary principal stresses $(p',q')_z$ for the light propagating in the Z direction in the fiber core have to be calculated [5-14]

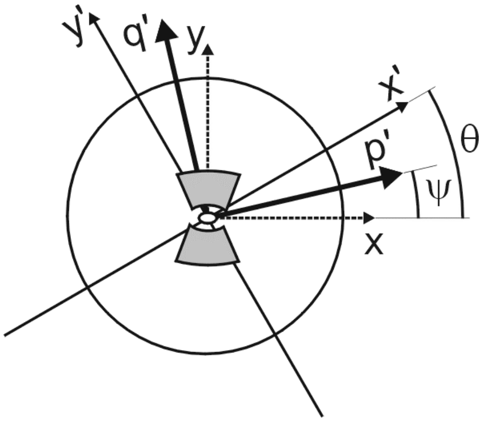

Fig. 5-24 : Reference (X,Y) of the fiber, (X',Y') of the diametric load, (p',q') of the secondary principal stresses

$$\begin{cases}(p',q')_z = \dfrac{\sigma_x+\sigma_y}{2}\pm\dfrac{1}{2}\sqrt{4\tau_{xy}+\left(\sigma_x-\sigma_y\right)^2}\\ \tan(2\psi) = \dfrac{2\tau_{xy}}{\sigma_x-\sigma_y}\end{cases} \tag{5-24}$$

where ψ : Angle between the X axis and the p' axis (Fig. 5-24)

Due to equation ((5-24), PM fibers subjected to transversal loads display a different behavior with respect to isotropic fibers. Namely, the relationship between the applied transversal strains ε_x and ε_y and the measured Bragg wavelength shifts is not necessarily linear, except when the strains are directed along the symmetry axes of the fiber. This theoretical development explains the experimental non-linearity observed in other works but not understood until now [5-17].

The hypothesis of fiber core isotropy and Plane Strain are also valid, then the model developed for the low-birefringent fiber can be applied, but with the secondary principal stresses (p',q') instead of σ.

$$\begin{pmatrix}\Delta\lambda_{B,x}/\lambda_{B,x}\\ \Delta\lambda_{B,y}/\lambda_{B,y}\end{pmatrix} = c\cdot\begin{pmatrix}P_{11} & P_{12}\\ P_{12} & P_{11}\end{pmatrix}\cdot\begin{pmatrix}1-\nu & -\nu\\ -\nu & 1-\nu\end{pmatrix}\cdot\begin{pmatrix}p'\\ q'\end{pmatrix}$$

$$c = -\frac{n_0^2}{2}\cdot\frac{1+\nu}{E} \tag{5-25}$$

The variation ζ_i of the Bragg wavelength with the applied load is

$$\begin{pmatrix}\zeta_x\\ \zeta_y\end{pmatrix}=\frac{\partial}{\partial P}\begin{pmatrix}\Delta\lambda_{B,x}/\lambda_{B,x}\\ \Delta\lambda_{B,y}/\lambda_{B,y}\end{pmatrix}=c\cdot\underbrace{\begin{pmatrix}\lambda_{B,x} & 0\\ 0 & \lambda_{B,y}\end{pmatrix}}_{\boldsymbol{\lambda}}\cdot\underbrace{\begin{pmatrix}P_{11} & P_{12}\\ P_{12} & P_{11}\end{pmatrix}}_{\mathbf{P}}\cdot\underbrace{\begin{pmatrix}1-\nu & -\nu\\ -\nu & 1-\nu\end{pmatrix}}_{\boldsymbol{\nu}}\cdot\begin{pmatrix}\partial p'/\partial P\\ \partial q'/\partial P\end{pmatrix} \tag{5-26}$$

For θ=0° or 90° $p'=\sigma_x=\hat{\sigma}_x+\tilde{\sigma}_x$ and $q'=\sigma_y=\hat{\sigma}_y+\tilde{\sigma}_y$, and is therefore independent of the natural fiber birefringence. Since $\hat{\boldsymbol{\sigma}}$ is independent of the load P the variation of the secondary principal stresses with external load is given by

$$\begin{pmatrix}\partial p'/\partial P\\ \partial q'/\partial P\end{pmatrix}_{0°,90°}=\begin{pmatrix}\partial\tilde{\sigma}_x/\partial P\\ \partial\tilde{\sigma}_y/\partial P\end{pmatrix}=\begin{pmatrix}\alpha_1\cdot\partial\tilde{\sigma}_{0,x}/\partial P\\ \alpha_2\cdot\partial\tilde{\sigma}_{0,y}/\partial P\end{pmatrix}=\begin{pmatrix}\partial\tilde{\sigma}_{0,x}/\partial P & 0\\ 0 & \alpha_2\cdot\partial\tilde{\sigma}_{0,y}/\partial P\end{pmatrix}\cdot\begin{pmatrix}\alpha_1\\ \alpha_2\end{pmatrix}=\frac{\partial}{\partial P}\tilde{\boldsymbol{\sigma}}_{\mathbf{0}}\cdot\begin{pmatrix}\alpha_1\\ \alpha_2\end{pmatrix} \tag{5-27}$$

Matrix inversion leads to

$$\begin{pmatrix}\alpha_1\\ \alpha_2\end{pmatrix}=\frac{1}{c}\cdot\left[\frac{\partial}{\partial P}\tilde{\boldsymbol{\sigma}}_{\mathbf{0}}\right]^{-1}\times\boldsymbol{\nu}^{-1}\times\mathbf{P}^{-1}\times\boldsymbol{\lambda}^{-1}\times\begin{pmatrix}\zeta_x\\ \zeta_y\end{pmatrix} \tag{5-28}$$

For the investigated fiber the following values are obtained:

$$\begin{cases}(\alpha_1,\alpha_2)_{0°}=(0.43\,;0.97)\\ (\alpha_1,\alpha_2)_{90°}=(0.51\,;1.08)\end{cases} \tag{5-29}$$

Fig. 5-25 shows experimental and calculated values of Bragg wavelength as a function of applied load for different angle, θ, between load direction and the principle axis of the fiber. Each graph represents the response along slow (p') and fast (q') fiber axis. The agreement between experiment and model is good for small load. The slope depends strongly on θ.

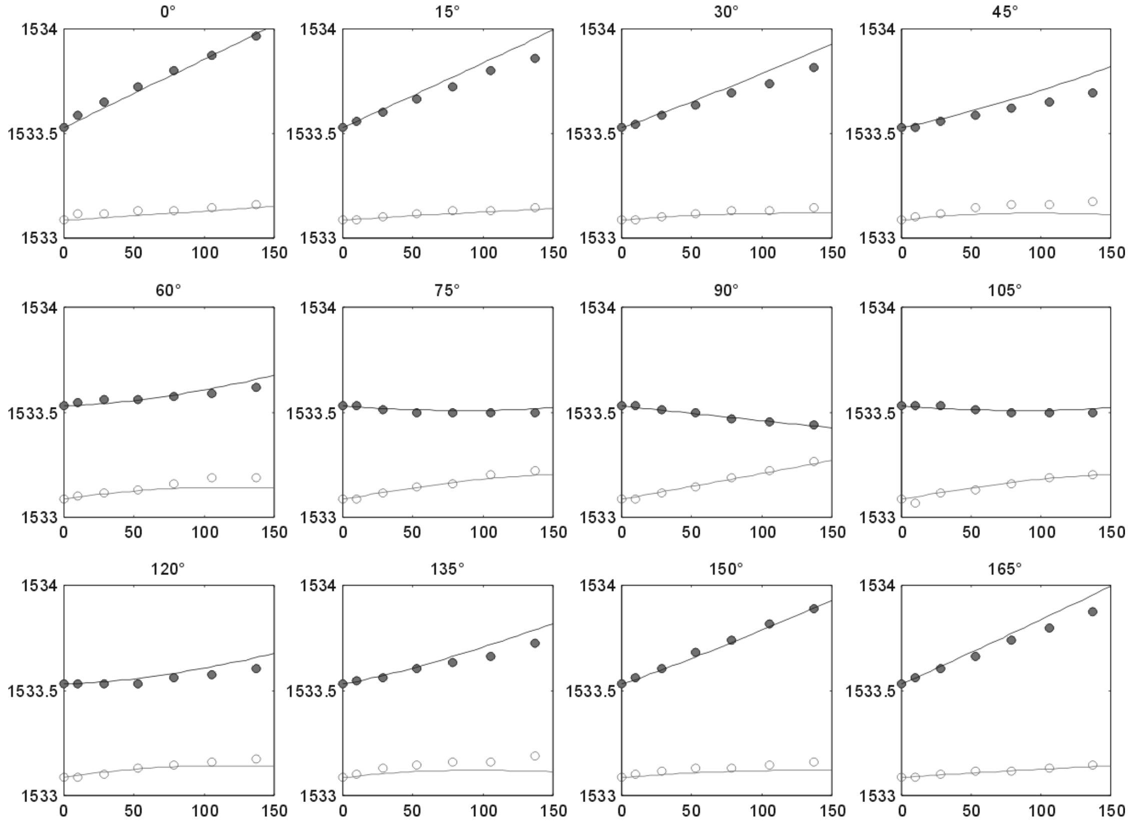

Fig. 5-25 Bragg wavelength of a FBG written in a PM fiber under diametric load for different angle of loading (x axis : diametric load [N] and y axis : Bragg wavelength [nm]).

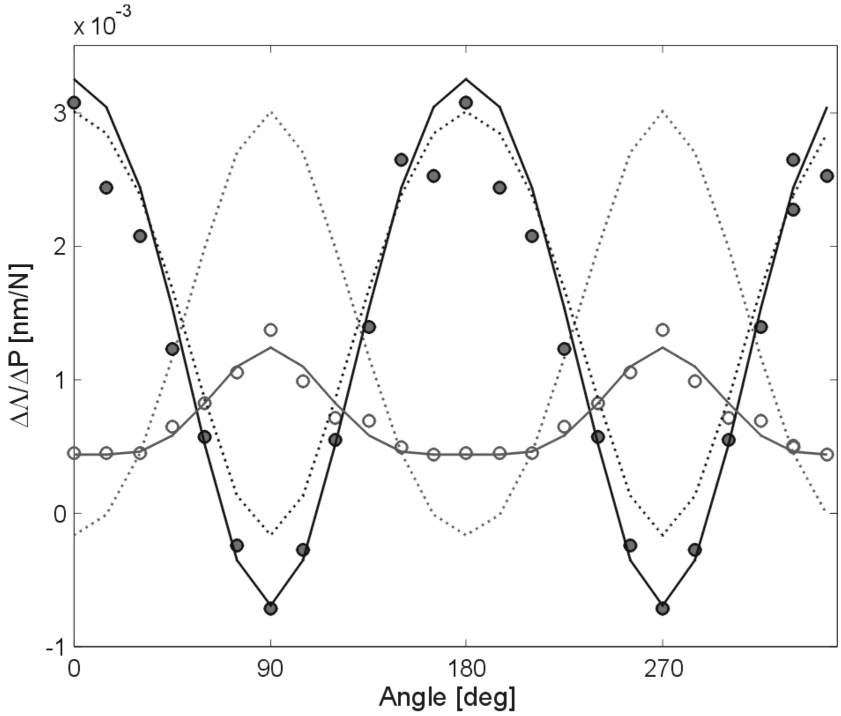

Fig. 5-26 Sensitivity of the FBG sensor for diametric load; circles(slow) and crosses(fast) are experimental values, dashed lines for (α_1,α_2)=(1,1) and solid line for (α_1,α_2)=(0.47,1.03).

Fig. 5-26 shows the measured slopes ζ_i, (FBG sensitivity) as a function of angle θ. Two theoretical cases are represented, for (α_1,α_2)=(1,1) and (α_1,α_2)=(0.47,1.03). It is clear that the stress field has to be modified using effective stresses to take into account the anisotropy of the fiber. The sensitivity is a periodic function of the angle (180° period) and the response of slow and fast axis are phase shifted by 90°. The model describes clearly the non-sinusoidal behavior of the experimental data in contrast to references [5-12, 5-13], which describe similar experimental results by a sinusoidal approach.

With the analytical model, it is possible to develop a demodulation algorithm to retrieve the stresses from Bragg wavelength variations. It has to be noticed that, if we consider the shear stresses in the (X,Y) plane, we have four unknowns : σ_x, σ_y, τ_{xy}, and θ. With two superimposed FBG's in a PM fiber, the complete state of stresses can be obtained.

5.2.5 Study on the PM fiber strain anisotropy sensitivity

An important work has been performed to find the physical origin that could explained the experimental strain anisotropy sensitivity observed in the diametric loading of a PM fiber. A finite element model of the PM fiber has been realized in the LMAF laboratory by Federico Bosia. The simulation of diametric load has been conducted to retrieve the strain field at the fiber core where the FBG is located. Using the material parameters provided by the manufacturer, a very small strain anisotropy is observed at the core location (less than 5 % compared to the isotropic fiber case). Other material parameters have been found in the literature and applied to the simulation. The found anisotropy is more important and explains partially the transverse stress sensitivity anisotropy of the FBG in PM fibers. The results presented hereafter are partly based on the joined-papers written in collaboration with the LMAF group [5-7, 5-8]. Nevertheless, it remains open questions to completely describe the behavior of FBG written in PM fibers subjected to transverse stress and further studies are required.

a) Finite element modelization

Due to the complex structure of the fiber in this case, finite-element-method (FEM) simulations need to be carried out to determine the strain distributions generated in the fiber core and derive numerical predictions to be compared with experimental measurements. In order to do this, the residual strains responsible for the initial birefringence of the fiber need to be estimated, and then the response to diametrical compression evaluated. The FEM simulations are performed using the I-DEAS code.

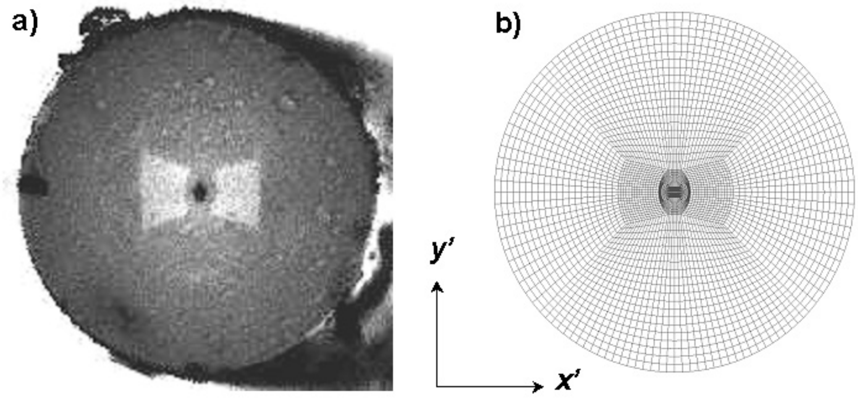

Fig. 5-27 Micrograph view of the PM fiber (a) and finite element mesh used for the simulations

Fig. 5-27a illustrates a micrograph of the PM-fiber section. The borosilicate bow ties are clearly visible. Based on this geometrical information and on manufacturer specifications, the 2-D FEM mesh is constructed (Fig. 5-27b). The diameter of the fiber is 125μm and that of the mode field is 9μm. The mesh correctly models the borosilicate bow ties (about 15x20μm) and the silica-glass core and cladding, and is refined in the central fiber-core region where strains are calculated [5-23]. A Young's modulus of E_B=67 GPa and a Poisson's ratio of ν_B=0.17 are used for borosilicate (data provided by Fibercore). As mentioned previously and as indicated in Fig. 5-28a, the coordinate axes parallel and perpendicular to the bow ties are indicated as x' and y', whilst those parallel and perpendicular to the loading direction are indicated with x and y.

b) Simulation of the natural birefringence and of the diametric load

The residual strains responsible for the birefringence are estimated assuming a linear elastic thermal loading problem. The approach is similar to that employed in [5-18]. Thermal expansion coefficients of α_B = 14x10^{-7}°C^{-1} and α_G = 5.5x10^{-7}°C^{-1} are used for borosilicate and silica glass, respectively (data provided by Fibercore). Simulations are performed using both plane-strain and plane-stress elements. The assumption that the resulting residual strains generated in this type of geometry are equal and opposite along the slow and fast axes, respectively, can thus be verified. The ratio between the two strains is found to be $\varepsilon_{R,1}/\varepsilon_{R,2}$ = -0.89, therefore the previous assumption can be modified and this correction, though small, accounted for in calculations.

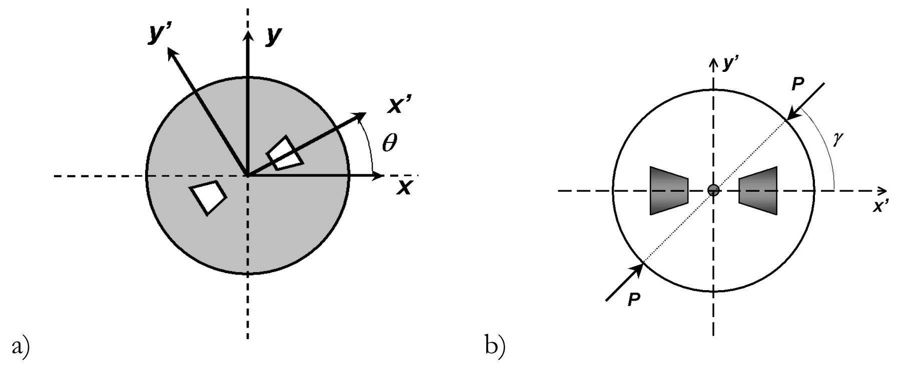

Fig. 5-28 Axes definition (a) and diametric load geometry (b)

Additionally, simulations are carried out to determine the strains generated in the fiber core by diametrical loads in the same loading range as that considered experimentally. The strains are determined as a function of loading angle γ (Fig. 5-28b). Due to the structure of the PM fiber, some anisotropy is expected, i.e. loading in the direction of the *x'*-axis in Fig. 5-28b should give smaller ε_1 strains than the ε_2 strains obtained when loading in the *y'*-direction. This is indeed the case, however, due to the small mismatch between the elastic properties of silica and borosilicate, this effect is found to be negligible. A difference of 5% at most is obtained with the strains calculated in a homogeneous isotropic fiber with no bow ties, as is the case for the standard SM fiber.

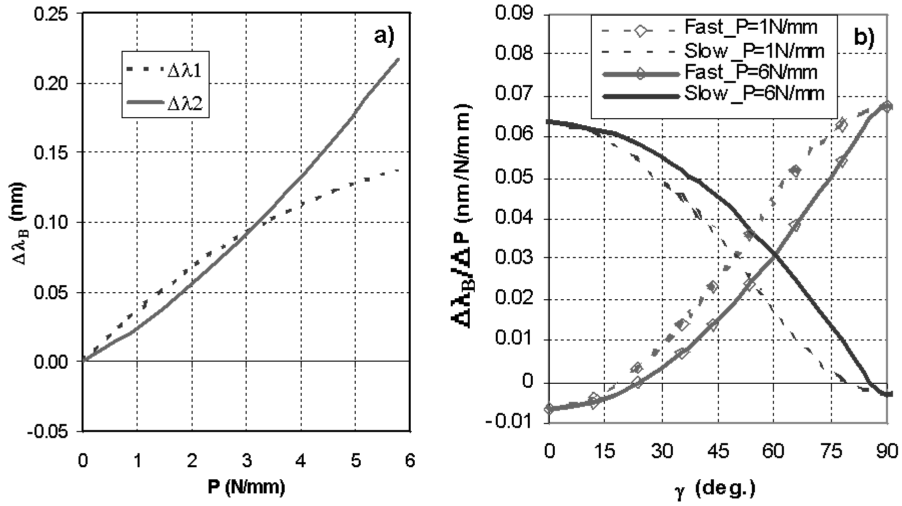

Fig. 5-29 Bragg wavelength deviation for an applied diametric load at an angle γ = 54° (a) and FBG diametric load sensitivity calculated by linear fit for different loading ranges (b)

Having calculated the strains in the fiber core as a function of loading angle γ, it is possible to highlight the influence of the initial birefringence of the PM fiber on the sensor response to transversal loading. Using the approach illustrated earlier, the expected Bragg wavelength shifts are calculated as a function of applied diametrical load for various loading angles. Whilst the response is linear when loading is directed along one of the polarization axes (γ =0° or γ =90°), this is no longer true for all other loading angles. For example, results are plotted for γ =54° in Fig. 5-29a : the nonlinearity in this case is evident. This is due to the load-dependent rotation, described by equation (5-24), of the principal axes with respect to the initial polarization axes. Thus, the response of a FBG sensor written in PM-fiber to transverse loads applied at an angle to the fast and slow axes is nonlinear, at least in the range where the strains due to loading are of the order of the residual strains generating the birefringence. This is also consistent with experimental results.

Due to this behavior, an error is introduced when an angular sensitivity per unit load is defined, as done in [5-13, 5-21], because the slope of the wavelength shift changes with the load. Figure Fig. 5-29b shows the numerically calculated sensitivities when the slopes are taken at P/l=1N/mm and P/l=6N/mm. In both cases, the sensitivities for the fast and slow axes are plotted. It is apparent that for increasing loads, a deviation from the expected sinusoidal behavior is obtained.

Furthermore, only a very small anisotropy is observed, i.e. the sensitivity is nearly identical when loading is directed along the slow axis at γ =0° and fast axis at γ =90°. This is not the behavior encountered experimentally. The experimental measurements indicate that in fact the fast axis is considerably less "sensitive" to diametrical compression, by a factor close to 2. These results are also obtained in similar experiments in the literature [5-21, 5-22]. The reasons for this mismatch between experimental and numerical results are thus far unclear. One possibility is a rather large uncertainty on material properties of borosilicate. For example, in references [5-18] and [5-13] a Young's modulus and Poisson's ratio of 50.8 GPa and 0.21 are used, respectively. These values differ considerably from those provided by the manufacturers of the fibers used in this study. Therefore, both sets of material parameters are used in FEM simulations, and results are compared.

Fig. 5-30 shows the experimentally measured and numerically calculated sensitivities as a function of the loading angle for P/l =1 N/mm. The numerical values are determined using both E_B=67 GPa and E_B=50 GPa. It is clear that a greater mismatch between the Young's moduli of silica and borosilicate improves the agreement between experimental and simulated results, however, a considerable discrepancy remains. Other possible explanations for this discrepancy are an oversimplified model for the loading configuration or the effect of a displacement of the grating location in the core with respect to the geometrical center of the fiber.

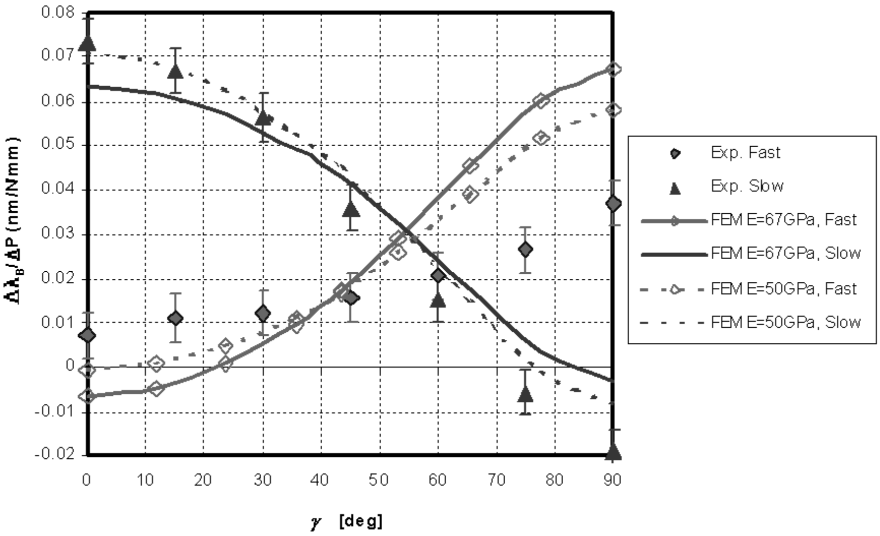

Fig. 5-30 Experimental FBG sensitivity to small diametric loading force and simulated sensitivity by finite elements for two sets of borosilicate material parameters

5.2.6 Conclusions

The analytical model developed to simulate the diametric load on FBGs correctly predicted the behavior of FBGs written in low-birifringent and the non-linear behavior of FBGs written in polarization maintaining fibers. Nevertheless, the anisotropic sensitivity to transversal strain fields observed experimentally for the gratings in PM fibers could not be completely explained, requiring further investigations.

5.3 References

5-1 M. Studer, J. Pietrzyk, K. Peters, J. Botsis, Ph. Giaccari, "*Studies on Bridging Tractions – Simultaneous Bridging Tractions and COD measurements*", International Journal of Fracture, Vol 114, pp. 379 (2002)

5-2 M. Studer, J.Pietrzyk, K. Peters, J. Botsis, Ph. Giaccari, "*Experimental and numerical studies on bridging tractions using embedded OFBG sensors*", Proceedings, MESOMECH (2000)

5-3 M. Studer, J. Pietrzyk, K. Peters, J. Botsis, Ph. Giaccari, H.G. Limberger, R. Salathe, "*Optical fiber Bragg grating applied to study bridging tractions*", Mesomechanics 2000, G.C. Sih, Vol 1, pp. 519 (2000)

5-4 F. Bosia, J. Botsis, M. Facchini, Ph. Giaccari, "*Deformation Characteristics of Composite Laminated, Part I: speckle interferometry and embedded Bragg grating Composite*", Science and Technology, Vol 62, pp. 41 (2002)

5-5 F. Bosia, G. Zambaz, M. Facchini, J. Botsis, Th. Gmür, Ph. Giaccari, "*Electronic Speckle Pattern Interferometry and Embedded Fibre Bragg Grating Sensors for Composite Plate Bending Measurements*". Proceedings of the SEM IX International Congress on Experimental Mechanics, Orlando, Society for Experimental Mechanics, Bethel, pp.147-150 (June 5-8 2000)

5-6 F. Bosia, G. Zambaz, M. Facchini, Th. Gmür, J. Botsis, Ph. Giaccari, "*ESPI and Embedded FBG Sensors for Composite Plate Bending Measurements*", Proceedings of the SEM IX International Congress on Experimental Mechanics, Orlando (June 5-8 2000)

5-7 F. Bosia, Ph. Giaccari, J. Botsis, M. Facchini, H.G. Limberger, R. Salathé, "*Characterization of fibre Bragg grating sensors subjected to 2-D strain fields*" (in preparation)

5-8 F. Bosia, Ph. Giaccari, M. Facchini, J. Botsis, H.G. Limberger, R. Salathe, "*Characterisation of embedded fibre Bragg grating sensors written in high-birefrigent optical fibres sebjected to transverse loading*", Smart Sensor Technology & Measurement Systems, SPIE, Vol 4694, pp. 175 (2002)

5-9 K. Peters, Ph. Pattis, J. Botsis, Ph. Giaccari, "*Experimental verification of response of embedded optical fiber Bragg grating sensors in non-homogeneous strain fields*", Journal of Optics and Lasers in Engineering, Vol 33, pp. 107 (2000)

5-10 K. Peters, Ph. Pattis, J. Botsis, Ph. Giaccari, "*Experimental verification of embedded optical fiber Bragg grating sensors in non-homogeneous strain fields*", Proceedings, International Conference on Trends in Optical Nondestructive Testing, pp.435-445 (May 2000)

5-11 R. Wagreich, W. Atia, H. Singh, J. Sirkis, "*Effects of diametric load on fiber Bragg gratings fabricated in low birefringent fiber*", Electronics Letters, 1996, Vol 32, No 13, pp. 1223-1224

5-12 C. Lawrence, D. Nelson, E. Udd, "*Multi-Parameter Sensing with Fiber Bragg Gratings*", SPIE, Vol 2872, 1996, pp. 24-31

5-13 C. Lawrence, D. Nelson, E. Udd, "*Measurement of transverse strains with fiber Bragg gratings*", SPIE, Vol 3042, 1997, pp. 218-228

5-14 Max Mark Frocht, "*Photoelasticity*", Vol III, John Wiley&Sons, NY (1948)

5-15 A. Bertholds, R. Dändliker, "*Determination of the Individual Strain-Optic Coefficients in Single-Mode Optical Fibers*", JLT, Vol 6, No 1, 1988, pp. 17-20

5-16 A. Bertholds, R. Dändliker, "*Deformation of Single-Mode Optical Fibers Under Static Longitudinal Stress*", JLT, Vol LT-5, No 7, 1987, pp. 895-900

5-17 Lawrence C, Nelson D, Udd E, Bennett T. "*A fiber optic sensor for transverse strain measurement*", Experimental Mechanics 1999; 39 (3): 202-209

5-18 Y. Lo, J. Sirkis, K. Ritchie, *"A study of the optomechanical response of a diametrically loaded high-birefringent optical fiber"*, Smart Materials and Structures, 4, p. 327-333 (1995)

5-19 F. Bosia, Ph. Giaccari, M. Facchini, J. Botsis, H.G. Limberger, R.P. Salathé, *"Characterization of embedded fibre Bragg grating sensors written in high-birefringent optical fibres subjected to transverse loading"*, SPIE, Vol. 4694, p. 175-186 (2002)

5-20 paper submitted to ???

5-21 C. Lawrence, D. Nelson, E. Udd, T. Bennett, "*A fiber optic sensor for transverse strain measurement*", Experimental Mechanics, 39 (3), p. 202-209 (1999)

5-22 C.C. Ye, S.E. Staines, S.W. James, R.P. Tatam, *"A polarisation maintaining fibre Bragg grating interrogation system for multi-axis strain sensing"*, SPIE, Vol. 4694, p. 195-201 (2002)

5-23 F. Bosia, *"Internal strain measurements in composite laminates using fibre Bragg grating sensors*", PhD Thesis n.2621, EPFL (2002)

Chapter 6

FBG based humidity and temperature sensor

This chapter presents the results obtained in collaboration with the civil engineering department of EPFL on the development of a FBG based humidity sensor. The first section, based on a conference paper presented in 2001, reports the influence of temperature and relative humidity on polyimide coated FBG. The following section presents the published joined paper appeared in Optics letters in 2002. A theoretical approach of diffusion based on Fick's law has also been developed and numerically implemented to study the swelling properties of the polyimide used for fiber recoating. The results are not presented hereafter but can be found in the thesis work of Pascal Kronenberg (Thesis work, EPFL, 2002).

6.1 Influence of humidity and temperature on polyimide-coated fiber Bragg gratings

This section is based on the paper presented at the BGPP conference (Bragg Gratings, Photosensitivity, and Poling in Glass Waveguides) organized by the Optical Society of America in Stresa (June 2001). The contributing authors were :

- Philippe Giaccari, Hans G. Limberger : Institute of Applied Optics, Swiss Federal Institute of Technology
- Pascal Kronenberg : Institute of Structural Engineering and Mechanics, Swiss Federal Institute of Technology

6.1.1 Abstract

The influence of humidity and temperature on a polyimide coated in-fiber Bragg grating was investigated. The obtained normalized Bragg grating responsivities are $4.36 \cdot 10^{-6}$ RH%$^{-1}$ and $1.06 \cdot 10^{-5}$ K^{-1}, respectively.

6.1.2 Introduction

Intra-core fiber Bragg gratings (FBG's) have a huge application potential in telecommunication and sensor networks. The reliability of these devices is crucial for their long-term applications [1]. In addition, a channel spacing of 50 to 100 GHz in dense wavelength division multiplexing systems (DWDM) or precise temperature monitoring requires high wavelength stability over time in standard or harsh environments. Environmental parameters such as temperature and stress are known to alter the filter characteristics of FBG's [2, 3].

Here we report on first results on the sensitivity of polyimide coated FBG's to relative humidity with a cross-sensitivity to temperature. Bare fiber FBG's are insensitive to humidity as bulk glass. However, polyimide polymers are hygroscopic and swell in aqueous media. This coating swelling induces axial and radial strain in the fiber, modifying the Bragg condition of the FBG.

6.1.3 Experiment

A bare fiber Bragg grating (FBG1) and a polyimide coated FBG (FBG2) have been exposed to temperatures and relative humidity in a climate chamber (Fig. 6-1).

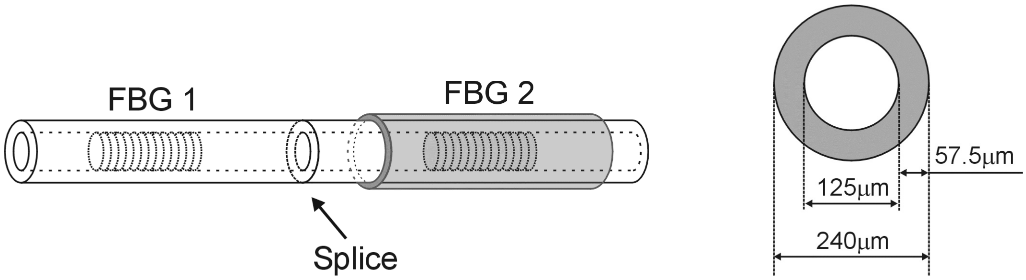

Fig. 6-1 Tests fiber Bragg gratings (left) and polyimide coated FBG geometry (right)

The experimental setup is shown in Fig. 6-2. The first grating around 1535 nm without coating has been fabricated in a SMF 28 fiber using ArF excimer laser and phase mask. The second FBG around 1550 nm is a commercial FBG that was recoated with a polyimide by the manufacturer. The re-coated fiber diameter was measured under a microscope and the coating thickness was determined to 57.5 μm. The gratings were spliced together and integrated into an FBG measurement setup. The reflectivity of both gratings is measured using a tunable laser and a photo detector with A/D converter.

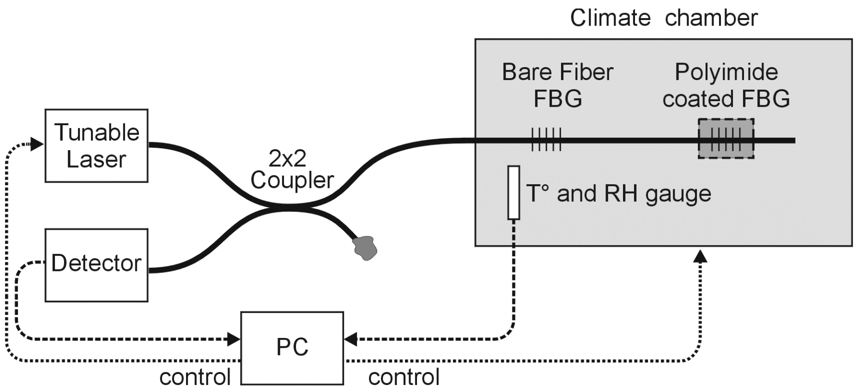

Fig. 6-2 Measurement set-up

A calibrated "Rotronic" electrical temperature (PT100) and relative humidity sensor (capacitive) are placed in the climate chamber. The sensor has a response time of less than one minute. A computer controls the environmental conditions in the climate chamber, controls the tunable laser, and performs the read out of the optical signal. From the reflection spectra of both gratings their Bragg wavelengths were obtained for different (RH, T) conditions.

The climate chamber maintains a constant temperature during RH variations. For six different temperatures from 23 °C up to 50 °C the relative humidity was changed from 10 RH% to 90 RH% in steps of 20 RH%. Unfortunately, the "Rotronic" sensor limited the maximal temperature. For every (RH, T) combination a measurement time of 120 minutes was taken to allow for a saturation of water within the polyimide. Every two minutes the changes of environmental conditions (RH, T) in the climate chamber were obtained from the "Rotronic" sensor and a full reflection spectrum of each FBG was taken. All data were stored on a computer for data processing.

The polyimide coating of the FBG has been removed after the experiment and the temperature sensitivity of both FBG's has been measured in a separate measurement setup. It consists of a temperature controlled water recipient with a mercury thermometer and the FBG reflection measurement set-up (Fig. 6-3).

Sensitivities of $6.78 \cdot 10^{-6}$ and $6.31 \cdot 10^{-6}$ K^{-1} were obtained for the SMF 28 and the commercial fiber, respectively. These values are in good agreement with published results [2,3]. The temperature obtained from the reference grating agreed well with the value obtained from the "Rotronic" sensor.

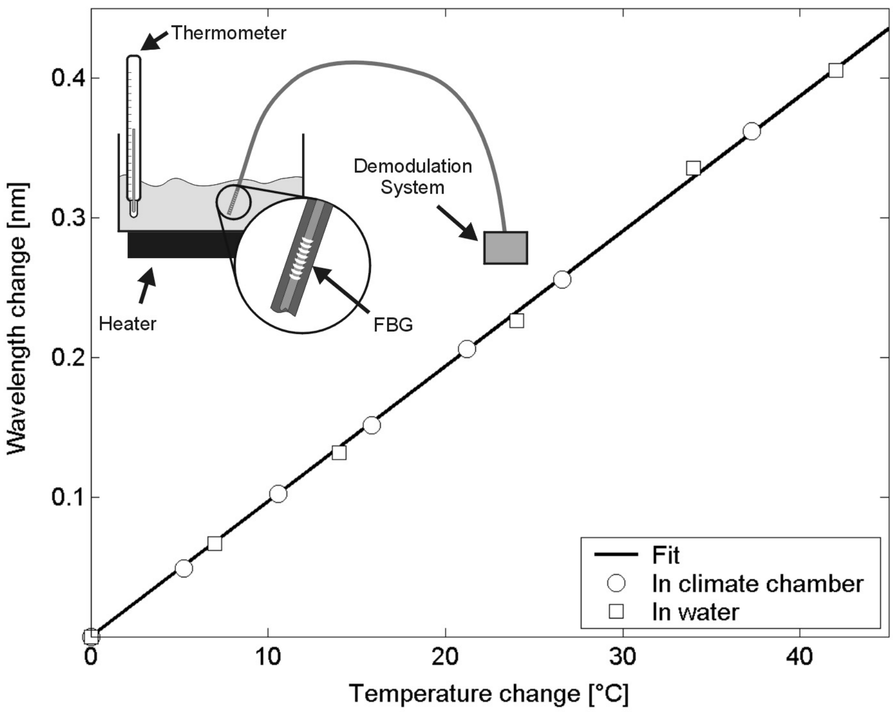

Fig. 6-3 Temperature sensitivity of FBG measurement and set-up (insert)

6.1.4 Results and discussion

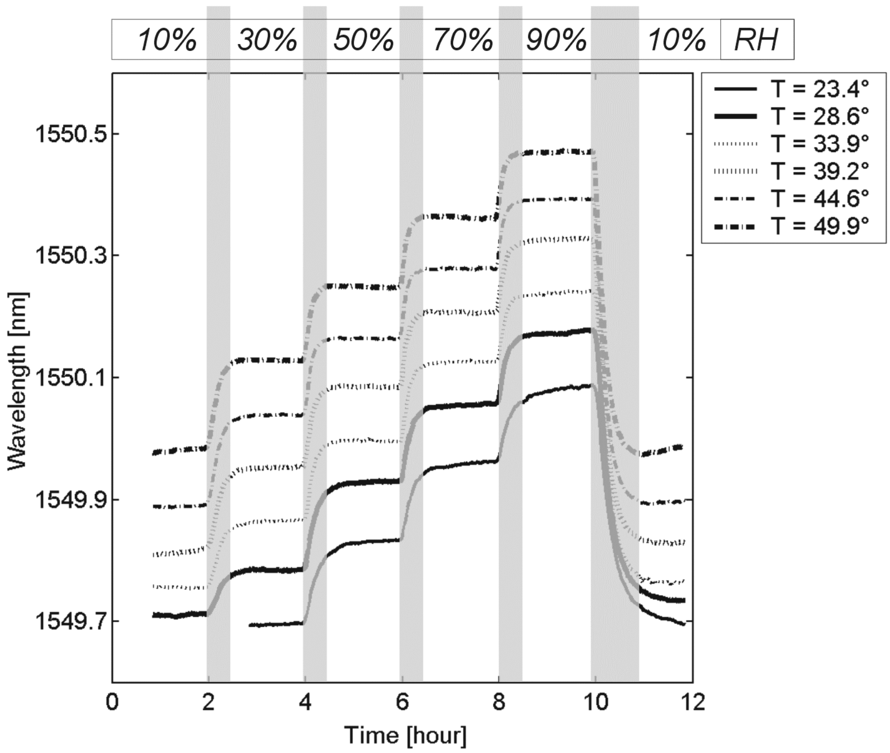

Fig. 6-4 Bragg wavelength of polyimide recoated in-fiber Bragg grating for different relative humidity and temperature

Fig. 6-4 shows the Bragg center wavelength of the polyimide recoated FBG as a function of time. At constant temperature an increase in humidity shifts the Bragg wavelength to higher values. The RH influence on the polyimide seems to be reversible, as the Bragg center wavelength is the same at the beginning and the end of the RH-cycle for constant temperature. Previous experiments have shown a non-reversible component depending on the maximum temperature that the FBG has experienced in the past. It may be due to a thermal curing process of the polyimide. This effect is not well understood and will be studied in the future.

For bulk polyimide, the volume variation for a RH change is isotropic in all directions. Since the polyimide is tightly attached to the fiber, polyimide longitudinal strains are transferred to the fiber. A volume change induced by the water content inside the polyimide matrix will lead to a fiber elongation or retraction.

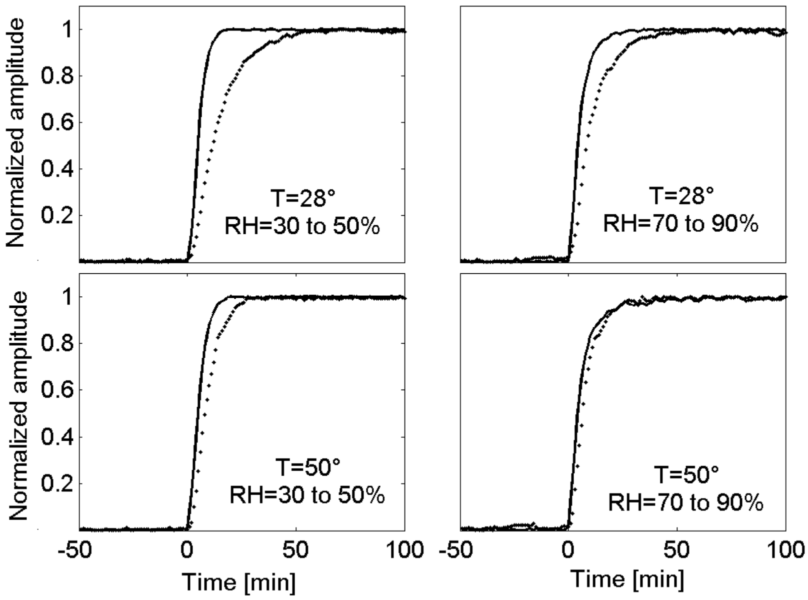

Fig. 6-5 Normalized FBG time response at 28 °C and 50 °C is compared to the normalized response of the RH sensor.

At each step the saturation level is obtained after several tens of minutes. The time constant of the process depends on temperature (Fig. 6-5). At low temperature the polyimide coated FBG responds much slower than the climate chamber RH evolution measured by the reference gauge ("Rotronic" sensor). With increasing temperature the response accelerates. Diffusion of water molecules through the coating determines probably the time constant [4].

Fig. 6-6 shows the Bragg wavelength shift as a function of relative humidity (steady state average values) for the different temperature cycles. For each temperature we obtain a linear function for the Bragg wavelength shift vs. relative humidity. Small deviations from linearity are within the measurement errors. We can describe the relative wavelength shift with temperature and relative humidity as:

$$\frac{\Delta\lambda}{\lambda} = A_T \cdot \Delta T + B_{RH\%} \cdot \Delta RH\% \qquad (1)$$

where A_T and $B_{RH\%}$ are the respective T and RH sensitivities of the polyimide recoated FBG. A two dimensional regression to the temperature and relative humidity data leads to

$$A_T = 1.06 \cdot 10^{-5} \pm 1 \cdot 10^{-7}\ \mathrm{K}^{-1} \qquad B_{RH\%} = 4.36 \cdot 10^{-6} \pm 5 \cdot 10^{-8}\ \mathrm{RH\%}^{-1},$$

where the errors are obtained as the respective standard deviations from the fit.

A relative humidity variation of 80% leads to a maximum wavelength shift of 0.54 nm at 1550 nm. This corresponds to a 33 °C temperature variation. This wavelength shift is more than 2/3 of the channel spacing in 100 GHz DWDM systems and may cause system failure. Polyimide re-coatings are generally used in high temperature environments (T > 120 °C). In such environments where relative humidity and temperature can change, temperature sensing needs the measurement of relative humidity by an additional grating. The observed linearity of the Bragg wavelength with relative humidity may find use in an all-fiber RH sensor [5].

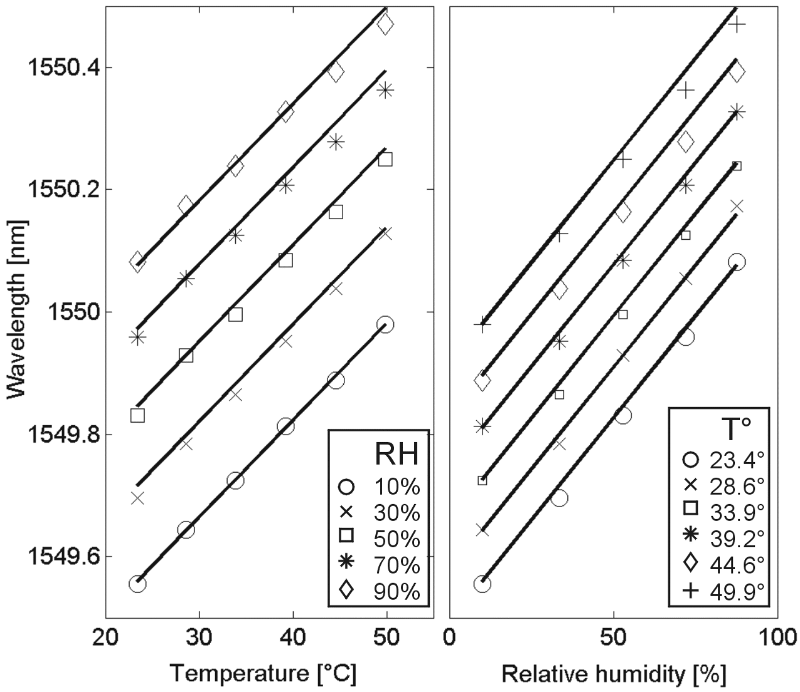

Fig. 6-6 Bragg wavelength shift of polyimide recoated FBG as a function of relative humidity for different temperatures.

6.1.5 Conclusion

The polyimide used for FBG re-coating leads to a sensitivity of the FBG wavelength to humidity and enhances its temperature sensitivity as expected. The polyimide coated FBG shows sensitivities of $4.36 \cdot 10^{-6}$ $RH\%^{-1}$ and $10.6 \cdot 10^{-6}$ K^{-1}. Relative humidity changes can lead to a wavelength shift of more than 0.5 nm at 1550 nm. For applications where the narrowband filter wavelength stability is essential like DWDM, less sensitive coatings or sealing have to be employed. In high temperature sensor applications, where polyimide coatings are necessary the RH cross sensitivity has to be considered.

6.1.6 References

1. H.G. Limberger and D. Varelas, "*Advances in Fiber Gratings: Technology, Applications, and Reliability.*", Proceedings of SPIE: Critical Reviews of Fiber Optic Components & Systems Reliability, vol. **CR73**, addendum, 1999.
2. G. Meltz, "*Overview of Fiber Grating-Based Sensors*", Proceedings of SPIE, vol. **2838**, pp. 2-21, 1996.
3. A.D. Kersey, M.A. Davis, H.J. Patrick, L. M., K.P. Koo, C.G. Askins, P. M.A., and E.J. Friebele, "*Fiber Grating Sensors*", Journal of Lightwave Technology **15** (8), pp. 1442-1463, 1997.
4. J.L. Armstrong, M.J. Matthewson, and C.R. Kurkjian, "*Moisture Penetration Through Optical Fiber Coatings*", International Wire & Cable Symposium, pp. 732-739, 1998.
5. P.Kronenberg, D. Inaudi, I. F.C. Smith, "*Development of an "optical hair"-hygrometer: A novel way to measure humidity using fibre optics*", Int. Conf. on trends in optical non-destructive testing, D. Inaudi, P.K. Rastogi ed., Lugano, pp. 467-474, 2000.

6.2 Relative Humidity Sensor Using Optical Fiber Bragg Gratings

This section presents the paper that has been published in Optics Letters, 27 (16), p. 1385–7. The authors are :

- Pascal Kronenberg, Pramod K. Rastogi : Institute of Structural Engineering and Mechanics, Swiss Federal Institute of Technology
- Philippe Giaccari, Hans G. Limberger : Institute of Applied Optics, Swiss Federal Institute of Technology

This paper presents a novel concept for an intrinsic relative humidity sensor using polyimide-recoated fiber Bragg gratings. Tests in a controlled environment indicate that the sensor has a linear, reversible and accurate response behavior between 10 and 90 %RH and between 13 and 60 °C. The relative humidity and temperature sensitivities were measured as a function of the coating thickness and the thermal and hygroscopic expansion coefficients of the polyimide coating were determined.

Numerous applications such as chemical processing, air conditioning, agriculture, food storage and civil engineering require humidity sensing. Several researchers have reported on the measurement of relative humidity in air using optical fiber sensors, which are particularly valued for their performance in harsh environments [1]. Optical sensing techniques proposed so far include extrinsic interferometric [2, 3] and spectroscopic [4] point sensors, as well as intrinsic evanescent-field [5] and microbend loss based [6] distributed sensors. Recently we presented a study on the influence of relative humidity and temperature on a commercial polyimide-recoated fiber Bragg grating [7]. Here we explore a novel concept for an intrinsic relative humidity point sensor using polyimide-recoated fiber Bragg gratings. We describe the steady state relative humidity and temperature response of the sensor as a function of the fiber coating thickness, which also allows us to determine the thermal and hygroscopic expansion coefficients of the polyimide.

Fiber Bragg grating sensors have been a topic of sizeable research efforts in recent years [8]. A fiber Bragg grating is a permanent, periodically index-changing structure written into the core of an optical fiber. Fiber Bragg gratings are attractive sensing elements since they feature a response that is reversible, accurate and stable over long time periods, can be used for absolute measurements and can be readily applied to in-line multiplexed sensor chains. The latter makes it possible to set up multi-point and multi-parameter (e.g. strain, temperature) single-fiber sensors.

Bare silica fibers are not sensitive to humidity. Polyimide polymers, however, are hygroscopic and swell in aqueous media as the water molecules migrate into them. Analogous to the hair in a mechanical hair hygrometer, the swelling of the polyimide coating induces strain in the fiber, which modifies the Bragg condition of the fiber Bragg grating and thus serves as the basis of the proposed sensor.

We have already shown that the response behavior of a polyimide-recoated fiber Bragg grating is a linear superposition of relative humidity and temperature effects [7]. In the presence of a variation in humidity and temperature, the relative Bragg wavelength shift, $\Delta\lambda/\lambda$, for relative humidity, ΔRH, and temperature changes, ΔT, is therefore given by

$$\Delta\lambda/\lambda = S_{RH}\Delta RH + S_T\Delta T \qquad (1)$$

where S_{RH} and S_T are the sensor sensitivities to relative humidity and temperature, respectively.

To relate the sensitivities to material properties, S_{RH} and S_T may be expressed as the sum of a mechanical, a strain- and, for S_T only, a thermo-optic contribution:

$$S_{RH} = \beta_{cf} - \hat{p}_e(\beta_{cf} - \beta_f) \quad \left[\%RH^{-1}\right] \tag{2}$$

and

$$S_T = \alpha_{cf} - \hat{p}_e(\alpha_{cf} - \alpha_f) + \xi \quad \left[K^{-1}\right] \tag{3}$$

where, β_{cf} and β_f are the hygroscopic expansion coefficients of the coated and the bare fiber – which is zero –, respectively; α_{cf} and α_f are the thermal expansion coefficients of the coated and the bare fiber, respectively. $\hat{p}_e = n_{eff}^2 (p_{12} + \varepsilon_{el,r} / \varepsilon_{el,z} (p_{11} + p_{12})) / 2$ is the effective photo-elastic constant of the coated fiber, where n_{eff} is the effective refractive index of the fiber, p_{ij} are the Pockel's (piezo) coefficients of the strain-optic tensor, and $\varepsilon_{el,r}$ and $\varepsilon_{el,z}$ are the radial and axial elastic strains of the coated fiber, respectively. ξ is the thermo-optic coefficient of the fiber core.

The mechanical behavior of the coated fiber is modeled with an infinitely long, bi-material composite rod wherein the two materials cohere perfectly. As both materials exhibit different relative humidity and temperature sensitivities, the humidity- and temperature-induced constrained expansion exerts strain on the fiber. Assuming a one-dimensional (1-D), purely axial model, the equilibrium and compatibility conditions are $\sigma_f A_f + \sigma_c A_c = 0$ and $\varepsilon_f = \varepsilon_c$, respectively, where, σ_i is the axial stress; A_i is the cross-section area; and ε_i is the total, i.e. elastic and thermal / hygroscopic, axial strain of the fiber (i = f) and of the coating (i = c). With the deformation obeying an elastic, Hookean law, the hygroscopic and thermal expansion coefficients of the coated fiber are the sums of the stiffness weighted expansion coefficients of the bare fiber and of the coating, $\beta_{cf} = k_f\beta_f + k_c\beta_c$ and $\alpha_{cf} = k_f\alpha_f + k_c\alpha_c$, respectively. β_c and α_c are the hygroscopic and thermal expansion coefficients of the coating, $k_i = E_iA_i / \Sigma E_jA_j$ is the stiffness proportion of the silica fiber and of the polyimide coating (i, j = f, c) with E_f and E_c being the moduli of silica and polyimide, respectively. Regarding $\hat{p}_e$, we notice that, using the 1-D model, $\varepsilon_{el,r}$ is set to zero (no radial strain). For a more realistic simulation of the mechanical behavior of the fiber, which also takes into account both radial and tangential effects, a 3-D finite element model was employed.

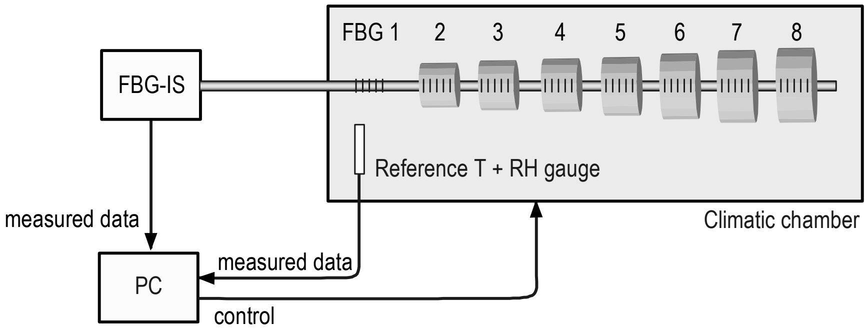

Fig. 1. Experimental setup.

The sensor response to relative humidity and temperature was experimentally measured in a computer controlled climatic chamber. An array of eight fiber Bragg gratings written in SMF 28 type fiber with different Bragg wavelengths in the 1550 nm band were spliced together and integrated into a fiber Bragg grating measurement setup (Fig. 1). The reflected spectrum was demodulated using a fiber Fabry-Perot tunable filter. For reference monitoring, an industry standards-compliant, combined resistive temperature (RTD) and capacitive relative humidity gauge from Rotronic was placed next to the gratings. A computer acquired the read out from the fiber Bragg grating interrogation system (FBG-IS) and from the reference gauge.

In order to quantify the influence of the coating thickness on the sensor sensitivity, one bare grating (FBG 1) and seven gratings with different average coating thicknesses of 3.6 (FBG 2), 6.6 (FBG 3), 11.8 (FBG 4), 18.7 (FBG 5), 21.3 (FBG 6), 27.3 (FBG 7) and 29.3 μm (FBG 8), respectively, were installed into the measurement system. The coating thickness, measured by microscope, exhibits an uncertainty of ± 1 μm due to non-homogeneity. All gratings were fabricated in-house and, with exception of FBG 1, mold-coated in a Vytran UV-recoater. The polyimide used for coating was obtained from HD MicroSystems (Pyralin®) and contains a UV-curable component, which is employed to transform the liquid polymer into a soft gel state before proceeding with the heat cure. The coating procedure had to be repeated several times to obtain thicker coatings.

For tests related to sensor characterization and calibration, the climatic chamber was set to maintain a constant temperature during relative humidity cycles. The relative humidity was incrementally raised from 10 to 90 %RH, and then lowered back down to 10 %RH, for five different temperatures between 13 and 60 °C. The highest temperature is limited by the maximum operating range of the electrical gauge. Yet additional tests have shown that the sensor is not damaged by being exposed to temperatures ranging from -20 up to 160 °C. For each relative humidity and temperature combination, measurements were taken in 1-minute intervals for two hours to make sure that the water content within the polyimide reaches an equilibrium state. As a rule, the Bragg wavelength shift saturates after a few minutes [7]. The changes in environmental conditions in the climatic chamber were monitored using the gauge, simultaneously with the recording of signals returned from each fiber Bragg grating.

Figure 2 shows the relative Bragg wavelength shift of FBG 8 as a function of relative humidity (steady state average values) for different temperatures. An increase in relative humidity or temperature shifts the Bragg wavelength to higher values. Experimental data are found to vary linearly with relative humidity and temperature changes, as assumed in the model described in eq. (1), confirming a linear relationship between relative humidity and polyimide expansion. A two-dimensional linear regression of the temperature and relative humidity data leads to temperature and relative humidity sensitivities of $S_T = (7.79 \pm 0.08) \cdot 10^{-6}$ K^{-1} and $S_{RH} = (2.21 \pm 0.10) \cdot 10^{-6}$ %RH^{-1}, respectively. The errors result from measurement uncertainties. Applying a quadratic regression, the quadratic and mixed terms are smaller than the uncertainties, which demonstrates that the material properties are not significantly influenced over the tested temperature range, neither by temperature nor by relative humidity.

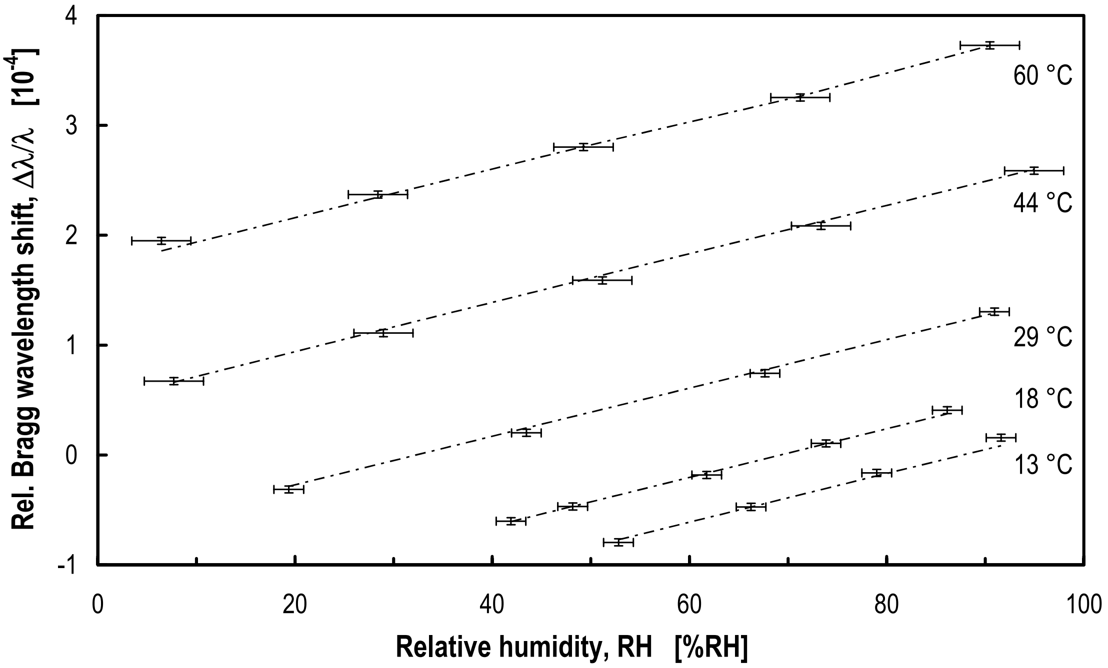

Fig. 2. Relative Bragg wavelength shift of FBG 8 as a function of relative humidity for different temperatures (zero relative Bragg wavelength shift arbitrary chosen).

The influence of relative humidity on the swelling of the polyimide is reversible, as the Bragg wavelength is the same at the beginning and at the end of a relative humidity cycle at constant temperature. Experiments have also shown a non-reversible component for temperatures exceeding values previously experienced. This may be due to a final thermal curing process needed for the polyimide to stabilize, and can be by-passed with an initial burn-in cycle.

Figure 3 shows the plots of the relative humidity, S_{RH}, and temperature sensitivities, S_T, with respect to cross-section areas of the polyimide coating, A_c, for all fiber Bragg gratings. For low coating to fiber cross-section area ratios, the fitted curves, which correspond to the sensitivity models (eqs. (2) and (3)), show an almost linear dependence of S_{RH} and S_T on A_c. The deviation from linearity is less than 4% for the coating thicknesses used in this work. For thicker coatings, the sensitivities eventually tend to saturate at values similar to those for bulk polyimide. As for the bare grating, $S_{RH} = 0\ K^{-1}$, whereas $S_T = (6.31 \pm 0.05) \cdot 10^{-6}\ K^{-1}$, which matches the temperature sensitivity obtained via an independent calibration measurement using a thermostatic water bath. Using the known thermal expansion coefficient of the fiber, α_f, we obtain the thermo-optic coefficient ξ (table 1). Our value is different from the values found in literature, e.g. [8], which might be due to the dependence of ξ on wavelength, temperature and core doping. Given the typical mechanical properties of a silica fiber, E_f = 72 GPa [10] and $\alpha_f = 0.05 \cdot 10^{-5}\ K^{-1}$ [9], the bare fiber diameter of 127 μm and the modulus of the polyimide, E_c = 2.45 GPa [11], we may determine the thermal and hygroscopic expansion coefficients of the polyimide. By fitting eqs. (2) and (3) based on the 1-D model to the corresponding S_{RH} and S_T data, the expansion coefficients become $\beta_c^{1-D} = 8.3 \cdot 10^{-5}$ %RH^{-1} and $\alpha_c^{1-D} = 5.5 \cdot 10^{-5}\ K^{-1}$, respectively. While α_c^{1-D} is higher than the value given by the supplier ($4 \cdot 10^{-5}\ K^{-1}$) [11], we could not trace any other value of β_c in the literature. With α_c^{1-D} and β_c^{1-D} used in the 3-D model, we calculated up to 16% higher sensitivities for the sensor geometries exploited in this work. Fitting the 3-D model to the experimental sensitivities gives estimations of $\beta_c^{3-D} = 7.4 \cdot 10^{-5}$ %RH^{-1} and $\alpha_c^{3-D} = 4.9 \cdot 10^{-5}\ K^{-1}$. Table 1 shows the material properties determined in this work as well as reference values. We notice that the mechanical contribution is higher for S_{RH} than for S_T; therefore, S_{RH} is more sensitive to coating thickness changes than S_T.

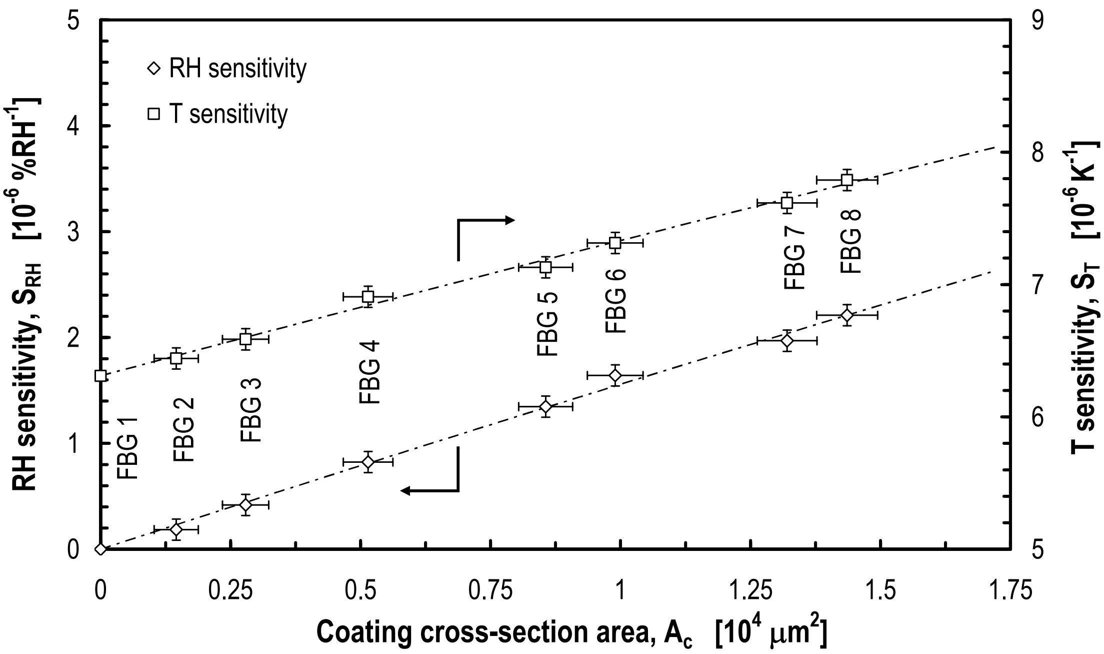

Fig. 3. Temperature and relative humidity sensitivities of fiber Bragg gratings with different polyimide coating thicknesses.

In summary, we presented a new fiber optic relative humidity sensor using polyimide coated fiber Bragg gratings. Tests in a controlled climatic chamber show a linear, reversible and accurate sensor response for temperature and relative humidity ranges from 13 to 60 °C, and 10 to 90 %RH, respectively. We may easily compensate for the temperature cross-sensitivity using an additional bare fiber Bragg grating, which is not humidity sensitive. The temperature and relative humidity sensitivities depend on the coating thickness, with the sensor becoming more sensitive with increasing coating thickness. Using this interrelation we were able to determine the hygroscopic and thermal expansion coefficients of the polyimide coating. From a practical point of view, the sensor proposed here is easy to implement, and may be readily integrated within a multipoint and -parameter optical fiber Bragg grating sensor network thanks to its multiplexing capabilities.

The authors would like to thank G. Tirabassi from Rotronic AG, Switzerland, who kindly agreed to lend us a calibrated temperature and relative humidity gauge.

Parameter	**This Work** 1-D	**This Work** 3-D	**Reference**	
Fiber (silica)				
Young's modulus, E_f [GPa]	-		72	[10]
Thermal exp. coeff., α_f [10^{-5} K^{-1}]	-		0.05	[9]
Hygroscopic exp. coeff., β_f [$\%RH^{-1}$]	0		0	
Thermo-optic coeff., ξ [10^{-5} K^{-1}]	0.581 (a)		0.617 (b)	[8]
Effective refractive index, n_{eff}	-		1.446 (a)	
Pockel's coeff., p_{11}	-		0.121	[9]
Pockel's coeff., p_{12}	-		0.270	[9]
Coating (polyimide)				
Young's modulus, E_c [GPa]	-		2.45	[11]
Thermal exp. coeff., α_c [10^{-5} K^{-1}]	5.5	4.9	4	[11]
Hygroscopic exp. coeff., β_c [10^{-5} $\%RH^{-1}$]	8.3	7.4	-	

(a) wavelength: 1550 nm; (b) wavelength: 1310 nm

Table 1. Fiber and coating material properties

1. J. Dakin, B. Culshaw, "*Optical Fiber Sensors*", vol. 1, Artech House Optoelectronics Library, Boston (1988).
2. F. Mitschke, "*Fibre-optic sensor for humidity*", Opt. Lett. **14** (1989), 967-969.
3. F.J. Arregui, Y. Liu, I.R. Matias, R.O. Claus, "Optical fiber humidity sensor using a nano Fabry-Perot cavity formed by the ionic self-assembly method", Sensors and Actuators B **59** (1999), 54-59.
4. M.R. Shahriari, G.H. Sigel Jr., Q. Zhou, "*Porous fiber optic for a high sensitivity humidity sensor*", Digest on Optical Fiber Sensors (1988), OSA, Washington D.C.
5. A. Kharaz, B.E. Jones, "*A distributed optical-fibre sensing system for multi-point humidity measurements*", Sensors and Actuators A **46-47** (1995), 491-493.
6. W.C. Michie, B. Culshaw, A. McLean, M. Konstantaki, S. Hadjiloucas, "*Distributed Water Ingress and Water Potential Measurements using Fibre Optics*", Cement and Concrete Composites **19** (1997), 35-44.
7. Ph. Giaccari, H.G. Limberger, P. Kronenberg, "*Influence of humidity and temperature on polyimide-coated fiber Bragg gratings*", BGPP, OSA, Stresa (2001), BFB2.
8. A.D. Kersey, M.A. Davis, H.J. Patrick, M. LeBlanc, K.P. Koo, C.G. Askins, M.A. Putnam, E.J. Friebele, "*Fiber Grating Sensors*", Journal of Lightwave Technology **15** (8) (1997), 1442-1463.
9. G.B. Hocker, "*Fiber-optic sensing of pressure and temperature*", Applied Optics **18** (9) (1979), 1445-1448.
10. F.P. Malinder, B.A. Proctor, "*Elastic constants of fused silica as a function of large tensile strain*", Physics of Chemistry of Glasses **5** (4) (1964), 91-103.
11. Pyralin® Product Information, HD MicroSystems (2001).

Chapter 7

OLCR based picometric vibration sensor

This chapter presents the paper (in preparation) about the development of a new OLCR based fiber optical vibration sensor for SNOM (Scanning Near-field Optical Microscopy) applications. This work has been conducted in collaboration with the SNOM group of the Applied Optics Institute (EPFL), in particular with Dr. Omar Sqalli.

The developed sensor exhibits remarkable potentials due to the very high sensitivity and the relative immunity against small air and vibrations perturbations.

7.1 Sub-pN shear-force feed back system in air and liquid

This section presents the paper currently in preparation. The authors are :

– Philippe Giaccari, Omar Sqalli and Hans G. Limberger : Institute of Applied Optics, Swiss Federal Institute of Technology

Scanning near-field optical microscopy requires a performant sensor to measure the tip-to-sample distance. In this letter, we report on a novel shear force detection scheme for scanning near-field optical microscopy applications. It is based on an all fiber low-coherence interferometer. This setup makes possible the measurements of the tip oscillation amplitude of less than 50 pm both in air and aqueous environment with a precision of 160 fm. Hz^{-1}, thus demonstrating the ability to perform topographic measurements both in air and in liquids with a resolution better than 1 nm in the height direction. Stable feedback in air and fluids is obtained with tip-sample interaction forces below 1 pN.

Scanning near-field optical microscopy (SNOM) has drawn considerable research interest in recent years since it allows the measurement of both the topography and the optical contrast of a sample with sub-wavelength resolution [7-1]. The instrument works by scanning a sub-wavelength size probe very close to the sample surface. The probe consists of a glass tip that can be covered with an opaque metal layer, with a clear aperture of sub-wavelength dimension at the tip apex [7-2]. A large majority of today's probe-sample distance control mechanisms works by detecting the damping of the oscillating tip by lateral forces (the so called "shear force") close to the surface [7-3]. Scanning-near-field optical microscopes require consequently performant sensors to measure nanometric oscillations of SNOM tips. Different methods have been proposed in the last ten years, such as a compact near-field optical module based on an external cavity laser interferometer [7-4] or the tuning fork [7-5,7-6] that allows measuring tip oscillation amplitudes of a few picometers in air. However, working in aqueous environment is more critical since a huge damping of the tip vibrations occurs upon immersion of several microns into liquid [7-7]. For investigations in aqueous environment, a new type of liquid cell was proposed, in order to limit the immersion depth of the SNOM probe [7-8]. Measurements in aqueous environment with the tuning fork system are possible only upon complete immersion of the tuning fork into liquid [7-9] with a typical vibrating tip amplitude of about 1 nm.

In this letter, a novel force detection scheme for scanning near-field optical microscopy applications is presented, theoretically described and experimentally tested. It is based on an all fiber low-coherence interferometer to measure extremely small SNOM tips oscillation amplitudes, both in air and aqueous environments.

The novel force detection scheme for scanning near-field optical microscopy applications is based on an all fiber low-coherence interferometer. The experimental set-up is presented in Fig. 7-1. A super luminescent laser diode (SLD) beam coupled into a single mode fiber (port 1) is used to illuminate a Michelson interferometer based on a 50/50% fiber coupler. At the end of the second interferometer arm (port 2), the measurement fiber, 4% of the light is reflected at the glass-air interface. 96% of the light is transmitted and partially reflected on the SNOM tip. The distance *d* between the SNOM tip and the end interface of the control fiber is typically 2 microns. Therefore, the tip interface and the fiber end face form a Fabry-Perot interferometer. A large part of the light reflected in this structure is coupled back into the optical fiber and is detected with a balanced detection system consisting of to photodiodes mounted at the other arms (port 3 and 4) of the Michelson interferometer. Monitoring the intensity of the interference fringes allows measuring the tip vibration amplitude. The balanced detection scheme improves the S/N ratio by reducing the source noise. The SLD source (SLD 56-MP SUPERLUM, 0.5 mW) spectrum has a full width at half maximum $\Delta\lambda$ of 44 nm centered at λo=1319nm, leading to a coherence length of the source of about 20 microns. The low coherence of the SLD source has ths advantage to eliminate spurious interference signals resulting from other reflections in the set-up (e.g., the coupler), thus leading to an increase of the signal-to-noise ratio of 30 dB. The SNOM-tip is mechanically excited by a piezoelectric element P2 located at x=0. The excitation is being supplied by a digital Lock-In Amplifier (SRS, RF Lock-In Amplifier, Model SR844). The measured optical interference signal is amplified by the Lock-in Amplifier and finally sent to a PC for storage and display.

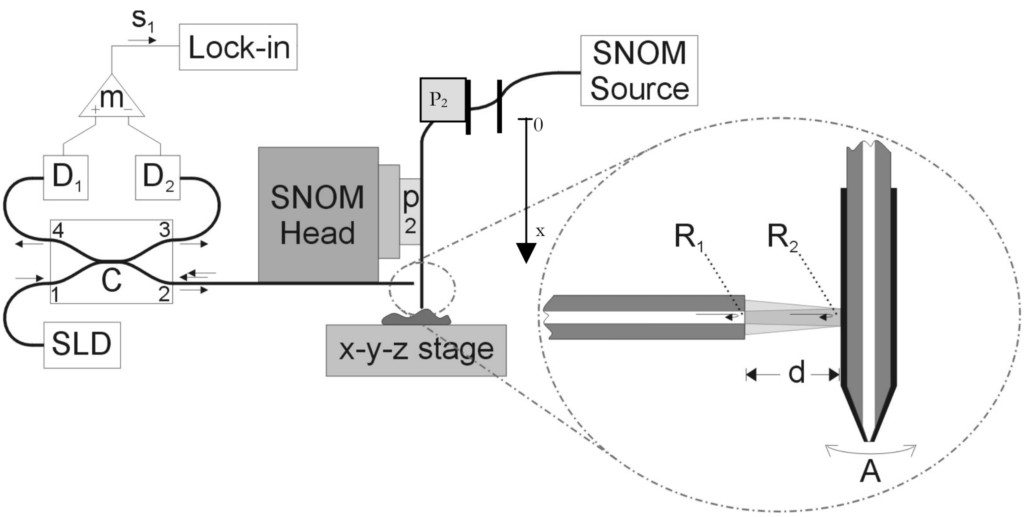

Fig. 7-1. Schematic drawing of the experimental set-up of the shear-force system based on low coherence interferometry. R1 (=4%) and R2 (=96%) are the reflection coefficients at the end of the control fiber and the SNOM tip, C a 50/50 optical coupler, D1 and D2 two detectors, p_2 a dithering piezo.

In order to calculate and characterize the SNOM fiber tip oscillations, we consider the vibration model of a beam clamped at one end and free at other [7-10]. The tip is described as a homogenous quartz cylinder, since the 100 microns long conical part of the tip is insignificant in comparison to several millimeters long cylindrical fiber. We thus consider a uniform radius *R* of 62.5 mm along the entire SNOM fiber length. The mass per unit length of the quartz is 8.6 mg/m, E the Young modulus is 72 GPa. For a given harmonic excitation frequency and a given fiber length, the vibrations amplitude at a distance from the clamped end is calculated by resolving the Euler fourth order differential equation [7-10]. Fig. 7-2 shows (a) the measured and (b) the calculated oscillations amplitudes at the middle of a 9.2 mm long quartz fiber that has a diameter of 125 mm. We observe six resonances with different amplitudes that correspond to the vibration modes. The precision of the vibration amplitude measurement is 160 fm/Hz$^{-1/2}$. The calculated resonance positions and relative amplitudes are similar to the experimental measurements.

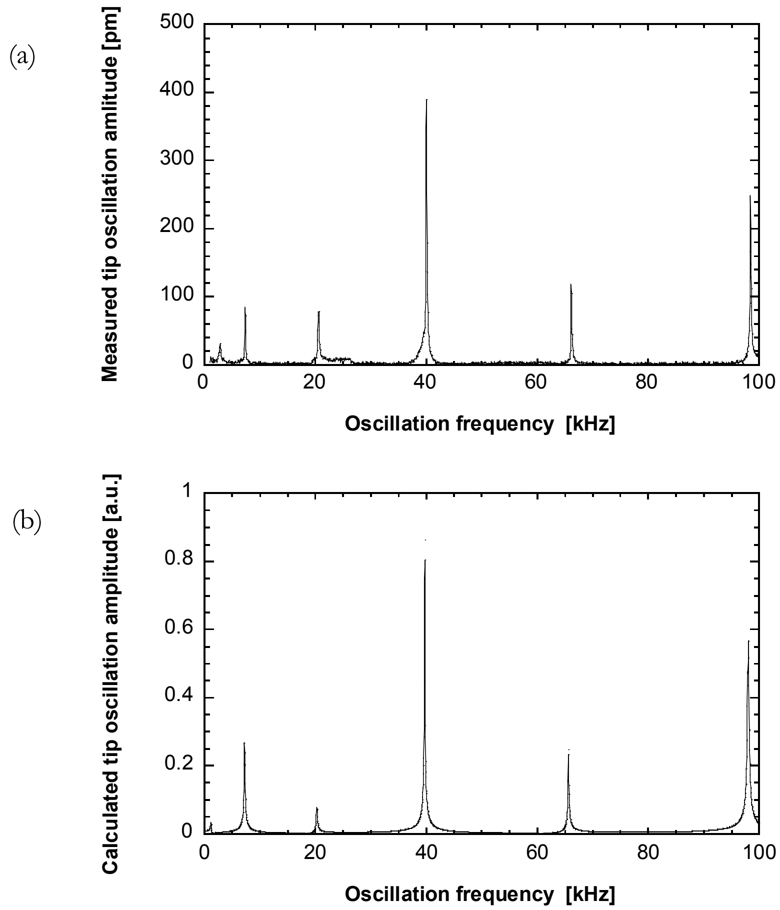

Fig. 7-2. Measured (a) and calculated (b) vibration amplitudes at the middle (x=4.6mm) of a 9.2 mm long SNOM tip.vibration amplitudes at the middle (x=4.6mm) of a 9.2 mm long SNOM tip.

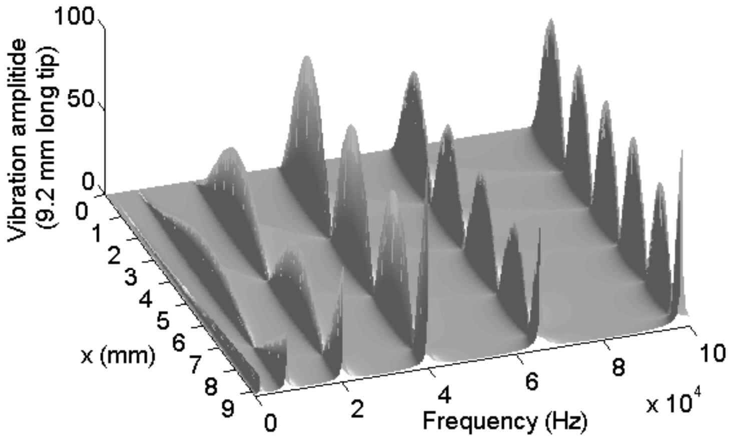

Fig. 7-3. Calculated vibration amplitudes of a 9.2 mm long SNOM tip as a function of the position x on the tip and the oscillation amplitude.

Fig. 7-3 illustrates the tip oscillations amplitudes calculated at a position x on the tip and as a function of the oscillation frequency. We observe six resonances with different amplitudes that correspond to the vibration modes. The theoretical calculations allow correctly estimating the oscillations at the end of the tip by measuring the oscillation amplitude in another part of the fiber tip, for a given eigenmode. The above described set-up makes possible to detect a minimal vibration amplitude of the SNOM tip of about 5 pm for a lock-in time constant of 1 ms, and of 1 pm for a time constant of 30 ms. Near-field optical microcopy measurements are consequently performed with typical oscillation amplitudes of 50-100 pm at the tip extremity, and a signal to noise ratio always superior to 10.

The vibration modes of the tip are experimentally investigated in aqueous solution. Fig. 7-4 illustrates the vibration amplitude measurements of 6.2 mm long quartz SNOM tip in air and in water, for different immersion depths of the tip in water. The vibrations measurements have been carried out at the middle of the fiber tip for the third eigenfrequency. First, a damping of the vibrations amplitude as well as a shift of the resonance frequency to lower values is observed when the immersion depth increases. The resonance position is shifted from 46.8 kHz to 44.5 kHz for a 2 mm immersion depth. Second, the Q factor decreases from 100 to 80 but remains always sufficiently high and makes possible performing SNOM measurements in water, even for immersion depth of 2 mm. The same behavior is observed for the other resonances showing that the vibration modes are preserved in water.

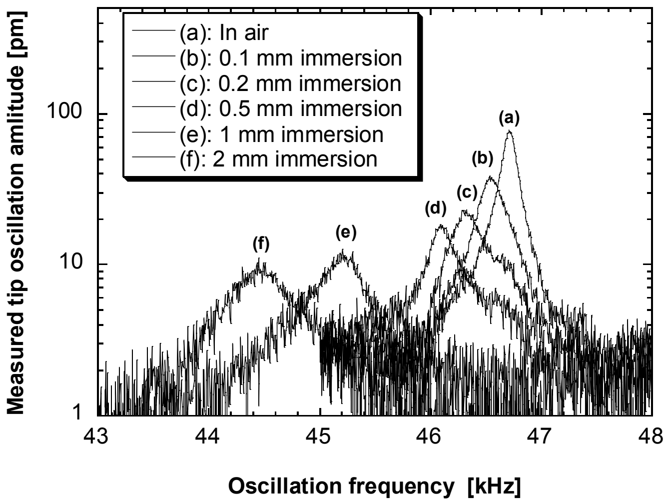

Fig. 7-4. Damping of the L=6.2 mm long tip oscillations, as a function of the oscillation frequency, for several tip immersion depths in water. The measurement is performed at x=3.1 mm, at the middle of the oscillating SNOM tip.

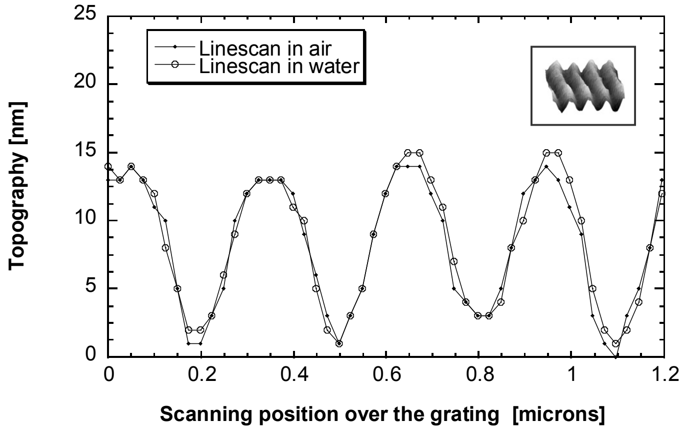

Fig. 7-5. Two topographic images of a 21 nm deep chromium on glass grating with a period of 372 nm performed with the same tip on the same sample in air then in water.

The previously described interferometric system is mounted in the SNOM set-up. A z-piezo vertically moves the tip, whereas an x-y piezo horizontally moves the sample. Fig. 7-5 shows two topographic slices of chromium on glass grating with a period of 372 nm performed with the same tip, in air and in water. The tip vibration amplitude at the tip extremity of 50 pm during the scan in both cases, with a signal-to-noise ratio was of about 50. The similarity of the images proves the reliability of the technique to perform accurate measurements both in air and aqueous environment with a height precision better than 1 nm. Moreover, the topographical contrast is nearly the same in air and in water. The lateral resolution is given by the probe shape.

To gain a better qualitative and quantitative understanding of the interaction force between the tip and the sample, a simple model called the effective mass harmonic model and described in reference [7-5,7-8] is used. Again, the SNOM fiber tip is considered as an uniform cylinder with a static spring constant k_{spring}. The tip-sample interaction shear-force Fint is obtained by measuring the free U_l and attenuated U_{int} vibration amplitude, at a specific resonance frequency with a precise Q quality factor: $F_{int} = k_{spring}(U_l - U_{int})/\sqrt{3}Q$. The SNOM tip described in Fig. 7-3 has a length L of 9.2 mm, a spring constant $k_{spring}=3EI/L^3$ of 3 N/m (fundamental eigenfrequency), where $I=\pi R^4/4$ is the inertia mement of the tip, a working free oscillation amplitude U_l at 2 kHz of about 50 pm, a Q factor of about 80. By choosing U_{int} equal to $0.9{*}U_l$, the measured shear force F_{int} is about 0.2 pN. Note that an increase of the probe length leads to a decrease of the probe static spring constant, and therefore to the detection of a smaller shear force for the same vibration amplitude. Higher eigenfrequencies are usually characterized by a higher Q factor, that allows measuring smaller forces, but also a higher spring constant of the tip, since the nodes reduce the effective oscillating length of the tip.

In conclusion, a new low coherent system has been implemented in force detection schemes for scanning near-field optical microscopy applications. It allows characterizing the SNOM-tip oscillation modes and amplitudes on the one hand, and, on the other hand, performing topographical measurements with a high precision both in dry and aqueous environments using the shear-force technique. The SNOM tip vibration amplitudes are typically 50-100 pm at the tip extremity during the scan. Topography measurements with a precision better than 1 nm in the z direction were performed without any control of the ambient temperature and humidity.

7.2 References

7-1 D.W.Pohl, W. Denk and M. Lanz, , Appl. Phys. Lett. 44, 651-653 (1984).

7-2 P.Lambelet, A. Sayah, M. Pfeffer, C. Philipona and F. Marquis-Weible, Appl. Opt. 37, 7289 (1998).

7-3 E.Betzig, P. L. Finn and J. S. Weiner, Appl. Phys. Lett 60, 2484 (1992).

7-4 M. Pfefffer, P. Lambelet and F. Marquis-Weible, Rev. Sci. Instr 68, 4478 (1997).

7-5 K. Karrai and I. Tiemann, Phys. Rev. B, vol.62, no.19; 13174 (2000).

7-6 A. G. T. Ruiter, K. O. van der Werf, J. A. Veerman, M. F. Garcia-Parajo, W. H. J. Rensen, N. F. van Hulst, Ulramicroscopy 71, 149 (1998).

7-7 O. Hollricher, R. Brunner and O. Marti, Ultramicroscopy 71, 143 (1998).

7-8 P. Lambelet, M. Pfeffer, A. Sayah and F. Marquis-Weible, Ultramicroscopy 71, 117 (1998).

7-9 W. H. J. Rensen, N. F. van Hulst, S. B. Kämmer, Appl. Phys. Letter 77, 1557 (2000).

7-10 W.T.Thomson, Theory of vibration with applications, Prentice HallIntroduction

Chapter 8

Conclusions and future work

8.1 Conclusions

The main parameter that describes a fiber Bragg grating is the refractive index distribution that can be expressed with three independent functions, the refractive index modulation amplitude, the average effective refractive index change and the grating period. A FBG is also spatially described by its complex coupling coefficient, which mixes the period chirp and the average refractive index chirp in a single phase function. The variations of these distributions can lead to various spectral and impulse responses.

A FBG can be described in three domains :

- space (z) domain with the refractive index distribution or the complex coupling coefficient function
- frequency (ν) domain with the reflection and transmission responses (complex)
- time (τ) domain with the complex impulse response (in reflection or transmission)

The T-matrix method has been used to calculate the complex spectral response $r(\nu)$ when the complex coupling coefficient distribution $q(z)$ is known. Inversely, $q(z)$ has been retrieved from $r(\nu)$ by the layer-peeling method. A modified T-matrix and the layer-peeling methods has been presented that take into account homogeneous distributed loss inside the grating.

For a wavelength bandwidth where the fiber dispersion is negligible, the complex OLCR response of a FBG corresponds to the convolution of the complex impulse response of the grating with the degree of coherence of the light source. A new OLCR set-up was developed that simultaneously measure the amplitude and the phase response of FBGs. The main results concerns the time-multiplexing OLCR set-up that exhibits a noise level of -120 dB for optical fiber devices (limited by the Rayleigh back-scattering) and a large range of allowed OPLD resolution due to the phase difference measurement principle. The high dynamic range of the OLCR opens the possibility to measure very weak gratings. The time-multiplexing OLCR set-up also offers the possibility to directly measure the complex spectral response of FBGs.

The complex coupling coefficient is obtained by application of the layer-peeling method. In order to distinguish the period chirp from the DC refractive index chirp, at least two reconstructions at different temperatures or axial strains are required.

The reconstruction process by layer-peeling has been simulated, while systematically varying the reconstruction parameters. It was shown that the required dynamic range of the starting spectral or impulse response is not fundamental and that the number of spectral points has to exceed 10 times the number of layers. Observation of the reconstruction of noisy data has shown that the influence of noise is less important for the reconstruction starting from the impulse response. Finally, the reconstruction process by layer-peeling is less accurate when applied to gratings that exhibit a spectral bandwidth saturation in reflection. Measurements from both sides and inducing a temperature or an axial strain ramp can improve the reconstruction of these gratings.

This reconstruction procedure was applied on homogeneous and non-homogeneous FBGs. The main results are an axial resolution of 20 μm and a maximal error of 5 % calculated by comparison between the reconstructions conducted from both side of the FBG. The reconstruction of a FBG that exhibits loss has also been performed using the modified layer-peeling method. The preliminary results show that a good matching between the reconstructions from both sides can be obtained with minimal remaining coupling coefficient amplitude behind the grating.

A fiber Bragg grating has been embedded in an epoxy sample and a non-homogeneous strain field has been induced in the sample by application of an axial stress. The results of the experiment are fairly good as the strain distribution is obtained along the grating (except for a little part less than 1 mm at each grating sides) and the global behavior is more or less corroborated by a finite element analysis. Nevertheless, this experiment needs to be performed a second time, as the applied loads were very high, inducing not-wanted plastic deformations of the epoxy sample.

An analytical model has been developed that simulates the diametric loading of fiber Bragg gratings. The behavior of FBG's written in low-birefringent fibers is completely described with this model. For gratings written in polarization maintaining fibers, the model completely explain the observed non-linear behavior (rotation of the fiber principal axis) but failed to explain the observed anisotropy between the transverse strain sensitivity of the fast and slow axis.

It has been shown that FBGs coated with polyimide show sensitivities to temperature and relative humidity change. A new fiber optic relative humidity sensor using polyimide coated fiber Bragg gratings has been presented. Tests in a controlled climatic chamber have shown a linear, reversible and accurate sensor response for temperature and relative humidity ranges from 13 to 60 °C, and 10 to 90 %RH, respectively. The dependence of this sensor to the coating thickness has been experimentally and mathematically studied.

A new low coherent system has been implemented in force detection schemes for scanning near-field optical microscopy applications. It allows characterizing the SNOM-tip oscillation modes and amplitudes on the one hand, and, on the other hand, performing topographical measurements with a high precision both in dry and aqueous environments using the shear-force technique.

8.2 Future work

More experiments needs to be performed in non-homogenous strain fields to completely validate the preliminary experiments. Further experiments are also required to study all the potentials of the evolution of the layer-peeling method for gratings that exhibit loss. It could even be possible to retrieve the local loss parameters by combining the reflection and transmission responses of the grating (in this case, the OCLR set-up has to be configured to measure the complex impulse response in transmission).

Another important perspective is to reconstruct the grating parameters for very strong FBGs. We have proposed a method where the grating is placed in a non-homogeneous axial strain field (or temperature field) and this method needs to be tested.

Important potentials of the presented reconstruction procedure exist, for example for controlling the FBG writing process or in the field of distributed sensing.

Appendix A

Slab waveguide and circular core fibe

This annex presents the basics of slab waveguides and optical fibers. It is based on the reference book of L.B. Jeunhomme, "Single-mode fiber optics", Second edition, Chapter 1 "Basic theory", Marcel Dekker, Inc (New York, Basel), 1990.

A.1 Slab waveguide

A.1.1 Maxwell's equations and solutions

We consider a symmetric slab waveguide of width 2a, core refractive index n_2 and cladding refractive index n_1 (Fig. A-1). The propagation direction is z, the direction orthogonal to the guide is x.

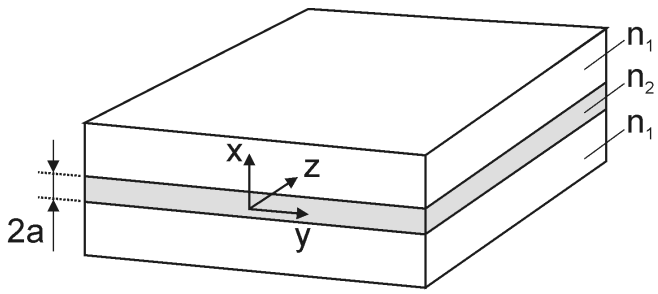

Fig. A-1 Slab waveguide geometry

The Maxwell's equations in dielectric materials lead to two self-consistent types of solutions. The first involves only E_y, H_x and H_z (transverse electric TE) and the second H_y, E_x and E_y (transverse magnetic TM), where E and H are the electric and magnetic fields. For the TE case, the Maxwell's equations reduce to

$$\frac{\partial^2 E_y}{\partial x^2} = -\left(k^2 n_j^2 - \beta^2\right) E_y \qquad \textit{(A-1)}$$

where β is the propagation constant ($\beta = \omega/c = 2\pi/\lambda$). A similar equation can be found for TM case (we limit further the study to the TE case only). The field variation along the x-axis will exhibit sinusoidal behavior where $k^2 n_j^2 > \beta^2$ (oscillating field) and exponential behavior elsewhere (evanescent field). Guided modes have propagation constant that fulfill the following relation

$$kn_2 \le \beta \le kn_1 \qquad \textit{(A-2)}$$

For β greater than kn_1 the field is evanescent everywhere and thus, carries no energy. For β smaller than kn_2, the field is oscillating everywhere and radiates laterally the energy (radiative modes).

We define a transverse propagation constant u/a and a transverse decay constant v/a defined as

$$\beta^2 = k^2 n_1^2 - u^2 / a^2 = k^2 n_2^2 + v^2 / a^2 \qquad \textit{(A-3)}$$

where u and v are chosen positive. We define also a dimensionless parameter V called the normalized frequency

$$V^2 = u^2 + v^2 = (ak)^2 \left(n_1^2 - n_2^2\right) \qquad (A\text{-}4)$$

Two kind of solutions are found from the field continuity condition at $|x| = a$

- Even TE modes

$$\left.\begin{array}{r} E_y, H_x \sim \cos(ux/a) \\ H_z \sim \sin(ux/a) \end{array}\right\} \quad |x| \le a$$

$$E_y, H_x, H_z \sim \exp(-v|x|/a) \quad \mathit{for} \quad |x| \ge a \qquad (A\text{-}5)$$

$$v = u \tan(u)$$

- Odd TE modes

$$\left.\begin{array}{r} E_y, H_x \sim \sin(ux/a) \\ H_z \sim \cos(ux/a) \end{array}\right\} \quad |x| \le a$$

$$E_y, H_x, H_z \sim \exp(-v|x|/a) \quad \mathit{for} \quad |x| \ge a \qquad (A\text{-}6)$$

$$v = -u / \tan(u)$$

The continuity conditions $v = u \cdot \tan(u)$ or $v = -u/\tan(u)$ and the condition $u^2 + v^2 = V^2$ imply that the structure can only support discrete modes. The fundamental mode TE_0 is always present and unique as long as the $V < \pi/2$. The first odd mode TE_0 appears for $V = \pi/2$. The third mode (even TE_1) appear at $V = \pi$ and so on. Each time the parameter V reaches a multiple of $\pi/2$, a new mode reaches its cutoff (for which $v = 0$ and $\beta = kn_2$).

A.1.2 Fundamental mode propagation constant and dispersion

We assume that there is no material dispersion (n_1 and n_2 are frequency independent). At zero frequency we have $\beta = kn_2$. When the optical frequency increases, V increases proportionally and u tends toward an asymptotic value of $\pi/2$ (β tends toward kn_1). In many case the waveguide is illuminated by a small bandwidth light centered at ω_0. In this case, the propagation constant can be developed at the second order

$$\beta(\omega) \cong \beta_0 + (\omega - \omega_0)\beta_0' + (\omega - \omega_0)^2 \beta_0'' / 2 \qquad (A\text{-}7)$$

where $\beta_0 = \beta(\omega)$, $\beta_0' = d\beta/d\omega$ and $\beta_0'' = d^2\beta/d\omega^2$ evaluated at ω_0. The term β_0' represents the group time delay per unit length and the term $-\beta_0''$ the chromatic dispersion due to the waveguide.

A.2 Optical Fiber Waveguide

A.2.1 Comparison with a slab waveguide

In circular core fibers, the general behavior of the electromagnetic field and of the modes is qualitatively similar to that of the slab waveguide. However, the presence of a dielectric discontinuity on a surface involving both the x and y variables has two consequences

- The modes label will contain two indices instead of one, the first index being related to the radial propagation constant and the second index to the azimutal periodicity of the field
- It is no longer possible to assume that there is no variation of fields along the y-axis, and we will thus find that some eigenmodes (especially the fundamental one) are not

purely transversely polarized but rather have a small longitudinal component for both the electric and magnetic fields. These modes are called HE and EH modes

A.2.2 Maxwell's equations

We consider a circular core fiber (Fig. A-2).

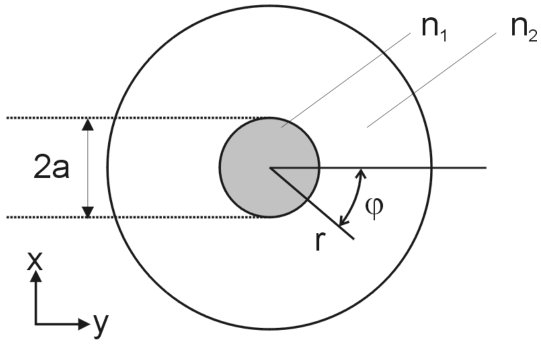

Fig. A-2 Circular core fiber geometry

We define the relative refractive index difference Δ as

$$\Delta = \frac{n_1 - n_2}{n_2} \tag{A-8}$$

In practice, Δ is smaller than 1 %, allowing the use of the scalar wave approximation (errors below 0.1 % are found for the mode characteristics) where in cylindrical coordinates the Maxwell's equations reduce to

$$\left[\frac{\partial^2}{\partial r^2} + \frac{1}{r}\frac{\partial}{\partial r} + \frac{1}{r^2}\frac{\partial^2}{\partial \varphi^2} + \left(k^2 n_j^2 - \beta^2\right)\right]\begin{bmatrix} E_z \\ H_z \end{bmatrix} = 0 \tag{A-9}$$

The normalized frequency V can be expressed in terms of Δ

$$V = \frac{2\pi a}{\lambda}\sqrt{n_1^2 - n_2^2} \cong akn_2\sqrt{2\Delta} \tag{A-10}$$

A.2.3 Fundamental mode HE_{11}

For V < 2.405 the fiber only support the fundamental mode HE_{11} (for slab waveguides the condition value was π/2). There are two HE_{11} modes, one polarized along the x-axis and the second one along y-axis, but they are degenerated due to the circular symmetry of the fiber. In this case, the fiber is called "single-mode". The cutoff wavelength is defined as

$$\lambda_c = V\lambda / 2.405 \tag{A-11}$$

The field distribution of the HE_{11} mode is given by (either E_x of E_y can be taken as 0)

$$E_{y,x} = \mp\frac{Z_0}{n_2}H_{x,y} = E_0 \cdot \begin{cases} J_0(ur/a)/J_0(u) & for \quad r \le a \\ K_0(vr/a)/K_0(v) & for \quad r \ge a \end{cases}$$

$$E_z = -i\frac{E_0}{kan_2}\left(\sin(\varphi), \cos(\varphi)\right) \cdot \begin{cases} uJ_1(ur/a)/J_0(u) & for \quad r \le a \\ vK_1(vr/a)/K_0(v) & for \quad r \ge a \end{cases} \tag{A-12}$$

$$E_z = -i\frac{E_0}{kan_2}\left(\cos(\varphi), \sin(\varphi)\right) \cdot \begin{cases} uJ_1(ur/a)/J_0(u) & for \quad r \le a \\ vK_1(vr/a)/K_0(v) & for \quad r \ge a \end{cases}$$

where the first of (sin(φ),cos(φ)) for E_z and of (cos(φ),sin(φ)) for H_z holds if $E_x = 0$, and the second holds if $E_y = 0$. Z_0 is the vacuum impedance, $J_{0,1}$ are the Bessel functions of order 0 and 1, $K_{0,1}$ the modified Bessel functions. The continuity equation is given by

$$u\frac{J_1(u)}{J_0(u)} = v\frac{K_1(v)}{K_0(v)} \qquad (A\text{-}13)$$

The longitudinal components of the fields are on the order of u/kan with respect to the transverse components. Using (A-4) and (A-10) and the fact that Δ is smaller than 1 %, we can consider the mode as transversely polarized with a linear polarization. This leads to the denomination of the LP_{01} mode.

A useful approximation for v(V) is given by

$$\mathrm{v} \cong 1.1428 \cdot V - 0.9960\left(= 2.7484 \cdot \lambda_c / \lambda - 0.9960\right) \qquad (A\text{-}14)$$

The corresponding u value is obtained from (A-4). The relative error in u compared to the exact solution is less than 0.1 % for 1.5 < V < 2.5 and increase to 1 % for 1 < V < 3.

The propagation constant β is also defined as in (A-3) and we define an effective refractive index of the mode, n_{eff}, as

$$n_{eff}{}^2 = \beta^2 / k^2 = n_2^2 + \frac{1}{(ak)^2}(1.1428 \cdot V - 0.9960)^2 \qquad (A\text{-}15)$$

We define the normalized propagation constant b, varying between 0 and 1 (only dependent of V)

$$b(V) = \frac{\beta^2 - k^2 n_2^2}{k^2 n_1^2 - k^2 n_2^2} = \left(\frac{\mathrm{v}}{V}\right)^2 = 1 - \left(\frac{u}{V}\right)^2 \qquad (A\text{-}16)$$

Using the fact that Δ is small, we can write

$$\beta = kn_2(1 + b\Delta)$$
$$b(V) \cong (1.1428 - 0.9960/V)^2 \left(= \left(1.1428 - 0.4141 \cdot \lambda / \lambda_c\right)^2\right) \qquad (A\text{-}17)$$

The error is less than 0.2 % for V between 1.5 and 2.5 (less than 2 % for V between 1 and 3).

The group delay τ, characterizes the propagation delay time per unit length of a modulated signal transmitted by the optical wave. It is obtained as

$$\tau = \frac{d\beta}{d\omega} = \frac{1}{c}\frac{d\beta}{dk} \qquad (A\text{-}18)$$

where c is the vacuum light speed. Neglecting the difference in the dispersive properties between the core and the cladding, the time delay can be expressed as

$$\tau = \frac{N_2}{c}\left(1 + \Delta(Vb)'\right) \qquad (A\text{-}19)$$

where $N_2 = d(kn_2)/dk$ is the group index of refraction of the material with refractive index n_2, and (Vb)' = d(Vb)/dV well approximated by

$$(Vb)' \cong 1.3060 - (0.9960/V)^2 \qquad (A\text{-}20)$$

The error is less than 1 % for 1.6 < V < 2.4 (less than 4 % for 1 < V < 3).

The dispersion description in fibers is more difficult as there is a mixing between the material dispersion (variation of N_2 and Δ with λ) and the waveguide dispersion (variations of b and (Vb)' with λ).

Appendix B

Modified phase mask technique description

B.1 Introduction

The schematic view of the writing set-up with the modified phase mask technique is presented in Fig. B-1. The cylindrical concave and convex lens should not be confounded with the lenses used for the beam reducer (aligned in the orthogonal direction). The parallel laser beam is $2h_0$ wide before entering the convex lens. The focal length of the convex lens is f_x and the one for the concave lens is f_v. The distance between the lenses is d_1, the distance between the concave lens and the phase mask output is d_2, and the distance between the phase mask surface and the center of the fiber is d_3.

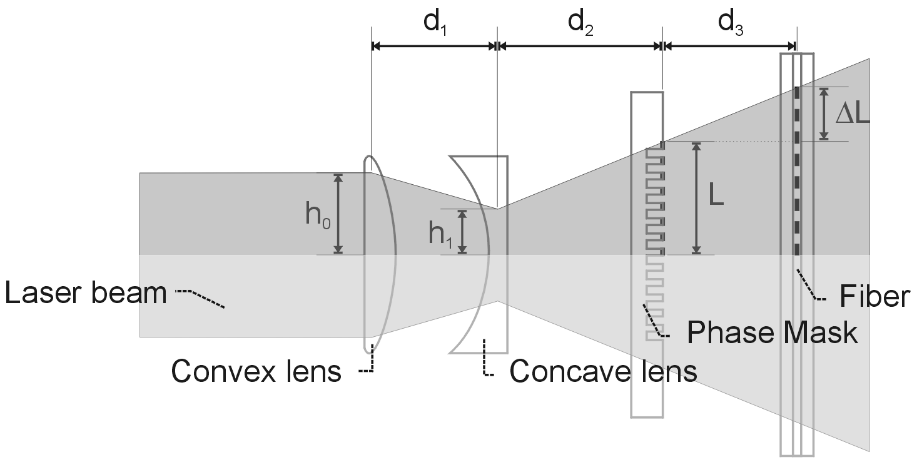

Fig. B-1 Principal parameters of the modified phase mask technique set-up

B.2 Ray optic concatenation of lenses

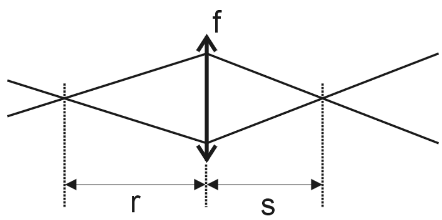

Fig. B-2 Single lens in ray optics approximation

For a single lens (Fig. B-2), the distance s is given by

$$s = \frac{r \cdot f}{r - f} \quad or \quad \frac{1}{f} = \frac{1}{r} + \frac{1}{s} \tag{B-1}$$

where f is the focal length (imaging equation). For a parallel entering light ($r = \infty$), $s = f$. Negative distance are possible for virtual converging points.

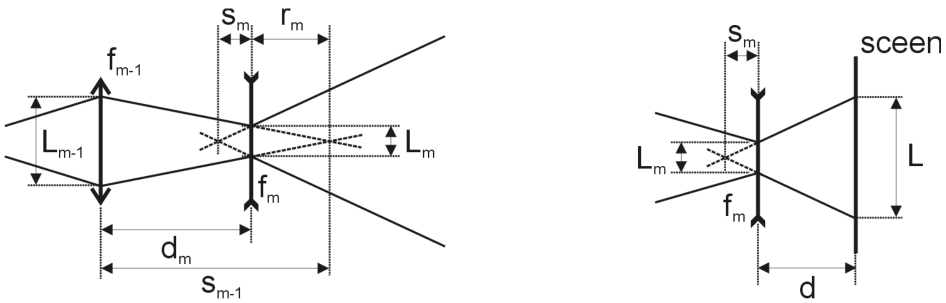

Fig. B-3 Two cascaded lens in ray optics approximation (left) and screen placed after the last lens (right)

For two cascaded lenses (Fig. B-3), we have the following relations

$$\begin{aligned} r_m &= d_m - s_{m-1} \\ s_m &= \frac{r_m f_m}{r_m - f_m} \\ L_m &= L_{m-1} \left| \frac{r_m}{s_{m-1}} \right| \end{aligned} \tag{B-2}$$

For the case with the screen, the spot size L is given by

$$L = L_m \left| \frac{d - s_m}{s_m} \right| \tag{B-3}$$

We note that in the case presented in Fig. B-3, the parameters s_m, r_m and f_m are negative. It is possible to use these equations in a recursive way for an arbitrary number of lenses.

B.3 Modified phase mask technique

From Fig. B-1 we see that $r_0 = \infty$, $s_0 = f_x$ and $L_0 = 2h_0$. We then obtain

$$\begin{aligned} r_1 &= d_1 - f_x \\ s_1 &= \frac{r_1 f_v}{r_1 - f_v} = \frac{(d_1 - f_x) \cdot f_v}{d_1 - (f_x + f_v)} \\ h_1 &= h_0 \left| \frac{d_1}{f_0} \right| \end{aligned} \tag{B-4}$$

The distances L and L+ΔL are given by

$$\begin{aligned} L &= h_1 \left| (d_2 - s_1) / s_1 \right| \\ L + \Delta L &= h_1 \left| (d_2 + d_3 - s_1) / s_1 \right| \end{aligned} \tag{B-5}$$

The relative Bragg wavelength change $\lambda_b/\lambda_{b,0}$ and the absolute Bragg wavelength shift $\Delta\lambda_b$ correspond to

$$\frac{\lambda_b}{\lambda_{b,0}} = \frac{L+\Delta L}{L} = \left|1+\frac{d_3}{d_2-s_1}\right| = 1+\frac{d_3}{d_2-\dfrac{(d_1-f_x)\cdot f_v}{d_1-(f_x+f_v)}} = 1+\alpha\cdot d_3 \qquad \text{(B-6)}$$

$$\Delta\lambda_b = \lambda_{b,0}\cdot\alpha\cdot d_3$$

where he magnification is close to 1 and then the |.| is omitted. We have realized a set-up with the following parameters :

- f_x = 100 mm
- f_v = -20 mm
- d_1 = 32 mm
- d_2 = 13 mm

We observe that for these parameters, the beam width is identical at the phase mask location to the beam size at the entrance ($L = h_0$). For an initial Bragg wavelength of 1550 nm, the parameter α has a value of 24.2 m^{-1}. For the fiber touching the phase mask, the distance d_3 = 62.5 μm (fiber radius) and then the Bragg wavelength shift is 2.35 nm as can be seen in Fig. B-4.

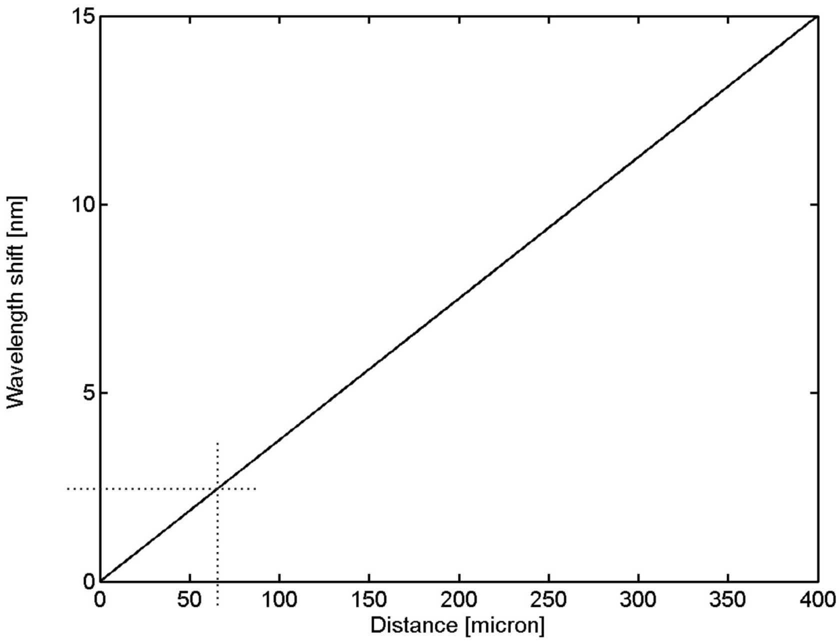

Fig. B-4 Wavelength shift for the realized set-up and a phase mask for FBG writing at 1550 nm

Appendix C

Coupled-mode description of FBG

This appendix is based on the work of J. Skaar in his thesis work, Chapter 2 "Fiber Bragg grating model" [C-1].

C.1 Scalar wave approximation

The fiber is assumed lossless, single mode and weakly guiding (small refractive index difference between the claddings $n_{cladding}$ and the fiber core n_{core}). The electromagnetic field is considered transverse to the fiber axis z and that the polarization state is conserved along the propagation (x-polarized). These hypotheses reduce the field description to the scalar wave equation [C-2]. A forward propagating wave with positive propagation constant β and pulsation ω has a phase term $e^{i(\beta z-\omega t)}$.

The fiber Bragg grating is treated as a perturbation of the fiber waveguide. The refractive index distribution of the fiber prior to the grating inscription is given by $\overline{n}(x,y)$ and the perturbed refractive index n(x,y,z) is z-dependant. The total electric field E_x is written as a superposition of the forward and backward propagating modes (b_+ and b_- respectively)

$$E_x(x,y,z) = b_+(z)\psi(x,y) + b_-(z)\psi(x,y) \tag{C-1}$$

The coefficients $b_\pm$ contain all the z-dependence of the modes when ψ describes the transverse dependence. The function ψ satisfies the scalar wave equation for the unperturbed fiber

$$\left\{\frac{\partial^2}{\partial x^2} + \frac{\partial^2}{\partial y^2} + k^2\overline{n}^2(x,y) - \beta^2\right\}\psi = 0 \tag{C-2}$$

where $k = \omega/c_0$ is the vacuum wavenumber (c_0 is the vacuum light speed) and $\beta = n_{eff}k$ (n_{eff} is the mode effective refractive index). The total electric field satisfies the scalar wave equation for the perturbed waveguide

$$\left\{\frac{\partial^2}{\partial x^2} + \frac{\partial^2}{\partial y^2} + \frac{\partial^2}{\partial z^2} + k^2n^2(x,y,z)\right\}E_x = 0 \tag{C-3}$$

From equations (C-1), (C-2) and (C-3) the following equation is obtained

$$\frac{d^2}{dz^2}(b_+ + b_-)\psi + \left(\beta^2 + k^2\left(n^2 - \overline{n}^2\right)\right)(b_+ + b_-)\psi = 0 \tag{C-4}$$

This equation is multiplied by ψ and integrated over the fiber section and then

$$\frac{d^2}{dz^2}(b_+ + b_-) + \left(\beta^2 + 2kn_{core}D(z)\right)(b_+ + b_-) = 0 \tag{C-5}$$

$$D(z) = \frac{k}{2n_{core}} \frac{\iint dxdy\left(n^2 - \overline{n}^2\right)\psi^2}{\iint dxdy\psi^2}$$

C.2 Coupled mode equations

The equation (C-5) can be separated in a set of two first order differential equations

$$\begin{aligned} \frac{db_+}{dz} - i(\beta + D)b_+ &= iDb_- \\ \frac{db_-}{dz} + i(\beta + D)b_- &= -iDb_+ \end{aligned} \qquad \text{(C-6)}$$

In absence of the grating, the modes propagate without affecting each other. Otherwise, the modes will couple to each other through the quantity D(z). The grating index perturbation can be expressed as

$$n^2 - \overline{n}^2 = \Delta\varepsilon_{ac}(z)\cos\left(2\pi z/\Lambda_d + \theta(z)\right) + \Delta\varepsilon_{dc}(z) \qquad \text{(C-7)}$$

where the design period Λ_d is chosen in order to guaranty a slowly varying phase function $\theta(z)$. The functions $\Delta\varepsilon_{ac}$ and $\Delta\varepsilon_{dc}$ are real and slowly varying function much smaller than n^2_{core}. The quantity D(z) can also be expressed as a quasi-sinusoidal function

$$D(z) = \kappa(z)\exp\left(\frac{i2\pi z}{\Lambda_d}\right) + \kappa^*(z)\exp\left(-\frac{i2\pi z}{\Lambda_d}\right) + \sigma(z) \qquad \text{(C-8)}$$

where $\kappa(z)$ is complex, slowly varying with z and $\sigma(z)$ is real, also slowly varying and represents the contribution of $\Delta\varepsilon_{dc}$. The forward and backward components $b_\pm$ are written as

$$\begin{aligned} b_+(z) &= u(z)\exp\left(\frac{i\pi z}{\Lambda_d}\right)\exp\left(i\int_0^z \sigma(z')dz'\right) \\ b_-(z) &= v(z)\exp\left(-\frac{i\pi z}{\Lambda_d}\right)\exp\left(-i\int_0^z \sigma(z')dz'\right) \end{aligned} \qquad \text{(C-9)}$$

The new variables u and v can be treated as the fields themselves once the reference planes have been fixed since they only differ from $b_\pm$ by constant, frequency independent phase factors. Starting from (eq. (C-6), using equations (C-8) and (C-9) and neglecting the rapidly oscillating terms that contribute little to the energy coupling we obtain the coupled-mode equations

$$\begin{aligned} \frac{du}{dz} &= i\delta u + q(z)v \\ \frac{dv}{dz} &= -i\delta v + q^*(z)u \end{aligned} \qquad \text{(C-10)}$$

where $\delta = \beta - \pi/\Lambda_d$ is called the wavenumber detuning and where q(z) is called the coupling coefficient and is defined as

$$q(z) = i\kappa(z)\exp\left(-2i\int_0^z \sigma(z')dz'\right) \qquad \text{(C-11)}$$

We note that the function u, v and q are slowly varying with z compared to the period Λ_d because β is close to π/Λ_d when the wavelength is close to the Bragg wavelength ($2n_{eff}\Lambda_d$).

C.3 Physical interpretation

We assume that the refractive index perturbation of the grating is homogeneous and restricted to the fiber core ($n_{cladding} = \bar{n}$) and then the D parameter is given by

$$D(z) = \frac{k}{2n_{core}}\left(n^2 - \bar{n}^2\right)\cdot\eta \qquad \text{(C-12)}$$

where η is the fraction of the modal power that is contained in the fiber core. From equations (C-7), (C-8) and (C-12) we see that $2|\kappa| = \eta k\Delta\varepsilon_{ac}/2n_{core}$, $\theta = \mathrm{Arg}(\kappa)$ and $\sigma = \eta k\Delta\varepsilon_{dc}/2n_{core}$. The refractive index change is small and then $\Delta\varepsilon = \Delta(n^2_{core}) = 2n_{core}\Delta n$ and using (eq. (C-11) we obtain

$$\begin{aligned} \left|q(z)\right| &= \eta\pi\cdot\Delta n_{ac}(z)/\lambda \\ Arg\left(q(z)\right) &= \pi/2 + \theta(z) - 2\eta k\int_0^z \Delta n_{dc}(z')\,dz' \end{aligned} \qquad \text{(C-13)}$$

Since the index perturbation is small, equation (C-7) can be written

$$n - \bar{n} = \Delta n_{ac}(z)\cos\left(2\pi z/\Lambda_d + \theta(z)\right) + \Delta n_{dc}(z) \qquad \text{(C-14)}$$

where Δn_{ac} and Δn_{dc} are the "ac" and "dc" index change, respectively. The following approximation has been used

$$n^2 - \bar{n}^2 \cong 2n_{core}\left(n - \bar{n}\right) \qquad \text{(C-15)}$$

The modulus of the coupling coefficient q is proportional to the refractive index modulation amplitude. The coupling coefficient phase corresponds to the excess optical phase of the grating; the term θ(z) is the spatial grating phase and the integral term gives the optical modification to the spatial phase due to the dc index change.

The derivative of the coupling coefficient phase gives the extra spatial frequency of the grating in addition to $2\pi/\Lambda_d$

$$dArg\left(q(z)\right)/dz = d\theta/dz - 2\eta k\Delta n_{dc}(z) \qquad \text{(C-16)}$$

and then an effective grating period can be defined for wavelength close to the Bragg grating as

$$\Lambda_{eff}(z) = \Lambda_d\left(1 + \frac{\Lambda_d}{2\pi}\cdot\frac{d\theta}{dz} - \eta\frac{\Delta n_{dc}(z)}{n_{eff}}\right)^{-1} \qquad \text{(C-17)}$$

C.4 References

[C-1] J. Skaar, PhD dissertation, The Norwegian University of Science and Technology, Ch. 2, 5-15 (2000)

[C-2] A.W. Snyder and J.D. Love, "Optical Waveguide Theory", Chapman & Hall (1983)

Appendix D

Fourier Transforms, Gaussian Function and FFT requirements for complex impulse response calculation

D.1 Fourier Transforms

D.1.1 Definition

Several notations and conventions are in use for Fourier transforms. In this work, the following relations are used [D-1]

$$TF\left(f\left(x\right)\right)=F\left(\xi\right)=\int_{-\infty}^{\infty}f\left(x\right)e^{-i2\pi\xi\alpha}d\alpha \qquad \textit{(D-1)}$$

$$TF^{-1}\left(F\left(\xi\right)\right)=f\left(x\right)=\int_{-\infty}^{\infty}F\left(\xi\right)e^{i2\pi\beta x}d\beta \qquad \textit{(D-2)}$$

where *TF* and TF^{-1} are the Fourier transform and inverse Fourier transform respectively.

D.1.2 Properties

Some fundamental properties are summarized hereafter

$$TF\left(f\left(x-x_0\right)\right)=e^{-i2\pi x_0\xi}F\left(\xi\right) \qquad \textit{(D-3)}$$

$$TF\left(f\left(\frac{x}{b}\right)\right)=\left|b\right|F\left(b\xi\right) \qquad \textit{(D-4)}$$

D.2 Gaussian Function

D.2.1 Definition

The Gaussian function *Gaus* is defined as

$$Gaus\left(\frac{x-x_0}{b}\right)=e^{-\pi\left(\frac{x-x_0}{b}\right)^2} \qquad \textit{(D-5)}$$

This function centered at x_0 has a height of unity and its area is equal to |b|.

D.2.2 Properties

Gaussian functions are often used for distributions like spectral density of a light beam. In this case, an important parameter is the distribution bandwidth found at mid-height Δx_{FWHM}, where FWHM means full width at half maximum. It is interesting to connect this value of Δx_{FWHM} with the Gaussian parameters b and x_0 and to find the corresponding points $x_{1,2}$ where the Gaussian is 0.5 (half the maximum)

$$|b| = \frac{\Delta x_{FWHM}}{2}\sqrt{\frac{\pi}{\ln(2)}} \tag{D-6}$$

$$x_{1,2} = x_0 \pm |b|\sqrt{\frac{\ln(2)}{\pi}} \tag{D-7}$$

The Fourier transform of a Gaussian is also a Gaussian

$$TF\left(Gaus(x)\right) = Gaus(\xi) \tag{D-8}$$

$$TF\left(Gaus\left(\frac{x-x_0}{b}\right)\right) = |b|e^{-i2\pi x_0\xi}Gaus(b\xi) \tag{D-9}$$

where (D-9) is a consequence of equations (D-3) and (D-4). The Fourier transform is complex with a maximum amplitude of |b| at $\xi=0$. The position $\xi_{1,2}$ where the Fourier transform amplitude reach the half of its maximum and the FWHM $\Delta\xi_{FWHM}$ are given by

$$\xi_{1,2} = \pm\frac{1}{|b|}\sqrt{\frac{\ln(2)}{\pi}} = \pm\frac{2\ln(2)}{\pi\,\Delta x_{FWHM}} \tag{D-10}$$

$$\Delta\xi_{FWHM} = \frac{2}{|b|}\sqrt{\frac{\ln(2)}{\pi}} = \frac{4\ln(2)}{\pi}\frac{1}{\Delta x_{FWHM}} \tag{D-11}$$

D.3 Matlab FFT and Gaussian example

D.3.1 Theory

The Matlab fast Fourier transform <fft> of a linearly discrete function $y(f_n)$ of the frequency f_n with steps of δf, is a linearly discrete function $Y(t_n)$ of the time t_n (impulse response) with steps of δt, $n \in [1..N]$. With the inverse Fourier transform <ifft>, $y(f_n)$ is calculated from $Y(t_n)$. Optimal calculation is found when $N=2^m$, m integer. To obtain a linear scale from negative to positive positions, the Matlab function <fftshift> has to be applied to the discrete Fourier transform, i.e. <fftshift(fft)> or <fftshift(ifft)>. The definition of f_n and t_n are

$$\textit{fftshift(fft)}: [t_n] = \left[-\frac{N}{2}, -\frac{N}{2}+1, \ldots, -1, 0, 1, \ldots, \frac{N}{2}-1, -\frac{N}{2}\right]\frac{1}{N}\cdot\frac{1}{\delta f} \tag{D-12}$$

$$\textit{fftshift(ifft)}: [f_n] = \left[-\frac{N}{2}, -\frac{N}{2}+1, \ldots, -1, 0, 1, \ldots, \frac{N}{2}-1, -\frac{N}{2}\right]\frac{1}{N}\cdot\frac{1}{\delta t} \tag{D-13}$$

The relation between δf and δt are

$$\delta t = \frac{1}{N \cdot \delta f} \qquad and \qquad \delta f = \frac{1}{N \cdot \delta t} \tag{D-14}$$

If f_n (or t_n) is not symmetric across zero, a constant phase shift factor is added to the Fourier or inverse Fourier transform. To increase the Fourier transform resolution, padding with zeros is possible directly with Matlab by calling the function with a size parameter, i.e. <fft(y(tn),M)>. In this case, the number M replace the parameter N in the equations (D-12), (D-14) and (D-13). It should be remembered that the maximal frequency that can be found by iFFT is determined by δt as $f_N=1/\delta t$.

D.3.2 Example

A SLD light source with Gaussian shape is chosen with $\Delta\lambda_{FWHM} = 40$ nm and centered at $\lambda_c = 1318$ nm. The SLD intensity *I(ν)* is

$$I(\nu) = Gaus\left(\frac{\nu-\nu_c}{b}\right) = e^{-\pi\left(\frac{\nu-\nu_c}{b}\right)^2} \tag{D-15}$$

The relations between ν_c, b, Δλ and λ_c are

$$\nu_c = \frac{c_0}{\lambda_c} \tag{D-16}$$

$$\Delta\nu = \frac{2c_0}{\Delta\lambda}\left(\sqrt{1+\frac{\Delta\lambda^2}{\lambda_c^2}}-1\right) \cong c_0\frac{\Delta\lambda}{\lambda_c^2} \tag{D-17}$$

$$|b| = \frac{\Delta\nu}{2}\sqrt{\frac{\pi}{\ln(2)}} \tag{D-18}$$

where c_0 is the light speed in vacuum ($2.9979 \cdot 10^8$ m/s). The discrete intensity between 1210 and 1410 nm with 5000 points is presented in Fig. D-1.

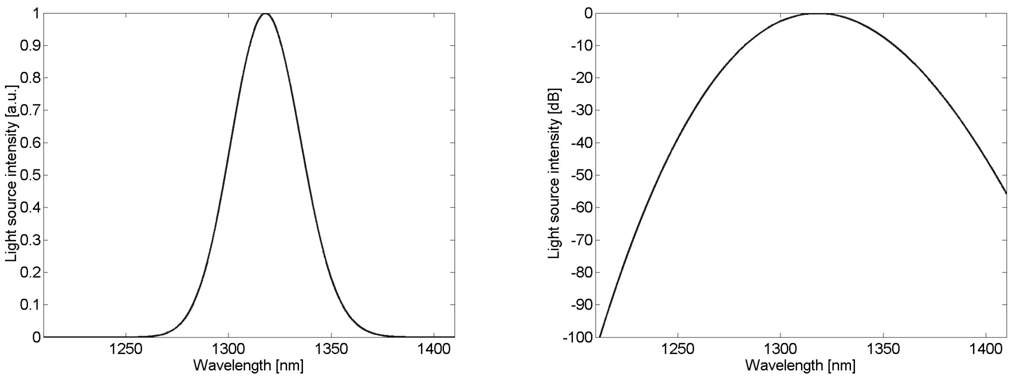

Fig. D-1 : Gaussian light source intensity in linear (left) and dB scale (right)

The Fourier transform of the light spectrum, which is the impulse response h(τ) of the light source and the pulse width $\Delta\tau_{FWHM}$ are given by

$$h(\tau) = TF(I(\nu)) = |b|e^{-i2\pi\nu_0\tau}Gaus(b\tau) = |b|e^{-\pi(b\tau)^2}e^{-i2\pi\nu_0\tau} \tag{D-19}$$

$$\Delta\tau_{FWHM} = \frac{2}{|b|}\sqrt{\frac{\ln(2)}{\pi}} \cong \frac{4\ln(2)\lambda_c^2}{c_0\Delta\lambda_{FWHM}} \tag{D-20}$$

The pulse width $\Delta\tau_{FWHM}$ is found to be 38.3µm/c_0. The calculated impulse response amplitude is presented in Fig. D-2. The impulse axis is the optical path difference between –120 and 120 µm corresponding to the travel distance in vacuum for the corresponding impulse time.

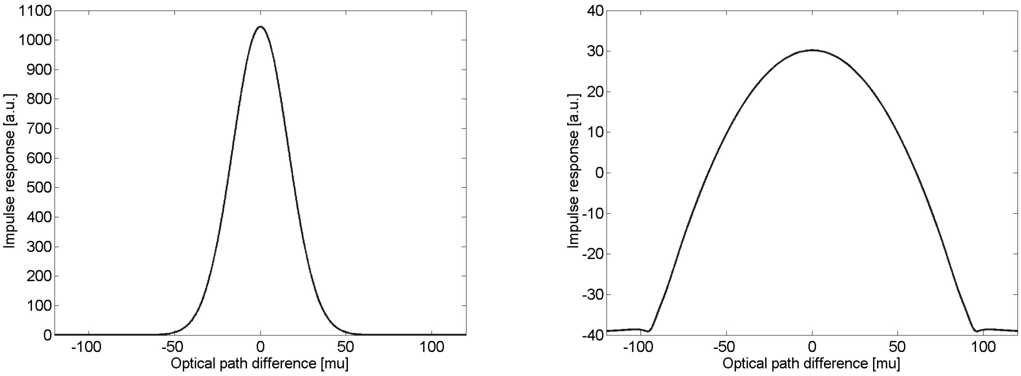

Fig. D-2 : Impulse response amplitude of the Gaussian light source intensity in linear scale (left) and in dB scale (right)

The impulse response outside the ±95 µm is no more the expected Gaussian function due to roundings in the calculation process.

D.4 References

D-1 J.D. Gaskill, "**Linear Systems, Fourier Transforms, and Optics**", John Wiley&Sons, NY (1978)

Appendix E

Polarization rotation effect on OLCR measurements

E.1 OLCR set-up

Fig. E-1 presents a simplified OLCR set-up where the propagation direction in the reference arm is denoted z and a polarization controller is placed in the test arm.

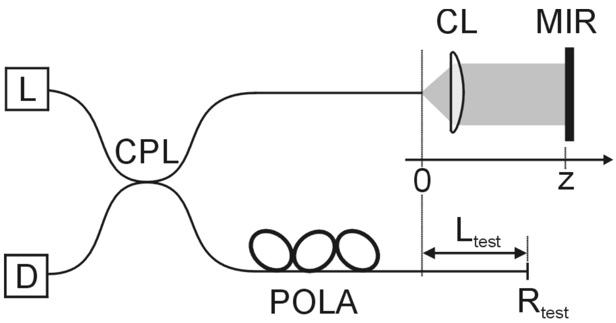

Fig. E-1 Simplified OLCR set-up : low coherent light source (L), coupler (CPL), converging lens (CL), mirror (MIR), polarization controller (POLA) and detector (D)

E.2 Interference intensity

To explain the polarization effects, the scalar description of the signal amplitudes is not adequate as it assume a single stationary polarization state that cannot be modified by the travel in the interferometer. We assume a stationary non-polarized light. For convenience, we define two orthogonal directions x and y which form with z a complete orthogonal reference system. The propagating light in the all-fiber interferometer is assumed to be a transverse electromagnetic (TEM) plane wave orthogonal to the traveling direction z. A vectorial amplitude signal E is then written in terms of its projection E_x and E_y on the directions x and y respectively

$$E(t) = \begin{bmatrix} E_x(t) \\ E_y(t) \end{bmatrix} = \begin{bmatrix} E_x(t) & E_y(t) \end{bmatrix}^T \qquad \text{(E-1)}$$

If θ is the polarization angle difference between the reference and the test light arriving at the detector, the signal amplitudes E_r and E_t are given by

$$E_r(t) = \alpha \cdot M(\theta) \cdot E(t+\tau) = \alpha \begin{bmatrix} \cos(\theta) & -\sin(\theta) \\ \sin(\theta) & \cos(\theta) \end{bmatrix} \begin{bmatrix} E_x(t+\tau) \\ E_y(t+\tau) \end{bmatrix}$$

$$E_r(t) = \beta E(t) = \beta \begin{bmatrix} E_x(t) \\ E_y(t) \end{bmatrix} \tag{E-2}$$

where β includes the complete reflection response of the test sample. The signal amplitude E_d and intensity I_d at the detector are given by

$$E_d(t) = E_r(t) + E_t(t) = \begin{bmatrix} E_{dx}(t) \\ E_{dy}(t) \end{bmatrix}$$

$$I_d = \left\langle |E_{dx}|^2 \right\rangle + \left\langle |E_{dy}|^2 \right\rangle = I_{dx} + I_{dy} \tag{E-3}$$

After some algebric manipulations we obtain

$$\begin{aligned} I_d(\tau) = {} & \left(\alpha^2 + \beta^2\right)\left(\left\langle |E_x|^2 \right\rangle + \left\langle |E_y|^2 \right\rangle\right) \\ & + 2\alpha\beta \cdot \cos(\theta) \cdot \mathrm{Re}\left(\left\langle E_x(t) E_x^*(t+\tau) \right\rangle + \left\langle E_y(t) E_y^*(t+\tau) \right\rangle\right) \end{aligned} \tag{E-4}$$

The spectral distribution is identical for all polarizations (same complex degree of coherence γ) and for non-polarized light, both orthogonal components have half the total source intensity I_s. This allows a reformulation of I_d

$$\gamma_x(\tau) = \frac{\left\langle E_x(t) E_x^*(t+\tau) \right\rangle}{I_s} = \gamma_y(\tau) = \gamma(\tau)$$

$$I_x = \left\langle |E_x|^2 \right\rangle = \left\langle |E_y|^2 \right\rangle = \frac{I_s}{2} \tag{E-5}$$

$$I_d(\tau) = \left[\left(\alpha^2 + \beta^2\right) + 2\alpha\beta \cos(\theta) \mathrm{Re}\left(\gamma(\tau)\right)\right] \cdot I_s$$

For θ = 0, the intensity I_d corresponds to the case where the polarization effects are neglected and the interferences are not perturbed. For other values of θ, the cosinus factor reduce the fringe visibility and in the worst case for θ = π/2, no interference at all will be detected.

Remerciements

Je tiens tout d'abord à remercier le Professeur René Salathé, mon directeur de thèse, pour la chance qu'il m'a offerte de parfaire ma formation au travers d'un projet enthousiasmant au sein d'un institut de grande qualité tant sur le point technique qu'humain. Les nombreuses discussions m'ont toujours permis de canaliser mon énergie vers les aspects importants, tout particulièrement en ce qui concerne l'interférométrie à basse cohérence. La gentillesse et la compétence du Professeur Salathé resteront longtemps gravés dans ma mémoire.

Mes jours à l'Institut d'Optique Appliquée n'auraient jamais été aussi profitables sans l'aide permanente apportée par le Docteur Hans Limberger, mon chef de projet, avec qui j'ai eu l'occasion de parfaire mes connaissances dans le domaine des réseaux de Bragg, de la fabrication à la caractérisation en passant pas de nombreux autres aspects. Son sens critique et sa motivation ont contribué pour une part importante dans la réussite de ce travail de thèse.

Je remercie fièrement mon pays, qui, au travers du fond national pour la recherche (projet "Experimental Stress Analysis of Composites Using Embedded Optical Fiber Sensors") et le soutient à l'EFPL, a financé en mes recherches (salaire et matériel de laboratoire).

Mon travail quotidien a été rempli de discussions constructives avec de nombreux collaborateurs, et en particulier mes collègues du groupe Telecom : Dimitris Varelas, Alessandro Iocco, Daniele Costantini, Marcel Zeller et Florian Dürr. Merci pour l'amitié dont ils m'ont gratifié et bonne chance pour leur carrière professionnelle. Je profite de l'occasion pour remercier chaleureusement le Docteur Thomas Sidler qui a toujours fait preuve d'une extrême gentillesse pour résoudre maints petits problèmes techniques ou pour dénicher la pièce dont j'avais besoin. Un merci également au personnel technique de l'institut (Ronald Gianotti, Claude Amendola et Alejandro Salamanca) et ses secrétaires (Martine Peter, Yvette Bernhard et Manuelle Borruat).

Durant mes deux premières années à l'IOA, j'ai partagé avec Claude Philipona la charge de l'informatique de l'institut. Le travail était conséquent mais grâce à la compétence et le l'amitié de Claude, nous sommes parvenus à un parc homogène de qualité. Encore merci !

Ce travail de thèse est le fruit de nombreuses collaborations à l'intérieur de l'école, en particulier avec le LMAF avec qui de nombreux travaux sur les capteurs de contrainte ont été réalisés. En particulier je tiens à remercier le Professeur John Botsis, la Professeur Kara Peters, Michel Studer, Laurent Humbert, Gabriel Dunkel, Philip Pattis et Federico Bosia. Le projet sur la sensibilité des réseaux de Bragg avec une gaine de polyimide ainsi que le développement du capteur d'humidité a été possible grâce au grand travail commun réalisé avec l'IMAC et en particulier avec mon collègue Pascal Kronenberg, dont la perpétuelle bonne humeur a grandement facilité l'accomplissement de la tâche.

Je tiens à faire une mention spéciale pour Omar Sqalli, arrivé en même temps que moi à l'institut, et avec qui j'ai partagé non seulement le bureau mais également une partie du travail, au travers du développement du capteur de vibration pour le SNOM ou de nombreuses discussions sur nos projets respectifs. Son amitié a toujours été sans faille, au travail et en dehors, comme pour les activités de marche ou de vélo, ou autour d'un verre (de vin du Valais, bien sûr).

La musique a toujours tenu une place importante dans ma vie et depuis plus de quinze ans, je partage les joies et les peines de ma société de musique, l'Harmonie Municipale de Sion. Merci à mes amis musiciens qui m'ont ouvert l'esprit et favoriser mon épanouissement personnel. Pour terminer, je désire remercier mes parents, ma famille (en particulier ma sœur Myriam, son mari Antonio et mes neveux Sarah et Jeremy, mon oncle Pascal et ma tante Yvonne) pour leur soutient, leur encouragement, leur patience et leur amour.

List of Publications

Journals

1. Ph. Giaccari, H.G. Limberger and R. Salathé, "*Local Characterization of Fiber Bragg Gratings Complex Coupling Coefficient*", Optics Letters, Submitted and Accepted for publication
2. Ph. Giaccari, H.G. Limberger, and R. Salathé, G. Dunkel, L. Humbert and J. Botsis, "*Longitudinal strain measurements with micrometer resolution using fiber Bragg gratings and low coherence reflectometry*", in preparation
3. Ph. Giaccari, O. Sqalli and H.G. Limberger, "Sub-pN shear-force feed back system in air and liquid", in preparation
4. P. Kronenberg, P.K. Rastogi, Ph. Giaccari and H.G. Limberge, "*Relative Humidity Sensor Using Optical Fiber Bragg Gratings*", Optics Letters, 27 (16), p. 1385–7 (2002)
5. K. Peters, Ph. Pattis, J. Botsis, Ph. Giaccari, "*Experimental verification of response of embedded optical fiber Bragg grating sensors in non-homogeneous strain fields*", Journal of Optics and Lasers in Engineering, Vol 33, pp. 107 (2000)
6. F. Bosia, J. Botsis, M. Facchini and Ph. Giaccari, "*Deformation characteristics of composite laminates, part I: speckle interferometry and embedded Bragg grating sensor measurements*", Composites Science and Technology, 62 (1), p. 41-54 (2002)
7. F. Bosia, Ph. Giaccari, J. Botsis, M. Facchini, H.G. Limberger, R. Salathé, "*Characterization of fibre Bragg grating sensors subjected to 2-D strain fields*", in preparation
8. M. Studer, J. Pietrzyk, K. Peters, J. Botsis, Ph. Giaccari, "*Studies on Bridging Tractions – Simultaneous Bridging Tractions and COD measurements*", International Journal of Fracture, Vol 114, pp. 379 (2002)

Conferences

9. Ph. Giaccari, H.G. Limberger and R. Salathé, "*Local Coupling Coefficient Characterization of Fiber Bragg Gratings by Optical Low Coherence Reflectometry*", Summer School on Photosensitivity in Optical Waveguides and Glasses (POWAG), Saint-Petersburg (2002)
10. Ph. Giaccari, H.G. Limberger and P. Kronenberg, "*Influence of humidity and temperature on polyimide-coated fiber Bragg gratings*", BGPP, OSA, Stresa (2001), BFB2.
11. K. Peters, P. Pattis, J. Botsis, P. Giaccari, "*Experimental Verification of Response of Embedded Optical Fiber Bragg Grating Sensors in Non-Homogeneous Strain Fields*," proceedings of the International Conference on Trends in Optical Nondestructive Testing, Lugano (2000)
12. F Bosia, P. Giaccari, M. Facchini, J. Botsis, H. Limberger, R. Salathe, "*Characterisation of embedded fibre Bragg grating sensors written in high-birefrigent optical fibres sebjected to transverse loading*" SPIE, Smart Sensor Technology & Measurement Systems, Vol. 4694, p. 175-186 (2002)
13. F. Bosia, G. Zambaz, M. Facchini, J. Botsis, Th. Gmür, Ph. Giaccari, "*Electronic Speckle Pattern Interferometry and Embedded Fibre Bragg Grating Sensors for Composite Plate Bending Measurements*". Proceedings of the SEM IX International Congress on Experimental Mechanics, Orlando, Society for Experimental Mechanics, Bethel, pp.147-150 (June 5-8 2000)
14. F. Bosia, G. Zambaz, M. Facchini, Th. Gmür, J. Botsis, Ph. Giaccari, "*ESPI and Embedded FBG Sensors for Composite Plate Bending Measurements*", Proceedings of the SEM IX International Congress on Experimental Mechanics, Orlando (June 5-8 2000)
15. K. Peters, Ph. Pattis, J. Botsis, Ph. Giaccari, "*Experimental verification of embedded optical fiber Bragg grating sensors in non-homogeneous strain fields*", Proceedings, International Conference on Trends in Optical Nondestructive Testing, pp.435-445 (May 2000)
16. M. Studer, J.Pietrzyk, K. Peters, J. Botsis, Ph. Giaccari, "*Experimental and numerical studies on bridging tractions using embedded OFBG sensors*", Proceedings, MESOMECH (2000)
17. M. Studer, J. Pietrzyk, K. Peters, J. Botsis, Ph. Giaccari, H.G. Limberger, R. Salathe, "*Optical fiber Bragg grating applied to study bridging tractions*", Mesomechanics 2000, G.C. Sih, Vol 1, pp. 519 (2000)

Curriculum Vitae

Name	Giaccari
First Name	Philippe
Date of Birth	31.08.1973
Nationality	Swiss (Vouvry, VS)
Address	Rue des Grands-Prés 35, 1958 Uvrier
e-mail	philippe.giaccari@a3.epfl.ch

Formation

09.1998 – 01.2003	**Ph.D. in Science** Institute of Applied Optics, Swiss Federal Institute of Technology
10.2000 – 01.2003	**MBI** (Master of Science in Business of Information Systems) University of Lausanne, Haute Ecole Commerciale
10.1993 – 03.1998	**Diploma of Physicist Engineer EPF** Physics Department, Swiss Federal Institute of Technology
09.1988 – 06.1993	**Scientific Maturity** Lycée-Collège des Creusets, Sion (VS)

Experience

09.1998 – 01.2003	Thesis work "Fiber Bragg Grating Characterization by Optical Low Coherence Reflectometry and Sensing Applications", supervisor Prof. René Salathé and Dr. Hans Limberger Fabrication of fiber Bragg gratings, conception and realization of a new low coherence reflectometer
07.2002 – 12.2002	MBI practical work "Gestion des Processus Business et Modélisation des Processus Business d'une Start-up de Type Cybermédiaire", supervisor Prof. Silvio Munari
10.1998 – 06.2001	Management of the institute informatics : purchase, configuration and maintenance for 100 computers, 2 servers and 60 users
07.1998 – 08.1998	IASTE exchange : collaboration project between Seagate and the Physics Departement of the Queens University of Belfast, supervisor Prof. Ron Atkinson
02.1998 – 06.1998	Work at the IMO (Institute of Micro- and Opto-Electronics)
10.1997 – 01.1998	Diploma work "Realization and Characterization of Optical Waveguide incorporating Quantum Wires", supervisor Prof. Franz-Karl Reinhart (Physics Department, IMO)

Languages

French	Mother tongue
English	Fluent spoken and written
Italian	Good knowledge
German	Good knowledge

Hobbies

Music (saxophone player since 1986), sport (hiking, cycling, skiing)